IPP-Report

Max-Planck-Institut
für Plasmaphysik

Rodrigo Arredondo Parra

SIESTA: A new ion source setup and its application to erosion studies on first-wall materials for fusion reactors

IPP 2019-10
Mai 2019

Technische Universität München
Fakultät für Maschinenwesen

SIESTA: A new ion source setup and its application to erosion studies on first-wall materials for fusion reactors

Rodrigo Arredondo Parra, M. Sc.

Vollständiger Abdruck der von der Fakultät Maschinenwesen der Technischen Universität München zur Erlangung des akademischen Grades eines

Doktor-Ingenieurs (Dr.-Ing.)

genehmigten Dissertation.

Vorsitzender: Prof. Dr. mont. habil. Dr. rer. nat. h.c. Ewald Werner

Prüfer der Dissertation:
1. Prof. Dr. Rudolf Neu
2. Prof. Rafael Macián-Juan, Ph.D.

Die Dissertation wurde am 13.11.2018 bei der Technischen Universität München eingereicht und durch die Fakultät Maschinenwesen am 06.03.2019 angenommen.

Acknowledgments

This thesis would not have been possible without the help of many people.

I would first like to thank my supervisors, Dr. Martin Oberkofler, Dr. habil. Wolfgang Jacob and Prof. Dr. Rudolf Neu. Throughout the project, I have always been able to count on their continued support, and their ongoing assistance and insight has been inestimable. I could not have asked for better supervisors, and am very grateful to have been able to count on them.

There are many people I would like to thank from the Max-Planck-Instute for Plasma Physics. First among them are the members of my working group for their assistance and encouragement, for their helpful comments and suggestions during the PMI Round table every Thursday, and for the lively discussions every Wednesday at 8:00. From the beginning they have included me in the team, and have made me want to come to work every day. I would also like to thank all of the E2M technical specialists, especially Arne Friedrich of the electrical workshop. They have helped me immensely and, without them, SIESTA would not be what it is today.

Further, I would like to thank the pellet group of ASDEX Upgrade, who took me in when I came to the IPP as a intern and who supervised me during my master's thesis. Outside of the IPP I would like to thank Prof. Dr. Rafael Macián-Juan for guiding me through my studies at TUM and Prof. Dr. Antonino Cardella for introducing me to the world of nuclear fusion.

Lastly, I would like to thank my friends, family, and especially my girlfriend Carolin for their unrelenting encouragement and support, for which I am incredibly grateful.

Abstract

The interaction of plasma-facing components (PFCs) with the fusion plasma is a critical issue in the development of future fusion devices, as it imposes a series of safety, operational and economic constraints. Chiefly, it impacts the lifetime of the PFCs, dust production and tritium retention in – and permeation through – the inner walls of the device.

At the first wall, erosion is predominantly driven by physical sputtering due to bombardment with energetic neutrals with a typical energy of several hundred eV, though a small fraction of neutrals can impinge with energies in the keV range. This process has historically been studied in simulations modelling Coulomb interactions and experimentally in plasma devices and ion sources. Plasma devices aim to emulate the conditions at the plasma edge of a fusion reactor, and typically allow for high particle flux densities to the target surface, which are necessary to achieve fluences relevant for reactor operational lifetimes. However, quantitative analysis of results may be compromised due to the presence of multiple ion species, impurities in the plasma, the intrinsic energy spread of the impinging particles and difficulties in accurately determining the flux of neutrals reaching the target. In contrast to plasma devices, ion sources can produce a mono-energetic beam which can be mass-filtered, allowing for well-defined experiments. Typically the main disadvantage of ion sources is the substantially lower particle flux density to the target, which leads to longer exposure times to reach the desired fluence.

To bridge this gap, SIESTA (Second Ion Experiment for Sputtering and TDS Analysis) was developed at the Max-Planck-Institut für Plasmaphysik in Garching and constructed within this work. SIESTA is capable of providing a mono-energetic, mass-filtered ion beam (typically D_3^+), with a final impinging energy range of 200 eV − 10 keV/atom. With the novel inclusion of a quadrupole doublet lens, particle flux densities of several $10^{19}\text{m}^{-2}\text{s}^{-1}$ to the target are achieved without losing the advantages of the ion source setup. This value should be compared to the peak particle flux density of $10^{21}\text{m}^{-2}\text{s}^{-1}$ expected at the ITER first wall. The target can be rotated to study angle-dependent effects and heated via electron-impact heating up to 1300 K for high temperature erosion and implantation studies. The target chamber is equipped with a magnetic suspension balance for in-vacuo weight-loss measurements. A dedicated TDS (Thermal Desorption Spectrometry) chamber was commissioned for in-vacuo retention studies.

Using SIESTA, experiments were performed to study the impact of surface roughness on the sputter yield of smooth Fe and W thin films and of rough W thin films as a function of the angle of incidence. RBS (Rutherford Backscattering Spectrometry) was employed to determine the eroded layer thickness. The resulting sputter yields were compared to simulations

performed with the code SDTrimSP, a dynamic Monte-Carlo code capable of simulating transport of energetic particles through a target by employing the two-body collision approximation, and SDTrimSP-3D, a fully 3-D version of the SDTrimSP code. Good qualitative agreement was achieved in all cases, as well as agreement with literature data at normal incidence. Experiments were also performed to successfully validate SDTrimSP-3D. To this end, samples with periodic columnar structures of Si and Ta with dimensions in the range of $100 - 200$ nm were characterized via SEM (Scanning Electron Microscopy) imaging with FIB (Focused Ion Beam) cross-sections. The samples were exposed to a 5 keV Ar^+ beam at SIESTA to various fluence steps under several exposure geometries. The sample morphology was subsequently characterized at various positions after each fluence step and compared to the SDTrimSP-3D. In all cases the modelled target morphologies agreed very well with the experimental data at all fluence steps. The code is able to correctly model the geometry of both the eroded Ta columns and the Si substrate, thereby validating its use for fully 3-D targets of variable composition exposed under geometrically complex scenarios. Lastly, SIESTA was employed in experiments dedicated to studying the combined influence of surface roughness and W surface enrichment on the sputter yield of EUROFER steel when bombarded with 200 eV deuterium ions. The former was determined with the aid of SEM imaging and SDTrimSP-3D simulations. For the latter, sputter-XPS (X-ray Photoelectron Spectroscopy) depth-profiling and calculations with SDTrimSP were employed. The combined effect of surface roughness and W surface enrichment was compared with sputter yields determined experimentally via weight-loss measurements and with data from the literature. Two distinct surface morphologies were observed on the EUROFER sample, consisting of smooth and spiked textures. The combined effects of these two factors, surface roughness and W surface enrichment, are estimated to be responsible for a reduction in the sputter yield of 63 % ± 5 %, i.e., the sputter yield is approximately 1/3 of the original sputter yield. This value is compared with an experimentally determined reduction in the sputter yield of 71 % ± 5 %, based on initial EUROFER sputtering yields from literature and in-situ weight loss measurements performed in this work. Both surface morphology and W surface enrichment contribute significantly to the reduction of the sputter yield of EUROFER under the given experimental conditions, and are sufficient to fully explain the reduction in the sputter yield observed in weight-loss experiments and in the literature. Open questions remain regarding the two distinct surface morphologies formed and the disparate sputtering behaviours. This topic is the focus of current investigations.

Contents

Acknowledgments **iii**

Abstract **v**

Table of Contents **vii**

List of Figures **ix**

List of Tables **xv**

1 Introduction **1**
- 1.1 Current and future global energy demand . . . 1
- 1.2 Advantages of nuclear fusion . . . 3
- 1.3 Current research on nuclear fusion reactors . . . 5
- 1.4 Plasma-wall interactions in fusion reactors . . . 6
- 1.5 Commissioning of a new ion source setup and its application to erosion studies . 9

2 Theoretical principles **11**
- 2.1 Plasma behavior . . . 11
  - 2.1.1 Debye length . . . 11
  - 2.1.2 Plasma frequency . . . 12
  - 2.1.3 Plasma sheath and plasma potential . . . 12
- 2.2 Ion generation . . . 13
  - 2.2.1 Electron impact ionization . . . 14
  - 2.2.2 Thermionic emission . . . 14
  - 2.2.3 Perveance . . . 15
- 2.3 Ion optics . . . 16
  - 2.3.1 Beam emittance . . . 16
  - 2.3.2 Comparison with light optics . . . 16
  - 2.3.3 Space-charge and space-charge compensation . . . 17
  - 2.3.4 Magnetic deflection . . . 17
  - 2.3.5 Einzel lenses . . . 18
  - 2.3.6 Quadrupole lenses . . . 19

2.4 Ion-induced physical sputtering . . . 21
2.5 Preferential sputtering . . . 23

3 Supplementary methods employed **25**
3.1 AFM . . . 25
3.2 SEM . . . 26
3.3 XPS . . . 27
3.4 RBS . . . 27
3.5 Ellipsometry . . . 28
3.6 SDTrimSP . . . 29

4 Description and characterization of SIESTA **31**
4.1 Description of the experimental setup . . . 32
4.1.1 Overview . . . 32
4.1.2 DuoPIGatron ion source, gas supply & cooling system . . . 32
4.1.3 Vacuum system . . . 41
4.1.4 Beam-stopper . . . 44
4.1.5 Dipole magnet and quadrupole lens . . . 44
4.1.6 Target chamber and load-lock . . . 46
4.1.7 In-situ thermal desporption spectrometry . . . 51
4.2 Characterization . . . 54
4.2.1 Map of source parameters . . . 54
4.2.2 Magnetic sector field deflection . . . 63
4.2.3 Beam emittance and ion optics . . . 67
4.2.4 Beam footprint and neutral population at the target . . . 74
4.2.5 Current measurement . . . 78
4.2.6 In-situ weight-loss measurement . . . 81
4.3 Erosion of Au bulk samples . . . 84
4.3.1 Experimental procedure . . . 84
4.3.2 Sputter yield results . . . 85
4.4 Conclusions . . . 87

5 Leveraging SIESTA for erosion studies and code benchmarking **89**
5.1 Angle-dependent sputtering of smooth Fe and W and rough W thin films with keV D ions and comparison with SDTrimSP and SDTrimSP-3D . . . 90
5.1.1 Experimental procedure and simulations . . . 90
5.1.2 Comparison of simulations with the experimental data and discussion . . . 96
5.1.3 Summary . . . 99
5.2 Experimental validation of SDTrimSP-3D . . . 100
5.2.1 Characterization of morphology and sputtering of samples . . . 100
5.2.2 Experimental results and comparison to SDTrimSP-3D . . . 103
5.2.3 Summary of the SDTrimSP-3D validation experiments . . . 108

5.3 Sputtering behaviour of EUROFER97 under deuterium bombardment 112
5.3.1 Experimental methodology and simulations 113
5.3.2 Effect of surface morphology and surface enrichment on the sputtering of EUROFER 118
5.3.3 Additional analyses of the surface morphology of EUROFER 126
5.3.4 Summary and discussion 128

6 Summary **131**

7 Conclusions **135**

Bibliography **135**

Appendix **142**

A Calculation of uncertainty in the sputter yield **143**

B Calculation of uncertainty in the EUROFER experiments **145**

C Sputter yields simulated with SDTrimSP **147**

D SIESTA technical documentation **149**

List of Figures

1.1 IEA change in energy demand 2016 - 2040 1
1.2 IEA Global electricity generation forecast by source, 2000 - 2040 2
1.3 Comparison of fission- and fusion-generated nuclear waste radiotoxicity over time 4
1.4 Computer model of ITER 7

2.1 Potential drops between bulk plasma and the wall 13
2.2 Electron impact ionization cross-section 14
2.3 Emittance diagram showing emittance ellipse parameters 16
2.4 Ion beam focusing in a sector magnet 19
2.5 Einzel lens refractive power in accel-decel or decel-accel modes 20
2.6 Einzel lens and ion optics simulation of the lens with IBSimu 20
2.7 Electrostatic quadrupole lens 21
2.8 Influence of surface roughness on re-deposition of sputtered atoms 23
2.9 SDTRIMSP simulation showing preferential sputtering of iron in a bulk 99.67 at.% Fe 0.33 at.% W sample 24

4.1 CAD bird's-eye view of SIESTA 33
4.2 Ion beam impinging on the Mo aperture 34
4.3 Half-section view of the DuoPIGatron ion source 35
4.4 High-voltage cage of the DuoPIGatron ion source 36
4.5 Coiled ion source filament before coating 37
4.6 Ion source extraction grid with partly-melted steel screws 38
4.7 Draft of the gas connection scheme of SIESTA. 39
4.8 Schematic of the electrical connections of the DuoPIGatron ion source to the power supplies 42
4.9 Schematic of the vacuum system of SIESTA. 43
4.10 Beam-stopper employed at SIESTA 44
4.11 Half section cut of the dipole magnet 45
4.12 QM-60.100 Quadrupole lens from D-Pace employed in SIESTA. 47
4.13 Target chamber interior 48
4.14 Target platform with heating filament 48
4.15 Thermocouple push rods 49
4.16 Connection schemes of the target chamber 51

4.17 Beam defining aperture at the target chamber 52
4.18 Target holder with sample in TDS chamber 53
4.19 Ion current with extraction voltage 56
4.20 Ion current for several operating current configurations 57
4.21 Intermediate grid voltage with extraction voltage 57
4.22 Ion current versus pressure in differential pumping stage 59
4.23 Optimal gas pressure with extraction voltage 60
4.24 Gas pressure versus flow-controller gas throughput 60
4.25 Ion current at beam-stopper with Faraday cup set to varying bias voltages 62
4.26 Beam profile at beam-stopper 63
4.27 H and He ion current with dipole current 65
4.28 Square root of energy and mass of ions with dipole magnet current 66
4.29 Transfer-matrix calculation of ion optics between Mo aperture and target 68
4.30 Einzel lens in first differential pumping stage 69
4.31 Ion currents when operating einzel lens in first differential pumping stage 70
4.32 Beam profile on quartz glass at the exit of the dipole magnet 71
4.33 Reconstructed beam ellipses in the horizontal and vertical planes 72
4.34 Calculation of beam trajectories in magnetic quadrupole doublet 73
4.35 Ellipsometry of a-C:H sample with and without wobbling 76
4.36 Position-resolved neutral population at target 79
4.37 Measurement principle of the magnetic suspension balance 82
4.38 Microbalance viewport 83
4.39 Sputter yield of bulk Au samples exposed at SIESTA 86

5.1 AFM images of Fe thin films before and after Ar erosion 92
5.2 Slope distribution of rough and smooth Fe and W thin films 93
5.3 Scanning electron microscopy cross-section of a rough W sample 93
5.4 AFM images of smooth and rough W thin films 94
5.5 RBS spectra of a rough W sample before (red) and after exposure at SIESTA (black) under 0° incidence 95
5.6 Sputter yield of 2 keV D on Fe with incident angle 96
5.7 Sputter yield of 2 keV D on W with incident angle 97
5.8 SEM images of Si and Ta columnar structures 101
5.9 Schematic representation of the 3 exposure scenarios for the Si and Ta columnar structures 102
5.10 SEM image of Ta column cross-section and 3-D model of several columns 102
5.11 FIB cut directions in samples eroded under the (45°,15°) scenario 104
5.12 3-D model and cross-sections of Ta columns after several fluence steps, simulated with SDTrimSP-3D 105
5.13 Tilted SEM images of the Si sample exposed under the (0°,0°) scenario, imaged a various fluence steps 106

5.14 FIB-enabled cross-sections of the Si sample exposed under the (0°,0°) scenario, imaged a various fluence steps . . . 107
5.15 Birds-eye view of Ta sample exposed to a fluence of $7 \times 10^{20}\,\mathrm{Ar\,m^{-2}}$ . . . 108
5.16 Tilted SEM images of the Ta sample exposed under the (45°,15°) scenario, imaged a various fluence steps . . . 109
5.17 FIB-enabled cross-sections of the Ta sample exposed under the (45°,15°) scenario, imaged at fluences of $4 \times 10^{20}\,\mathrm{Ar\,m^{-2}}$ and $7 \times 10^{20}\,\mathrm{Ar\,m^{-2}}$ . . . 110
5.18 FIB-enabled cross-sections of the Ta sample exposed under the (45°,15°) scenario, imaged at fluences of $7 \times 10^{20}\,\mathrm{Ar\,m^{-2}}$ and $19 \times 10^{20}\,\mathrm{Ar\,m^{-2}}$ . . . 111
5.19 EUROFER sample imaged with SEM before exposure at SIESTA . . . 115
5.20 Spiked surface morphology of exposed EUROFER . . . 116
5.21 Tilted and non-titled SEM images of surface morphologies of exposed EUROFER 116
5.22 3-D model of spike used in SDTrimSP-3D simulations of EUROFER . . . 117
5.23 FIB-enabled cross-section of exposed EUROFER . . . 120
5.24 Spiked and smooth surface morphologies of exposed EUROFER . . . 121
5.25 Sputter-XPS elemental depth profiles of exposed EUROFER . . . 121
5.26 EDX map of W concentration on exposed EUROFER morphologies . . . 122
5.27 EDX map of W concentration on EUROFER before and after erosion . . . 123
5.28 Weight-loss measurements of EUROFER offset prior to degassing . . . 124
5.29 Weight-loss measurements of EUROFER offset after degassing . . . 125
5.30 EBSD image of exposed EUROFER . . . 128
5.31 EDX map of Cr concentration on EUROFER before and after erosion . . . 129

List of Tables

4.1 Typical currents and voltages applied by the ion source power supplies when using deuterium. . . . 41
4.2 Measured voltages and currents at ion source contact points 55
4.3 Twiss parameters in the horizontal and vertical planes at the exit of the dipole magnet 72
4.4 Surface area of beam footprint on a-C:H samples 76
4.5 Performance data at SIESTA 86

5.1 Root mean squared roughness values of Fe and W samples and the slope at the 95th percentile. 92
5.2 Sputter yields under normal incidence of 6 keV D_3^+ on Fe, W and Au and of 6 keV He^+ on W 99
5.3 Sputter yield of EUROFER determined experimentally via weight-loss 125
5.4 Comparison of modelled and experimental reduction of SY in EUROFER 127

C.1 Sputter yields calculated with SDTrimSP used in this work 148

Chapter 1

Introduction

1.1 Current and future global energy demand

There is global political and scientific consensus that finding a sustainable mid- and long-term energy plan is one of the key challenges of the 21st century. This complex issue is strongly tied to geopolitical matters of economic and population growth, and of course to important environmental issues, such as climate change. Under the "New Policies Scenario" of the International Energy Agency, global primary energy demand is predicted to continue to grow by 28 % between 2016 and 2040, with net growth being concentrated in non-OECD countries, particularly China and India (see Fig. 1.1) [1].

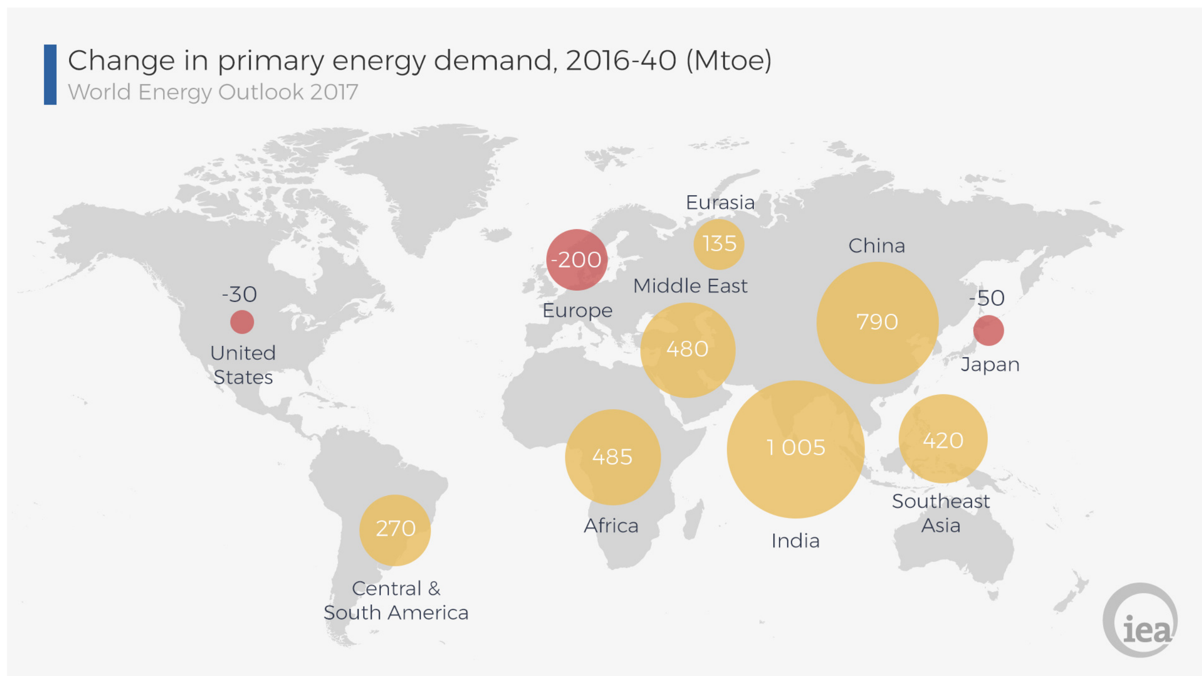

Figure 1.1: IEA Change in energy demand in 2016 - 2040 for selected regions. Units given in Mtoe (million of tonnes of oil equivalent. 1 toe ≈ 41.9 GJ). The orange circles indicate an increase in demand, whereas the red circles indicate a decrease [1].

Electricity demand is predicted to increase by 62 % compared to current values, with renewable energies overtaking coal as the largest source of electricity by between 2025 and 2030 (Fig. 1.2). In spite of this, the majority of electricity produced by 2040 will still come from sources that are not CO_2-free[1]. CO_2 emissions are still expected to rise by 10 % compared to present levels within this period [1].

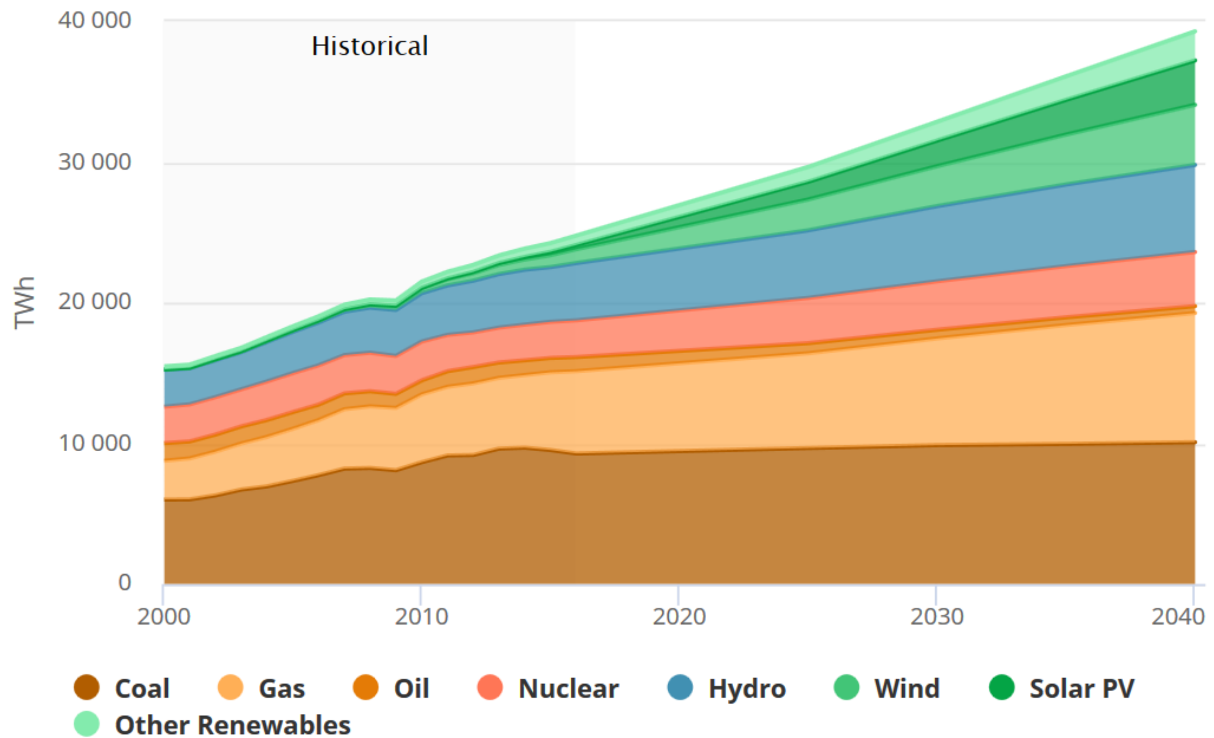

Figure 1.2: IEA Global electricity generation forecast by source, 2000 - 2040 [1].

In a global effort to combat climate change, the Paris Agreement, drafted within the United Nations Framework Convention on Climate Change with the goal of mitigating the emission of greenhouse gasses, was signed by 177 UNFCCC members on the 22nd of April, 2016. As of July 2018, 195 members have signed the agreement and 180 have become party to it. The agreement has among its aims the peaking of global emissions as soon as possible, and to undertake rapid reductions thereafter, in accordance with the best available science [2].

Within this context, if the imperative to reduce carbon dioxide emissions is to be addressed, it is clear that CO_2-free energy sources must be more widely used. The two currently employed options are nuclear fission energy and renewable energies. However, nuclear fusion provides a number of key advantages to both of these, which would make it an ideal energy source.

[1]Denoting CO_2-free energy sources as those that do not incur in CO_2 emissions during energy production, or are considered CO_2 neutral

1.2 Advantages of nuclear fusion

Nuclear fission is well established as a CO_2-free, very high capacity factor energy source, accounting for 11 % of electricity production in 2015, and is expected to continue to grow [1, 3]. Furthermore, total economically recoverable fuel supplies are believed to last 670 years with present reactor technology, according to the OECD and NEA. Breeder and fast reactor technology would in turn push this figure up to 160,000 years [4, 5].

However, nuclear fission is also the cause of a series of public concerns. The chief among these is the generation of long-lived nuclear waste, which poses problems both for post-use waste management and storage, and for accident situations. Although nuclear fusion also produces nuclear waste, originating primarily from the activation of structural materials by high-energy neutrons, this is much lower in total activity, decaying within 100 years to activity levels allowing for recycling and re-utilization, with $30 - 40$ % reaching free-release limits within 50 years [6]. In comparison, nuclear fission produces waste with decay times to admissible levels in the range of tens of thousands of years, though this can be partly mitigated via the implementation of advanced fuel cycles and breeding technology [5]. Fig. 1.3 shows relative radiotoxicity with time of different fusion power plant designs compared to a pressurized water reactor type fission power plant. Coal ash refers to the non-combustible residue of coal burnt in commercial power plants.

Moreover, fusion is also deemed highly resistant to nuclear proliferation attempts, since all efforts to harness either tritium or the strong fast neutron flux to breed weapons grade fuels would prove either easily detectable or easily preventable through adequate detection measures [8].

Thirdly, another major concern with nuclear fission is the potentially catastrophic consequences of a severe accident, as occurred in Chernobyl in 1986 or in Fukushima Daiichi in 2011. Such types of accidents are in practice not possible in a fusion power plant, or in a worst-case scenario severely limited, since given the nature of a controlled nuclear fusion reaction, temperature, pressure and magnetic field must be precisely controlled for the reaction to take place and produce a net energy gain. Any disruption of these parameters would effectively terminate the reaction, unlike in a fission power plant, where the reaction could continue self-sustained without any exterior intervention. Additionally, the fuel present at any given time within the fusion reactor is burnt up within seconds and amounts to a very low energy content, in comparison to a fission reactor, which typically contains at any given time enough fuel to power the reaction for several months. Lastly, the expected decay heat in fusion reactors is significantly smaller than that of fission reactors, which continue to generate heat for months after shutdown from beta-decay [9].

Renewable energies produce very little greenhouse gas emissions during their lifetimes, and are expected to grow strongly in the following years, especially in OECD countries [1]. However, of those with most room for growth, hydroelectric power is limited by geography and can therefore not be applied globally, whereas solar and wind power are dependent on the weather for their energy output, making their widespread use for base load supply challenging [10]. This would prove an important advantage for nuclear fusion energy, not as a competitor, but as com-

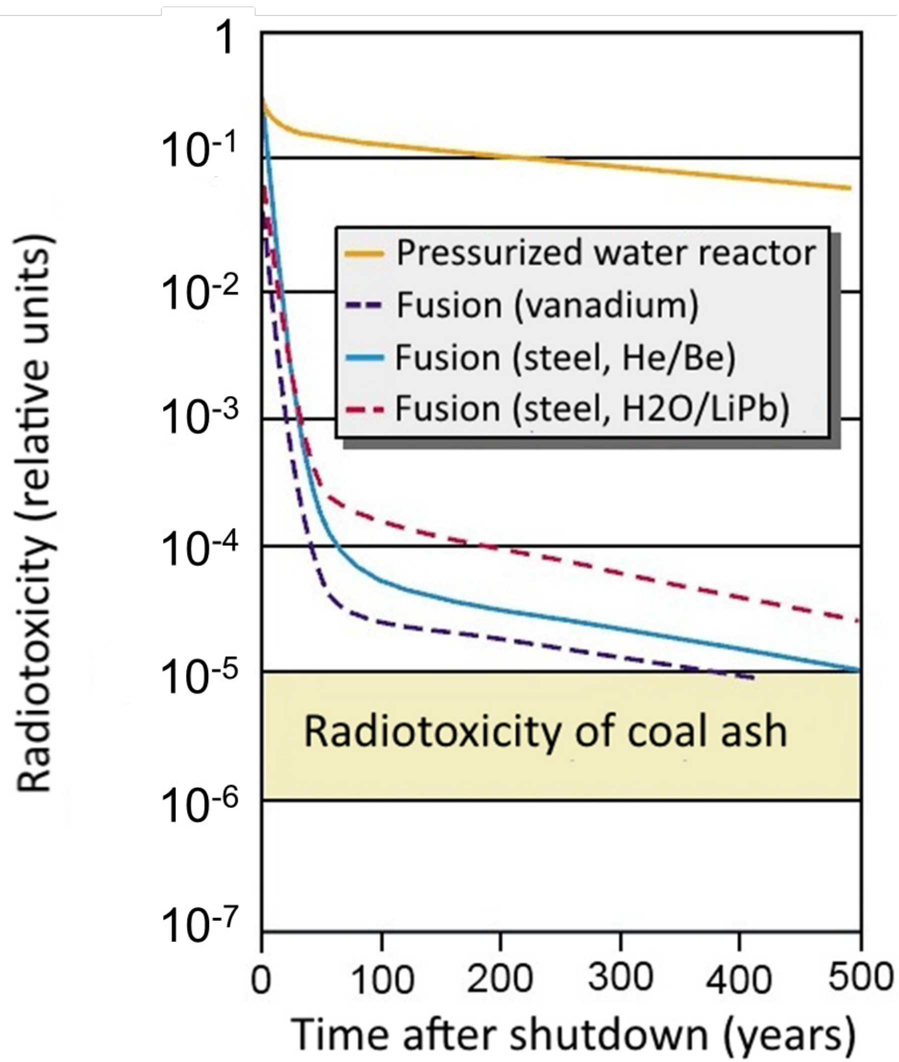

Figure 1.3: Comparison of fission- and fusion-generated nuclear waste radiotoxicity over time [7].

plementary to renewable energy, since the nuclear fusion process would make it best suited for base load power supply.

Lastly, regarding fuel reserves for nuclear fusion, deuterium[2] reserves in seawater are estimated to last for billions of years. Lithium, which is projected to be used in the tritium[3] breeding process, is estimated to last for 3000 years from known reserves, and would last for millions of years if it were extracted from seawater. Reserves of other raw materials necessary for fusion, namely beryllium, which is intended as a neutron multiplier, are more limited. However, beryllium in future fusion reactors could be substituted for lead, for which reserves would be estimated to last over 100,000 years [11]. This would make nuclear fusion power a long-term solution with regards to fuel availability, especially in comparison to fossil fuels, whose resources are estimated to last for another 40 years in the case of oil, 70 for natural gas, and 200 years for coal [12].

1.3 Current research on nuclear fusion reactors

Nuclear fusion research for energy production has been ongoing since the 1940s, with the first patent for a nuclear fusion device being published in 1946 in the UK [13]. Since then, different fusion principles and devices have been developed, with two main concepts dominating within the fusion community: inertial confinement and magnetic confinement.

Inertial confinement consists of compressing and heating the fuel via an imploding shell. Compression ratios of the order of 30 times its solid density must be produced. This can be achieved either through laser blasts hitting the target directly (direct drive) or through these laser blasts hitting a structure, known as *hohlraum*, which in turn emits x-ray radiation capable of compressing the fuel more uniformly than through direct drive. This second process is known as indirect drive [14]. Inertial confinement has been predominantly developed in the USA, tied in part to nuclear weapons research. The largest device in this field is the National Ignition Facility (NIF) at the Laurence Livermore National Laboratory in Livermore, California [15].

In magnetic confinement, the fuel is in plasma[4] state and magnets are employed to create strong magnetic fields. Due to the single particles of the plasma being charged, they will gyrate around the magnetic field lines, thereby being confined by them and limiting their flux to the walls of the device, which could potentially terminate the plasma discharge, as well as damage the device. The plasma is heated to fusion conditions by way of induced electric currents, electron and ion cyclotron resonant heating, and injection of energetic neutral particles.

Within magnetic confinement, the most advanced concept is known as toroidal magnetic confinement, where the magnetic field lines are arranged in the shape of a torus, thereby forming closed surfaces. This concept has been most developed in devices known as tokamaks, with the second most advanced devices being the stellarators. Toroidal magnetic confinement is the main

[2]An isotope of hydrogen with a nucleus consisting of one proton and one neutron, a key fuel in nuclear fusion
[3]Another isotope of hydrogen. Its nucleus consists of one proton and two neutrons
[4]Plasma is a state of matter in which atoms in a gas-like state have been fully or partly ionized, so that nuclei and electrons are unbound. As a result, plasmas are electric conductors

fusion research focus in Europe, with devices such as JET[5] in the UK or ASDEX[6] Upgrade and Wendelstein 7-X in Germany; though research is also being performed in North America and Asia with devices such as DIII-D, JT-60, EAST or KSTAR [9].
The next milestone in toroidal magnetic confinement research is ITER in France (shown in Fig. 1.4), a multinational project which aims to be the first nuclear fusion reactor capable of achieving a substantial power amplification of 10, thus reaching a fusion power of 500 MW in 300-1000 second long pulses. The first plasma experiments planned to start in December 2025 [16, 17].

Most current tokamaks are capable of operating in what is known as H-mode[7]. In this operational regime, discovered in the ASDEX tokamak in 1982, sufficient heating leads to significantly improved confinement. H-mode is considered crucial for commercial fusion power [19]. However, periodic plasma edge instabilities known as ELMs[8] appear in H-mode plasmas, and can prove hazardous both to plasma operation and overall integrity of the plasma-facing components. They are expected in ITER's standard operating scenario; ELM suppression or mitigation is for that reason a currently active field of research [20, 21].

1.4 Plasma-wall interactions in fusion reactors

The inner walls of a magnetic fusion device are subject to significant heat loads and particle impacts during operation, leading to a series of design and operational constraints on the device. Given its specific function and design, a part of the first wall, called the divertor, can be singled out.

Even with good magnetic confinement, the plasma edge comes into contact with the inner walls of the device. This leads to erosion of the wall materials via sputtering, with sputtered particles entering the plasma, thus hindering its control, cooling it down and diluting the fuel. Furthermore, the fusion reactions inside the plasma will lead to an accumulation of helium, which would also contribute to losses by fuel dilution in the plasma, and thus must also be removed. In modern reactors, the magnetic field lines at the edge of the plasma are shaped to allow particles to impinge on the wall in a specific region called the divertor, thus allowing them to cool down and be removed from the plasma. Since He particle impact is concentrated in this region, the divertor is subject to higher thermal loads than the rest of the inner wall (from now on referred to simply as first wall) [22].

The first wall of the rest of the reactor chamber is subject to a predominantly neutral flux of particles - typically ions that are neutralized close to the plasma edge, thus no longer being confined by the magnetic field lines and colliding with the first wall. This particle flux is estimated to be in the range of $10^{19} - 10^{21}$ m^{-2}s^{-1}, depending on the poloidal position in the torus. The mean impinging particle energy at each poloidal position ranges between 300 eV[9] and

[5]Joint European Torus
[6]Axial Symmetric Divertor Experiment
[7]Abbreviation of High-confinement mode
[8]Acronym for Edge Localized Modes
[9]1 electron volt (eV) $= 1.602 \times 10^{-19}$ J

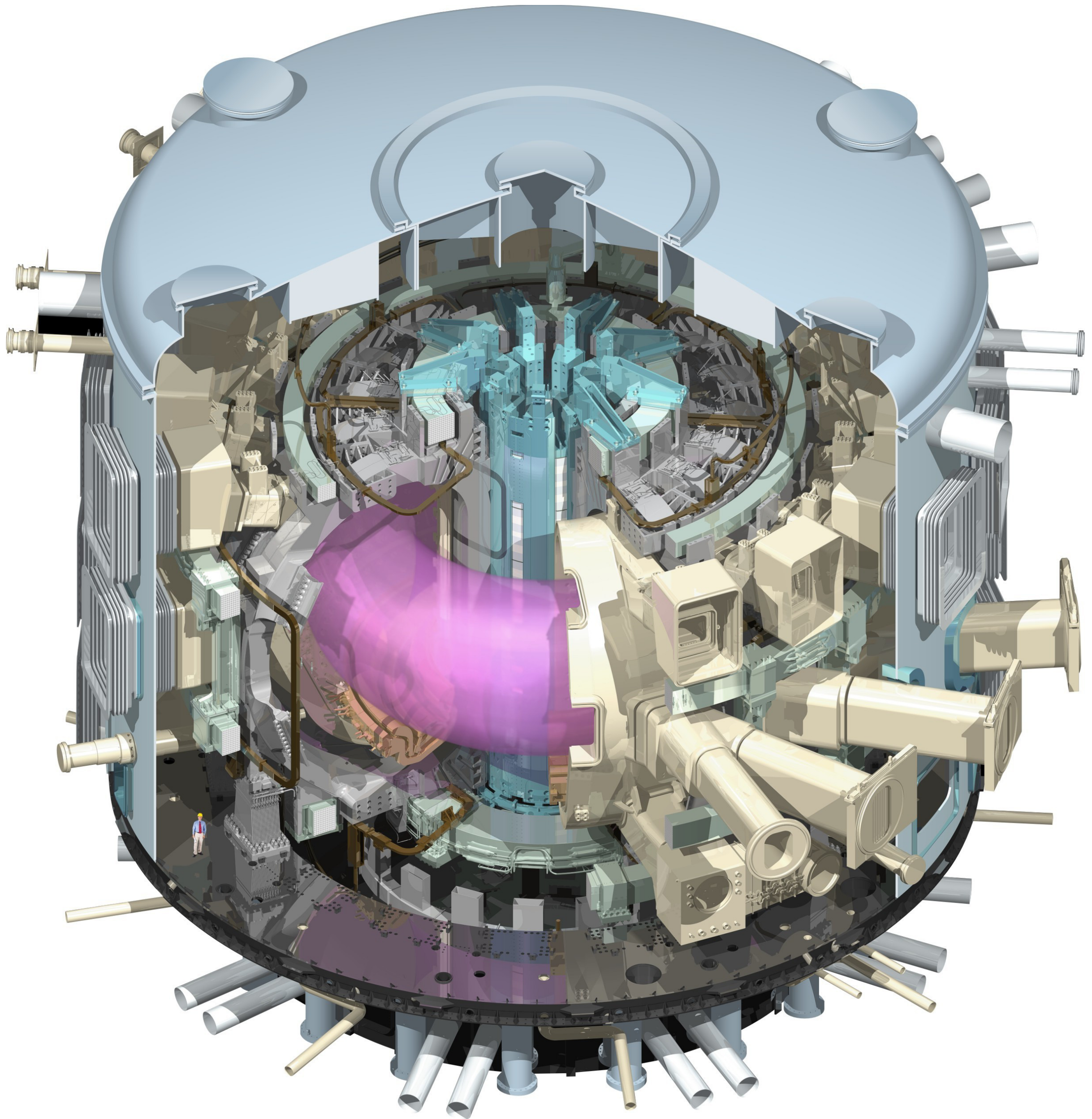

Figure 1.4: CAD model of ITER. On the lower left side of the image, a person is included for scale [18].

8 eV, though energies in the keV range are expected for a small fraction of the neutral particles [22, 23].

Three distinct challenges have been identified with regard to plasma-wall interaction in nuclear fusion devices. These are:

1. Erosion of the wall materials
2. Tritium retention
3. Dust production

If ELMs are present, wall damage and erosion could be a significant problem. These plasma instabilities are characterized by periodic high energy fluxes to the walls, potentially damaging them. It is believed that ELM-induced wall damage and erosion may severely limit the lifetime of plasma-facing components (PFCs) if ELM energies are not mitigated to values below 0.5 MJ. For this reason, ITER is planned to function in ELM-mitigated regimes [21, 23]. Even without ELMs, steady-state erosion will still play an important role in divertor (high flux of low-energy ions) and first wall (more moderate fluxes of higher energy neutrals). Lifetime estimates of these components are strongly dependent of the choice of wall material.

Tritium retention is considered an important safety and operational issue, with in-vessel tritium levels needed to be kept as low as reasonably achievable in order to minimize any possible hazard in the event of a leak to the environment. Candidate wall materials are low-Z Be and C and high-Z refractory metals such as W (and, in some areas, steel, as will be discussed in this thesis). For Be and C, which are more easily sputtered than e.g. W, tritium inventory buildup is mainly dominated by the co-deposition of tritium with eroded wall atoms. For W, a main wall-material candidate, the dominant processes for tritium in-vessel inventory buildup are implantation, diffusion and trapping in the bulk of the material. Current research is focused on studying retention in materials showing damage consistent with neutron irradiation, as would be the case in later ITER phases or in fusion power plants [23].

Dust generation due to erosion of the divertor and the first wall is important for the operation and overall safety of the machine, in particular as pertaining to hot dust. In case of an air leak, the hot dust could constitute a radiological hazard and could, in the presence of water or humidity, oxidize and produce hydrogen, thus creating a potentially explosive atmosphere [23].

Given the strong dependence of erosion, tritium retention and dust formation on the choice of wall materials, there is a strong need to develop and test new materials with suitable properties. Such tests are normally performed with devices designed to produce plasmas that mimic the plasma edge in nuclear fusion reactors, or with ion sources that produce well-defined ion beams of reactor-relevant characteristics. The former option typically allows much greater particle fluxes, leading to faster testing to achieve relevant fluences and often permitting the simultaneous testing of several samples. However, due to the nature of the plasma, the samples will be bombarded by a set of different ion species within a certain energy spectrum, leading to significant uncertainties. The later option, while supplying lower particle fluxes and thus typically leading to slower testing,

can be engineered to produce single-species ions with very precisely defined energies, thereby allowing their use for more well-defined experiments.

1.5 Commissioning of a new ion source setup and its application to erosion studies

Within this work, SIESTA (Second Ion Experiment for Sputtering and TDS Analysis), developed at the Max-Planck-Institut für Plasmaphysik in Garching, was designed, constructed and commissioned [24]. SIESTA is an experimental test bed capable of delivering high particle flux densities to target samples without losing the advantages of an ion-source setup. A DuoPIGatron type ion source is employed to provide particle flux densities of several $10^{19}\,\mathrm{m^{-2}s^{-1}}$, i.e., comparable to the lower limit of range of fluxes expected at the ITER first wall ($10^{19} - 10^{21}\,\mathrm{m^{-2}s^{-1}}$). With SIESTA, materials can be exposed to a mono-energetic, mass-filtered ion beam to investigate erosion and (beyond the scope of this work) hydrogen isotope retention under well-defined exposure conditions.

The theoretical basis of this work is explained in chapter 2. In chapter 3, several analysis techniques employed in this work are described, as is SDTrimSP, a Monte-Carlo code based on the binary collision approximation capable of dynamically simulating transport of energetic particles in matter. The construction and characterization of SIESTA is described in detail in chapter 4. Chapter 5 is dedicated to the experiments performed at SIESTA within the scope of this work. The first set of experiments (Sec. 5.1) corresponds to investigations of the influence of the angle of incidence on the sputtering behaviour of smooth and rough thin films. Section 5.2 details the experiments performed to successfully validate the SDTrimSP-3D code, which is capable of accurately modelling the effect of surface morphology on the sputtering behaviour. The last set of experiments, described in section 5.3, provide a case study of the erosion of EUROFER, a multi-phase steel for fusion applications, with dynamic evolution of surface morphology and elemental surface composition. A general summary is given in chapter 6. Chapter 7 provides the main conclusions of this work.

Chapter 2

Theoretical principles

2.1 Plasma behavior

Plasma consists partly or totally of positively and negatively charged particles, typically positively charged ions and electrons[1], creating an overall electrically neutral medium. This state can be achieved, for instance, through the use of an electrical current or electromagnetic waves to break the bonds between electrons and nuclei in atoms. The particles within the plasma are unbound, but their movement can generate electrical currents with associated magnetic fields. Plasma particles are affected by each other's fields, governing the whole plasma's collective behavior. Due to the presence of positive and negative charge carriers, plasmas are electrically conductive.

Three conditions must be met for a system to be considered a plasma:

1. The Debye length must be smaller than the size of the plasma.
2. The number of particles inside a plasma volume of the Debye sphere must be sufficiently large.
3. Lastly, the plasma frequency must be greater than the electron-to-neutral collision frequency [25].

2.1.1 Debye length

As previously stated, plasma is a macroscopically quasi-neutral medium, with the positive and negative particles producing a shielding effect. Without said quasi-neutrality, the strong electric fields present would quickly cause the particles to disperse. Although there is no neutrality at a microscopic scale given the discrete nature of the charges and perturbations in the system, at a macroscopic scale a change in charge distribution will be compensated by the movement of the other charges. A length scale can be associated to this plasma shielding effect, known as the Debye length. If an electrode is, for example, inserted inside a plasma, a plasma sheath region

[1] In the case of deuterium or deuterium-tritium fusion plasmas, since hydrogen atoms and its isotopes only possess one electron, these are formed by deuterium or tritium nuclei and electrons. In low-temperature plasmas, molecular ions may be the dominant ion species.

will form around this electrode, having a thickness of several Debye lengths. A plasma can only be considered quasi-neutral if its typical length is substantially larger than its Debye length:

$$L_D \ll L. \tag{2.1}$$

Since shielding is the effect of the collective movement of charges to compensate for a charge deviation, thereby preserving quasi-neutrality, the number of particles around said charge deviation must be sufficiently large. A criterion for employing the concept of Debye length is therefore that a large number of charged particles are contained inside the volume of a Debye sphere, a sphere of radius equaling the Debye length:

$$n_e L_D^3 \gg 1, \tag{2.2}$$

where n_e is the electron density. These two criteria can be expressed as follows:

$$\frac{1}{n_e^{1/3}} \ll L_D \ll L. \tag{2.3}$$

2.1.2 Plasma frequency

Due to the mass difference between electrons and ions, electrons - with their lower mass - will be faster to respond to a space-charge perturbation. Ions can for this purpose be considered immobile. Given the electrons' inertia, they will oscillate around the perturbation with an angular frequency of:

$$\omega_{pe} = \sqrt{\frac{n_e e^2}{\epsilon_0 m_e}}. \tag{2.4}$$

This is known as the plasma frequency, where e is the elementary charge, ϵ_0 the permittivity of space and m_e the mass of the electron.

The oscillation of the electrons will be damped by collisions with neutral particles. Therefore, the last criterion for the plasma to display collective behavior is for the plasma frequency ($\upsilon_{pe} = \omega_{pe}/2\pi$) to be greater than the electron-to-neutral collision frequency (υ_{en}):

$$\upsilon_{pe} > \upsilon_{en}. \tag{2.5}$$

2.1.3 Plasma sheath and plasma potential

The walls of a vacuum vessel act as a boundary for the plasma, serving as a particle sink, with ions and electrons neutralizing or being trapped in the wall, and as a source, through secondary ion and electron emission, sputtering, etc.

Due to the higher mobility of the electrons compared to the ions, the electron flux to the walls will initially be higher than the ion flux. If the vacuum vessel walls are then kept at a certain fixed potential ϕ_W, normally ground potential, the plasma will adopt a positive potential

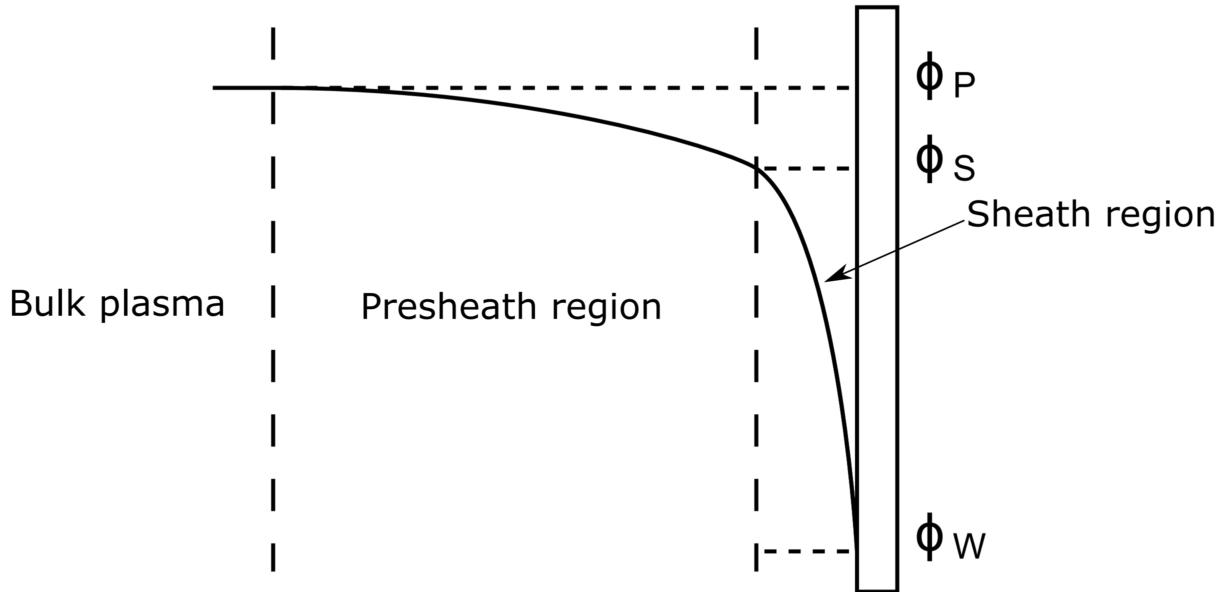

Figure 2.1: Potential drops between bulk plasma and the wall [28].

ϕ_P to compensate for the initially larger electron flux. The potential drop between the bulk of the plasma and the walls can be approximated as [26, 27]:

$$\phi_P - \phi_W \approx \frac{kT_e}{e} \ln \sqrt{\frac{m_i}{m_e}}, \tag{2.6}$$

where k is the Boltzmann constant, T_e is the electron temperature, e is the elementary charge, m_e is the mass of the electron and and m_i is the ion mass. The ions are accelerated towards the wall by this potential difference in the presheath and sheath regions, with most of the potential drop taking place in the plasma sheath region, which will have a thickness a few Debye lengths. An equilibrium will be reached when both positive and negative charge fluxes to the wall are equal. Fig. 2.1 illustrates the wall, plasma and sheath potentials in the vicinity of the wall.

2.2 Ion generation

Ion sources vary significantly in shape and size, operational principle and output. However, a general process for ion generation can be described as follows:

The element to be ionized is introduced into a constantly pumped vacuum chamber in a controlled manner. This will serve as “fuel” for the ion source. Ideally, if the element is available in gaseous form, it may be let in via a needle valve or flow controller. The vacuum chamber will also incorporate a device - typically an electron source or radio frequency coils - capable of supplying enough energy to the atoms or via collisions with free electrons to overcome the binding energies of one or several of the bound electrons, thus forming a plasma. By applying a high voltage at the extraction region, the ions can be separated from the plasma, forming an ion beam.

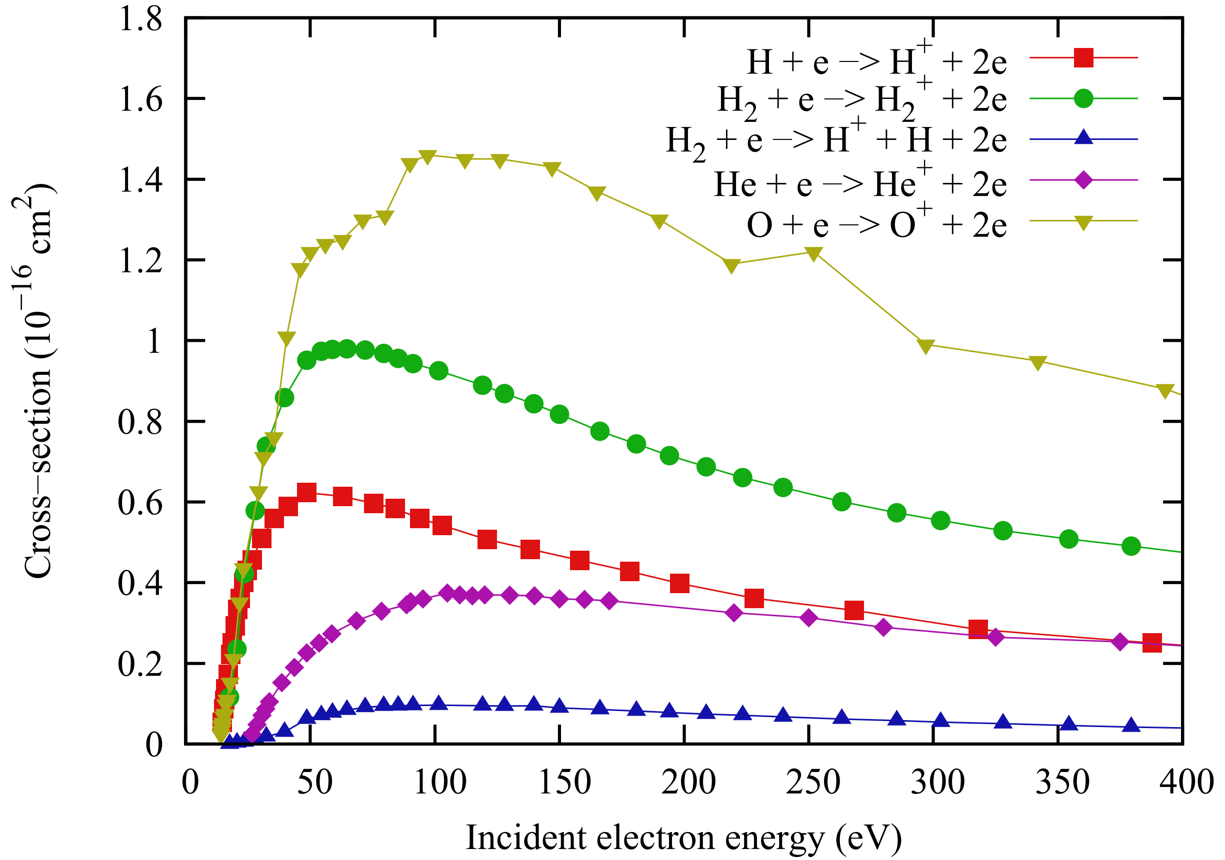

Figure 2.2: Electron impact ionization cross-section for different gasses and processes with incident electron energy [28, 29, 30, 31, 32].

2.2.1 Electron impact ionization

A simple way of ionizing a gas is through electron impact ionization. In this case, an electron with sufficient energy interacts with an atom or molecule, transferring part of its energy and causing a second electron to break free, thereby ionizing said atom or molecule.

The probability of ionization via electron impact is dependent on the element being ionized and the energy of the electron. In the case of molecular gasses, different competing processes may take place, producing molecular ions such as, in the case of hydrogen, H_2^+ and H_3^+, in addition to H^+. Fig. 2.2 shows the electron impact ionization cross-section for different gasses and processes with incident electron energy [28, 29, 30, 31, 32].

2.2.2 Thermionic emission

A sufficient flux of energetic electrons for ion generation can be obtained via thermionic emission: the emitter, usually a filament made of a material with a high melting point such as W, is heated up and set to a negative electric potential with respect to an anode. At high temperatures, a significant fraction of the electrons from the surface of the filament will have energies greater than

its work function[2], at which point said electrons will be emitted from the surface of the filament and be accelerated towards the anode due to the difference in electric potential. To enhance the output of the emitter, the filament may be coated with a material with a lower work function than that of the filament, for example cesium oxide, strontium carbonate or barium carbonate. It is worth noting that, by controlling the gas throughput to the ion source and the accelerating voltage for the electrons, the secondary electron emitted by the gas atom or molecule can be accelerated to high enough energies to in turn ionize other atoms, thus producing an ionization cascade.

2.2.3 Perveance

The physical limit to the current that can be extracted from an ion source is given by the Child-Langmuir law [33]:

$$I = \frac{4\pi\epsilon_0}{9}\sqrt{\frac{2e}{m}}\left(\frac{a}{d}\right)^2 U^{3/2}, \tag{2.7}$$

where I is the maximum current that can be extracted from an ion source aperture with radius a, with U the extraction potential and d the space between equipotential surfaces, e.g., between the extraction grid and a grounded grid. ϵ_0 corresponds to the vacuum permittivity, m is the mass of the extracted ions and e is the elementary charge. It can be deduced from equation 2.7 that high extraction potentials and a grid spacing as small as technically possible while avoiding breakdown are desirable.

In practice, perveance is defined as [34]:

$$\Pi = \frac{I}{U^{3/2}}. \tag{2.8}$$

Which only if operating an ion source in a space-charge-limited regime takes the form of:

$$\Pi_{max} = \frac{4\pi\epsilon_0}{9}\sqrt{\frac{2e}{m}}\left(\frac{a}{d}\right)^2. \tag{2.9}$$

The electric field in the gap between grids also has the effect of focusing the beam, thereby affecting the beam divergence at the exit of the ion source. This focusing effect is dependent on the plasma parameters, as these can affect the shape of the plasma meniscus, the equipotential surface at the extraction grid aperture that serves as an artificial boundary between the field-free plasma and the extraction region. There exists a perveance optimum $\Pi_{opt} < \Pi_{max}$ at which beam divergence is minimal [34, 28]. In practice, since high ion currents are typically desired at the target and not necessarily at the exit of the ion source, sources are often operated closer to the optimal rather than the maximum perveance to benefit from the decreased beam divergence [34].

[2] The minimum energy required to remove an electron from the surface of the solid

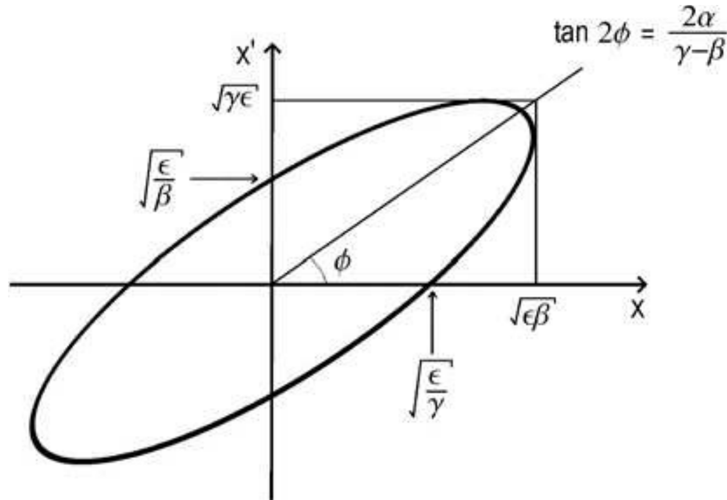

Figure 2.3: Emittance diagram showing the emittance ellipse parameters, also known as Twiss parameters. For a given position along a beam's trajectory z, the angular distribution of the trajectories along a direction transverse to the nominal path can be described by an ellipse in the (x, x') coordinate system where x denotes the distance along the transverse direction and x' denotes the angle of the beam with regards to z on the xz plane [35].

2.3 Ion optics

Ion optics refers to the study of the transport of charged particles. The field bears many resemblances with light optics, allowing a quick understanding of many topics by analogy. Although useful, this analogy is inherently limited, requiring a more in-depth study of some basic ion-optical phenomena.

2.3.1 Beam emittance

At a given position p along the trajectory of a beam, with the direction of the beam given by the z axis, the angular distribution of the particle trajectories along a transverse direction x can be plotted, forming an ellipse in the (x, x') coordinate system (Fig. 2.3), with x' denoting the angle of the beamlet in the xz plane at p. The emittance of a beam is the area of the ellipse divided by π, symbolized by ϵ. The ellipse parameters are denoted as (α, β, γ). Together with the emittance they are also known as the Twiss parameters [35]. As the particles continue on their trajectory, the shape of the ellipse is altered but the emittance remains constant.

2.3.2 Comparison with light optics

Ion optics can be studied in a first approximation much like geometric optics, with ion trajectories taking the form of rays moving in straight lines which can be bent by lenses. With charged particles, instead of a lens functioning because of a difference in refractive index, an ion lens will bend the "ion rays" with electric or magnetic fields. Despite the different mechanism, the geometric model governing both types of lenses is identical. Aberrations are another similarity of both systems, with most forms of optical aberration being also found in ion optics. An ion-

optical system is also affected by tilt, astigmatism, spherical and chromatic aberration[3]. Unlike with light optics, diffraction is not generally considered to be present in ion optics. Also, ion beams cannot be reflected as would be understood from an optics point of view. Ions can, on the other hand, follow a curved trajectory when in the presence of an electric or magnetic field. A case of particular importance when studying high-current-density ion optics is that of space charge [36, 37].

2.3.3 Space-charge and space-charge compensation

A fundamental difference between geometric and ion optics is that the charged particles influence their neighbors. An ion beam, whether positively or negatively charged, is non-neutral. Thus, the electrostatic field created by the charges will intrinsically cause the beam to diverge. This effect, known as space-charge, is directly dependent on the current density. At low current densities, the electrostatic forces are low and the system can be treated geometrically. When the current density is high, beam divergence due to space-charge will play a significant role and the ion optics will deviate substantially from a geometric ray model.

Under experimental conditions the space-charge of a charged particle beam may be partly compensated by opposite charge carriers (typically electrons in the case of a positive ion beam) becoming "trapped" in the potential well of the beam. A common source of these charges is from ion impact ionization of neutral gas present in the vacuum chamber after the beam's extraction.

Typically, a plasma source will not fully ionize the gas that is inserted through the feed-through. A sizable portion of the particles will remain neutral after exiting the plasma source through the extraction aperture. After acceleration, ions from the beam can ionize the gas and may produce a low-energy positive ion and an electron. In the case of a positive ion source, the low-energy ion will diverge from the beam due to coulomb repulsion, but the electron may be trapped in the potential well of the beam. It is important to note that any positive electric potential stronger than the potential well of the ion beam will remove the electrons from the beam, thereby eliminating the space-charge compensation effect. As a rule, space-charge will not be compensated inside electrostatic lenses. Magnetic lenses do not inhibit the space-charge compensation effect [38].

2.3.4 Magnetic deflection

A charged particle moving through electric and magnetic fields will follow a trajectory which can be derived from the Lorenz force $\overrightarrow{F_L}$:

$$\overrightarrow{F_L} = q\overrightarrow{E} + q\overrightarrow{v} \times \overrightarrow{B}. \tag{2.10}$$

Where q is the charge of the particle, $\overrightarrow{v}$ its velocity and $\overrightarrow{E}$ and $\overrightarrow{B}$ the electric and magnetic fields, respectively. The radius of curvature can be obtained by equaling the Lorenz force perpendicular to the particle's velocity to the centrifugal force on the particle. If it is assumed

[3]In the case of chromatic aberration, the difference in wavelength for light is translated into a difference in ion energy

that no electric field is present and the magnetic field is oriented perpendicularly to the particle velocity, setting $\overrightarrow{F}_{Lorentz} = \overrightarrow{F}_{centripetal}$, yields:

$$q \cdot \overrightarrow{v} \times \overrightarrow{B} = \frac{m \cdot |\overrightarrow{v}|^2}{r}. \tag{2.11}$$

Here m is the particle mass and r the radius of curvature. Treating the equation as a scalar (applicable in this case since $\overrightarrow{v}$ and $\overrightarrow{B}$ are perpendicular), it can be seen that:

$$Br = \frac{mv}{q} = \frac{p}{q} = R, \tag{2.12}$$

where p is the momentum of the ion. R is known as the rigidity, and is a measure of the resistance of an ion to deflection. Applying $E = \frac{1}{2}mv^2 \rightarrow v = \sqrt{\frac{2E}{m}}$ with E the kinetic energy of the particle yields:

$$R = Br = \frac{\sqrt{2Em}}{q}. \tag{2.13}$$

Therefore, given an identical accelerating potential, charge and magnet field strength, particles with higher mass (for example, H_2^+ compared to H^+) will have a larger radius of curvature, i.e., will be deflected less. This effect can be employed to separate different ion species in a monoenergetic beam, as each species will have a distinct radius of curvature.

An ion beam passing through a deflector magnet will also be focused in the plane of deflection, as shown in Fig. 2.4, where L_1 represents the distance to the virtual object point and L_2 that to the image point. Φ is the sector angle of the magnet. As a consequence of this, after passing through a magnet an initially circular beam will have an elliptic cross section, with the beam focusing differently in the horizontal and vertical plane. This astigmatism may be corrected through the use of lenses that allow for different foci in the horizontal and vertical plane, such as a series of quadrupole lenses [37].

2.3.5 Einzel lenses

An einzel lens typically consists of three apertures - often cylindrical or rectangular tubes - aligned on the same axis as the ion beam, where the first and third apertures are set at ground potential. The second aperture is set to a different potential, thus producing two opposite electric fields of equal strength between the first and second, and second and third electrodes. These fields will either accelerate or decelerate the ions, having first one effect and then the other, in this way maintaining the energy of the beam constant before and after the lens. While the ions are being accelerated or decelerated by the electric fields, their direction is altered, causing them to converge on the axis. Einzel lenses are therefore always focusing lenses. Assuming a positive ion beam, the potential of the second electrode can be positive, in which case the lens is said to be operating in "decel-accel" mode; or negative, where the lens would be operating in "accel-decel" mode. The refractive power of a lens in these two modes is illustrated in Fig. 2.5, with D the diameter of the aperture (assuming cylindrical apertures) and D/f quantifying the "lens strength" in relation to the potential of the middle electrode and the accelerating potential

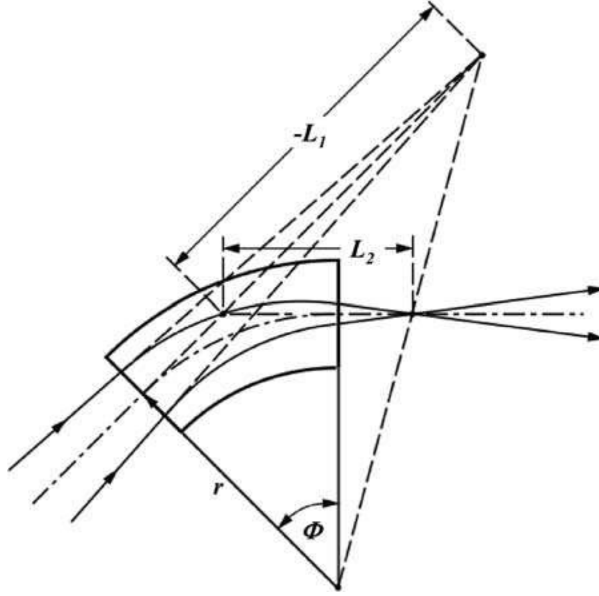

Figure 2.4: Ion beam focusing in a sector magnet. L_1 is the distance to the virtual object point. L_2 is the distance to the image point. r is the radius of curvature and Φ represents the angular sector of the magnet. [37]

of the beam [37].

In most practical applications, the decel-accel mode is preferred for two reasons: firstly, the accelerating potential and the potential at the middle electrode will be of the same sign, and so can be supplied from the same power source with the use of a voltage divider. Secondly, high refractive powers are achieved with a middle electrode potential comparable to the source potential. Accel-decel mode requires a separate voltage source of opposite polarity to the source potential, with higher voltages being necessary to achieve the same refractive power. However, if the extra power source and higher voltages for the required focal length are not an issue, accel-decel mode has the advantage of inducing smaller spherical and chromatic aberrations than decel-accel mode, and would therefore be preferred [37].

Fig. 2.6 shows an einzel lens and a simulation of the ion beam trajectory and electric field lines inside an einzel lens performed with the IBSimu ion optics simulations library [39].

2.3.6 Quadrupole lenses

Unlike a cylindrically symmetric einzel lens, which will focus the ion beam identically in all planes containing the beam axis, a quadrupole field will exhibit asymmetric focusing: The beam will be focused in one plane (for simplicity, horizontal or x plane) and defocused in the perpendicular plane (vertical or y plane). Such a field can be achieved with a quadrupole lens, ideally consisting of four hyperbolic surfaces of length L which are are arranged at 90° angles from one another. In the case of an electrostatic quadrupole lens, two opposite surfaces are set at a positive potential ϕ_0 and the other two are set at an equal potential of negative polarity $-\phi_0$. In practice, it is much easier to manufacture a lens that employs cylindrical surfaces instead of

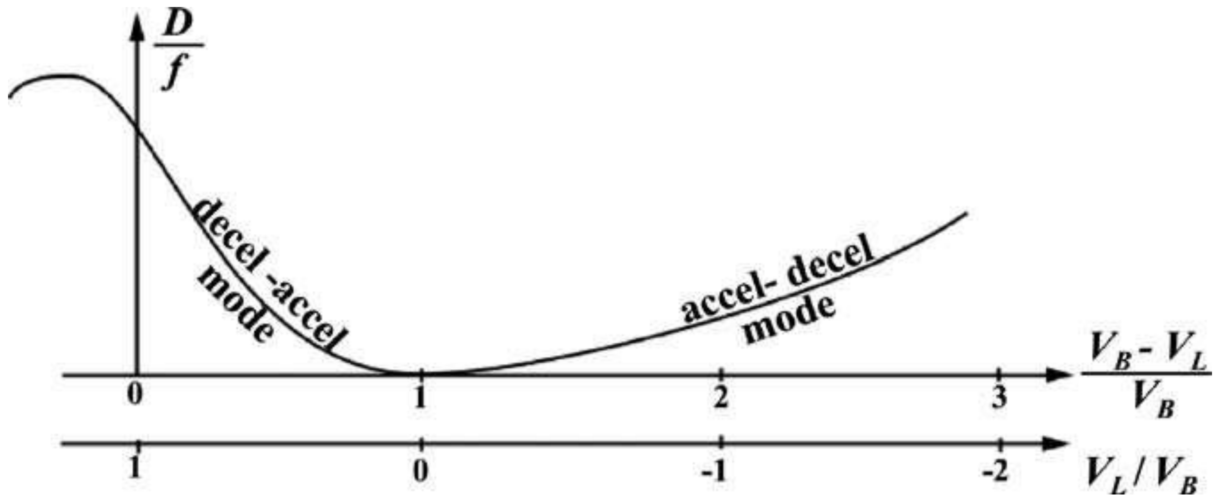

Figure 2.5: Typical dependency of the refractive power of an einzel lens on the potential of the middle electrode V_L for a beam energy eV_B [37].

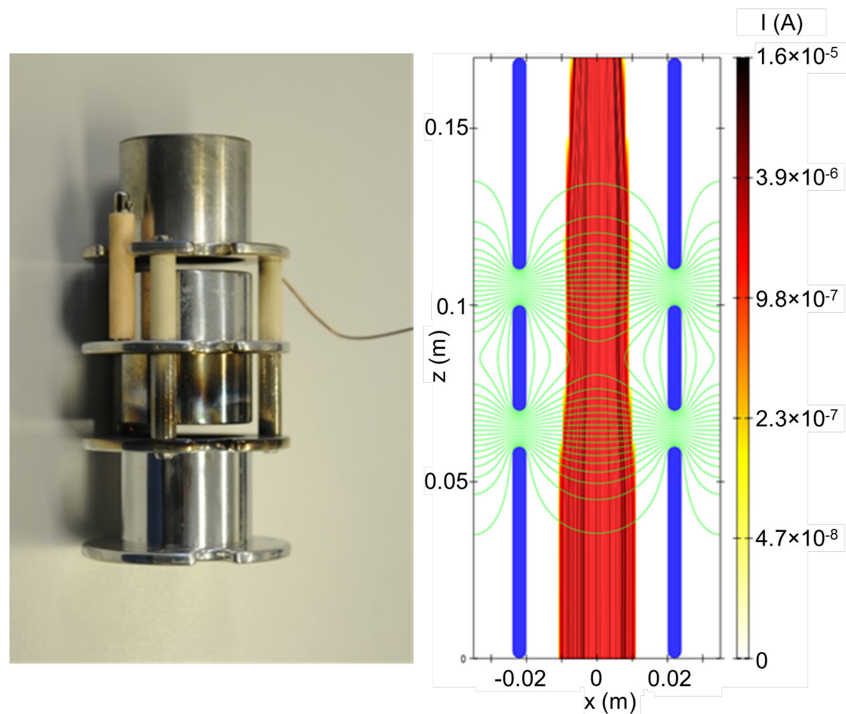

Figure 2.6: Einzel lens and ion optics simulation of a lens with IBSimu. In this simulation, the central electrode (blue) is set to a decelerating potential of +100 V while the first and third electrodes (blue) are grounded. In green the equipotential lines of the electric fields within the lens are shown. A 5 mA D^+ beam (red) with an extraction potential of +6 kV enters the einzel lens from the bottom. At the entrance of the lens, the beam is parallel (no divergence) and has a beam diameter of 20 mm. At the top of the lens (exit), the beam is converging and has a beam diameter of approximately 15 mm. The lens on the left does not have the same geometry as the simulated lens and is only included for visualization.

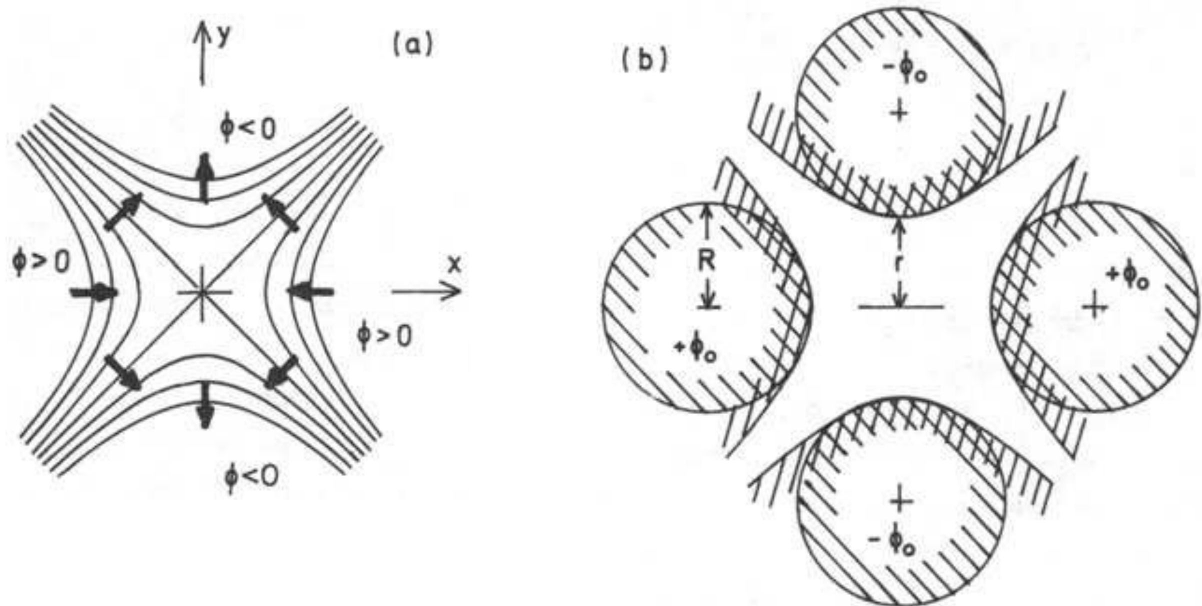

Figure 2.7: Electrostatic quadrupole lens [36]. a) Equipotential lines and field vectors in the quadrupole field are plotted. ϕ denotes the applied electric potential. b) Cross section of a quadrupole lens for a beam of bore radius r, either by using hyperbolic surfaces or cylinders of radius R. The surfaces are set to equal potentials of opposite polarity $+\phi_0$ and $-\phi_0$ in order to create the desired field.

hyperbolic ones. This constructive change causes higher order terms to appear, but these are minimized by choosing an optimal cylinder radius of $R = 1.15 \times r$, where r is the bore radius ($2r$ is the distance between two opposite cylinders) [36]. With such a design, the sixth order term of the quadrupole field is also zero and the greater terms can in general be safely ignored. Fig. 2.7 shows the equipotential lines and field vectors in a cross section of a quadrupole lens and the positioning of the hyperbolic surfaces or cylinders [36]. Quadrupole lenses cannot on their own focus in the horizontal and vertical plane independently, as the focusing power in both planes are dependent on the chosen electrostatic potential. This often makes the use of a single quadrupole lens impractical. Instead, a common solution is to stack up two or more quadrupole lenses, setting each at different potentials. This way, independent focusing in both planes can be achieved [36]. The construction of a magnetic quadrupole lens is analogous to that of its electrostatic counterpart. In this case, instead of electrically charged surfaces, four identical electromagnets are arranged at 90° angles from one another. Two opposite electromagnets are connected so that $\overrightarrow{B}$ points inwards, while the other two are connected so that $\overrightarrow{B}$ points outwards. A magnetic quadrupole lens is shown in chapter 4, Fig. 4.12.

2.4 Ion-induced physical sputtering

If a solid is bombarded with sufficiently high-energy particles, atomic interactions will take place between the impinging particle and the atoms of the target, leading to several different processes. The incident particle may be backscattered (i.e., reflected) in collisions with the

target atoms. If it is not backscattered, it may interact with electrons in the material, leading to a quasi-continuous loss of energy (i.e., electronic stopping). The incident particle may also interact with the atomic nuclei in elastic recoils (nuclear stopping), thereby transferring kinetic energy to its recoil partners, and, if the transferred kinetic energy is larger than the displacement energy, producing knock-on atoms. These can lead to the formation of collision cascades. At sufficiently high impinging particle energies, nuclear reactions may take place. If enough energy is transmitted to an atom of the material, it may break the bonds of the lattice and escape the solid. This process is known as sputtering. It is worth noting that sputtering generally requires momentum reversal (away from the surface as opposed to towards the surface). Momentum reversal may not be required if the target is sufficiently thin, i.e., if the collision cascade is larger than the thickness of the target.

Sputtering behavior is dependent on the ion and target species, the impinging ion energy and angle, the surface morphology and the lattice structure and orientation, proving a complex field of study. For energies in the 100 eV to keV range, sputtering is mainly caused by atomic collisions between the incoming ion and the atoms in the near-surface region of the target, with collision cascades taking place at depths of up to several 100 nm. This is known as physical sputtering. For physical sputtering to take place, the kinetic energy of a target atom moving normal to the surface must be larger than the surface binding energy. This can as a first approximation be taken as equal to the heat of sublimation and is usually below 10 eV. Physical sputtering occurs for all particle-target combinations if the impinging particle energy is above a threshold energy in the range of 10 eV to several 100 eV. Additionally, chemical reactions between the incident ion and the target may take place, enhancing or reducing sputtering, for example, if gaseous molecules are produced or if a strong carbide or oxide layer is formed, respectively. This phenomenon is known as chemical sputtering [40].

Sputtering is dependent of the incident angle of the impinging particle, with trajectories at an angle to the surface normal more likely to produce sputtering. A rough surface will lead to a distorted spectrum of local incident angles when compared with a perfectly smooth surface. Furthermore, an atom that is sputtered may impact another part of the solid's surface and be redeposited, and this event is much more likely if the surface roughness is high (as illustrated in Fig. 2.8) [41, 40].

The amount of surface erosion taking place is measured by the sputtering yield SY, defined as the average number of target atoms removed from the surface per impinging particle:

$$SY = \frac{\text{average number of target atoms removed}}{\text{impinging particle}}. \tag{2.14}$$

The number of atoms sputtered for each individual incident particle may vary widely. Because of this, the sputter yield cannot be used to describe sputtering when dealing with individual incoming particles, but is valid when the impinging particle fluence (total number of impinging particles per unit area) is sufficiently large. This definition is also only applicable when a proportionality exists between the number of atoms removed and the number of incident particles. This is in most cases true. However, in cases of heavy particles (for example molecular ions

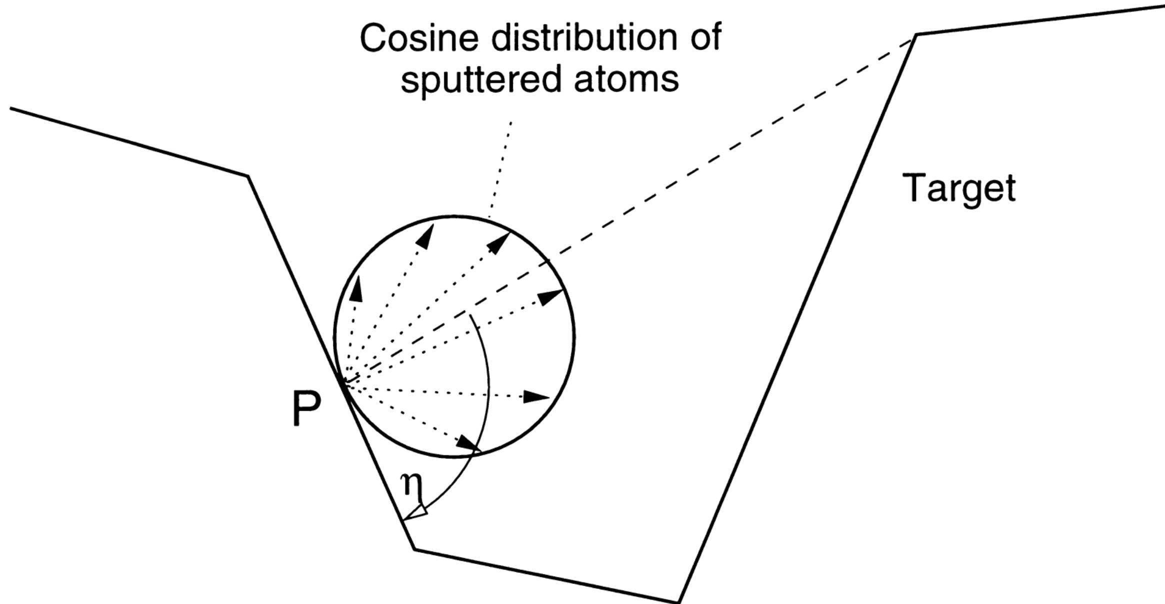

Figure 2.8: A sputtered atom may leave the surface of the target at a point P, following a trajectory corresponding to a cosine distribution. The dashed line between the edge and P cuts off a section of the cosine sphere, η, corresponding to the fraction of atoms that would be redeposited on the target. Figure from [41].

or atom clusters) impinging with energies greater than 10 keV, the sputter yield may depend non-linearly on the number of atoms in said molecular ion or cluster [40].

It is worth noting that the definition of sputter yield pertains only to the number of target atoms removed. Impinging particles that are backscattered or desorbed do not contribute to the sputter yield, nor do trapped impinging particles that are re-emitted.

2.5 Preferential sputtering

When the target is not a pure element but a solute or mixture, the impinging particles will sputter each element present on the surface of the solid differently, since momentum transfer is dependent on the mass of the target atom. Also, the surface binding energy of each atomic species may be different. With increasing fluence, the elements that exhibit a higher sputter yield will be depleted, and those with a lower sputter yield will be comparatively enriched. This process is known as preferential sputtering, and is especially significant when the energy of the impinging particles is greater than the threshold energy of one or more of the elements in the solid, and lower than the threshold energy of the other element(s). An example of this surface enrichment is shown in Fig. 2.9 with an SDTrimSP simulation of impinging 200 eV D^+ ions on a solid composed of 99.67 at.% Fe/0.33 at.% W [42].

This enrichment effect can be beneficial for fusion material applications, as it can allow the formation of a surface layer that exhibits a low sputtering yield, while retaining the physical properties of the bulk material. However, diffusion can occur between the target surface and

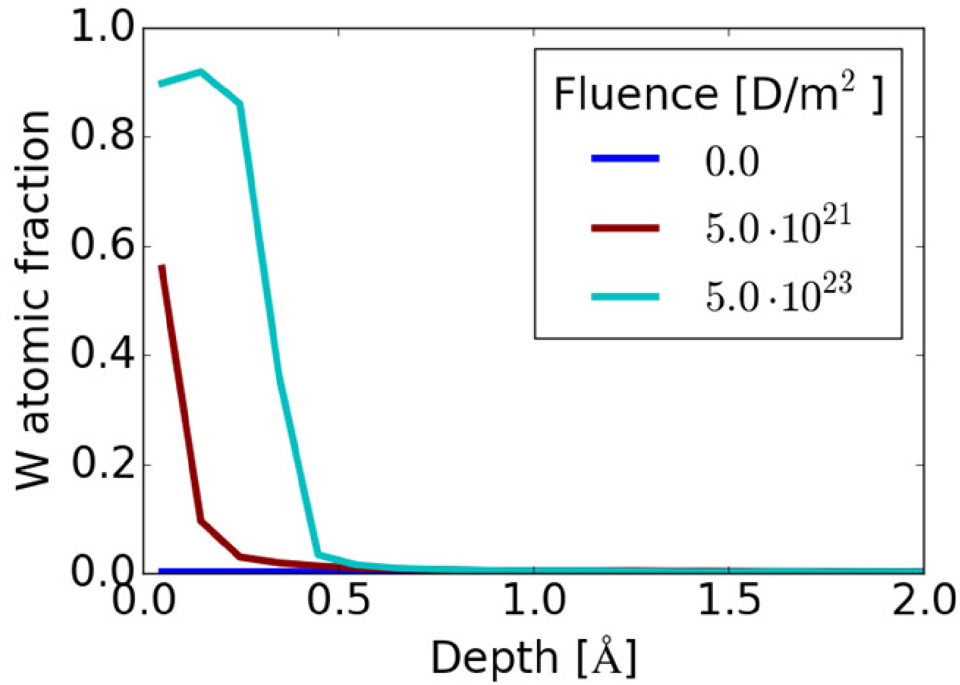

Figure 2.9: One-dimensional dynamic SDTrimSP simulation showing surface enrichment of tungsten in a bulk 99.67 at.% Fe/0.33 at.% W sample under an impinging flux of 200 eV D^+ ions. Depth profiles ($0-2$ Å, 1Å $= 0.1$nm) are rendered after selected fluence steps (0 to $5\cdot10^{23}$ D/m^2), showing a progressive enrichment of W at the surface [43].

bulk, thereby limiting surface enrichment. This effect will be especially pronounced at higher temperatures, since diffusion will be enhanced. Additionally, as previously mentioned, other factors such as the development of surface roughness during erosion will also impact the overall sputtering behavior of the material.

Chapter 3

Supplementary methods employed

3.1 AFM

Atomic force microscopy (AFM) is a high-resolution scanning probe microscopy (SPM) technique that allows three-dimensional imaging of a surface morphology. The operating principle of AFM is based on the accurate measurement of the position of a measurement tip relative to the sample surface. The measuring tip is connected to the open end of a cantilever and is scanned over the sample, typically by way of piezoelectric actuators. As the tip scans over the surface structures, the cantilever is deflected and the movement and deflection of the cantilever is registered by a detector (e.g., beam-deflection method, consisting of a laser beam reflected off the cantilever and two closely-spaced photodiodes). The data is used to measure the forces between the sample and the probe and to reconstruct the morphology of the sample surface. Typically, the so called "tapping mode" is used. In this mode, the cantilever and tip are driven to vibrate at their eigenfrequency, thereby "tapping" the surface. In ambient conditions, this mode is preferable as it avoids the formation of a liquid meniscus layer between sample and the tip. Additionally, it reduces contact between tip and surface, thereby limiting damage to the tip. Utilizing these methods, AFM is capable of imaging several to thousands of square micrometers of the surface morphology with a lateral resolution of the order of nanometers and a height resolution of less than 0.1 nm [44].

However, a key limitation of AFM is the susceptibility to image artifacts caused by tip defects and to unfavorable sample morphology. Due to wear and tear, the scanning tip may become rounded or may be deformed through contact with the sample, thereby altering the contact geometry, force balance and vibrational frequency of the cantilever. This has the effect of compromising the quality of the AFM scans. As such, AFM scanning tips should be exchanged regularly at the first signs of wear. Additionally, irrespective of the tip condition, small structures with high aspect ratios, steep walls and overhangs may not be imaged correctly, or may not be imaged at all, as these structures may not make contact with the end of the tip exclusively. Depending on the morphology of the sample, the surface structure may be "smoothed" over the tip radius (typically in the nm-range), or in the case of steep structures ($> 75°$), the sides of the scanning tip may come into contact with the structure before the end of the tip does.

3.2 SEM

Scanning electron microscopy (SEM) comprises a range of analysis techniques based on the use of a focused electron beam to scan the surface of a sample. The energy of the electron beam is typically in the keV range, though applications exist that utilize sub-keV energies. As the electrons interact with the atoms in the sample, various kinds of signals are produced which contain information on the sample composition and morphology. These signals are registered by corresponding detectors. Combined with the information of the position of the electron beam, an image of the sample surface can be formed with a maximum lateral resolution below 1 nanometer. Very narrow electron beams can be used in SEM, thereby producing images with a large depth of field. The optical magnification range is typically between 10 and 500000 times [45]. Unlike AFM, height information cannot be directly obtained from an SEM image, although stereophotogrammetry (e.g., producing images of the same features at different tilt angles) can be employed to infer said information [46]. Furthermore, also unlike AFM, SEM is typically performed under high vacuum conditions. Since SEM requires for electrons to impinge on the sample, the sample will collect electrical charge if it is not electrically conductive, which may lead to image artifacts.

The set of analysis techniques which can be employed by SEM contain, but are not limited to, secondary electron imaging (SE), backscattered electron imaging (BSE), energy-dispersive X-ray spectroscopy (EDX) and electron backscatter diffraction (EBSD). When employing SE, secondary electrons emitted close to the beam footprint on the sample surface are detected, enabling the production of high resolution images. BSE relies on the detection of electrons from the beam that are elastically backscattered. Since the backscattering efficiency of the electron beam is material-dependent, the intensity of the BSE signal correlates strongly with the atomic number of the material that is being imaged. BSE can, therefore, be coupled with other detection methods to gleam information about the composition of heterogeneous samples. In the context of SEM, EDX relies on characteristic X-ray emission from the sample due to electron excitation by the impinging electron beam. An energy-dispersive spectrometer is used to detect the energy and intensity of X-ray radiation emitted from the sample. Since the X-ray spectra are characteristic of the elemental composition of the sample, EDX can be used to identify the surface composition and relative concentration of the sample at each measured position. The interaction volume of EDX depends on the incident electron energy and on the target composition, and is typically in the range of 100 nm to several µm. EBSD is an analysis technique based on diffraction patterns produced by backscattered electrons from the electron beam. Said electrons may escape from the sample at angles near to the Bragg angle and diffract, thereby forming Kikuchi bands [47, 48]. These bands correspond to the lattice diffracting crystal planes, and can be used to identify the crystal phase and orientation of the material in the measurement region.

Focused ion beam (FIB) milling refers to the use of a focused ion beam (typically $\mathrm{G}a^{+}$) with keV energies to precisely erode material from a specimen via sputtering. With this method, materials can be milled in the nanometer and micrometer scale. FIB can be combined with scanning electron microscopy to produce cross-section SEM images of the sample. This is achieved by

first milling a trench into the material via FIB and then imaging the lateral view of said trench with SEM. Depending on the application, a protecting cover layer (e.g. Pt-C coating) may be deposited on the sample before FIB milling, as this helps to protect the surrounding surface from damage from the FIB. Another use of FIB milling for SEM imaging is the etching of markers onto a sample. Said markers can be useful in order to find the same position on the sample in successive imaging runs. An example of this use would be to mill FIB markers onto a sample, characterize the sample with SEM at a certain position relative to the FIB markers, subsequently expose said sample to some kind of modifying process (e.g. ion beam exposure), and to characterize the sample morphology again after exposure at the same position on the sample with the help of the FIB marks.

3.3 XPS

X-ray photoelectron spectroscopy (XPS) is an analysis technique which utilizes an X-ray source (e.g., a Al Kα source to produce a beam of 1486.7 eV) to irradiate the material to be investigated. Electrons are emitted from the sample surface, up to a depth of several nm, and are registered along with their kinetic energy by a detector. The resulting energy spectrum is characteristic of the elemental (and chemical) composition of the sample at the surface, since the emitted electrons have a discrete energy which directly depends on their electronic configuration in the atom from which they were emitted. When using XPS in ultra-high vacuum ($P < 10^{-9}$ mbar) conditions, the elemental composition of the sample at the surface can be determined with an accuracy in the range of $1 - 0.1$ at.%. The detection limit under such conditions is typically in the range of 0.1 at.%. Like SEM, XPS is a non-destructive, non-contact technique. However, it is not suitable for materials that cannot be exposed to a vacuum, though XPS systems that can operate at near-ambient pressure are currently under development [49, 50].

XPS can be used for depth profiling with the addition of ion beam etching, also known as sputter-XPS. An ion source (e.g., a keV-energy Ar^+ sputter gun) is used to sputter material from the sample surface in an area that is substantially larger than the XPS analysis beam-spot, which is typically of the order of $1\,\mathrm{mm}^2$. XPS measurements are performed periodically between successive ion beam exposures, thereby obtaining information on the elemental composition of the sample at successive depth intervals. If ion etching is used, sputter-XPS cannot be strictly considered a non-destructive analysis method, as material needs to be removed from the surface in order to perform depth profiling. Ion beam etching can also be useful to eliminate surface contaminants from the sample, such as hydrocarbons or oxides. However, it must be noted that the process of sputtering can also lead to unintended modifications of the surface via preferential sputtering, beam mixing, forward implantation or modification of the surface morphology [50].

3.4 RBS

Rutherford backscattering spectromety (RBS) is a quantitative ion beam analysis (IBA) technique which hinges on nuclear backscattering processes (mainly elastic recoils) to measure a

sample's depth-resolved elemental composition. In RBS, ions are extracted from an ion source and accelerated to energies typically in the MeV range (e.g., in a tandem accelerator). The energetic ions impinge on the target and may backscatter. In many cases, the backscattering cross-section can be calculated. Many cross-sections have been measured and are available from literature (e.g., IBANDL[1] from the Nuclear Data Section of the International Atomic Energy Agency [51]). A detector situated at an angle greater than 90° relative to the ion beam trajectory registers the energy of the backscattered particles that reach it. From the number of particles reaching the detector and their energy an energy spectrum is built, where the detector counts (number of backscattered particles) is usually plotted in the y axis and the backscattered particle energy is plotted in the x axis. An example of an RBS spectrum is shown in chapter 5, Fig. 5.5.

The energy of the backscattered particles is always lower than the initial ion energy. Two kinds of processes are responsible for the energy loss: scattering and electronic stopping. Scattering events are stochastic, dependent on the scattering cross section, and produce a discrete energy loss which is a function of the recoil angle, the mass and the atomic number of the projectile and target atom. For a given recoil angle (chosen by the placement of the detector), ion species and impinging energy, the energy loss due to scattering is characteristic of the target atom species. Electronic stopping results in a gradual energy loss as the projectile moves through the sample. This process lowers the measured energy of the projectiles that backscatter and reach the detector proportionally to the distance they have traveled into the sample (depth, if the sample is oriented normal to the ion beam). Different elements in the sample produce different peaks on the energy spectrum. The width of a peak is indicative of the thickness of the layer containing the element, while the energy shift of the peak indicates the depth at which the corresponding layer is found. The relative peak height can be used to quantify the concentration of each element. With the use of a calibration target, RBS can yield absolute measurements of particle densities [52].

When using this method, the thickness of thin films can be determined with sub-nm accuracy. The depth resolution of RBS is limited by the energy resolution of the detector [53]. For instance, when applied to determining the concentration of W at the surface in RAFM[2] steels, which contain small amounts of W, utilizing a time of flight detector (ToF), changes in concentration of the order of 1% are detectable with a depth resolution of a few nanometers.

3.5 Ellipsometry

Ellipsometry is an optical technique based on measuring the change of polarization of light upon reflection or transmission through thin films. The technique is applicable to sufficiently transparent materials and is very sensitive to changes in the optical response of the material. It has been used to successfully characterize several material properties, such as film thickness, composition, roughness, electrical conductivity and concentration of doping elements [54]. The

[1] Ion Beam Analysis Nuclear Data Library
[2] Reduced Activation Ferritic Martensitic

experimental setup consists of a light source (e.g., a laser), two polarizers, and a detector. Light emitted by the source is linearly polarized by the first polarizer and impinges on the sample at an angle. The reflected light passes through the second polarizer and reaches the detector. The second polarizer and the detector are placed specularly with respect to the sample, i.e., the angle of incidence between light source and sample normal is equal to the angle of incidence between sample normal and detector. Additional optical components, such as $\lambda/4$ plates, can be placed between each polarizer and the sample. When used, the $\lambda/4$ plate converts linearly polarized light into circularly or elliptically polarized light and vice versa.

When using ellipsometry to measure film thickness, as it was done in this work with amorphous hydrogenated carbon films, resolutions of fractions of a monolayer can be achieved [55]. The method is applicable to study layers whose thickness ranges from a few tenths of a nanometer up to several micrometers, and has been used in the past to quantify fluxes and angular distributions of sources of hydrogen and deuterium radicals [56]. Ellipsometry can be employed both in air and in vacuum applications. In all cases, since the technique is sensitive to a range of material and geometric properties of the sample, measurements are compared to an optical model. Typically, the optical model approximates the sample as a series of optically isotropic, homogeneous layers, though techniques have been developed to accommodate more complex models. The necessary use of an optical model is a drawback of ellipsometry, as an erroneous assumption in the properties of the sample will lead to a systematic error in the interpretation of the measured data.

3.6 SDTrimSP

SDTrimSP is a Monte-Carlo-based code used to simulate transport of energetic particles in matter based on the binary collision approximation, which has been shown to be valid in the eV - keV range [42]. The code is based on the previous TRIM.SP and TRIDYN codes, which used the same physics, and is suitable for both sequential and parallel architectures. SDTrimSP is capable of calculating fluence-dependent sputter yields, transmission ranges and reflection coefficients, as well as depth distributions of implanted particles and energy and angle distributions of backscattered and sputtered particles [57]. The projectile trajectory is calculated in three dimensions. The target is one dimensional, consisting of a series of perfectly smooth layers of variable composition. In the static simulation mode each layer thickness and composition is fixed, whereas in the dynamic mode the layer thickness and composition is allowed to change based on material transport between layers due to ion bombardment. However, since the target is one dimensional, surface roughness and lateral inhomogeneity are ignored. A 2-D version of the code was developed and successfully benchmarked [58, 59].

Recently, SDTrimSP was further parallelized to allow simulation of 3-D targets [60]. With this code, lateral inhomogeneity, surface roughness, and their evolution with increasing fluence can be taken into account in simulations. Instead of layers of variable concentration, the targets in the 2-D and 3-D versions of SDTrimSP consist of squares of infinite thickness and cubes, respectively. Since the surface is composed of discrete square- or cube-like elements, inclined

surfaces are approximated in the code as terraced surfaces, much like a ramp could be approximated by steps on stairs. This approximation is only valid if the trajectory of the projectile and the collision cascades extend over several cells. This condition sets a maximum size limit on the cell resolution of the target in the simulations, which is typically in the range of nanometers. The computation time of the 2-D and 3-D codes scales with the number of surface cells. As a consequence of this, the size of the simulated volume (in the 3-D case) is in practice limited, as simulating large volumes (e.g., substantially larger than $0.1 \times 0.1 \times 0.1\,\mu m^3$) may quickly become computationally expensive. As an example, an SDTrimSP computation of 5 keV Ar bombardment on a Si target with a depth resolution of 2.5 nm to a fluence of 5×10^{21} atoms m^{-2} can be performed in 15 minutes on 32 cores. An equivalent SDTrimSP-3D simulation with the same exposure conditions with a target comprising $40 \times 40 \times 80$ cubic cells of 2.5 nm length ($100 \times 100 \times 200\,nm^3$) running on the same number of cores requires 52 hours.

Within the scope of this work, a first static validation of SDTrimSP-3D is discussed in section 5.1.2 and the first dynamic validation of the code is discussed in section 5.2. All simulations with SDTrimSP-3D shown in this work were not performed personally by the author, but were the result of collaborative work within IPP.

Chapter 4

Description and characterization of SIESTA

As previously mentioned in chapter 1, erosion in the first wall is caused predominantly by an intense flux of neutral particles, which are neutralized close to the plasma edge and are, therefore, no longer confined by the magnetic field. The mean impinging particle energies are typically in the $8 - 300$ eV range [23]. Under these conditions, erosion is driven by physical sputtering [40], and can be accurately simulated by Coulomb interactions [61]. This process can also be studied experimentally, either in plasma devices which emulate the conditions of the plasma edge of a fusion reactor, or with the use of an ion source. Plasma devices allow for high particle flux densities to the target surface in the desired particle energy range. However, the presence of impurities, multiple ion species and a not easily determinable flux of energetic neutrals along with the intrinsic energy spread of the particles can make the quantitative analysis of results difficult. In contrast, ion sources have a number of distinct advantages over plasma devices, producing a mono-energetic beam which can be mass-filtered with magnetic sector fields, allowing for well-defined experiments. Historically, these machines have achieved significantly lower particle flux densities than their plasma counterparts, leading to longer exposure times to reach the desired fluence.

SIESTA (Second Ion Experiment for Sputtering and TDS Analysis) helps to bridge this gap, aiming to provide higher particle flux densities without losing the advantages of the ion source setup. SIESTA is the successor of the pre-existing HSQ (in German, *HochStromQuelle*) [62], which during its over 40 years of operation at the Max Planck Institute of Plasma Physics in Garching was instrumental in over 200 publications. At SIESTA, a DuoPIGatron type ion source is employed to provide particle flux densities of several 10^{19} $\mathrm{m^{-2}s^{-1}}$ to the target with a mono-energetic, mass-filtered ion beam (typically D_3^+), with a final operating energy range of $200\,\mathrm{eV} - 10\,\mathrm{keV}$. The device is described in detail in section 4.1, and section 4.2 details the results of the characterization of SIESTA. The sputter yield of Au by deuterium atoms with an impact energy of 2 keV was measured and contrasted with simulations and experimental data, shown in section 4.3. Finally, the main conclusions are summarized in section 4.4.

Substantial sections of this chapter have been presented in the article by the author [24].

4.1 Description of the experimental setup

4.1.1 Overview

A principle overview of the individual components of SIESTA is presented in this section. Fig. 4.1 shows a bird's eye view of SIESTA along with its main elements. The most important components are described in more detail in the following sections.

A plasma is generated inside the ion source, which is set to a high (positive) potential of maximum 10 kV, which determines the extracted ion energy. A series of three grids, the first at ion source potential and the last at ground potential, separate the ion source from the rest of the beam path. The ions that diffuse towards the grids are accelerated by the potential difference in the space between them, leading to a steady state ion beam of the desired energy. The intermediate grid serves to repel electrons away from the positively-biased ion source and is described in more detail in section 4.1.2.

The neutral gas from the ion source is mostly evacuated in the differential pumping stage. The beam diameter is limited at the exit of the differential pumping stage by a Ø 16 mm Mo aperture (Fig. 4.2). A pneumatically-actuated beam-stopper, described in more detail in section 4.1.4, is located directly behind this aperture.

Behind the Mo aperture and with the beam stopper retracted, the beam passes through the dipole magnet. Each ion species present in the beam is deflected, with a radius of curvature proportional to the square root of its mass, thereby splitting the beam (discussed in further detail in section 4.1.5). The magnetic field is varied to allow only the desired ion species to exit through the opening to the target chamber, situated at a 44° angle from the dipole magnet entrance.

The target is housed in a double cage that serves as an electrical screening element and as a secondary electron catcher for the ion current measurement at the target. On its trajectory, the beam is cropped by an adjustable aperture into a circular or elongated shape and passes through openings in the double cage before impinging on the target.

The target can be rotated and heated via electron-impact heating. Further it can be set to a positive potential in order to decelerate incoming ions and thus study erosion at low (i.e., sub-keV) particle energies while continuing to operate the ion source at a high accelerating potential, which produces high particle flux densities. A magnetic suspension balance enables in-situ weight-loss measurement of the sample.

Samples can be loaded via a lateral, separately-pumped load-lock with a horizontal manipulator. A vertical manipulator at the load-lock can be used to transfer the sample to the Thermal Desorption Spectrometry (TDS) chamber, located directly underneath. This enables in-vacuo retention experiments.

4.1.2 DuoPIGatron ion source, gas supply & cooling system

The DuoPIGatron ion source was developed by Davis et al. as a variation of the pre-existing 4-electrode duoplasmatron device, consisting of a Penning Ion Gauge (PIG) discharge with a

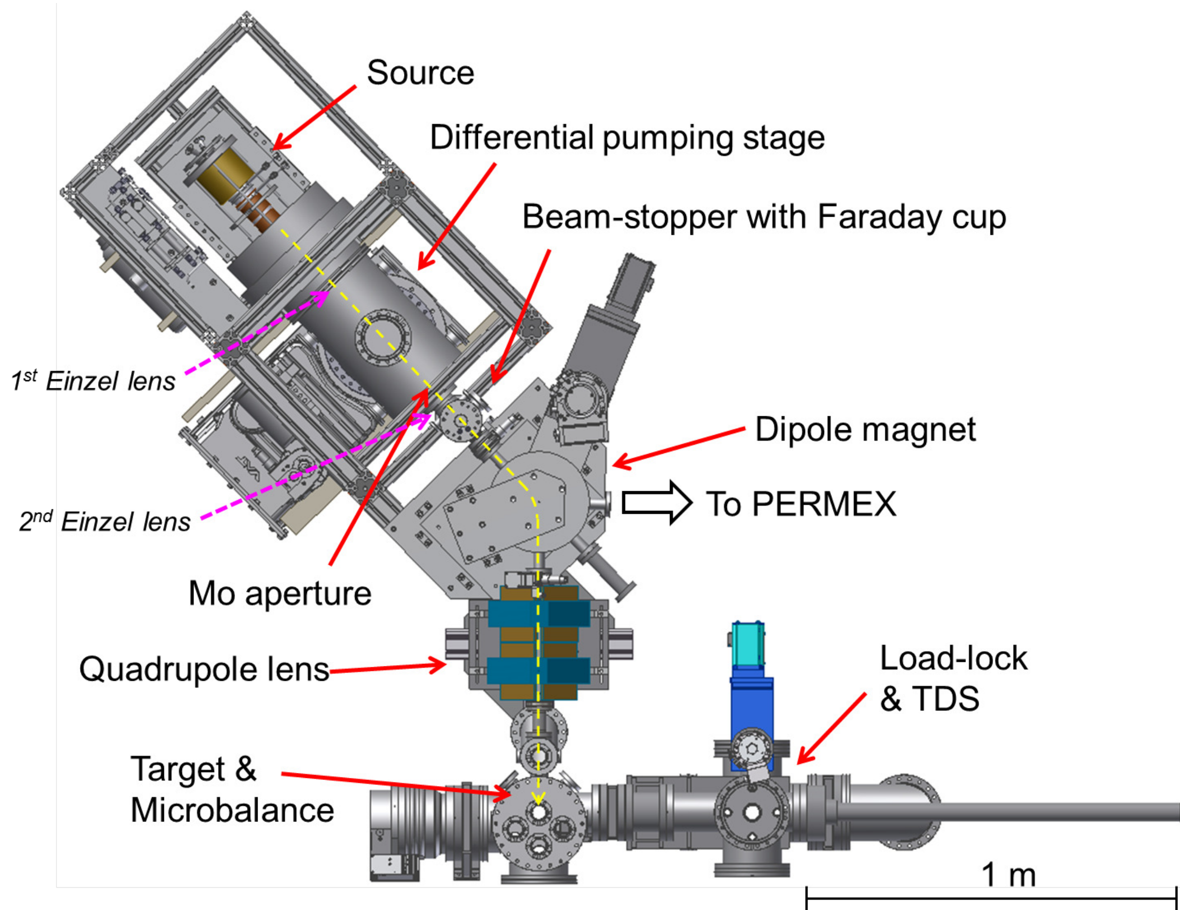

Figure 4.1: CAD bird's-eye view of SIESTA. The yellow dashed arrow indicates the ion trajectory from the ion source to the target. The einzel lenses (marked with dashed magenta arrows) were later removed and are described in more detail in section 4.2.3. The new version of the ion-driven permeation experiment PERMEX will be located at the exit of the dipole magnet labeled "To PERMEX" [63].

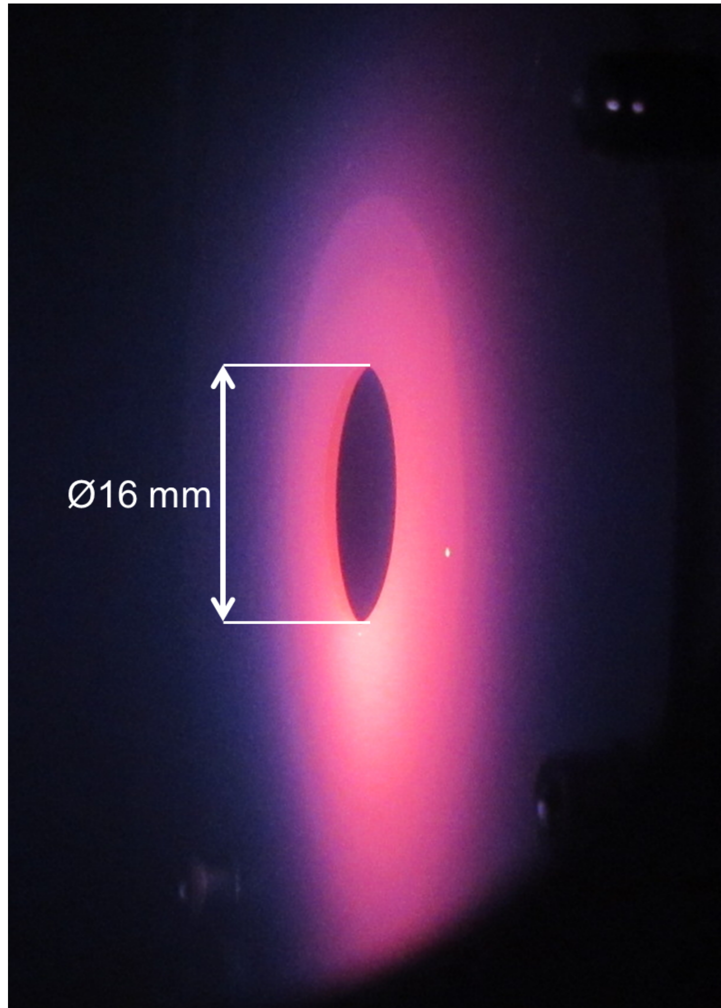

Figure 4.2: Deuterium ion beam impinging on the Mo aperture located at the end of the first differential pumping stage, as seen from the side facing the ion source through a lateral viewing port. Despite active water cooling, the heat load from the ion beam is sufficient to heat the aperture to temperatures at which it begins to glow. Given the layout of the cooling circuit, cooling efficiency is lower directly below the aperture, leading to higher temperatures in this region and causing it to shine brighter. The purple haze surrounding the aperture is due to recombination light emitted when the impinging D ions neutralize. The aperture is fixed to the differential pumping stage by hex socket head screws situated around the aperture. One such screw is visible on the lower left side of the image.

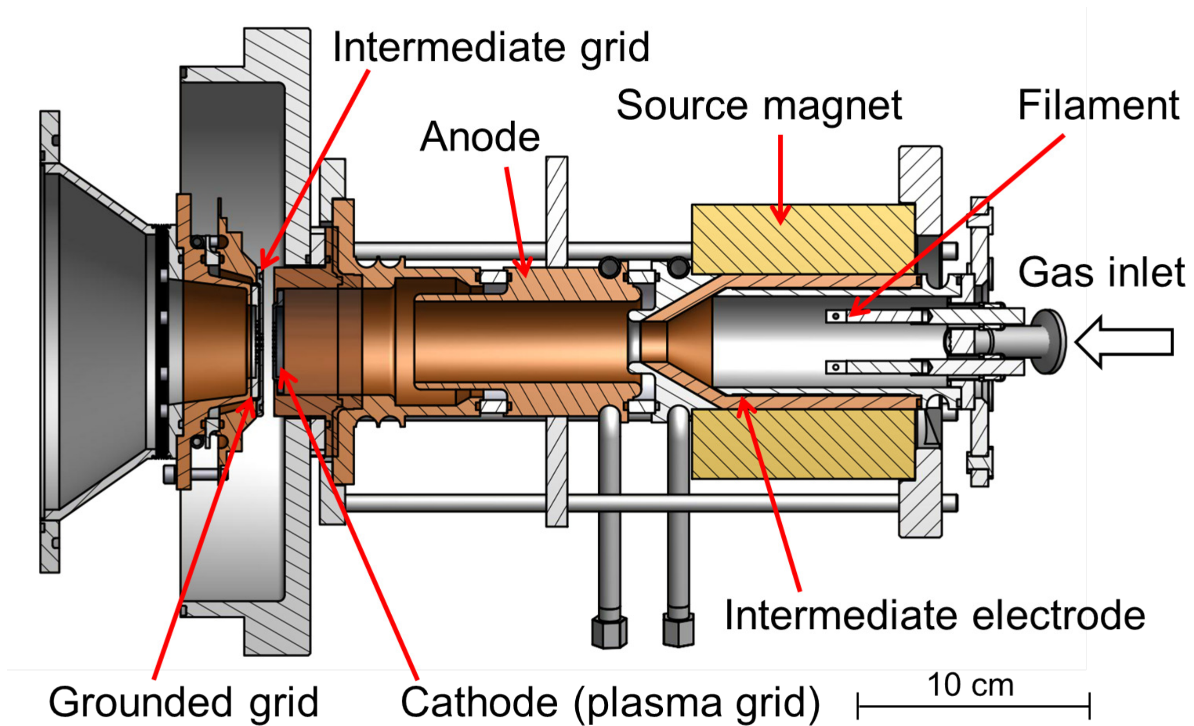

Figure 4.3: Half-section view of the DuoPIGatron ion source. No filament is in place in the figure.

plasma feed from the duoplasmatron source [64]. It was designed to serve as a high-current positive ion source for continuous or pulsed operation, and was used as main ion source for plasma heating via neutral beam injection [64, 65].

The coated filament in the ion source is heated to produce electrons through thermionic emission. A potential difference of 40 V is used to accelerate the electrons to the cylindrical anode (shown in Fig. 4.3), forming a stable arc typically set to an arc current of 12 A. As gas is let in through the chamber, a low-pressure gas discharge is formed and compressed to a high ionization degree in the ferromagnetic intermediate electrode, surrounded by an electromagnet. The ions exiting the intermediate electrode are confined in a PIG discharge, with the intermediate electrode acting as first cathode. It is separated from the plasma grid (taking the role of the complementary cathode) by the hollow anode. The plasma expands radially near the plasma grid, also known as extraction grid in the literature, and a radially homogeneous beam is observed at the plasma grid [65]. The source floats at the extraction voltage, which can be set up to 10 kV, as do the flow controllers for the gas inlet. Beyond the plasma grid, two more grids are present: an intermediate grid set to a low negative potential of up to -165 V and a final grounded grid. Ions are accelerated out of the source in the 3.7 mm gap between the first (extraction) and second (intermediate) grid. This intermediate grid serves to repel electrons emitted in beam charge exchange reactions in the first differential pumping stage that would otherwise be accelerated towards the ion source. These electrons facilitate high space charge compensation in the beam. The spacing between intermediate and grounded grid is 0.7 mm.

Figure 4.4: High-voltage cage of the DuoPIGatron ion source. Below the source, the cooling lines coiled into double spirals can be observed.

The source is located within an aluminum high-voltage cage made from item MB Building Kit System[1] standard parts, PEEK (PolyEther Ether Ketone, a thermoplastic polymer) and PMMA (Polymethyl methacrylate, acryllic glass), as seen in Fig. 4.4. The door to the cage is connected to an interlock which shuts off the ion source power supplies in the event of the door being opened.

The filament is composed of a tantalum wire, chosen for its high melting point, coated with a mixture of low-work-function compounds, which facilitate good thermionic emission at relatively low filament temperatures. Before coating, the filament is wrapped in a nickel mesh to increase the wettable surface for the coating to the filament. The coating is a mixture of nickel, barium carbonate and strontium carbonate, at a proportion of 8:1:1 in volume, respectively. Originally

[1] Registered trademark of item Industrietechnik GmbH

Figure 4.5: Coiled ion source filament before coating. In the background, the grooved brass cylinder used to coil the filament and an uncoiled tantalum filament, already wrapped in a nickel mesh, can be seen.

in powder form, the solid coating mixture is dissolved in pure analysis-grade ethanol and is applied to the filament with a brush, at which point it is allowed to dry for some $1-2$ minutes before applying another layer of coating. $2-3$ layers are usually required to achieve a sufficiently thick coating. After this step, the filament can be mounted on the vacuum flange housing the gas inlet and the electrical feed-throughs. Fig. 4.5 shows the coiled filament before coating, along with an uncoiled filament and the brass cylinder in the background.

All three grids present the same configuration, consisting of 37 Ø 2 mm holes with 1 mm spacing with an effective diameter of Ø 20 mm organized hexagonally for high transparency (up to 60 %). As a consequence of this design choice, the grids are only cooled around their respective edges, and so are not optimized to withstand high heat loads [65]. This limits the extraction voltage of the source and consequently the total extractable ion current, especially in steady state operation. The grids were manufactured from TZM, a 99 % molybdenum alloy with better mechanical and manufacturing properties than pure molybdenum, yet still retaining the

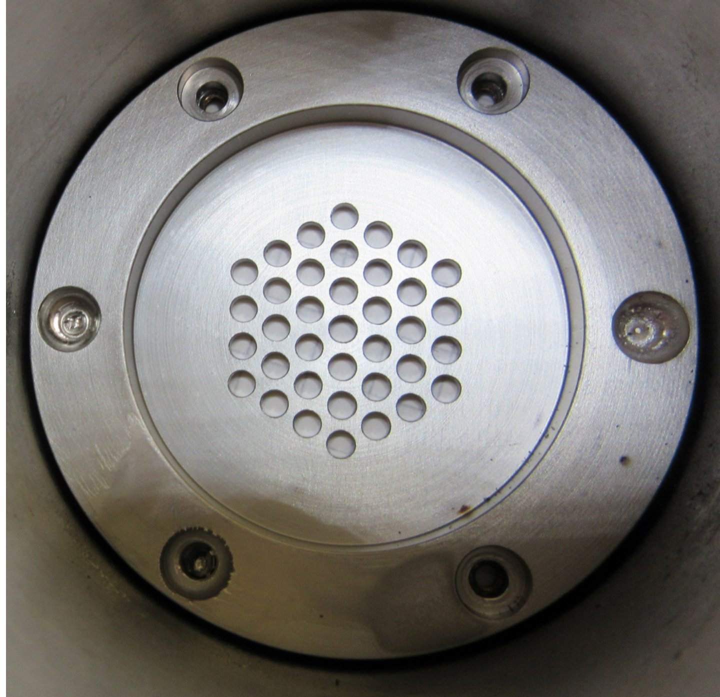

Figure 4.6: Ion source extraction grid with partly-melted steel screws. The screw heads have either melted or have broken off due to thermal stresses.

advantages of high melting point and very low coefficient of thermal expansion [66]. Molybdenum screws were used to secure the first grid to the copper cooling ring, as it was seen that stainless steel screws lead to partial melting and fracture from thermal stress, due to the two materials' different thermal expansion coefficients, as seen in Fig. 4.6. To maximize the beam transmission, the three grids were aligned hole-on-hole and all three were aligned co-axially with the rest of the ion source with stiff ∅ 2 mm rods of an adequate tolerance and optically via an adjustable precision telescope.

The gas supply consists of up to four 2-liter pressurized gas bottles, each connected to a pressure regulator with a maximum pressure rating of 300 bar and a maximum output rating of 10 bar. Each line has its own bypass leading to a common venting line which can be evacuated with a Kashiyama NeoDry 15E[2] dry vacuum pump. After the venting line bypass, the first and second lines are connected together, as are the third and fourth lines. Each line is then introduced into the high voltage cage via a ceramic insulator, as shown in Fig. 4.7 (labeled "To source"). To avoid a gas discharge within the ceramic insulator, the pressure in the lines must during operation be maintained at a value above the one dictated by the Paschen curve for the selected gas species [67]. This is assured with switch manometers in the gas lines connected to the ion-source interlock. At a pressure below 3 bar, the switches are open and it is impossible to operate the ion source. Stainless steel tubes with an outer diameter of 6 mm are used for the complete gas supply system. All connections are made with Swagelok[3] components.

[2] Trademark of Kashiyama Industries, Ltd.
[3] Registered trademark

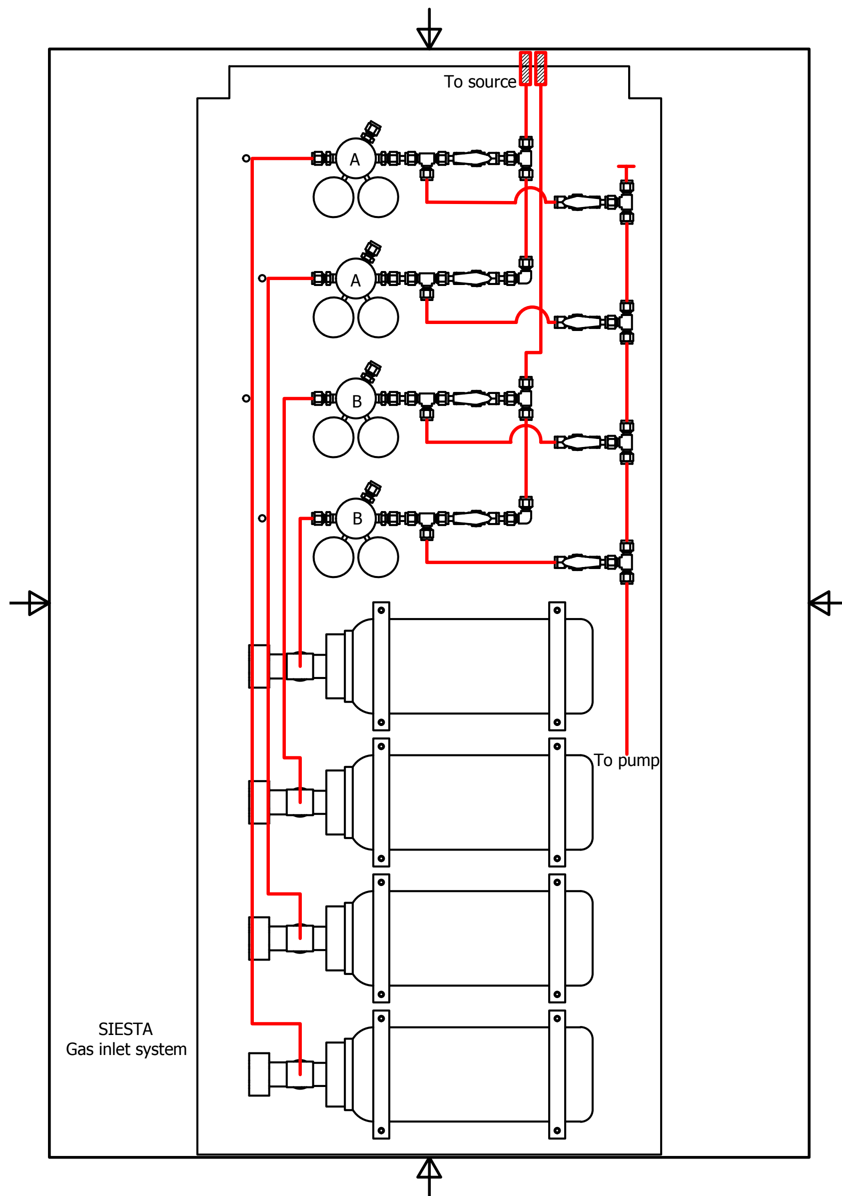

Figure 4.7: Draft of the gas connection scheme of SIESTA.

The gas flow is controlled by two Bronkhorst EL-FLOW[4] electronic flow controllers within the high voltage cage, allowing a maximum flow rate of 20 sccm (standard cubic centimeters per minute). A typical flow rate when using deuterium is 10 sccm. The flow controllers are operating at source potential and are powered through a galvanically separated transformer. They are controlled through proprietary Bronkhorst[5] software via an RS232 connection. Fiber-optic waveguides with RS232-frequency couplers are used to maintain the galvanic separation between computer and flow controllers.

Deuterium was used to characterize the ion source. Hydrogen, helium and argon have also been tested. However, when producing argon or helium plasma, the source must first be ignited with hydrogen, and then the hydrogen flow must be partially reduced in favor of the desired gas.

A series of FUG[6] power supplies are used to provide power to the ion source and to set it to the desired accelerating potential. All power supplies are insulated up to 15 kV and are grounded relative to the extraction grid potential. The connection scheme of the source components is detailed in Fig. 4.8. Typical values are listed in table 4.1.

To prevent overheating, three separate cooling lines are used to cool the ion source, ion source magnet, dipole magnet, beam stopper, ion source grids and Mo aperture. All ion source components, with the exception of the source magnet shown in Fig. 4.3 (i.e. filament, intermediate electrode, anode and cathode), are cooled by a dedicated cooling circuit with a de-mineralized water-water heat exchanger. (FCUN004 model from National Lab[7]) at a nominal pumping pressure of 2.9 bar. The source magnet is made of a coiled rectangular copper tube with channel dimensions of 1×2 mm, outer section of 3×4 mm and an uncoiled length of several meters, insulated with cellulose and resin. As a consequence of this design, the cooling water through the source magnet is subject to large pressure losses. For this reason, a separate cooling circuit with an air-water heat exchanger and pump delivering a nominal pressure of 3 bar (PCNO 10 from National Lab) is used for the source magnet. De-mineralized water is used to prevent current losses through these two cooling circuits between the ion source and the cooling water pumps and heat exchangers. The water conductivity is measured periodically. The cooling lines of both of these circuits are coiled into two sets of concentric spirals below the source, one for the inlet line and the other for the outlet, in order to increase the effective length of the cooling lines before exiting the housing cage of the source, helping to reduce current losses through the water lines. The coiled cooling lines are shown in Fig. 4.4. The second (intermediate) and third (grounded) grids are cooled separately with a third cooling circuit, which also supplies water to the Mo aperture, beam-stopper and dipole magnet, consisting of a water-water heat exchanger and pump (FCUN001 from National Lab). Since these components are either grounded or set to low voltages (lower than 200 V), no de-mineralized water is required in this cooling circuit. The secondary circuits of the two water-water heat exchangers are supplied with cooling water from the building at a constant temperature of 14°C. A pressure regulator is installed before the

[4]Trademark of BRONKHORST HIGH-TECH B.V.
[5]Trademark of Bronkhorst High-Tech B.V.
[6]Trademark of FuG Elektronik GmbH
[7]Trademark of National Lab GmbH

inlet of the secondary circuits, lowering the inlet pressure from 6 bar to 3 bar. A solenoid valve installed after the pressure regulator is connected to two water sensors placed on the floor. In case of a water leak, the sensors will open the electric circuit powering the solenoid valve, which will close, stopping the flow of water. Flow meters are installed in each primary and secondary cooling line. If the water flow in any of these lines is lower than a pre-defined value, the ion source is switched off to prevent over-heating of the source components.

Power supply	Voltage [V]	Current [A]
High Voltage	6000	0.028
Filament	4.2	20
Magnet	5.8	20
Arc	195	12

Table 4.1: Typical currents and voltages applied by the ion source power supplies when using deuterium.

4.1.3 Vacuum system

SIESTA can be divided into five separate high-vacuum chambers: The ion source and differential pumping stage including beam-stopper, the dipole magnet, the target chamber including quadrupole lenses and antechamber, the load-lock and the TDS chamber. Each chamber is separated from its neighbors by a high-vacuum gate valve and is outfitted with its own turbomolecular pump, which is also separated from the vacuum chamber by another gate valve. Each turbomolecular pump is connected to one of two rotary vane vacuum pumps. Operationally, these two rough vacuum pumps mean that SIESTA comprises two entirely separate vacuum systems: a “clean” vacuum system for the target chamber and TDS chamber, and a “general” system for the rest of the components. Additionally, the aforementioned dry vacuum pump for pumping of the gas inlet system (see Sect. 4.1.2) is used as a bypass pump and is connected to each turbomolecular pump and to the load-lock. This allows for each vacuum chamber and turbomolecular pump to be either pumped or vented independently of the rest, which is useful for maintenance operations. A schematic of the vacuum system is shown in Fig. 4.9.

The rotary vane pumps from the “clean” and “general” vacuum systems are each equipped with a coaxial foreline trap and a molecular sieve trap to prevent oil from reaching the turbomolecular pumps in the event of a blackout or pump malfunction. Additionally, an oil filter has been installed in the exhaust line of each of the pumps, which is then led outside of the building. They have each also been equipped with an automatic oil return line and a Pirani TPR 280[8] pressure gauge. To avoid the formation of a potentially explosive atmosphere at the exhaust of the vacuum pumps if hydrogen or other explosive gases are used in the ion source, each pump is provided with a gas ballast connected to an N_2 line. A Duo20M rotary vane pump[9] is used for

[8]Trademark of Pfeiffer Vacuum GmbH
[9]Trademark of Pfeiffer Vacuum GmbH

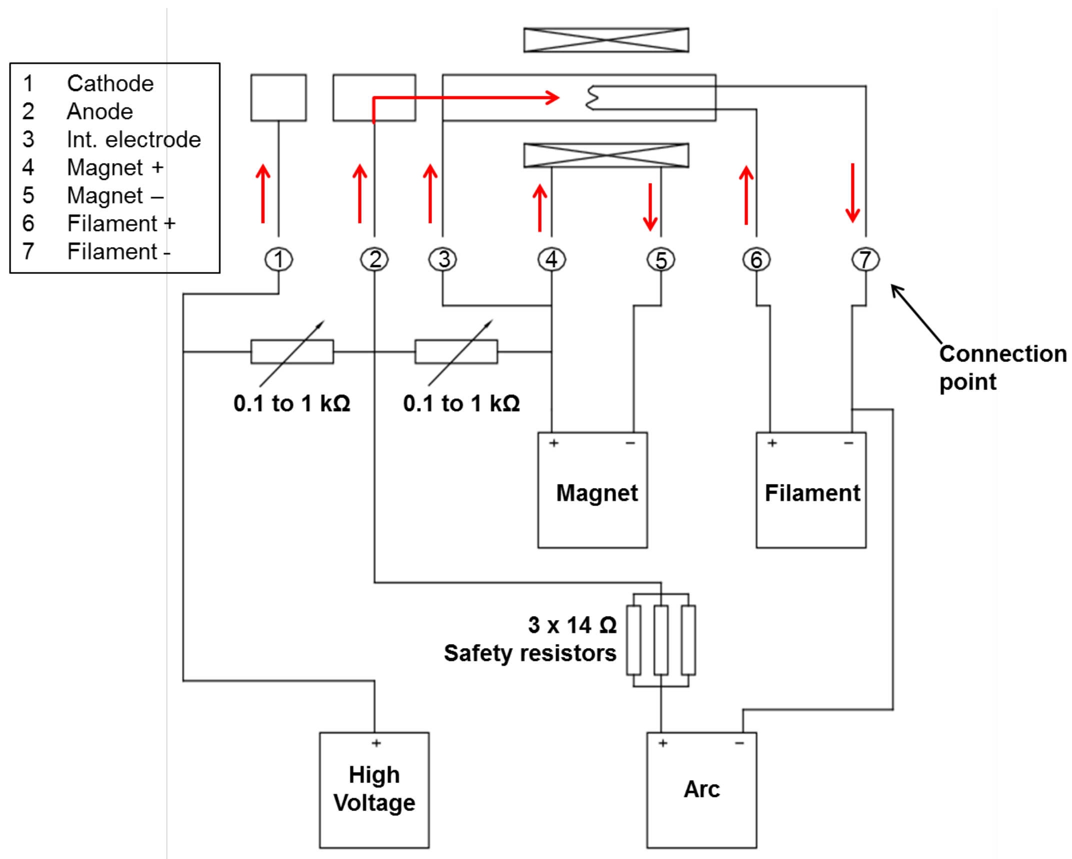

Figure 4.8: Schematic of the electrical connections of the DuoPIGatron ion source to the power supplies. The red arrows above the connection points represent the direction of the electric current. All connection points as well as the magnet, arc and filament power supplies are set to high voltage by way of the high voltage power supply.

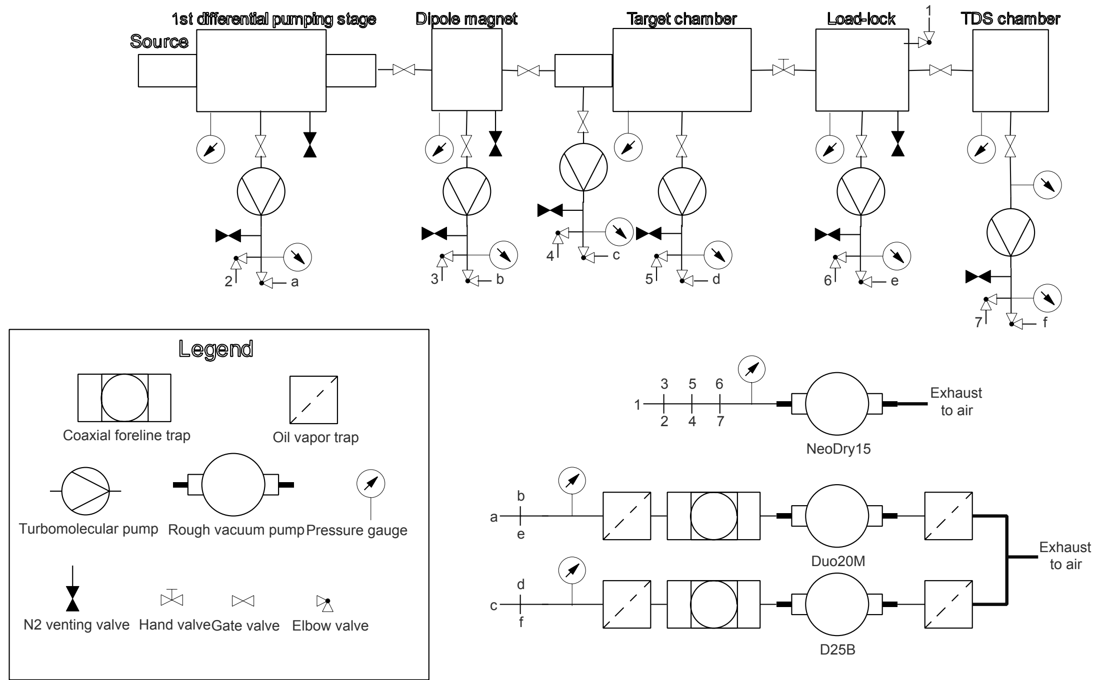

Figure 4.9: Schematic of the vacuum system of SIESTA.

the "clean" vacuum system. The "general" system employs a D25B pump[10]. The pressure in each separate vacuum chamber is measured with a PKR 251 Full-Range Cathode[11]. Additionally to the Pirani gauges located at the feed of the rotary vane pumps, pirani gauges are also present at the exhaust of each turbomolecular pump in the system, after which a manual elbow valve is located. This is useful in troubleshooting situations where it is unclear whether higher than nominal pressure (10^{-2} mbar) in the rough vacuum line is due to a problem with one of the turbomolecular pumps or with the rotary vane pump it is connected to.

A base pressure of 10^{-7} mbar is achieved in all the vacuum chambers. In the TDS chamber, the base pressure is below 5×10^{-9} mbar. Since each chamber is pumped separately and the cambers are separated by small apertures (e.g. Mo aperture, beam-defining aperture), during operation of the ion source, pressure differentials are maintained along the beam-line. The pressure in the (first) differential pumping stage is around 10^{-4} mbar, the pressure at the dipole magnet (second differential pumping stage) is of the order of 10^{-6} mbar and the pressure at the target chamber (third differential pumping stage) is typically around 5×10^{-7} mbar.

All vacuum connections in the high-vacuum chambers are made with CF[12] flanges, with the exception of the gas inlet (KF flanges), the N_2 venting lines (KF) and the differential pumping stage flanges (ISO-K). KF connections are used in all the rough vacuum lines (between the turbomolecular pumps and the rough pumps). All gate valves are pneumatically actuated,

[10]Trademark of Leybold GmbH
[11]Trademark of Pfeiffer Vacuum GmbH
[12]ConFlat is a registered trademark of Varian, Inc.

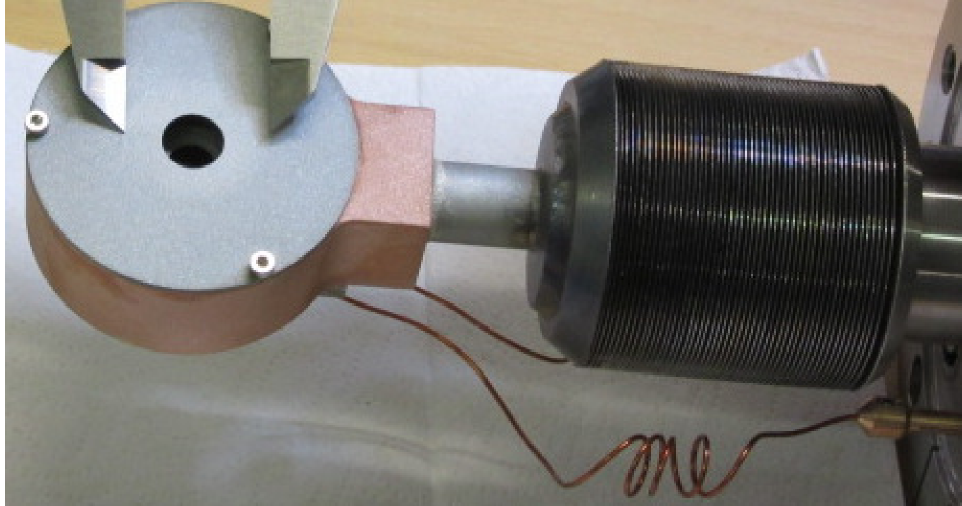

Figure 4.10: Beam-stopper employed at SIESTA equipped with a faraday cup to measure the ion beam current.

possessing a mechanic and electric switch, with the exception of the gate valve connecting the target chamber and the load-lock. This is actuated manually as a precaution: in case of loss of power while the horizontal manipulator is fully extended into the target chamber - as is the case when switching samples - the gate valve could shut automatically, damaging the gate valve and potentially also causing damage to the manipulator and target chamber.

4.1.4 Beam-stopper

The beam-stopper, shown in more detail in Fig. 4.10, can be inserted into the ion beam to obscure the target without shutting off the ion source. The beam-stopper is mounted on a vacuum bellow and is equipped with a pneumatic piston to extend or retract it. Additionally, the beam-stopper is also equipped with a Faraday cup (Fig. 4.10), which allows measurement of the beam current at this position. The metal sheet with the Ø 7 mm aperture in front of the Faraday cup is electrically isolated from the Faraday cup and can be biased to repel electrons trapped in the beam and inhibit secondary electrons from leaving the Faraday cup. As described in section 4.1.2, the beam-stopper is water-cooled.

4.1.5 Dipole magnet and quadrupole lens

The dipole electromagnet was custom-made by DANFYSIK[13], supplying a nominal uniform field of 0.13 T at a current of 27 A. The nominal curvature radius to deflect the ion beam towards the target is 150 mm. Operation with the magnet at higher currents is possible, up to 120 A, leading to a maximum induction of 0.7 T, enough to successfully deflect 10 keV Ar ions. To remove the heat resulting from the coils, the magnet is water cooled (section 4.1.2). Ferromagnetic yokes within the vacuum chamber of the dipole magnet (shown in Fig. 4.11) help ensure field uniformity and reduce stray fields. The two exits are situated at ±44° from the central axis

[13]Registered trademark

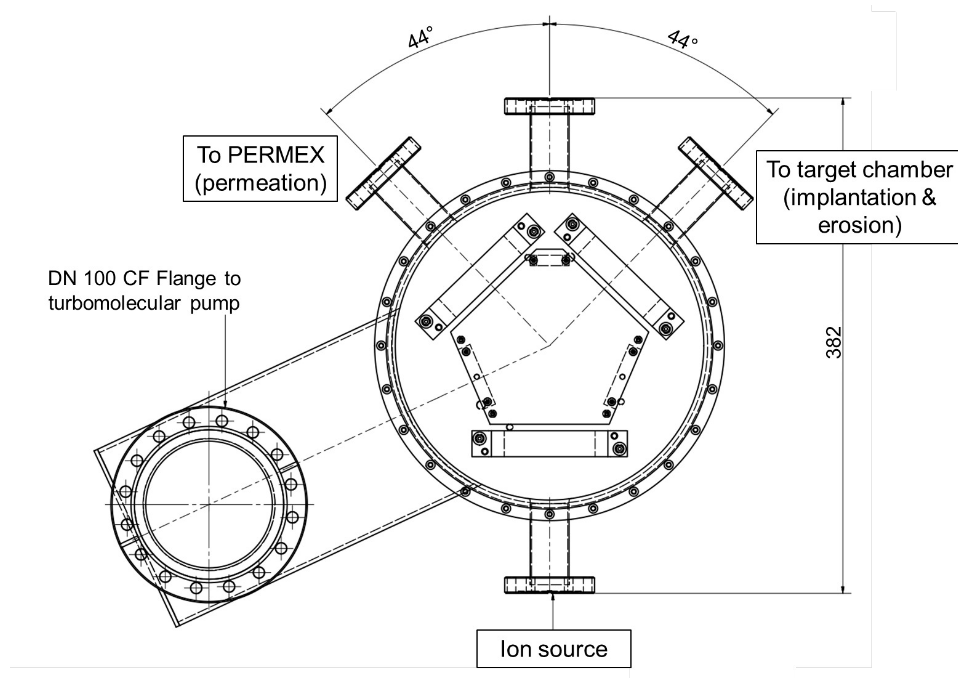

Figure 4.11: Half section cut of the dipole magnet. The beam enters the magnet through the lower CF 40 flange and can be deflected either left or right, depending on the direction of the magnetic field, so that the desired ion species exits the magnet through the corresponding CF 40 flange. Magnetic yokes are present inside the vacuum chamber to increase the uniformity of the magnetic field at the center of the magnet. The shaft on the left connects through a CF 100 flange to a turbomolecular pump, improving pumping of the chamber.

(Fig. 4.11). The magnet allows for symmetric deflection to either side, with the target chamber located to the right, as seen from the ion source. Another experiment, PERMEX (PERmeation EXperiment), is planned for the left exit of the dipole magnet [63]. Mass selection at the dipole magnet is accomplished by applying a voltage to the coils of the electromagnet, thereby producing a current which induces the desired magnetic field within the shunt regions. This will induce a curvature in the particle trajectories within the magnetic sector field, as described in section 2.3.4. In the case of SIESTA, the ion beam is mono-energetic, so by varying the applied voltage to the coils, the magnetic field can be chosen such that only the trajectories of ions of a certain mass exit the magnetic sector field and reach the target. Since in SIESTA the radius of curvature is constant, equal to 150 cm and, within error due to magnetic hysteresis, $\left\|\vec{B}\right\| \propto I$, with I the current though the dipole magnet, applying equation 2.13 yields:

$$I \propto R. \tag{4.1}$$

Consequently, for a given ion energy (chosen by setting the desired extraction potential at the ion source), the current which must pass through the magnet coils in order to deflect the desired ion species to the target will be directly proportional to the rigidity of said ion.

As previously detailed in section 2.3.4, an ion beam passing through a deflector magnet will also be focused in the plane of deflection. As a consequence of this, downstream from the magnet an initially circular beam will have an elliptic cross section, with a different beam emittance in the horizontal and vertical plane. In order to increase the flux density at the target, a magnetic quadrupole doublet lens consisting of two QM-60.100 quadrupoles from D-Pace[14] (shown in Fig. 4.12) was installed between dipole magnet and target chamber, as this lens allows for different foci in the horizontal and vertical plane [37].

4.1.6 Target chamber and load-lock

The target chamber is divided into two connected volumes: an antechamber with a length of 130 mm along the beam axis equipped with its own turbomolecular pump for improved differential pumping; and the main target chamber housing the sample to be exposed. The sample is placed within a cylindrical double cage, which is required for an accurate measurement of the ion-beam current under all operating conditions, as explained in more detail later in this section. The two volumes are connected by a tube of 46.8 mm in diameter. A beam-defining aperture is situated in the target chamber at the exit of this tube, and is described in more detail later in this section. The ion beam propagates along the axis of this tube towards the target, passing through the beam-defining aperture and two aligned diaphragms in the double cage before impinging on the target sample. The sample is fitted into a specifically-designed tripod, which rests atop a platform with each leg fitting on a cylinder. The platform can be rotated relative to the ion beam to alter the angle of incidence and can be moved in the vertical direction to adjust the height of the beam footprint on the sample. The manipulator is also used to mount the sample on the target platform from the load-lock. If a different ion energy at the

[14] Registered trademark

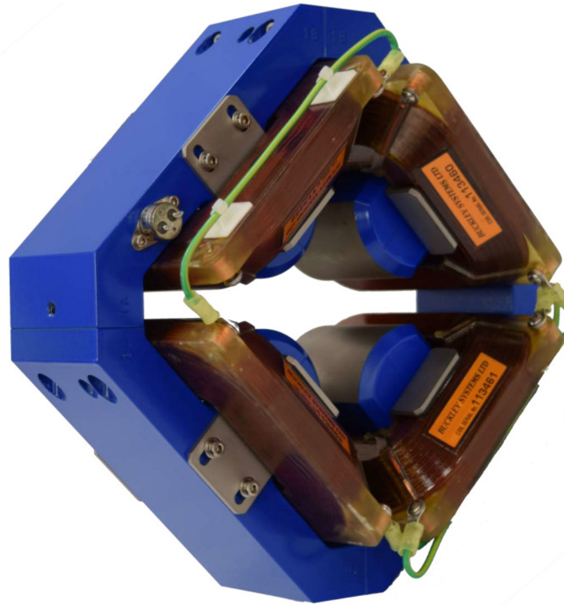

Figure 4.12: QM-60.100 Quadrupole lens from D-Pace employed in SIESTA.

target than the extracted energy is desired, the sample may be biased to ±6 kV. The general setup, without beam defining aperture, is shown in Fig. 4.13.

Additionally, the sample can be heated from its backside by electron impact. This is enabled by employing a filament located behind the sample: a current is passed through this filament to heat it, emitting electrons through thermionic emission. A potential difference is applied between the target and the filament, accelerating the emitted electrons towards the target. This electron current will heat up the target to temperatures of up to 1300 K. Radiative heating from the filament of the electron gun plays a role at moderate temperatures, and can be neglected at higher temperatures when compared to the power output of electron impact heating. The filament is taken from a P21W 12 V, 21 W OSRAM[15] light bulb. To improve the heating efficiency, a metallic cup surrounds the filament. This heating cup is electrically connected to the filament, shielding the filament from all other external fields and effectively "directing" the emitted electrons towards the target. This can be accomplished by either biasing the target to a positive potential, or by biasing the filament negatively and leaving the target grounded. The heating filament, cup and target holder (with target) can be seen in Fig. 4.14.

The temperature is measured with a type-K thermocouple connected to the target through the two hind legs of the tripod sample holder. In order to improve contact between the target and the thermocouple, two push rods (not shown in Fig. 4.13) can be used to press down on the hind legs of the sample holder. These rods are located on the left and right side of the target platform, i.e., on either side of the sample holder, and are outfitted with springs to apply a downwards force on the target holder legs. The push rods are shown in Fig. 4.15. Since the thermocouple is in electrical contact with the target, it is also biased to the same potential as the target. The thermocouple display electronics is at ground potential. If the thermocouple were connected

[15]Trademark of OSRAM GmbH

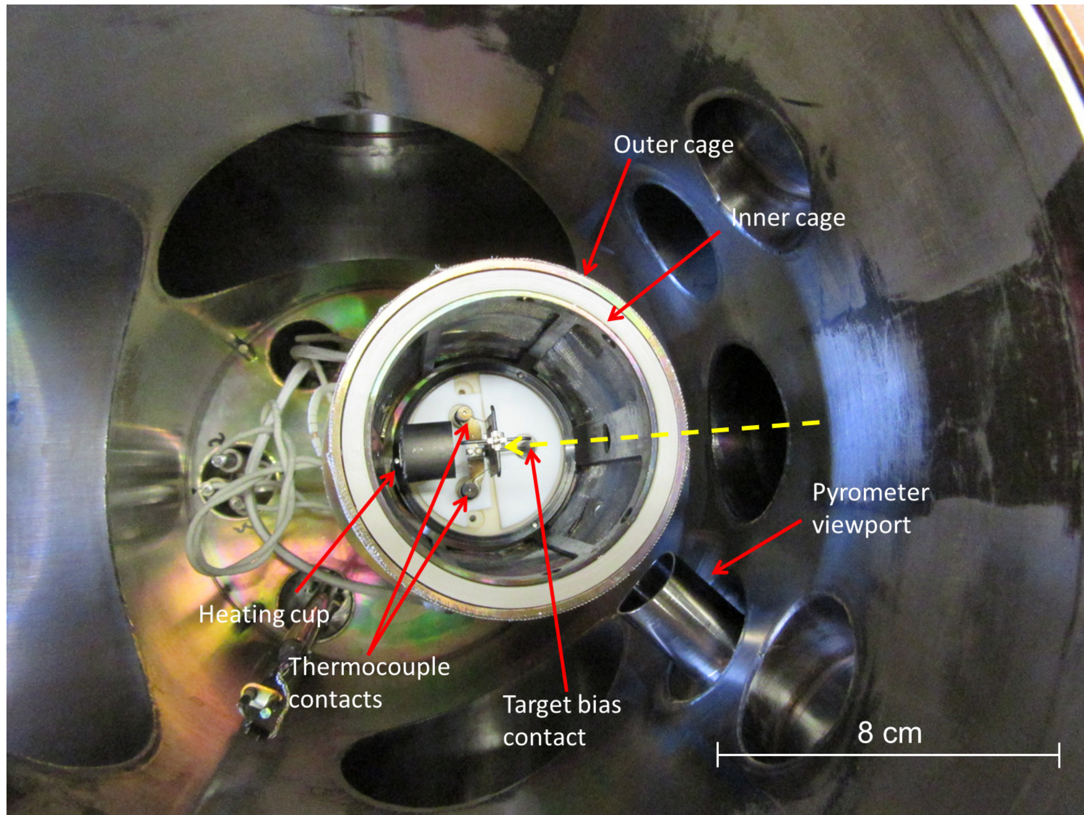

Figure 4.13: Top view of target chamber interior showing the double cage, pyrometer viewport, heating cup and target holder with thermocouple and target bias contacts. The beam defining aperture is absent. The beam direction is from right to left as indicated by the yellow dashed arrow.

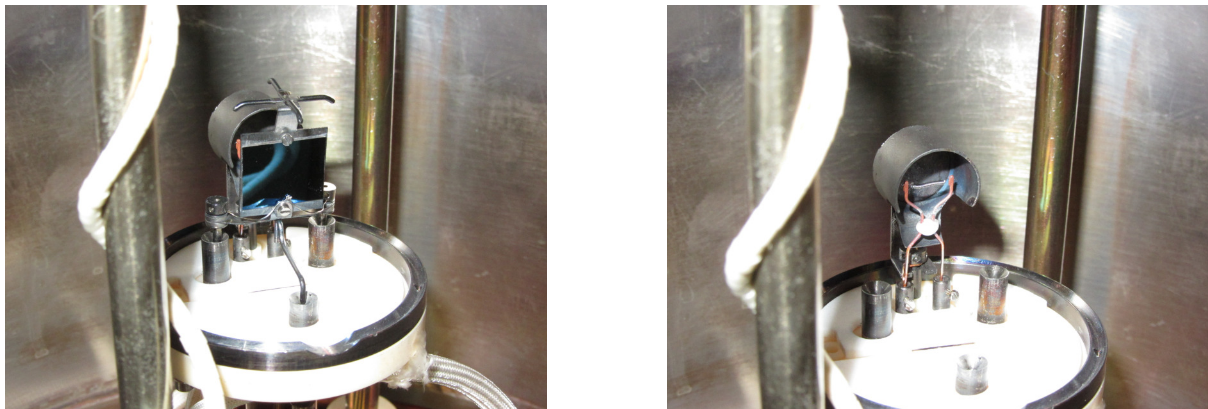

Figure 4.14: Target platform with heating filament, with (left) and without target (right). The two hind legs of the target holder are connected to a type-K thermocouple. The front leg is connected to a power supply which sets the bias of the sample. The heating cup is electrically connected to the heating filament. The hooks situated on top of the target holder are used to weigh the sample and to transport it between target chamber, load-lock and TDS chamber.

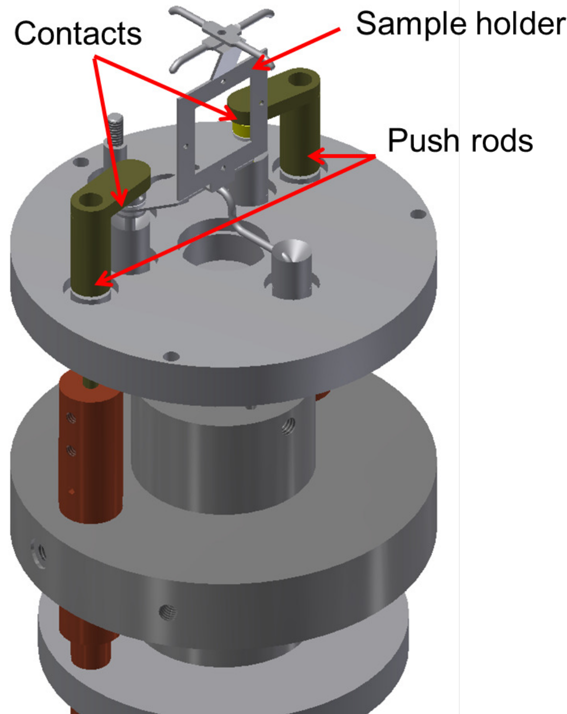

Figure 4.15: Push rods can be used to press down on the sample holder hind legs, thereby improving the electrical contact between thermocouple contacts and the target.

directly to the display electronics, it would short-circuit the target bias power supply, potentially damaging the equipment and constituting an electrical hazard. The biased thermocouple signal is transmitted to the grounded display electronics via a voltage-to-frequency converter (on the thermocouple end), a fiber-optic wave-guide and a frequency-to-voltage converter (on the display electronics end). A Maurer type TMRS 95/105[16] infrared pyrometer with a measuring range of 50°C - 1000°C is located outside the vacuum chamber and also has direct line of sight to the target, allowing for a second independent temperature measurement. The target heating filament was tested at a target bias of 3 kV with filament currents between 0 and 1.6 A. At 1.6 A, an electron current reaching the target of 21 mA was measured, from which a heating power of 63 W can be calculated.

The ion current reaching the target must be measured accurately, as this is required to determine the ion flux. Secondary electrons are emitted when the ion beam impinges on the target, potentially being registered as an additional positive current. The current measurement would thus be overestimated. If the sample is positively biased, low-energy electrons that are trapped in the potential well of the positive ion beam would be accelerated towards the target, leading again to an erroneous current measurement, this time underestimating the ion current. To avoid both of these issues, the outer cage surrounding the target is set to a low negative bias (-10 V) and the inner cage is included in the current measurement and grounded. With this setup, electrons trapped in the potential well of the beam are repelled by the outer cage and so

[16]Trademark of Dr. Georg Maurer GmbH Optoelektronik.

do not reach the target, whereas those emitted at the target are collected by the grounded inner cage and included in the current measurement.

If the sample is heated during ion irradiation, the electron current to the target backside will constitute an additional negative current. Typically, this current is orders of magnitude larger than the impinging ion current (mA vs. µA). To allow accurate measurement of the ion current, one end of the filament is also connected to the current measurement. This way, the "electron current circuit" is closed and no current due to electrons from the heating filament is registered at the current measurement. The contact point of the grounded current integrator will differ, depending on whether the target is biased positively and the filament is grounded (connection scheme A, Fig. 4.16), or the target is connected to the 0 V connection point of the high-voltage power supply and the filament is set to a negative bias (connection scheme B, Fig. 4.16).

Finally, during operation it is occasionally useful to measure the ion beam current at the target without exposing the sample. This is of use for example when tuning the dipole magnet current before exposure. Since the cup surrounding the heating filament is also connected to the current measurement, this can be achieved by rotating the target platform 180°, in which case the ion beam impinges on the back of the heating cup. The ion current is thereby measured accurately at the target and the dipole magnet, gas flow, etc., can be adjusted before exposing the sample. When all systems have been correctly tuned, the target platform can be rotated back 180° to commence exposure of the sample to the ion beam. A high-voltage switchboard is used to alter the connection scheme of all of the components as desired, allowing for other connection schemes than the ones mentioned if needed. Since all the electrical connections may be set to a high voltage using the switchboard, grounded aluminum caps have been fastened around the electrical connections at the target chamber, preventing any possible contact with the high voltage components. Additionally, a door with a grating has also been installed under the target chamber. A relay connected to the high-voltage power supply is attached to the door-frame, so that if the door is opened - for instance to access the vertical manipulator - the high-voltage power supply for the target is automatically switched off.

The beam-defining aperture, located between the outer cage and the tube connecting main target chamber and antechamber (shown in Fig. 4.1), consists of a molybdenum plate with a series of holes and slits of different sizes aligned vertically along its axis. The plate is screwed to a vertical manipulator located above the target platform. By adjusting the height of the plate, the desired shape of the beam-defining aperture can be selected. Circular holes with diameters of 4, 5 and 6 mm are available, as are vertically elongated stadiums with dimensions of 1.5×6, 2×6 and 3×6 mm. The beam-defining aperture can be seen in its installed position in Fig. 4.17. In order to avoid contact of the ion beam with the inner and outer cages, the outer cage hole diameter is 8 mm and the inner cage hole has a diameter of 9.3 mm. The beam footprint at the beam-defining aperture can be large enough to encompass more than one of the holes. If this were to happen, part of the beam would not only impinge on the sample, but also needlessly erode the cages, possibly affecting the current measurement. To avoid this, a thin plate has been installed between the beam defining aperture and the tube connecting the two vacuum volumes, with a hole 12 mm in diameter aligned with the ion beam trajectory. The plate covers

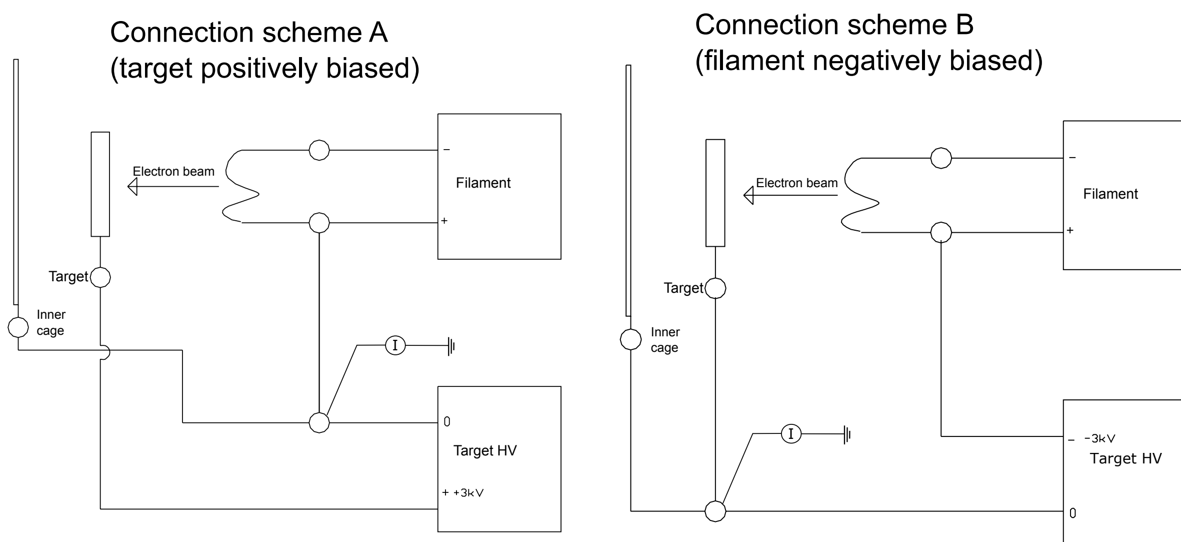

Figure 4.16: Connection schemes for the target chamber of SIESTA, allowing for the target to be positively biased and the heating filament set to ground potential (A), or conversely for the target to be grounded and the heating filament set to a negative bias (B). In both cases the ion beam impinges on the target from the left, passing through a hole in the grounded inner cage. A current integrator, labeled "I", is used to measure the ion current.

the rest of the tube connecting the antechamber and the target chamber, so that all the lines of sight between the ion beam and the target chamber pass through only one hole of beam-defining aperture.

A magnetically-coupled suspension balance is located directly above the target chamber. Before or after exposure in SIESTA, a sample may be hung from the measuring hooks of the balance and weighed. The magnetic suspension balance measuring point is located above the target platform. Therefore, the target cannot be simultaneously exposed to the ion beam and weighed with the balance. As such, the term "in-situ" does not strictly apply. However, since the target is not moved to a separate vacuum chamber and can be weighed almost immediately after exposure, the term "in-situ" is used instead of "in-vacuo" when referring to measurements performed with the balance. The measurement procedure of the microbalance is described in more detail in section 4.2.6.

The load-lock enables the quick and easy exchange of samples in the target chamber by limiting the volume to be vented and re-evacuated during the procedure to the load-lock vacuum chamber. As can be seen in Fig. 4.14, two pairs of hooks are situated on top of the target holder. They are used to transport the sample to and from the target chamber through the manually operated CF 100 gate valve that connects the target chamber and the load-lock.

4.1.7 In-situ thermal desporption spectrometry

A thermal desorption spectroscopy chamber is located directly below the load lock. As with the target chamber, a manipulator - in this case vertical - is equipped with a hook and is used

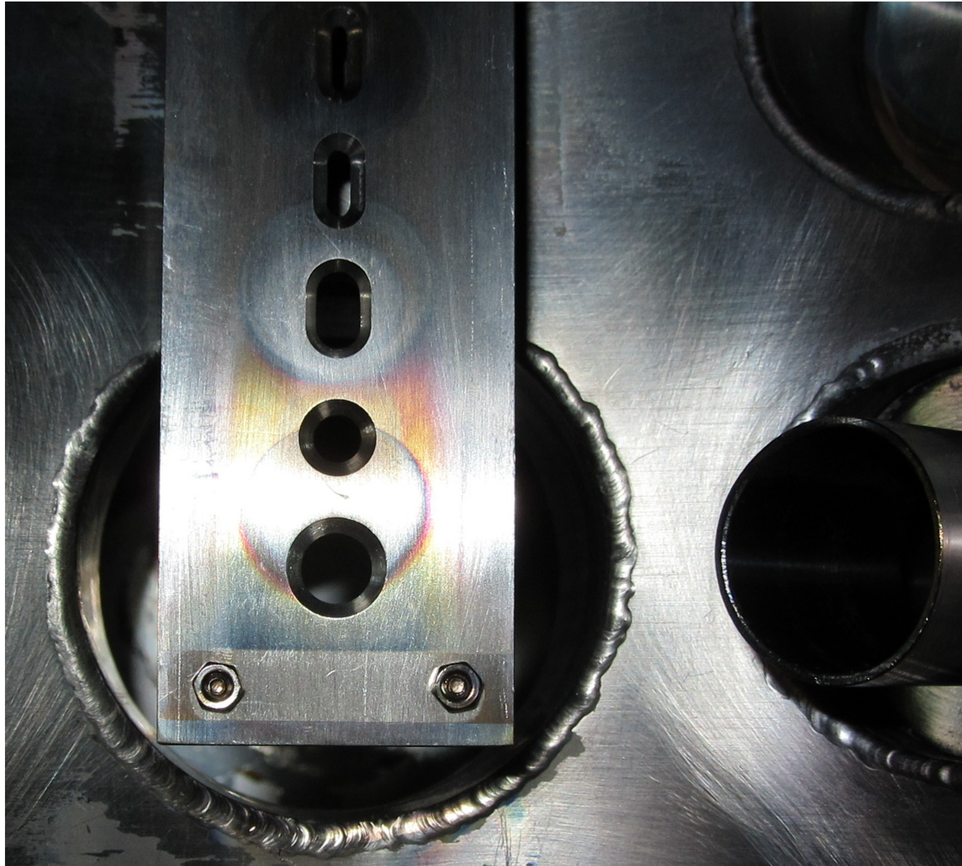

Figure 4.17: Beam defining aperture in the target chamber. In the picture, the bottom hole is aligned with the ion beam trajectory. The thin plate installed between beam defining aperture and connecting tube to the antechamber is not present. The tube on the right provides a line of sight between the pyrometer and the sample.

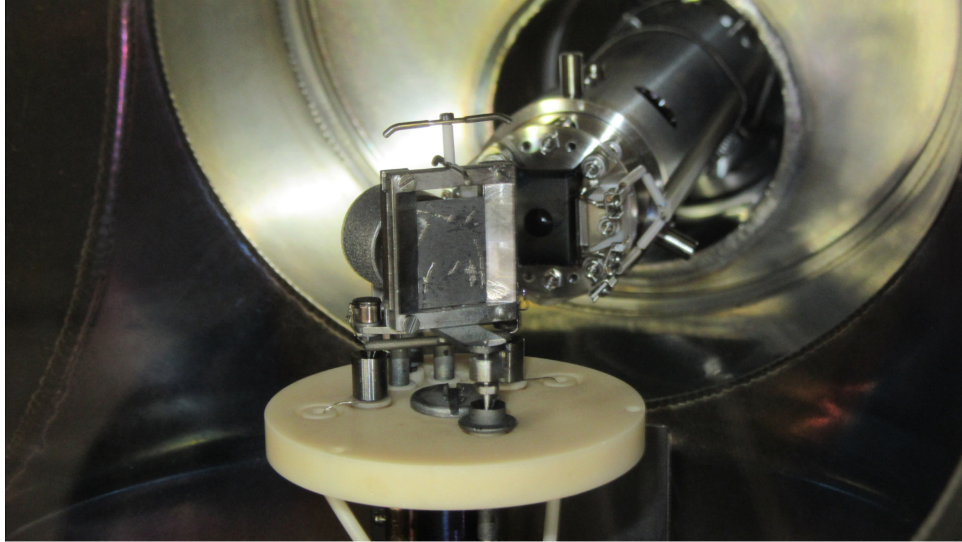

Figure 4.18: Target holder with sample in TDS chamber. The sample can be biased and can be and heated by a filament located at the backside of the sample, providing electron impact heating. The quadrupole mass-spectrometer, located behind the target holder, is used to analyze the composition of the gas that is desorbed from the sample.

to transfer a sample from the load-lock to the TDS chamber. A thermocouple and heating mechanism identical to the ones in the target chamber are employed to heat up the sample to temperatures of more than 1000 K. A PID system may be used to control the sample temperature. A quadrupole mass spectrometer (QMS) is situated at a distance of approximately 6 cm from the sample with direct line of sight. With this setup, a previously-loaded sample may be de-gassed at high temperatures and the released gas composition will be measured by the QMS, leading to information about the gas retention properties of the sample. A base pressure of less than 5×10^{-9} mbar is achieved with a dedicated turbomolecular pump. The TDS chamber is also equipped with a liquid nitrogen getter pump, helping to reduce the pressure during operation. The sample platform with heating cup and quadrupole mass spectrometer are shown in Fig. 4.18

Since the sample is also heated via electron-impact heating, another dedicated power supply is used to bias the target up to 6 kV. As in the case of the target chamber, the thermocouple measuring the temperature at the sample is also biased and aluminum caps have been installed to prevent contact with the electrical connections of the TDS chamber. Since the load-lock is connected to both the target chamber and TDS chamber, a sample can be irradiated and taken to the TDS chamber to be analyzed without the need to vent at any point, allowing for in-vacuo TDS of irradiated samples.

4.2 Characterization

4.2.1 Map of source parameters

The ion source was fully characterized for use with deuterium. Hydrogen (protium), hydrogen-helium and hydrogen-argon plasmas were also successfully produced. The latter two behave similarly to hydrogen and deuterium, unless stated otherwise.

With the goal of maximizing the ion current reaching the target, parameter scans were performed to study the effect on the ion current of the extraction voltage, the pressure in the differential pumping stage (controlled by varying the neutral gas throughput) and the ion source magnet, filament and arc currents. Additionally, the optimal pressure in the differential pumping stage and the optimal intermediate grid voltage were also systematically studied as a function of the extraction voltage. For these tests, the ion current was measured with the Faraday cup located at the beam-stopper, between the differential pumping stage and the dipole magnet (figs. 4.1 and 4.10). The measuring cup was set to ground potential, while the aperture in front of the cup was set to a negative bias of -25 V to repel thermal electrons trapped in the potential well of the ion beam and to deflect secondary electrons emitted at the measuring cup back towards the cup. A vertical cross section of the beam profile was measured with an aperture of Ø 1 mm as explained further below.

The parameters detailed in table 4.1 were taken as reference values: whenever any of the parameters were varied, the other parameters were set to the values listed in the table. These reference values were obtained from earlier experience with the precursor of SIESTA, the HSQ [62], as there they were proven to enable reliable, steady state operation while fulfilling the experimental requirements of the device. However, it must be noted that even employing the same set of parameters, the same ion current measured at the beam-stopper was not always obtained. Differences in the measured current of up to 20 % were observed, which could be attributed to the conditioning of the source for use with a certain gas species and the "aging" of the coating on the filament, which degrades over time and affects the long-term stability of the beam.

The measuring procedure was in general as follows:

1. The beam-stopper (Faraday cup) was inserted and the Ø 7 mm aperture in front of the cup was set to -25 V.

2. The desired extraction voltage was set, as were the operating currents of the ion source magnet, filament and arc. The ion source magnet, filament and arc voltages were allowed to vary.

3. Gas was let into the source through the flow controller until the arc current increased to the desired level, prompting an ion current being measured by the Faraday cup at the beam-stopper. The arc was not yet stable, as evidenced by oscillations in the arc voltage of the order of 50 V. These oscillations diminished over time without any action being required within $1-2$ minutes.

Element	Voltage relative extraction voltage (= 6010 V) [V]	Current [A]
Cathode	0	0.12
Anode	+20	11.7
Intermediate electrode	-30	0.28
Magnet +	-30	30.5
Magnet -	-40	30.5
Filament +	-24	8.1
Filament -	-27	20.3

Table 4.2: Measured voltages and currents at the several contact points of the ion source (Fig. 4.8). Voltages shown are relative to the cathode (plasma grid) voltage, which was 6 kV. Currents are measured in the direction indicated by the arrows above the connection points in Fig. 4.8. The voltages and currents applied by the power supplies under the same conditions are listed in Tab. 4.1.

4. Once the arc current was stable (indicating the source was now running in steady state), the (negative) intermediate grid voltage was increased, leading to a rapid increase of the ion current measured by the Faraday cup. Once the negative voltage had increased to a certain level, the ion current would reach a maximum. Beyond this point, further increase of the negative intermediate grid bias potential led to a slight decrease in the measured ion current. The voltage at which the ion current reached its maximum was noted as the optimal intermediate grid voltage.

5. The gas flow into the source through the flow controllers was then varied while the arc was maintained at the desired operating current. An optimal gas flow was found which led to the highest ion current at the beam stopper. The pressure at the first differential pumping stage and the maximum measured ion current were recorded.

For the following tests, deuterium was used. The voltages at each point shown in figure 4.8 were measured relative to the cathode (plasma grid) voltage of 6 kV. The electric currents were also measured at each connection point, in the direction depicted by the red arrows above the connection points in the diagram. During these measurements (table 4.2), the ion source was operated at the source parameters shown in table 4.1 (see section 4.1.2). The arc current can be calculated as the difference between the filament currents at the + and - connections, equaling in this case 12.2 A. This current reaches the anode (11.7 A), intermediate electrode (0.28 A) and the extraction grid (0.12 A). The measurements agree with the displayed values of the power supplies within the measurement uncertainties.

Fig. 4.19 shows the maximum ion current measured with the Faraday cup at the beam-stopper with the extraction voltage ranging from 0.7 to 15 kV when optimizing the gas flow to the ion source. The data were fitted by applying equation 2.8 with constant perveance, showing good agreement. It must be noted that the Child-Langmuir law only describes the current that is extracted from the source (Eq. 2.7), while the data points correspond to the current measured at the beam stopper, i.e., after the beam has passed through the differential pumping stage and has

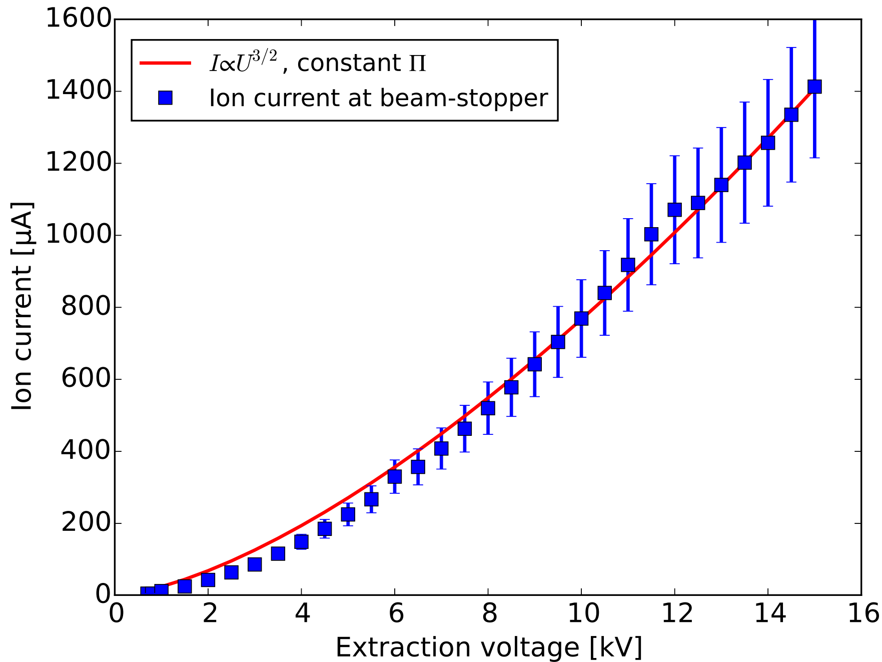

Figure 4.19: Ion current measured at the beam-stopper with increasing extraction voltage, fitted with a curve of constant perveance as described in Eq. 2.8 [34]. The increase in the size of the error bars for ion currents above 1 mA is due to a change in the measurement range of the current integrator.

been partly cut off by the Mo aperture. Under these conditions, the currents through the source magnet, filament or arc show no effect on the extracted ion current within the experimental uncertainty, as can be observed in figure 4.20. However, the source is not space-charge limited, since the perveance of the source is significantly smaller than the maximum perveance given by the Child-Langmuir law (Eqs. 2.7 & 2.8) and the ion current emitted from the source varies with the gas throughput (Fig. 4.22).

The correlation of the optimal intermediate grid voltage with the extraction voltage was also investigated (Fig. 4.21). The negative potential at the intermediate grid must be strong enough to repel back-streaming electrons, "screening" the ion source, without de-focusing the ion beam too strongly. The required potential to accomplish this should, therefore, be directly proportional to the extraction potential and inversely proportional to the gap between grids, which is constant ($U_{intermediate} \propto U_{extraction}$). This was experimentally confirmed, with a strongly linear relationship between the extraction and optimal intermediate grid voltages being observed, i.e., the optimal grid voltage is a constant fraction of the extraction voltage (approximately 1 %).

The ion current variation around the optimal pressure in the differential pumping stage was also studied. Figure 4.22 shows the ion current emitted from the source (measured at the extraction voltage power supply) divided by 1000, the ion current measured with the Faraday cup at the beam-stopper when using an aperture of Ø 5 mm and the ion current measured at the target chamber, plotted as a function of the gas pressure in the differential pumping stage when

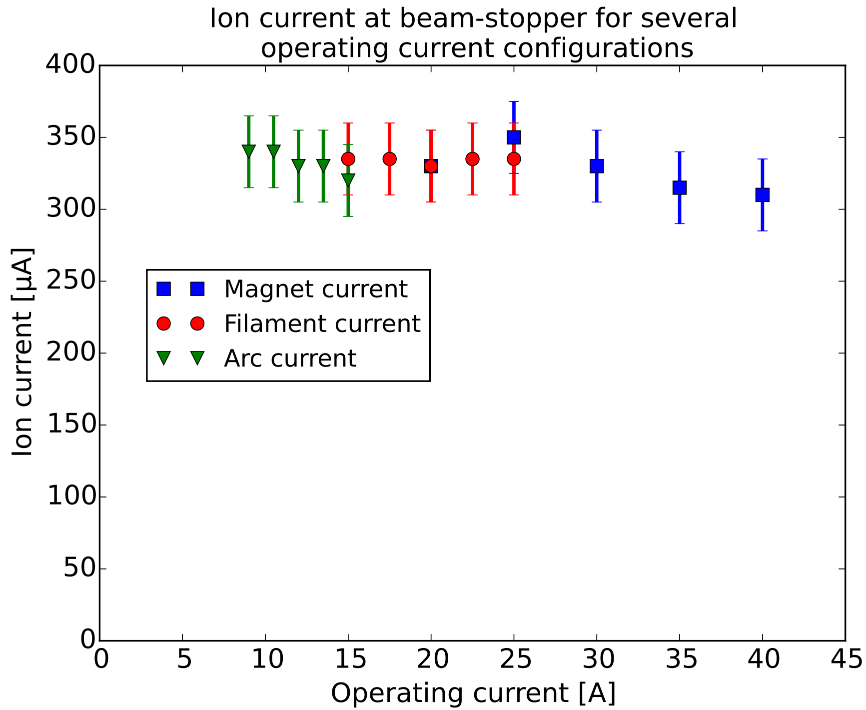

Figure 4.20: Ion current measured at the beam-stopper with the source magnet, filament and arc set to various operating currents, with all other parameters set to maximize ion current. Within the error of the experimental measurement, no effect of these parameters on the extracted ion current could be observed.

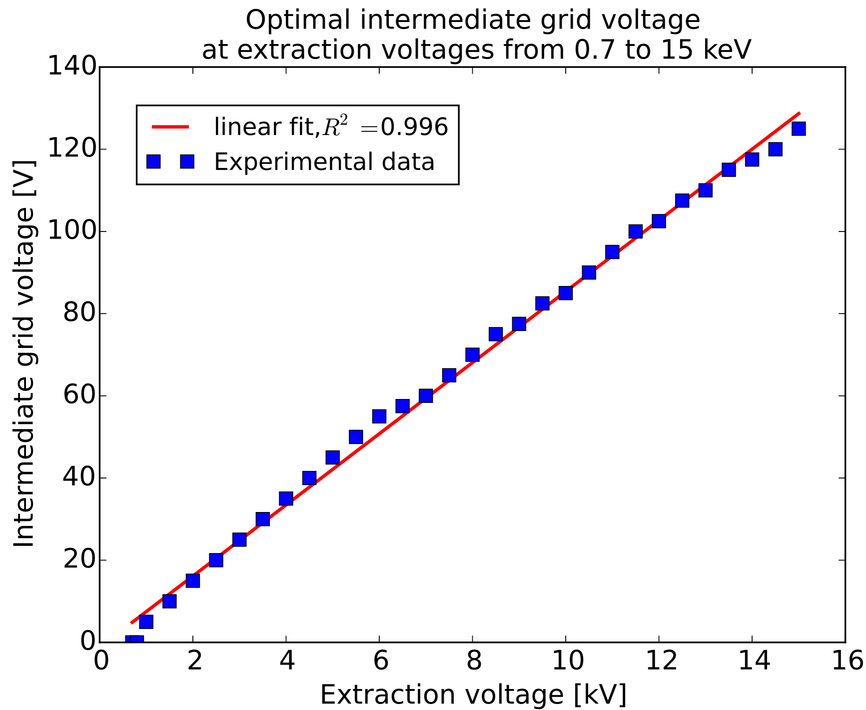

Figure 4.21: Optimal intermediate grid voltage (negative) for increasing extraction voltages. The error bars for the experimental values are smaller than the size of the markers.

extracting a 6 keV D_3^+ beam. The currents are measured at different positions with differing beam-defining apertures and beam optics, and therefore cannot be directly compared with one another. For instance, the current measured at the beam-stopper Faraday cup through the Ø 5 mm aperture is approximately 10 % of the current that passes through the Ø 16 mm Mo aperture, as can be estimated from the beam profile at the beam-stopper shown in Fig. 4.26 and discussed further in this section. Due to the focusing effect of the quadrupole lenses, and the fact that the beam-defining aperture at the target is larger than the one used at the Faraday cup, the ion current measured at the target is larger than the current measured at the Faraday cup. Below a pressure of approximately 4×10^{-5} mbar, the ion source cannot be operated reliably because the arc discharge in the ion source becomes unstable. Given the trend of the curve towards higher extracted ion currents at lower gas pressures, it can be assumed that a space-charge limited regime would be reached if the pressure in the plasma source could be further reduced. However, this cannot be achieved with the current plasma feed, since at lower gas pressures the DuoPIGatron source is not able to maintain the plasma discharge. A pressure optimum is observed for the ion current measurement at the beam-stopper Faraday cup and at the target. At pressures below this optimum, a higher current is extracted from the ion source, but due to increased beam divergence, a large fraction of the beam impinges on the Mo aperture and, in the case of the measurement at the target, the vacuum tubes at the entrance and exit of the dipole magnet. This increase in beam divergence occurs in the ion extraction stage (gap between plasma and grounded grids) and between the grounded grid and the measurement point due to insufficient space-charge compensation at the exit of the ion source [34]. Near the pressure optimum, the beam achieves a high degree of space-charge compensation, which leads to a relatively low divergence. The pressure optimum is at slightly lower pressure for the current measured at the beam-stopper Faraday cup than for the ion current measured at the target. This can be explained by the smaller distance between measurement point and ion source. Because the beam stopper Faraday cup is much closer to the source than the target, the current at this position is less influenced by beam divergence. The increase in the loss of current due to insufficient space charge compensation is partially overcompensated by the increase of ion current extracted from the ion source. At pressures higher than the optimum, the beam is already highly space-charge compensated. A further increase of pressure leads to a decrease of current due to beam neutralization.

It was observed that the pressure optima vary slightly on a day to day basis. This could be due to the reproducibility of the Full-Range Cold Cathode pressure gauges used, and does not seem to depend heavily on the extraction voltage, as can be seen in Fig. 4.23. The pressure optimum was typically around 10^{-4} mbar. Dependences between the intermediate grid voltage and the pressure optimum and other source parameters (current through ion source magnet, filament and arc current) were also tested, but none were found.

To test the flow controllers, the gas pressure at the differential pumping stage was measured while increasing the flow controller nominal gas throughput, showing a linear increase with the throughput, as is shown in Fig. 4.24, indicating that the flow controllers can be used to reliably adjust the gas pressure at the differential pumping stage.

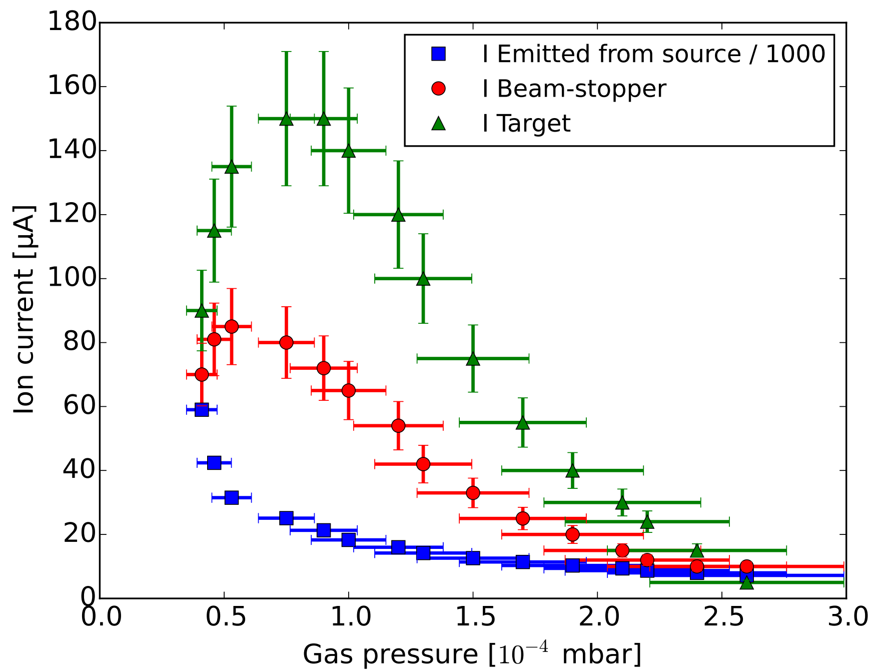

Figure 4.22: Ion current from a 6 kV D_3^+ beam measured at the exit of the ion source (divided by 1000, squares), at the beam-stopper Faraday cup (circles) and at the target (triangles) as a function of pressure in the first differential pumping stage. The ion current measured by the beam-stopper Faraday cup and at the target shows a peak at a specific pressure "optimum" for a given discharge. No optimum is observed for the ion current emitted from the source. A larger current is measured at the target because the beam is focused before reaching the target and the beam-defining aperture at the target is larger than the one used at the Faraday cup.

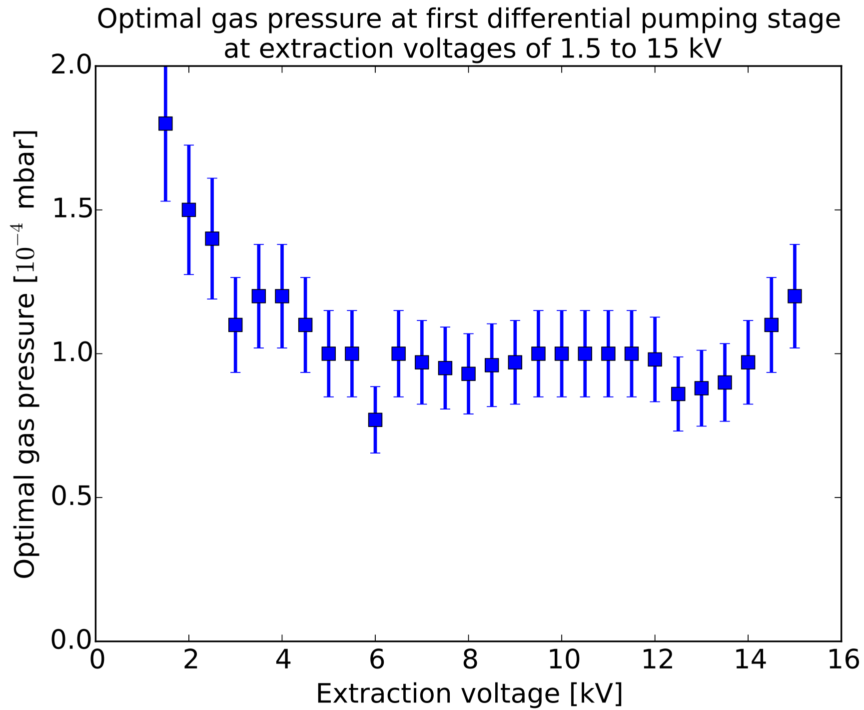

Figure 4.23: Optimal gas pressure with increasing extraction voltage when using deuterium. For extraction voltages below 4 kV, lower extraction voltages lead to a higher optimal gas pressure. For voltages of or above 4 kV, the pressure optimum is typically in the range of 1×10^{-4} mbar.

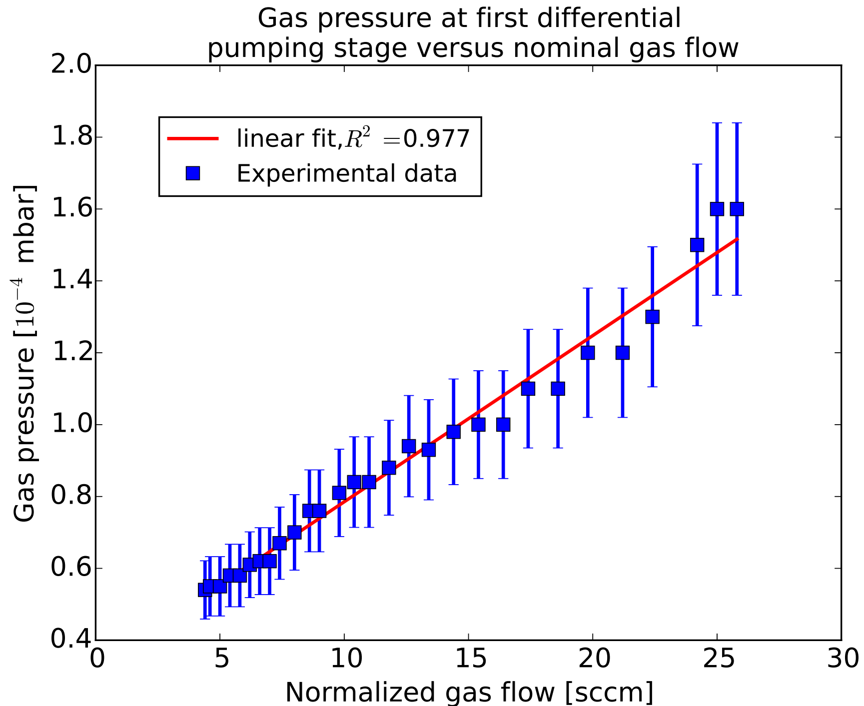

Figure 4.24: Gas pressure at the first differential pumping stage is plotted versus the flow-controller gas throughput. A linear regression was added, providing a good fit within the experimental error of the gas pressure measurement.

As stated before, the Faraday cup at the beam-stopper is typically grounded and the insulated aperture in front of the Faraday cup is negatively biased to repel secondary electrons and electrons trapped in the ion beam's potential well. To understand the effect of the potentials of the Faraday cup and insulated aperture on the ion current measurement, the ion current was measured while the aperture was set to varying negative potentials, with the Faraday cup grounded or set to +36 V. This can be seen in Fig. 4.25, which shows that at aperture bias potentials close to ground potential, measurements diverge when the Faraday cup is grounded or positively biased. Electrons trapped in the potential well of the ion beam or secondary electrons produced at the beam-stopper aperture may impinge on the Faraday cup, being registered as a "negative" current and therefore reducing the measured ion current. When the cup is grounded however, an additional effect may be observed: secondary electrons are emitted from the cup due to ion impact and are not repelled back into the cup by the insulated aperture, constituting an additional "positive" current. In this scenario, this second effect dominates, and so a higher current is measured, leading to an overestimation of the real ion current. These two competing effects can be eliminated by increasing the bias voltage applied at the aperture in front of the Faraday cup. If the aperture is sufficiently negatively biased, it will deflect the secondary electrons emitted at the Faraday cup back to the cup, so that the current is not overestimated, while repelling the electrons trapped in the potential well of the beam, so that the current is not underestimated either. At aperture bias voltages larger than -15 V, secondary electrons are retained in the Faraday cup and electrons trapped in the potential well of the beam are repelled from the cup. In this case, no difference is observed between a grounded Faraday cup and one set to +36 V. Based on these findings, it was decided to operate the beam-stopper with a grounded Faraday cup and at a bias voltage for the aperture of -25 V.

To measure the beam profile at the beam-stopper, a negatively biased aperture of Ø 1 mm was installed onto the Faraday cup. The vertical position of the beam-stopper was then varied, to measure the off-axis current density of the beam, leading to a line scan through the beam. Given the rotational symmetry of the ion source and extraction grids, the beam is assumed to be cylindrically symmetric. The measured beam profile is shown in Fig. 4.26. The ion current density appears to have a uniform value around the beam axis of $\sim 3\ \mu\text{A/mm}^2$. Beyond a diameter of 16 mm, the ion current density drops quickly to zero. The width of the beam "edge" at this position is approximately 2 mm.

The ion source behaves similarly when operating with hydrogen (protium), with the exception of the optimal operating pressure in the first differential pumping stage, which is increased to about 2×10^{-4} mbar. The source cannot be ignited if helium is used as working gas. For this reason, in order to produce a He beam, the source was ignited with hydrogen and then helium was admixed through the second flow controller, up to a flow ratio of 1:1. The optimal pressure is in this case not affected by the helium concentration. The He ions are then mass selected in the magnetic sector field which is explained in the following section (sec. 4.2.2). It is worth noting that a helium-containing ion beam can also be achieved by first igniting the source with deuterium. However, in this case D_2^+ ions will have a very similar mass as He^+ ions, so the two ion species will not be mass-separated when passing through the dipole magnet.

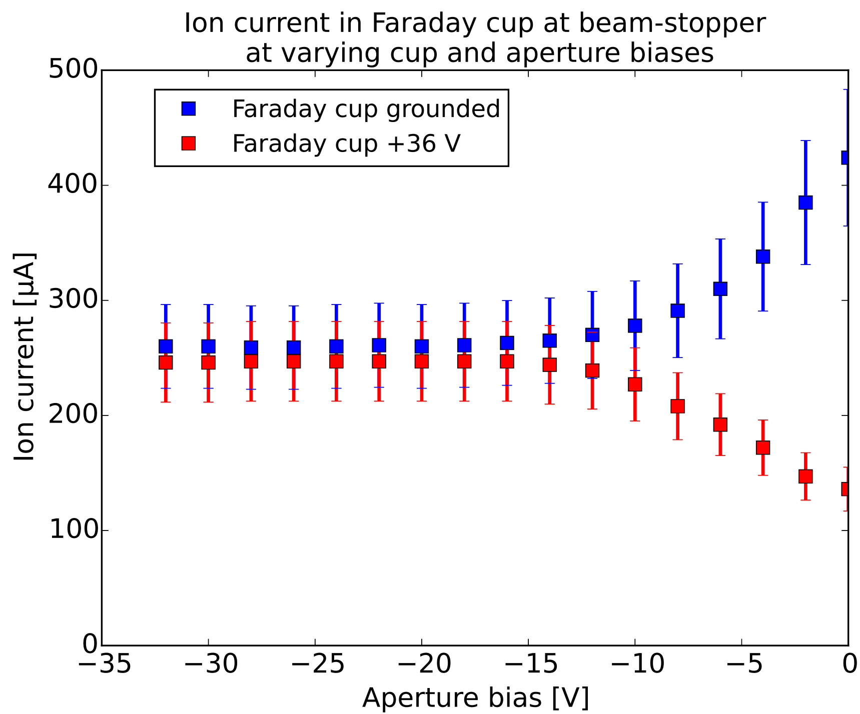

Figure 4.25: Ion current measurement at the beam-stopper Faraday cup with varying bias at the aperture in front of the Faraday cup and the cup either grounded or positively biased. For low (or no) aperture bias, the grounded Faraday cup leads to higher ion current measurements. Conversely, if the Faraday cup is set to a positive bias, the measured current is reduced. When a negative bias of 15 V or greater is applied at the aperture in front of the Faraday cup, whether the cup is biased or grounded does not play a role in the ion current measurement.

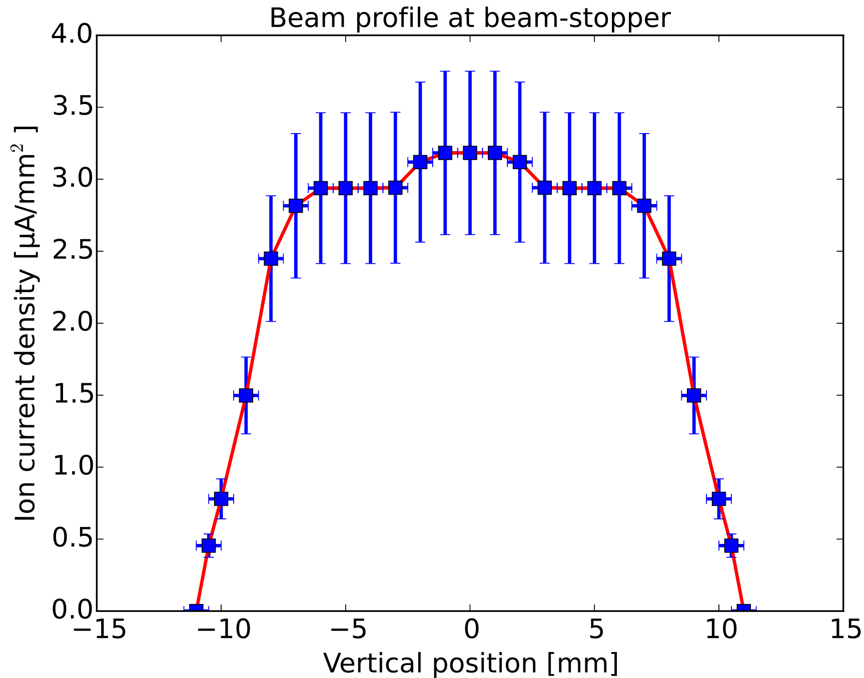

Figure 4.26: Beam profile at beam-stopper measured with Faraday cup. A line has been added to guide the eye. The ion current density appears to be uniform near the beam axis within the uncertainty of the measurement, with an edge width of approx. 2 mm.

As with helium, the source does not ignite with argon. Similarly, the source must be ignited with hydrogen or deuterium and argon must then be admixed to produce an Ar beam. It must be noted that argon degrades the coating of the filament in a matter of hours. This coating is sputtered onto the ceramic insulators, which become slightly electrically conductive. Depending on the desired Ar fluence to be achieved, the filament may have to be re-coated. Because of this, long-term operation with argon requires intensive and continuous maintenance.

4.2.2 Magnetic sector field deflection

The ion beam deflection through the magnetic sector field in the dipole magnet was characterized with the current measurement at the target. Once a stable 6 kV deuterium ion beam had been achieved, the beam-stopper was retracted and the strength of the magnetic sector field was slowly increased, while the current at the target was measured with an ORTEC 439 Digital Current Integrator. When using deuterium, three discrete, strong peaks were observed, corresponding respectively to the three ion species D^+, D_2^+ and D_3^+. The same test was repeated with a 6 kV hydrogen beam and a 6 kV hydrogen-helium beam from a mixed plasma with a 7:3 flow ratio. The deuterium, hydrogen and hydrogen-helium peaks are shown in Fig. 4.27. Again, three relatively large peaks were observed when using only hydrogen, corresponding to H^+, H_2^+ and H_3^+, respectively. Three small additional peaks are observed near magnet currents of 10, 12 and 20 A for deuterium and 7, 9 and 15 A for hydrogen. These are due, in the case of hydrogen,

to H_2^+ and H_3^+ ions dissociating in-flight between the ion source and the dipole magnet into a neutral molecule or atom and an ion. The ion will continue its flight with a fraction of the rigidity (Eq. 2.13) of the initial molecule, consequently achieving the same deflection in the magnetic sector field at lower magnetic field strengths, and thus lower currents through the dipole magnet. In this case, the 7 A peak corresponds to H_3^+ ions separating into H^+ ions with one third of the initial rigidity. This can be confirmed by applying equation 2.13 with constant gyroradius, showing that a peak at one third of the magnetic field strength is expected, which neglecting hysteresis and saturation effects corresponds to one third of the current for the H_3^+ peak (Eq. 4.1). If the H_3^+ ion separates into a H_2^+ ion and a neutral H atom, the ion retains two thirds of the initial rigidity and the peak is expected to be found at a magnetic field strength that is two thirds that of the H_3^+ peak. Similarly, the 9 A peak corresponds to H_2^+ ions separating into a neutral H and a H^+ ion, retaining each half the rigidity of the original molecular ion. The neutral particle will not be deflected by the magnetic field. If helium is added to the gas mixture, a new He^+ peak is observed in addition to the previous hydrogen peaks, shown in red in figure 4.27 at 24.7 A. A very weak additional peak was observed at a magnet current of approximately 28 A. It is believed this small peak corresponds to trace amounts of HeH^+ ions [68].

If argon is used in the ion source, ArH^+ is also produced. This ion, with molecular mass 41, is the dominant ion species under a wide range of operating parameters [69]. Consequently, a peak may be observed in the current measurement which can be hard to separate from the Ar^+ peak of mass 40. For this reason, it is advised to admix the argon gas with deuterium instead of hydrogen in the ion source, since in this case ArD^+ will be produced, with molecular mass 42. Since the rigidity difference between the two ions is in this case larger, the two peaks in the ion current measurement are distinguished more easily.

The dipole magnet was also tested in the same way with a Faraday cup mounted on the opposite exit (PERMEX exit in Fig. 4.11). The polarity of the current through the electromagnets, i.e., the B-field, was flipped in order to deflect ions in the other direction. The sets of peaks observed were identical, regardless of the direction of the deflection. This proves the symmetric behavior of the magnet.

These tests were also repeated at differing ion energies. Figure 4.28 shows the rigidity of each ion, plotted as a function of the magnet current (which is proportional to the B-field) at which the corresponding peaks in the ion current measurement were observed. Hydrogen and helium ions with an energy of 6 keV are shown, as are deuterium ions at energies of 1, 3, 6 and 9 keV. As described in Eq. 2.13, the rigidity of the ions scales linearly with the magnetic field at a given bending radius. In cases where the rigidity of the ions is approximately the same, for instance for 1 keV D_3^+ ions, 3 keV D^+ ions and 6 keV H^+ ions, it can be seen that the dipole magnet currents at which those peaks occur also coincide. It must be noted that the extrapolated linear regression from the data does not pass through the origin, as would be expected from the equation. This is believed to be due to the hysteresis of the dipole magnet: when magnetized from a zero-field value, the iron follows a non-linear magnetization curve. The magnetic field strength "lags behind" the current through the dipole magnet.

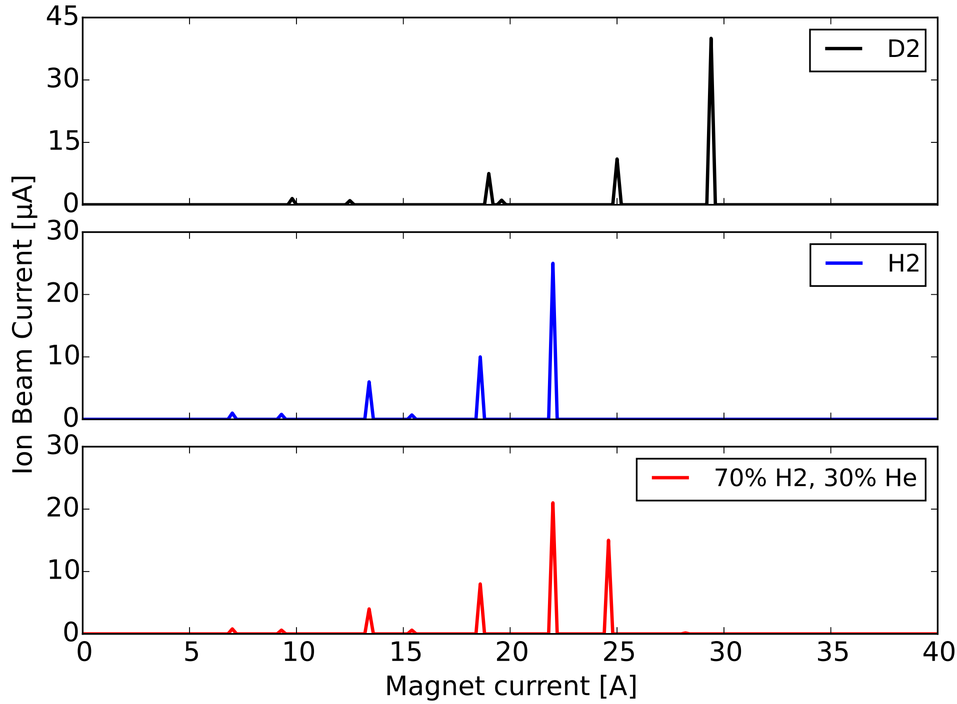

Figure 4.27: Ion currents from a 6 keV deuterium, 6 keV hydrogen and a 6 keV hydrogen (70 % flow) and helium (30 % flow) beam measured at the target chamber beyond the dipole magnet, as a function of the dipole magnet current, which is proportional to the magnetic field. In the upper plot, the peaks occurring in a pure deuterium beam are shown, with the three largest peaks corresponding to D^+, D_2^+ and D_3^+, respectively. In the middle plot, the respective H^+, H_2^+ and H_3^+ peaks corresponding to a pure hydrogen beam are shown. In the case of a 70 % hydrogen and 30 % helium beam, shown in the lower plot, in addition to the hydrogen peaks, a peak corresponding to He^+ is observed. The three smaller peaks occurring at magnet currents of approximately 10, 12 and 20 A in the case of deuterium and 7, 9 and 15 A for hydrogen correspond to ions that dissociate before reaching the dipole magnet, resulting in ion populations with lower rigidity. A very small peak at a magnet current of approximately 28 A is believed to correspond to a relatively small percentage of HeH^+ ions [68].

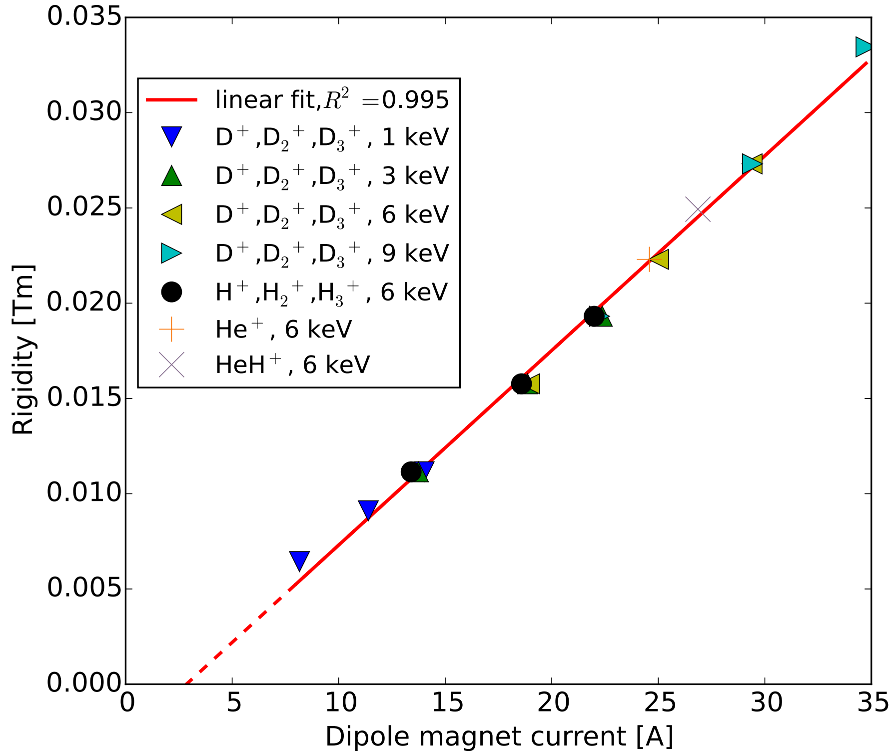

Figure 4.28: The rigidity of several ion species at energies ranging from 1 to 9 keV are plotted relative to the current applied to the dipole magnet at which the corresponding ion current peaks were measured. As predicted by equation 4.1, the rigidity is directly proportional to the current through the magnet, which is proportional to the magnetic field. It can be observed that ions whose mass times energy are identical coincide on the graph, such as 1 keV D_3^+, 3 keV D^+ and 6 keV H^+ ions. In discrepancy to the equation, the linear regression of the data does not connect to the origin. This is attributed to the magnet hysteresis.

4.2.3 Beam emittance and ion optics

In order to maximize the ion flux density arriving at the target, it was necessary to study and characterize the optical properties of the ion beam, as this would determine the final selection and placement of the ion lenses to be used. As a first step, the optical beam paths of the ions were calculated using the transfer-matrix method, as, e.g., described in [37, 36]. This method ignores beam divergence due to space-charge effects and is based on the assumption of ideal beam emittance (i.e., emittance ellipse has zero area), but it is nevertheless useful as a first-order approximation. Figure 4.29 shows the ion trajectories calculated by transfer matrices between the Ø 16 mm Mo aperture at the exit of the differential pumping stage and the target through the dipole magnet, with the addition of two einzel lenses, one at the position of the beam-stopper (i.e., directly in front of the entrance to the dipole magnet) and one before reaching the target chamber [70]. As a consequence of the deflection, the dipole magnet focuses the beam in the deflection (horizontal) plane but not in the perpendicular (vertical) plane. As a result, even in the case of initial cylindrical symmetry, the trajectories in the horizontal and vertical planes are not identical. Since einzel lenses are cylindrically symmetric, they cannot focus the beam onto the target simultaneously in both planes, leading to strong beam divergence and significant beam losses as a substantial part of the beam impinges on the apertures and walls of the vacuum tubes (e.g., entrance and exit tubes of the dipole magnet) and does not reach the target. The einzel lenses were also simulated with the open-source ion optics library IBSimu, which has been used in the past to simulate ion optics of lenses and ion sources [28, 39]. Fig. 2.6 in chapter 2 shows an einzel lens that was used in the HSQ alongside a simulation of a similar lens without considering space-charge effects.

As previously stated, the beam at the differential pumping stage and beyond is strongly space-charge compensated: the thermal electrons trapped in the potential well of the ion beam neutralize the beam, strongly reducing beam divergence due to Coulomb repulsion [38]. The use of electrostatic einzel lenses thus intrinsically entails a trade-off: in order to effectively focus the beam, (at least) the central electrode must be set to a positive or negative potential typically of the same order of magnitude as the extraction potential of the beam. Electrons trapped in the ion beam will be repelled by or attracted to this electrode, leaving the beam and eliminating the space-charge compensation effect. As a consequence of this, the beam emittance would increase, potentially worsening beam transport, since the resulting space-charge would cause the ion beam to diverge significantly.

To test beam focusing and loss of space-charge compensation, two einzel lenses were installed: one located in the differential pumping stage at the exit of the ion source, shown in figure 4.30, and one located between the Mo aperture and dipole magnet. Due to space constraints, the beam-stopper had to be removed to install the second lens. The location of both lenses is shown in figure 4.1. The lenses were tested by applying decelerating (positive) and accelerating (negative) potentials to the central electrode of the lens with deuterium beams of 1.5, 3 and 6 keV. The ion current was measured with the Faraday cup at the beam-stopper in the case of the lens in the differential pumping stage and, due to the removal of the beam-stopper for the

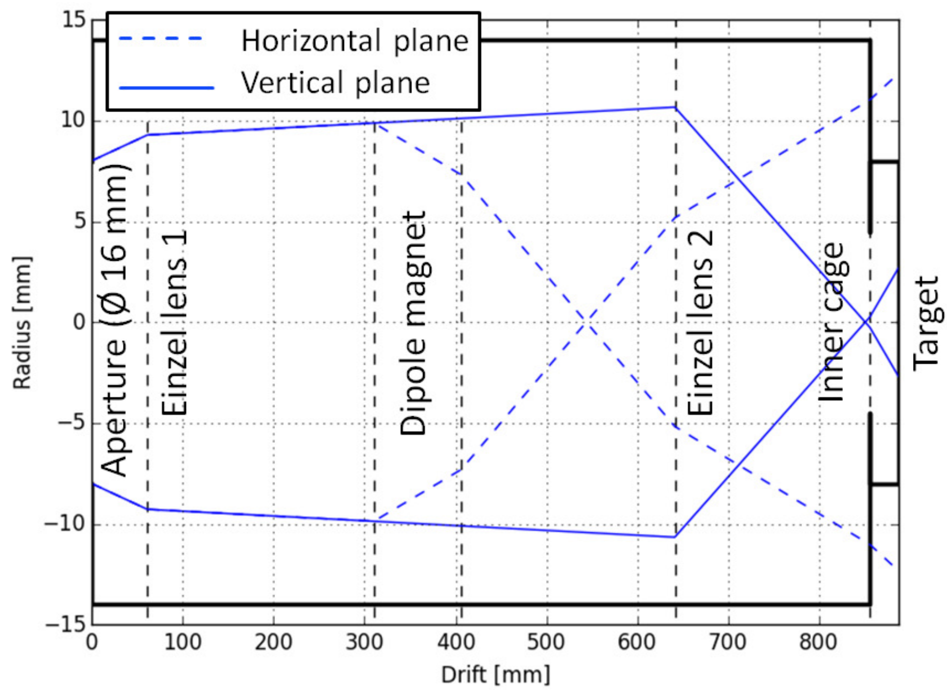

Figure 4.29: Calculation of the ion beam path by the transfer-matrix method [36, 37] between the Ø 16 mm molybdenum aperture and the target, passing through two einzel lenses and the dipole magnet. Due to the magnetic focusing effect in the horizontal plane (dashed blue lines in the diagram, also shown in Fig. 2.4), the beam is no longer cylindrically symmetric after passing through the dipole magnet. For this reason, the lens located after the magnet ("Einzel lens 2") cannot focus the beam in both planes simultaneously, leading to a large part of the beam being lost [70].

Figure 4.30: Einzel lens installed in the first differential pumping stage at the exit of the ion source, marked 1st einzel lens in the bird's-eye view of SIESTA (Fig. 4.1).

installation of the second lens, at a Faraday cup at the exit of the dipole magnet in the case of the lens mounted between the Mo aperture and the beam-stopper. Both lenses showed the same behavior, displayed in Fig. 4.31 for the lens in the differential pumping stage. In all cases, once a modest potential was set on the central electrode the measured ion current rapidly dropped by an order of magnitude. This is due to the loss of space-charge compensation. The effect was more pronounced when the einzel lens was set to a positive potential, since in this case the electrons were attracted towards the lens. When the lens was set to a negative potential, electrons were repelled by the lens. In this case, a significant decrease of the ion current occurred only for larger negative lens potentials, since space-charge compensation was only lost in the vicinity of the lens. The lens potential at which a significant decrease of the ion current is observed is proportional to the energy of the beam. As described in [36], a focus optimum occurs in all cases when operating the lens with positive polarity, at a potential slightly below and proportional to the extraction potential of the beam. This was evidenced by an increase in the measured ion current reaching the Faraday cup when setting the lens to the required potential. If the lens voltage is larger than the extraction potential of the beam, the ions are decelerated, and so the measured ion current drops to zero. This does not occur if the lens is operated at negative polarity because in this case the beam is accelerated towards the lens. If operated in this way, a more negative lens potential leads to stronger beam focusing, as evidenced by the slow increase in the measured current with negative lens potential. In all cases where the ion lenses were used, the ion currents that were measured were smaller than those measured when no lens was employed. The increase in focusing power does not outweigh the current losses due to emittance growth from space-charge.

The ion optical characteristics of the beam (beam profile and divergence) were studied at the

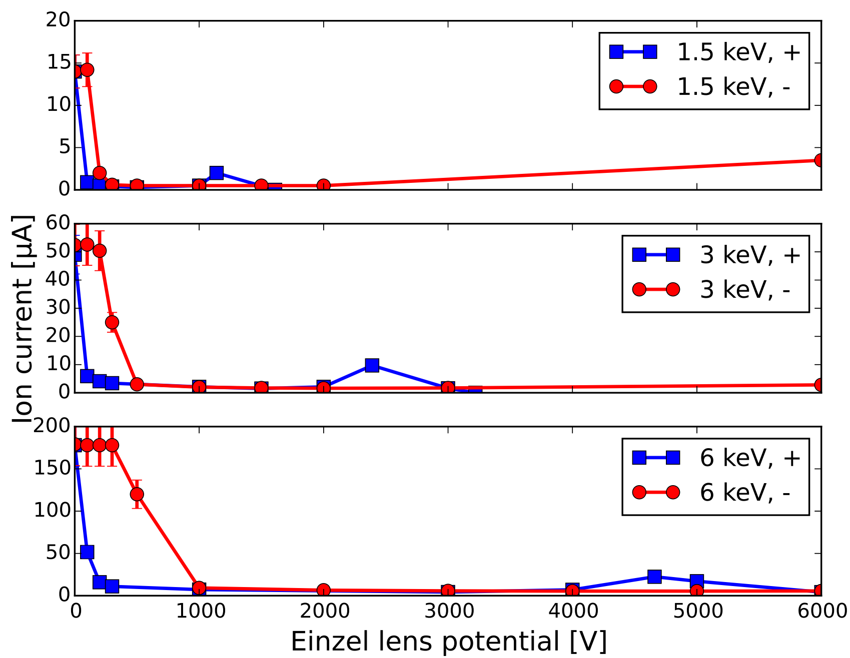

Figure 4.31: Ion currents measured at the beam-stopper from D beams of 1.5, 3 and 6 keV when operating an einzel lens at the exit of the ion source at varying accelerating and decelerating potentials. Space-charge compensation was lost after applying a modest potential to the lens, as evidenced by the rapid drop in the measured ion current. In no case were ion currents achieved that were larger than without a lens. Lines have been added to guide the eye.

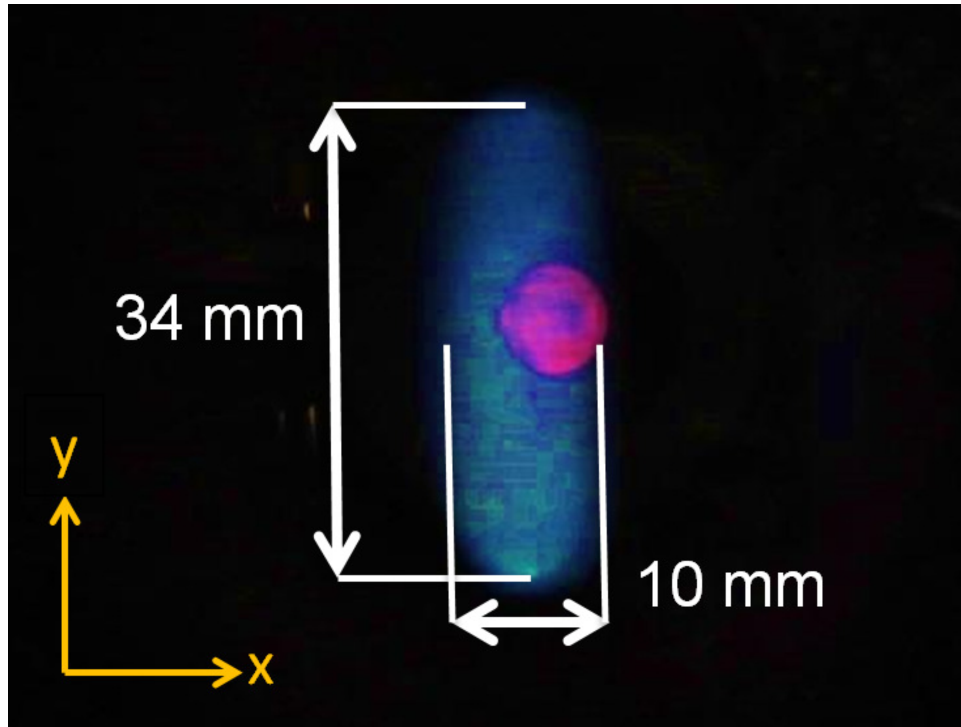

Figure 4.32: Beam profile of a 10 keV D_3^+ beam on Ce-doped quartz glass 16 cm away from the exit of the dipole magnet. The beam is focused within the magnet in the deflection plane (x), leading to an astigmatic beam with a beam-waist smaller than 10 mm at the quartz glass. The red spot in the middle of the image is light from the ion source that is reflected inside the dipole magnet, and bears no relation to the beam spot.

exit of the dipole magnet. To visualize the beam, a Heraeus M-382 Plus[17] Ce-doped quartz glass was installed at a distance of 16 cm from the dipole magnet's exit flange. When ions impinge on the glass, light is emitted due to fluorescence. In order to avoid charge accumulation on the surface of the glass, a fine nickel mesh was attached to the glass with Kapton[18] tape. At the Mo aperture, the beam diverges equally in the horizontal and vertical plane and has a diameter of 16 mm. As can be seen in Fig. 4.32, the focusing of the beam in the horizontal plane within the magnetic sector field leads to an elongated beam at the exit of the dipole magnet, with a narrow beam diameter of approximately 10 mm. In the vertical plane, the beam is not focused and the beam diameter is 34 mm. The real focusing effect at the position of the quartz glass in the horizontal plane is, therefore, from a diameter of 34 mm to one of 10 mm. At positions further downstream from the dipole magnet, the beam waist in the horizontal plane is reached and the beam again diverges in the horizontal plane. As previously stated, this beam astigmatism cannot be corrected with cylindrically symmetric lenses. Instead, asymmetric lenses such as quadrupole lenses, capable of applying different foci in the horizontal and vertical plane, must be used. Since the loss of space-charge compensation incurs in significant beam losses, magnetic lenses - which will not attract / repel the electrons trapped in the beam - are preferred to electrostatic lenses.

[17]Trademark of Heraeus Quarzglas GmbH & Co. KG
[18]Trademark of E. I. du Pont de Nemours & Co.

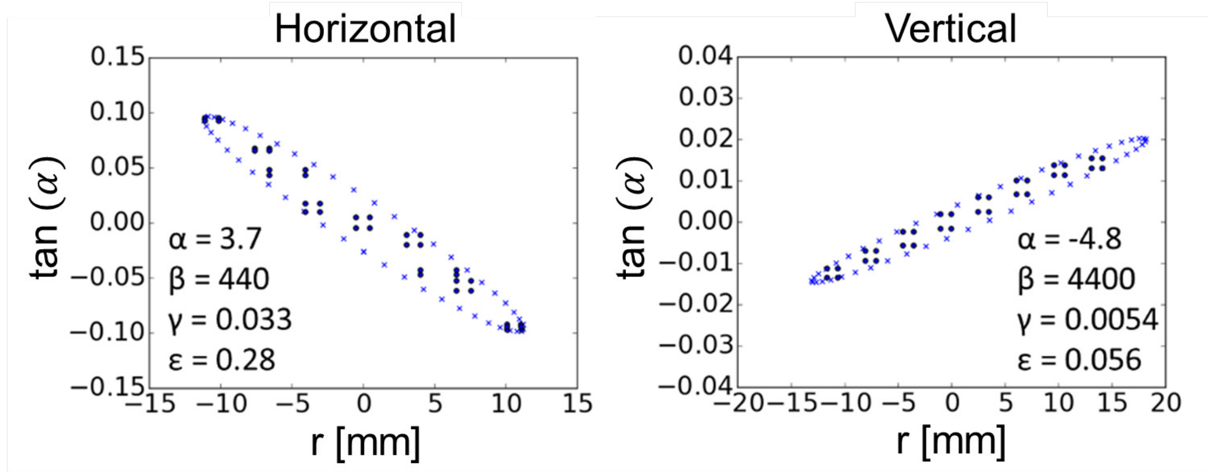

Figure 4.33: Reconstructed beam ellipses from a 10 keV D_3^+ beam in the horizontal and vertical planes at the exit flange of the dipole magnet with the calculated Twiss parameters. Dots correspond to the measured points. Crosses indicate the circumscribing ellipse. The beam is converging in the horizontal plane (negative angles for positive distances), while diverging in the vertical plane (positive angles at positive distances). The area of the ellipse is $\varepsilon \cdot \pi$ in mm·rad.

Parameter	Horizontal	Vertical
α	3.7	-4.8
β	440	4400
γ	0.033	0.0054
ϵ	0.28	0.056

Table 4.3: Twiss parameters in the horizontal and vertical planes at the exit of the dipole magnet

The emittance ellipse was measured by the pepper-pot method, as described in [71, 72]. A plate with equally spaced holes (pepper-pot) was placed at the exit flange of the dipole magnet. As the beam passed through the holes, the beamlets produced individual beam footprints on the quartz glass. With this information, the angular distribution of the beam at the position of each hole on the pepper pot was measured, from which the beam ellipse is reconstructed to obtain the Twiss parameters [35]. Figure 4.33 shows the reconstructed ellipse in the horizontal and vertical planes along with the values of the Twiss parameters at the exit flange of the dipole magnet, also listed in table 4.3.

The measured Twiss parameters were used in ion optical calculations to design the magnetic quadrupole doublet lens. The magnetic fields of the quadrupole doublet were optimized in order to maximize the ion flux at the target. A single quadrupole focuses the beam in one plane while simultaneously de-focusing in the perpendicular plane. The horizontal and vertical focal points are, therefore, not independent. A combination of two allows for an additional degree of freedom, so that both focal points may be adjusted freely, and so net focusing in both planes can be achieved. Calculations showed the use of such a magnetic quadrupole could entail an increase of ion current at the target by up to a factor of 20 compared to values without installing

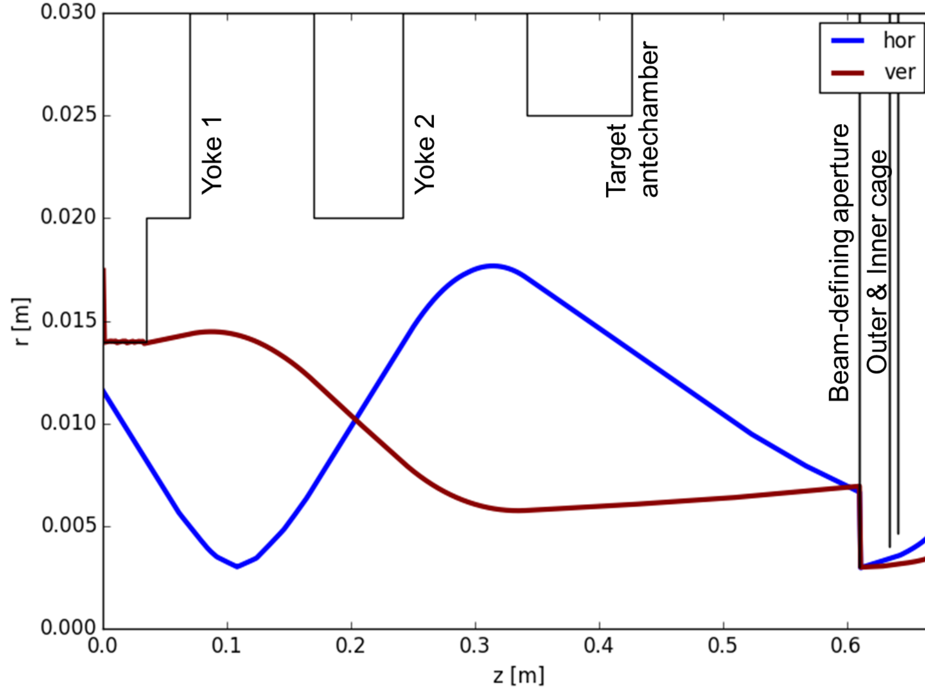

Figure 4.34: Numerical calculations of the edge of the beam trajectory through a magnetic quadrupole doublet between the dipole magnet (z = 0 m) and the target (z = 0.6 m) in the horizontal (hor) and vertical planes (ver) when focusing a 6 keV D_3^+ beam. Between the grounded inner cage and the target (right edge of the image), the ions are decelerated to an impinging ion energy of 600 eV/D. The first quadrupole along the z axis focuses vertically with a pole tip field of 0.041 T and the second focuses horizontally with a pole tip field of 0.073 T.

the lens. Fig. 4.34 shows calculated trajectories of the edge of the beam in the horizontal and vertical plane between the dipole magnet and the target if a fully-optimized quadrupole doublet lens is used. Based on these results, a magnetic quadrupole doublet model QM-60.100 from D-Pace with a bore diameter of 60 mm and a peak pole-tip field of 0.15 T was ordered and installed (quadrupole shown in Fig. 4.12). The quadrupole doublet is situated outside of the vacuum system. The position of the quadrupole lens system is shown in Fig. 4.1. As is visible in Fig. 4.34, the beam trajectories may expand significantly within the quadrupole lens during focusing. In order to prevent contact with the walls of the vacuum tube connecting the dipole magnet and the target chamber under a wide range of possible operating conditions, the 321 mm long vacuum tube used to connect the two systems was custom built to have a larger internal diameter (Ø 49.8 mm instead of the nominal Ø 38 mm for a CF 40 tube). In agreement with the simulations, the highest current at the target chamber was measured when the quadrupole closest to the dipole magnet was configured to vertically focus the beam and the quadrupole closest to the target chamber focused the beam horizontally. The position of the quadrupoles along the beam axis was varied by ±40 mm from their nominal position. Experimentally, this was not seen to have any significant effect on the maximum ion current measured at the target chamber.

When focusing a 6 kV D_3^+ ion beam with the quadrupole doublet lens, an increase of a factor of 4 in the ion current was achieved. The discrepancy between this and the factor of 20 increase predicted by the calculations is attributed to two factors. Firstly, the ion density of the beam was assumed to be uniform in the simulations and under this assumption, when no quadrupole lens is used, a large part of the ion current would impinge on the stainless steel walls of the vacuum chambers and the beam-defining aperture. If the ion density is not uniform, but instead higher near the center of the beam, then a larger fraction of the beam would reach the target without the use of a lens, in which case the possible increase in ion current at the target due to the addition of said lens would be smaller than predicted. Secondly, the focusing effect of the quadrupole lens is highly sensitive to the correct alignment of each of the two quadrupoles. It was observed that a sub-mm precision is required to adequately focus the beam. This was not foreseen when designing the support structure for the quadrupole doublet lens, and it is possible that the lens is not yet sufficiently well aligned with the target. If this is the case, then better alignment may provide larger ion currents at the target. In view of this, a fine-adjustment support structure is to be installed in the future.

4.2.4 Beam footprint and neutral population at the target

The beam footprint at the target was measured without focusing from the quadrupole lens by exposing samples consisting of a 70-nm-thick layer of amorphous hydrogenated carbon (a-C:H) on a Si substrate to a deuterium ion beam. For these samples, a change in layer thickness of a few nanometers leads to a change in color. This change in layer thickness was quantitatively measured applying ellipsometry [56]. Two a-C:H samples were eroded by a 6 keV D_3^+ beam when using a Ø 6 mm beam-defining aperture. Figure 4.35 shows the 2D-ellipsometry measurements and horizontal line scans of the samples, from which 20 nm on average were eroded in each case. On both samples, the ion beam footprint corresponds to the horizontally-elongated ellipse. Since the beam diverges differently in the horizontal and vertical planes between the beam-defining aperture and the target (stronger divergence in the horizontal plane), the footprint of the beam is elliptical. As mentioned in the previous section, in Fig. 4.32, the beam is imaged 16 cm away from the exit of the dipole magnet, at a position where the beam is focused in the horizontal plane to a beam-waist smaller than 10 mm. Downstream from this position, the beam again diverges in the horizontal plane. At the target, the beam divergence (and beam diameter) is larger in the horizontal plane than in the vertical plane. Since the beam diverges between beam-defining aperture and target, the surface area of the beam-defining aperture cannot be taken as the surface area of the beam footprint. A second vertically elongated ellipse is also visible on the sample. This ellipse is assumed to be caused by a small percentage of neutral particles which impinge on the a-C:H layer, altering the optical properties of the surface. It is unclear why the ellipse formed by the neutral particles is vertically elongated. The neutral population of the ion beam is quantified at the end of this section.

In the topmost image, evenly-spaced vertical lines are visible along the horizontal axis of the sample. This is due to areas with different erosion. These vertical lines, of approximately

1 mm in width, are a consequence of the horizontal beam focusing effect of the dipole magnet: after passing through the magnetic sector field the beam is focused in the deflection (horizontal) plane, forming an image of the openings of the last (grounded) of the three grids (described in section 4.1.2) located at the exit of the ion source. The first and second grids are shown in figure 4.3. No image is formed in the vertical plane, because in this plane the focal point is not located upstream from the target chamber. Since the holes of the grids are vertically aligned, they appear as vertical stripes on the sample. Due to the construction of the grids, it is not possible to rotate them in a way that will eliminate the stripes. To accomplish this, new grids with an altered geometry would have to be manufactured. One way to avoid the formation of these vertical stripes is to periodically vary the current through the dipole magnet back and forth by a small amount, typically ± 0.2 A , thereby "sweeping" the ion beam over the beam-defining aperture. This was performed when eroding the second a-C:H sample (lower image of figure 4.35).

When using the quadrupole doublet lens to focus the beam, similar inhomogeneities in the beam footprint at the target are also observed, although depending on the lens focusing effect, these may not necessarily take the shape of vertically elongated lines. As was the case without focusing with the quadrupole lens, oscillating the current through the dipole magnet to sweep the beam over the beam-defining aperture also helps to "smooth out" the inhomogeneities in the beam-footprint at the target. Another alternative to reduce said inhomogeneities would be to induce vertical and horizontal beam-sweeping by operating each of the four coils of the quadrupoles separately. However, this method would compromise the beam focusing effect of the quadrupole lens which is responsible for the increase in ion flux to the target. Since this was the main application of the quadrupole lens, this method to homogenize the beam footprint was not attempted. Electrostatic beam-sweeping with capacitor plates was also not implemented, as this would have led to a loss of space-charge compensation in the ion beam, as was evidenced in the tests with einzel-lenses in section 4.2.3.

a-C:H samples were also used to measure the surface area of the beam footprint at the target, which is required together with the impinging ion current to calculate the ion flux density (and fluence) at the target. Table 4.4 shows the measured surface areas eroded by a 6 keV D_3^+ beam under various angles of incidence. To prevent part of the beam from extending beyond the target and impinging on the inside of the double cage, the appropriate beam-defining aperture had to be chosen for each angle of incidence at which a measurement took place.

Ions can be neutralized in-flight in between the ion source and the target by charge exchange collisions. Neutral particles produced between ion source and dipole magnet will not be deflected and, therefore, will not reach the target. If experiments with low-energy ions are desired, the target will be biased to decelerate the ions. However, high energy neutral particles produced between the exit of the dipole magnet and the target will not be decelerated and may impinge on the target with the full primary energy. Given the difference in impinging energy, the effect of these impinging neutral particles on the sample can, in some cases, be of comparable magnitude to the effect of the much higher flux of low-energy ions. Therefore, if the impinging neutral particles are not taken into account, this neglect can severely compromise the interpretation

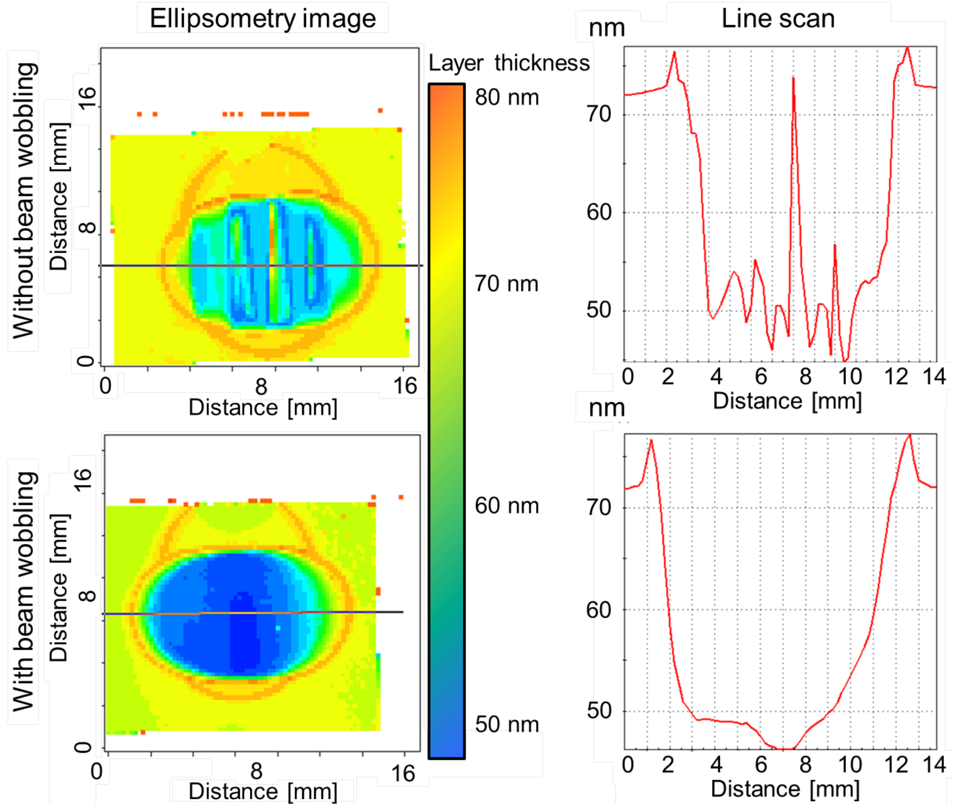

Figure 4.35: Ellipsometry measurements of the beam footprint at the target obtained by exposing a 70-nm-thick a-C:H layer on Si to a 6 keV D_3^+ beam, when using a Ø 6 mm beam-defining aperture. Two pairs of images are shown: the left images show a 2D pattern of the a-C:H layer erosion, the right images are line scans along the lines indicated in the left figures. In the left images, yellow indicates no erosion, green corresponds to moderate erosion (about 10 nm eroded) and blue corresponds to strong erosion (about 20 nm eroded). Orange indicates layer thicknesses larger than before exposure. In the upper pair of images, erosion of the sample within the elliptical beam spot is not uniform: vertical lines are present, corresponding to areas of more pronounced erosion alternating with areas of less erosion. In the lower pair of images, the ion beam was scanned over the beam-defining aperture, thereby homogenizing the beam profile. The increase in layer thickness at the edge of the beam-spot visible in both images (orange) is an artifact of the ellipsometry measurement. D implantation into the a-C:H layer leads to a change of the optical properties of the layer which are interpreted by the analysis software as an increase of the layer thickness [56]. The vertically elongated ellipses visible in the two images on the left are believed to be caused by a small flux of neutral particles.

Angle [°]	Surface Area [cm^2]	Aperture [mm]
0	0.51	Ø 6
45	0.75	3×6
60	0.82	2×6
75	0.94	1.5×6

Table 4.4: Measured surface area of the beam footprint on a-C:H samples eroded under varying angles of incidence by a 6 keV D_3^+ beam. The required aperture was chosen for each angle to ensure the beam only impinged on the sample.

of the experimental results. In order to assess the impact of the neutral particles, the neutral population of the beam at the target was quantified. As a first step, the neutral population was estimated analytically by equating the neutral population with the probability of neutralization P, which is taken as a first approximation as:

$$P = \sigma n L, \tag{4.2}$$

where σ is the charge exchange cross section. No charge exchange cross section data could be found for [D_3^+,D_2], but as a first approximation the cross section is assumed to be similar to that of [D^+,D_2], which for 3 keV [D^+,D_2] is $2\times10^{-19}\,\mathrm{m}^2$, taken for H from [73] with the corresponding energy correction. n is the density of neutral gas between dipole magnet and target and is derived from the gas pressure by applying the ideal gas law at room temperature. As a conservative assumption, the neutral gas density was calculated with the pressure in the dipole magnet (5×10^{-6} mbar), which is higher than the pressure in the target chamber (5×10^{-7} mbar), leading to $n = 1.2\times10^{17}\,\mathrm{D_2/m^3}$. L is the distance between dipole magnet and target, which in the case of SIESTA is 0.6 m. By applying equation 4.2, the neutral population is estimated at 1.4 %.

To measure the neutral fraction in the beam a thin gold layer on a silicon substrate was exposed to a D ion beam. Physical Vapor deposition was used to produce a sample consisting of a 45 nm Au layer on a smooth Si substrate, with a 5 nm Ti interlayer included to ensure adequate adhesion of the Au layer and to act as a diffusion barrier between Au and Si. The 2-dimensional thickness distribution of the Au layer was measured by Rutherford Backscattering Spectrometry (RBS) with 2 MeV He^+ ions with an analysis beam-spot size of approximately $1\times1\,\mathrm{mm}^2$. The maximum variation of the thus-determined Au layer thickness across the surface of the sample was 0.5 nm, indicating the very good homogeneity of the Au layer. The sample was subsequently exposed at SIESTA to a neutral deuterium beam of 1.2 keV/D by employing an extraction potential of 3.6 kV to extract D_3^+ ions and positively biasing the target to 3.8 kV. By biasing the target in this fashion, all deuterium ions are deflected away from the target and do not reach the sample, while the fraction of neutral particles in the beam is not affected by target biasing and thus impinges with full extraction energy on the sample. The sample was exposed in this manner for 32 hours. During this exposure, the D_3^+ ion current was measured periodically by rotating the target platform 180º and allowing the beam to impinge on the backside of the grounded heating cup, which as stated in section 4.1.6 is connected to the current measurement for this purpose. The current was determined to be uniform, with a variation below 1 % during exposures. The day to day variability of the current between exposures was registered and accounted for.

After erosion, the Au layer thickness was again measured by RBS and the eroded Au layer thickness was determined. Measurements were carried out in 1 mm steps along the longitudinal midplane of the sample and perpendicular to the midplane at the position of the measured erosion maximum. The measured beam spots are marked with an X in Fig. 4.36. The sputter yield for 1.2 keV/D on Au is 0.0305 and was taken from [61]. With this method, the neutral fluence at each of the positions measured with RBS was calculated. These data were contrasted

with the exposure time and average ion current to determine the neutral population of the ion beam at said positions. The neutral population is calculated as the number of energetic neutral D atoms divided by the number of D atoms arriving in form of ions, i.e., in the case of D_3^+ ions the latter number is three times the ion flux. The erosion - and thus neutral population - at other positions on the sample was interpolated from these measurements by applying the tensor-product method. The maximal measured thickness change was 41.7 nm corresponding to 93 % of the 45-nm-thick Au layer. At its maximum, the neutral population is of 1.5 %, while the average among the measurement points is of 0.8 %. As shown in figure 4.36, the neutral beam is predominantly concentrated off-center on the upper-right quadrant of the sample. The beam footprint of the neutral "beam" differs from that of the ion beam under equivalent exposure conditions (i.e., if the target were not biased) because the ion beam would be focused by the quadrupole doublet lens, whereas in the case of the neutral "beam", those ions neutralized between the exit of the dipole magnet and the first quadrupole (the majority, since the pressure in the dipole magnet is larger than in the target chamber) would not be focused at all. Those neutralized between the quadrupoles would be focused by the first one and not by the second one, and only those ions neutralized between the second quadrupole and the target would be focused in the same way as the ion beam. The neutral "beam" can be considered a combination of these three beams. Due to small errors in the adjustment of the quadrupoles (mentioned briefly at the end of section 4.2.3), the axes of the two quadrupoles and the exit of the dipole magnet do not completely coincide, so the overall neutral "beam" trajectory is slightly off-axis with regard to the ion beam.

The neutral population of the ion beam has been estimated to be approximately 1 % under the given exposure conditions. Based on this information, e.g., in the case of sputtering at low incident ion energies, if the sputter yield of the high-energy neutrals is larger than the sputter yield of the low-energy ions by a factor of 100 or more, the neutral particles will substantially contribute to or even dominate the sputtering process, and therefore cannot be neglected. In such cases, it may be necessary to perform a dedicated measurement of the neutral population analogous to this one under the required experimental conditions.

4.2.5 Current measurement

The target high-voltage power supply was modified to avoid unintentional charging of the sample when this was irradiated by an ion beam. When this happened, the sample would accumulate charge if the power supply was set to positive polarity. At an ion current of 50 μA, this would lead to an unintended sample bias of between 1 and 2 kV. When operating the power supply in this fashion, the diodes are opposing the flow of a "positive" (i.e. ion) current, so the sample charges up until arcing with another component occurs. To understand why this was not an issue in the HSQ, the circuit schematics of the old Heinzinger HNCs 6000[19] power supply and the new FUG 430M-6000 were compared. It was found that a bridge with a 400 kΩ resistor between the high voltage pin (HV) and the 0 V pin was present in the Heinzinger power supply and

[19]Trademark of Heinzinger electronic GmbH

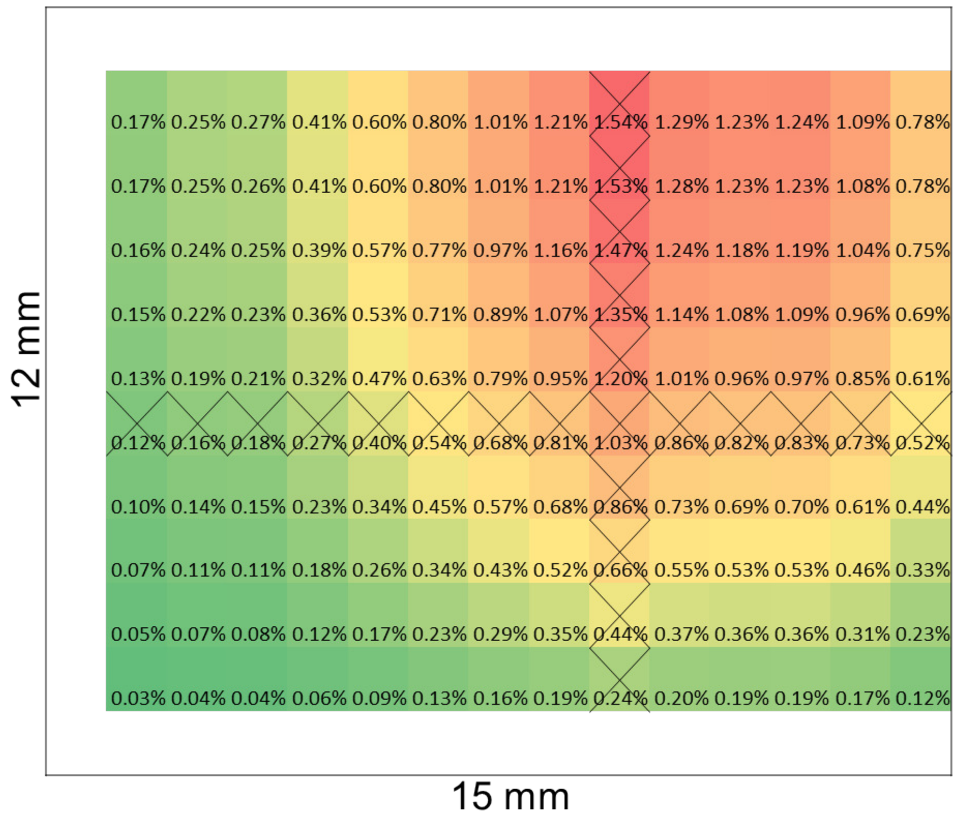

Figure 4.36: Position-resolved neutral population at target measured on a $12 \times 15\,\mathrm{mm}^2$ sample. The percentage in each cell represents the neutral population of the impinging beam on that $1 \times 1\,\mathrm{mm}^2$ cell. Red corresponds to areas where the neutral population is larger than 1 %. Yellow indicates it is between 0.5 % and 1 %. Green indicates the neutral population is below 0.5 %. X marks the positions where the neutral population was measured by RBS. The neutral populations at all other positions were interpolated by the tensor product method from the measured data.

absent in the FUG power supply. When using the Heinzinger power supply at positive polarity, the positive ion current would flow through the resistor to the 0 V pin, thereby preventing the target from charging up dramatically. It must be noted, however, that the flow of current does induce slight potential difference proportional to the resistance that is installed (in the case of 400 kΩ and 50 μA, the potential will be $U = R{\times}I = 20$ V). If the target is set to a certain potential, current will also flow through the bridge, leading to an ohmic power loss inversely proportional to the installed resistance. If the bias is 6 kV, $P = U{\times}I = \frac{U^2}{R} = 90$ W.

Based on this, the FUG power supply was modified by the manufacturer to include a similar bridge with a 200 kΩ resistor, leading in the aforementioned cases to an additional bias of 10 V under an ion current of 50 μA and leading to a power loss at 6 kV of 180 W. Thanks to this bridge, no additional charging of the sample has been observed.

The current measurement was tested under both connection scheme configurations (scheme A and scheme B, Fig. 4.16), while varying the target bias and outer grid voltage, and was already described in section 4.1.6. If the target and outer grid are unbiased, the ion current is overestimated by the current measurement due to secondary electrons emitted at the target. If the outer grid is negatively biased, these secondary electrons are repelled by the outer grid and are collected at the inner grid, which is connected to the current measurement. Increasing the outer grid negative bias led to a decrease of the measured ion current up to a bias of -7 V, beyond which point the ion current was stable. As a precaution, a nominal negative bias at the outer cage of -10 V was chosen, as at this bias the current measurement is stable and the bias is well above the measured threshold of -7 V. If the outer grid was grounded, a positive bias set to the target also had an effect on the measured ion current (secondary electrons are retained, electrons trapped in the potential well of the beam are attracted). It was however observed that, once the negative bias of the outer cage was set to -10 V the bias at the target no longer played a role in the beam current measurement. As a precaution, it was decided that a positive bias of 100 V (or greater, if required to achieve lower ion energies) at the target should be used to retain any secondary electrons. The inner cage is kept grounded through the current measurement at all times (Fig. 4.16).

The energy of the beam at the position of the target was checked by employing the target holder and heating cup as a retarding field analyzer. The ion current was measured only at the grounded heating cup located behind the target holder and a fine, optically thin Ni mesh (transparency 73 %) was attached to the target holder instead of a sample. The target could be grounded or positively biased. All other components were grounded. When the target was grounded, the ion beam passed through the openings in the mesh unimpeded and reached the heating cup, where the current was measured. At low target biases, the beam was partly deflected, but part reached the heating cup, producing secondary electrons which were accelerated towards the target holder, leading to an increased current measured at the heating cup. The bias at the target holder was progressively increased until the measured current abruptly fell to zero. When this happened, the bias of the Ni mesh corresponded to the energy of the beam. The beam was completely deflected by the Ni mesh at the target holder and no ions were reaching the heating cup. With this method, the energy of a 3 keV beam was confirmed to within 30 eV.

4.2.6 In-situ weight-loss measurement

As previously mentioned in section 4.1.6, a microbalance is installed above the target chamber, directly over the target platform, and is used for in-situ weight-loss measurements. The balance is a Rubotherm LP-type[20] magnetic suspension balance with a maximum load of 20 g with ±1 µg nominal resolution.

The operating principle of the balance, depicted schematically in figure 4.37, is as follows: The balance including sensor coil and electromagnet is located outside of the vacuum system. A double-walled copper tube closed on its upper end is used as separation between the sample in the vacuum system and the balance. A measuring rod consisting of a permanent magnet and a measuring load coupling is located inside the copper tube and is secured with a deposit screw inside the vacuum system. The vertical position of the measuring rod is registered by the sensor coil and the current through the electromagnet can be regulated by the microbalance to elevate and suspend the permanent magnet. The load to be measured is attached to two hooks hanging from the measuring load coupling. If the rod is elevated sufficiently, the measuring load coupling with load is also lifted. The measuring rod with load is kept suspended at a fixed vertical position (measuring point) and the weight of the measuring rod with load can be determined from the current passing through the electromagnet. The measuring rod can be suspended at another fixed vertical position labeled zero point, which is lower than the measuring point. At this position, the load is not lifted and the balance may be calibrated and tared. In the case of SIESTA, the load (sample mounted on sample holder) is attached to the measuring hook by elevating and rotating the sample with the vertical manipulator on which the target platform is mounted.

The microbalance is highly sensitive to vibrations and electromagnetic fields. For this reason, the magnetic quadrupoles, dipole magnet and ion source power supplies must be switched off during measurement with the microbalance. To reduce transmission of vibrations from the vacuum pumps to the microbalance through the walls of the vacuum system, the microbalance is connected to the target chamber with a CF 40 bellows with a nominal length of 105 mm. Another CF 40 tube with a CF 40 viewport is also used to connect these two systems. Through this viewport the measuring load coupling, deposit cage and screw can be observed (shown in Fig. 4.38). The microbalance is placed on top of an aluminum fine adjustment plate which allows lateral placement of the microbalance to within 0.1 mm. The fine adjustment plate is in turn located on top of a second Al plate connected to the target chamber support structure by rubber vibration dampers, serving to further insulate the microbalance from vibrations. To facilitate outgassing of the microbalance in the vacuum system, the double-walled copper tube was baked at 70°C for 10 days. Future improvements to the experimental setup could include thermal and magnetic shielding of the measuring head and sensor housing.

The microbalance control electronics is connected via an RS232 serial bus to a computer. Proprietary control software is used to operate the balance remotely and to carry out automated weight-measurement procedures. The general measurement procedure at SIESTA is as follows:

[20] Trademark of Rubotherm GmbH

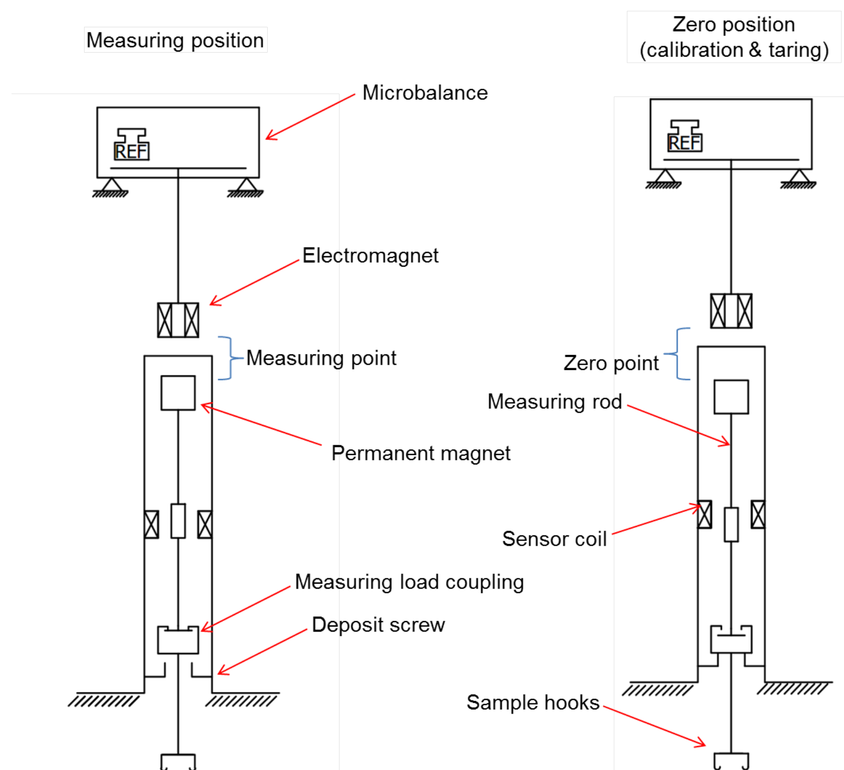

Figure 4.37: Measurement principle of the Rubotherm magnetic suspension balance. When set to "Zero" mode, the permanent magnet is suspended to the zero point (load not suspended) and the balance is tared and automatically calibrated. When in "Measuring" mode, the permanent magnet is suspended at the measuring point, lifting the sample.

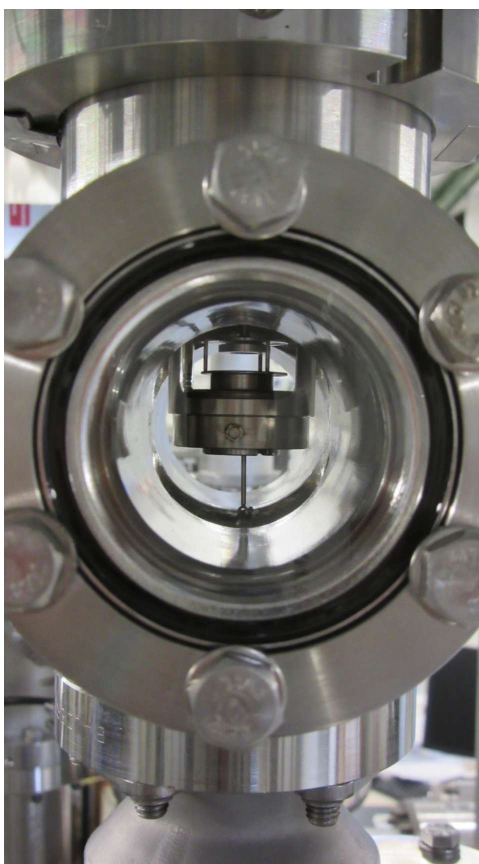

Figure 4.38: Microbalance measuring load coupling observed through CF 40 viewport above the target chamber.

Once the sample is placed on the target platform via the load-lock horizontal manipulator, it is allowed to degas for 30 minutes. The sample is elevated and rotated so that the target holder upper hooks (visible in Fig. 4.14 left and in Fig. 4.15) are hooked on the microbalance measuring hook. Before weighing the sample, the microbalance is set to "Zero" position (diagram on the right in Fig. 4.37) and is automatically calibrated and tared. The microbalance is subsequently set to "Measure" position and the sample weight is measured at 1 s intervals for 3 minutes. After this time the microbalance is once again set to "Zero" position, the drift in the weight measurement is corrected and the balance is once again tared. This "Measurement" and "Zero" cycle is repeated for 30 minutes.

By weighing the sample in this fashion before and after erosion, the mass loss of the sample due to erosion can be determined with a measurement uncertainty in the range of tens of μg. The microbalance was tested by comparing an in-situ weight-loss measurement with an ex-situ measurement of the same sample. The experimental procedure and measured mass loss in these two cases are described at the end of section 4.3.

4.3 Erosion of Au bulk samples

4.3.1 Experimental procedure

Gold was chosen as target material for the characterization of SIESTA due to three material properties: firstly, due to the high molar mass of Au, significant weight-loss can be achieved with moderate erosion. Secondly, the sputter yield (SY) of D on Au in the keV range is relatively high compared with that of its neighbors in the periodic table, so a comparatively lower fluence is required to achieve the desired erosion (e.g., SY of 2 keV D on Au is 0.037; SY of 2 keV D on W is 0.005 [40]). Thirdly, since Au is a noble metal, in-situ and ex-situ weight-loss measurements can be directly compared without the need to consider the possible formation of an oxide layer.

In order to test SIESTA, four pure gold bulk samples of $12 \times 15\,\mathrm{mm}^2$ were mechanically polished to a mirror finish and were eroded by a $6\,\mathrm{keV}\,\mathrm{D}_3^+$ ion beam (yielding 2 keV/D) at room temperature under normal incidence. All samples were weighed before and after exposure in an ex-situ microbalance. The sputter yield was determined by mass loss, and was compared to data from literature and simulations with the simulation code SDTrimSP [42]. Said simulations were performed with the standard parameters (Gauss-Mehler quadrature integration method with 8 pivots and ipot set to 1).

To include the slight day-to-day variability in the operation of the ion source (slightly different pressure or gas flow in the source, source filament aging...), the samples were exposed on different days. On each day, the samples were weighed ex-situ in the morning, exposed during the day and weighed again after exposure in the evening. A reference sample was weighed alongside the exposed sample on each occasion to correct for potential drift in the linearity of the ex-situ microbalance measurement during the day due to environmental factors such as temperature or humidity. The samples were weighed several times on each occasion, with a 5-10 minute wait between measurements to allow the balance to stabilize. The balance was also tared between

measurements. Additionally, one of the samples was weighed in-situ immediately before and after D ion beam exposure following the procedure described in section 4.2.6.

4.3.2 Sputter yield results

The sputter yield was calculated by applying:

$$SY = \frac{\triangle mass\,[\mathrm{g}] \times N_A\,[\mathrm{atoms/mol}]}{N_{ions} \times M(Au)\,[\mathrm{g/mol}]} \tag{4.3}$$

Here $\triangle mass$ is the mass loss due to erosion, N_A is Avogadro's number, $M(Au)$ is the standard atomic weight of gold and $N_{ions} = 3{\times}Q\,[\mathrm{C}]/e\,[\mathrm{C}]$ is the total amount of impinging particles. Q is the collected charge at the target and e is the elementary charge.

The results are shown in figure 4.39. The average of the sputter yields obtained experimentally in this work is approximately 14 % higher than the yield calculated by SDTrimSP, and approximately 25 % higher than the average of the data points from literature [40, 74], though it must be noted that these show a significant scatter. The value given by SDTrimSP is within the scatter of Behrisch's data points [40] and shows good agreement with Bay [74]. It was decided to take the SDTrimSP value as the benchmark for SIESTA. Given that the experimental data points from SIESTA show comparatively low scatter ($<$ 4 %), it is unlikely that the deviation of 14 % between the experimentally obtained average and the SDTrimSP sputter yield is due to an issue with reproducibility at SIESTA. The deviation could possibly be attributed to a systematic error in the current measurement. Sputtering due to the presence of energetic neutral particles (explained and quantified in section 4.2.4) would also contribute to this error in measurement (though it would not be sufficient on its own to explain the discrepancy), as could a possible systematic error in the weight-loss measurement.

In the case of the sample weighed in-situ and ex-situ (magenta diamonds in figure 4.39), the difference in the weight-loss measurements is 20 µg (759 µg ex-situ versus 739 µg in-situ). This is substantially larger than the standard deviation of the measurements, which in both cases is below 3 µg. While this difference is statistically significant, the relative difference of the in-situ and ex-situ weight-loss (and sputter yield) measurements is 2.6 %, which is within the scatter observed in the ex-situ measurements. As such it can be stated that the in-situ microbalance is an adequate tool for determining the sputter yield through mass loss at SIESTA in this case, where the measured mass loss is large and therefore the relative error is small. However, further tests are needed to ensure its reproducibility under experimental conditions where the expected weight-loss is lower than 100 µg. As stated in section 4.2.6, thermal and electromagnetic shielding may have to be installed to minimize the influence of external perturbations on the in-situ weight-loss measurement.

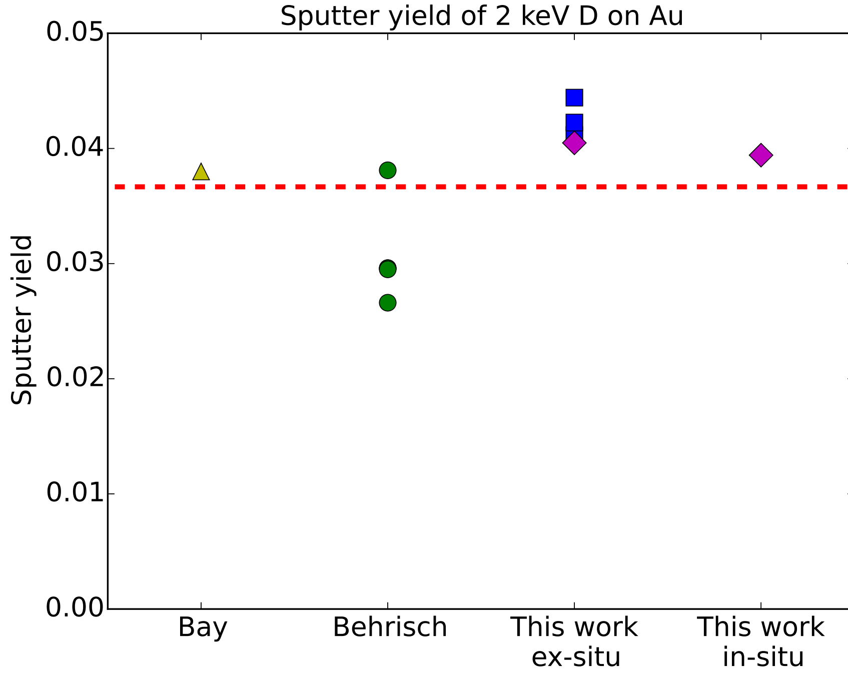

Figure 4.39: Sputter yield of bulk Au samples exposed to a 2 keV D beam (6 keV D_3^+) at SIESTA, determined by ex-situ and in-situ weight-loss. In the case of the magenta diamonds, ex-situ and in-situ weight-loss measurements were performed on the same sample. An SDTrimSP simulation and literature values from Behrisch [40] and Bay [74] are included for comparison. The uncertainty of the experimental sputter yield measurements ("This work ex-situ" and "This work in-situ") is contained within the size of the markers. (Color online).

Ion species	Energy at target [eV/atom]	Flux density [10^{19} atoms $m^{-2}s^{-1}$]	With quad. lens [10^{19} atoms $m^{-2}s^{-1}$]
H^+	6000	0.22	
H_2^+	3000	0.37	
H_3^+	2000	0.94	
D^+	6000	0.28	
D_2^+	3000	0.41	
D_3^+	2000	1.5	6.0
D_3^+	1000	1.3	
D_3^+	200	1.0	3.7
He^+	6000	0.45	
Ar^+	5000	0.10	0.37

Table 4.5: Performance data for SIESTA. Ion flux densities at the target are listed for varying ion species and energies at normal incidence. In the case of 6 keV D_3^+ (equaling 2 keV/D), 600 eV D_3^+ (200 eV/D) and 5 keV Ar^+, flux densities achieved when using the quadrupole doublet lens to focus the beam at the target are also listed

4.4 Conclusions

SIESTA (Second Ion Experiment for Sputtering and TDS Analysis) is a fully operational setup with a high-current ion source which is suited for well-defined ion-induced erosion and retention studies. It can supply a mass-filtered ion beam of H, D, He or Ar ions with an energy of 200 eV – 10 keV with ion flux densities (in the case of 6 keV D_3^+ = 2 keV/D) of up to several 10^{19} atoms $m^{-2}s^{-1}$ at the target when employing the quadrupole lens to focus the beam. Achieved operational parameters for several ion species and energies are summarized in table 4.5 for several ion species and energies. Other gas species may potentially be used, but were not tested. Mass filtering is achieved with a dipole magnet capable of deflecting a 10 keV Ar^+ beam. The beam footprint at the target can be modified with the selection of the different beam-defining apertures. The beam footprint measures 0.5 cm^2 in the case of a 6 keV D_3^+ beam at 0º incidence to the target (i.e., normal to the sample surface) with a Ø 6 mm beam-defining aperture. The sample may be rotated to study angle-dependent effects and sample temperatures of up to 1300 K are achieved via electron impact heating on the sample backside. The temperature can be measured with an infrared pyrometer and a type-K thermocouple. Samples are inserted into the target chamber with the use of a load-lock. The sample can be weighed in-situ with a magnetic suspension balance located above the target chamber for in-situ weight-loss measurements. Thermal desorption spectrometry is available in a dedicated vacuum chamber located below the load-lock for in-vacuo retention studies, though this capability of SIESTA has not yet been tested. The new version of the ion-driven permeation experiment PERMEX [63] is planned for the left exit of the dipole magnet (PERMEX exit in Fig. 4.11).

In this work, the device was assembled and extensively characterized. A parameter scan was performed on the DuoPIGatron ion source, showing an optimal gas flow at which ion currents to the target were maximum. When operating in this regime, the measured ion current at the beam-stopper Faraday cup was proportional to the extraction voltage to the power of 3/2 ($I \propto U^{3/2}$), indicating a constant perveance (Eq. 2.8), which would also be the case if the ion source were operating at optimal perveance. Effective mass-filtering was tested for a wide range of ion species and energies. The ion trajectories were simulated with a custom-written code based on the transfer-matrix method and the measured beam emittance. Einzel lenses were tested at two positions in the ion optical system, leading in all cases to a strong decrease in the ion current at the target due to loss of space-charge compensation. A quadrupole doublet lens was installed between the dipole magnet and target chamber and is used for simultaneous focusing of the ion beam in the horizontal and vertical plane. If no quadrupole lens is used, the flux density at the target at SIESTA is comparable to that of its predecessor, the HSQ [62]. If the quadrupole lens is employed, the flux density at the target is increased by up to a factor of 4 compared to the HSQ. Table 4.5 lists deuterium and argon ion flux densities with and without the focusing effect of the quadrupole lens.

The beam footprint at the target was measured with ellipsometry after erosion of 70-nm-thick amorphous hydrogenated carbon (a-C:H) films on Si substrates. A homogeneous beam footprint at the target was achieved by sweeping the ion beam over the beam-defining aperture

by oscillating the current passing through the dipole magnet. Sample heating was tested on W samples up to 1300 K and a push-rod mechanism was introduced to improve the thermocouple temperature measurement.

The spatially-resolved neutral population within the beam at the position of the target was measured by eroding a 50-nm-thick Au film on a Si substrate and measuring the change of the layer thickness by Rutherford Backscattering Spectrometry (RBS). These experiments resulted in a maximum neutral population of 1.5 % and an average population over the measured positions of 0.8 %. The magnetic suspension balance was tested by comparing in-situ and ex-situ weight-loss measurements of Au samples eroded by a 6 keV D_3^+ beam (2 keV/D), showing a measurement uncertainty in the range of ±3 µg in both cases. The sputter yield of pure Au under these exposure conditions was determined from the ex-situ and in-situ weight-loss measurements. The results are within the experimental scatter found in the literature and agree within 14 % with the sputter yield calculated by the sputtering code SDTrimSP [42].

Chapter 5

Leveraging SIESTA for erosion studies and code benchmarking

As discussed in chapter 2, physical sputtering by energetic particle bombardment is the main physical process driving erosion of plasma-facing materials in a nuclear fusion device [23]. Physical sputtering also plays an important role in other plasma-surface interaction processes such as magnetron sputtering, ion milling or analysis methods such as sputter-XPS or SIMS, and it has been the focus of extensive experimental and theoretical research in the past. Monte Carlo codes simulating sputtering by Coulomb interactions have been developed (e.g., SDTrimSP [42]), providing good agreement with experimental values for a wide range of ion-target combinations [40]. This process can be studied experimentally, either in plasma devices or with the use of an ion source. Ion sources have a number of distinct advantages over plasma devices, as they enable the extraction of a mono-energetic beam which can be mass-filtered with magnetic sector fields. The ensuing knowledge of the impinging particle species and energy can be coupled with accurate ion current measurement techniques to allow for well-defined experiments.

Several factors are known to affect sputtering, such as incident angle of the impinging particle, surface morphology, material composition, grain orientation, etc. [40]. Additionally, sputtering may dynamically modify the surface roughness and composition of the target. Therefore, the effect of these dynamic (i.e., not static) surface characteristics on the sputtering behaviour of a target is an area that warrants further study. Within the scope of this work, experiments were carried out to better understand the effect of angle of incidence on smooth and rough Fe and W thin films (sec. 5.1). Experiments were also carried out to validate the dynamic 3-D version of the SDTrimSP code, SDTrimSP-3D (sec. 5.2) and to attempt to bridge the gap between simulated and experimentally determined sputter yields of deuterium on EUROFER97 by separately studying the contributions on sputtering of (1) surface morphology and (2) W surface enrichment via preferential sputtering, as well as their combined effects (sec. 5.3).

5.1 Angle-dependent sputtering of smooth Fe and W and rough W thin films with keV D ions and comparison with SDTrimSP and SDTrimSP-3D

Significant parts of section 5.1 are covered in the paper by the author [75].

As noted in e.g. [41] and [76], target surface roughness can have a significant impact on the net sputtering behaviour of a material under bombardment. Depending on the specific surface morphology and nominal angle of incidence (i.e., the angle of incidence measured relative to the global surface normal), increased or decreased sputtering with regards to a perfectly smooth surface may occur, based on a superposition of two effects. On the one hand, due to surface roughness, the local incident angle will differ from the nominal incidence, as the nominal incident angle will be offset by the local slope at each point on the surface. This variation typically leads to increased sputtering when the nominal incidence is close to normal [77]. On the other hand, on rough surfaces re-deposition may play a role, as a particle sputtered from one point on the surface has a chance of impinging on another point on the surface and being re-deposited, thereby reducing global net erosion. Within this work, as part of ongoing research into the influence of surface roughness on sputtering, the previously unmeasured angle-dependent sputter yields (SY) for D bombardment of W and Fe were determined. This was achieved by exposing smooth W and Fe thin films to a 6 keV D_3^+ (2 keV/D) ion beam at SIESTA [24] and measuring the ensuing eroded layer thickness by Rutherford backscattering spectrometry (RBS) with a 2 MeV He^+ ion beam. The sputter yield data are compared with SDTrimSP simulations (assuming perfectly smooth samples) and experimental data from literature at normal incidence. Additionally, the angle-dependent sputter yield of rough W samples was measured and compared with static SDTrimSP-3D [60] simulations based on the sample surface morphology extracted from atomic force microscopy (AFM) scans, constituting the first experimental benchmark of the 3-D version of the code. The sputtering behaviour of rough Fe was not studied, as this was not the focus of the investigations. Results are presented and discussed in section 5.1.2. Section 5.1.3 constitutes a summary of these results.

5.1.1 Experimental procedure and simulations

As mentioned in sec. 5.1, part of the goal of this work was the comparison of sputter yields for smooth and rough samples. For this purpose, it was decided that the surface morphology of the samples to be studied should be modified as little as possible by the impinging ion beam. To comply with this restriction, it was decided to expose the samples to low fluences, of the order of $10^{22}\,\mathrm{D/m^2}$, corresponding to eroded layer depths of the order of tens of nm. This motivated the use of RBS to measure the thickness of nm-thin films, as the film thickness averaged over the analysis beam-spot (approx. $1 \times 1\,\mathrm{mm}^2$ in our case) could be measured before and after irradiation with sub-nm accuracy.

In [60] the effect of roughness on the sputter yield was evaluated on a synthetic sinusoidal cone surface. It was shown that at an aspect ratio of one, corresponding to a maximum incident

angle of 45° and R_{RMS} (Root Mean Square Roughness) value of approximately 7 nm, surface roughness plays a significant role on the sputter yield, as it is reduced by around 30 %. A similar geometry is illustrated in section 5.3, Fig. 5.22. Based on these findings, in this work, the maximum incident angle is used as a criterion to define whether a surface is smooth or rough. A surface is considered smooth if the maximum incident angle measured by AFM is much lower than 45°. To reduce the influence in this evaluation of potential outliers in the AFM measurement, the value of the incident angle at the 95th percentile of the slope distribution was used to judge whether the surface was considered rough or smooth.

500 nm-thick Fe films were deposited by magnetron sputtering on mirror-polished Si samples of 12×15 mm^2 surface area. As deposited, the samples exhibited a corrugated surface morphology in the nm-scale (Fig. 5.1) and an angle of incidence at the 95th percentile of the slope distribution of 48°. The samples were, therefore, considered rough. To reduce the surface roughness of the films, they were eroded for 3 hours to a thickness of 260 nm by an Ar radiofrequency plasma coupled to the substrate holder of the magnetron sputter device with a DC self bias set to -200V at a pressure of 1 Pa. AFM was performed with an Asylum Research MFP-3D[1] device to characterize the surface morphology of the samples before and after erosion with Ar (Fig. 5.1). The morphology changed from a corrugated structure with R_{RMS} values of 13 nm to smooth hills and valleys of $R_{RMS} < 4$ nm. The slope distribution of the smoothed samples is such that 95 % of all measured points on the sample are on areas with an inclination lower than 15°. Typical local slope distributions are shown in figure 5.2. As expected, progressive smoothing increases the preponderance of flat angles, confirming that after erosion with Ar the sample is smooth. The smooth W samples were produced by magnetron sputtering a 60 nm thick Cr interlayer on smooth 12×15 mm^2 Si samples and depositing a 60 nm-thick W layer on top of the Cr layer. The Cr interlayer served to improve adhesion of the W layer. AFM scans showed that the as-deposited samples were sufficiently smooth (Fig. 5.4), with $R_{RMS} \simeq 0.5$ nm and a distribution of inclination angles lower than 7° for 95 % of the measured points on the sample (Fig. 5.2). The rough W samples were produced by depositing a 100 nm-thick W layer on a 150 nm-thick Ti interlayer on a nanostructured Si substrate via magnetron sputtering. The Ti interlayer served the same purpose as the Cr interlayer for the smooth samples. The nanostructured silicon was prepared by means of a mask-less plasma process employing tetrafluoromethane and hydrogen as reaction gases. Surface texturing was achieved by an overall etching process with a simultaneous random deposition of a passivation layer produced by H particles, CFx radicals and the partially etched product SiFx. The competition between passivation layer deposition and its removal by bombardment with energetic ions causes local variations of the etching rate on the Si surface, leading to the growth of random silicon nanostructures over the process time [78]. A focused-ion-beam-prepared cross-section of a rough W sample is shown in figure 5.3. AFM scans of these samples indicated a $R_{RMS} \simeq 20$ nm and a distribution of local slopes lower than 50° for 95 % of all measured points (Figs. 5.4, 5.2). The roughness values of these samples and their slopes at the 95th percentile are listed in table 5.1.

[1]Trademark of Oxford Instruments Asylum Research, Inc.

Sample	R_{RMS} [nm]	Slope dist. (95 %)
Fe rough	13.4	48°
Fe smooth	3.7	15°
W rough	19.6	50°
W smooth	0.6	7°

Table 5.1: Root mean squared roughness values of Fe and W samples and the slope at the 95th percentile.

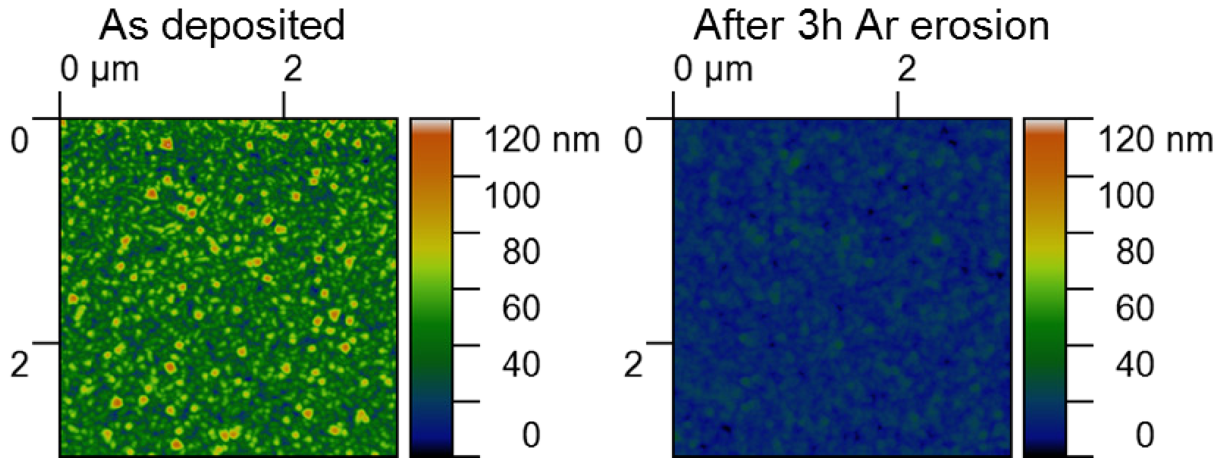

Figure 5.1: AFM images of 500 nm magnetron-deposited Fe thin films on Si, before (left) and after 3 hours of erosion under an Ar plasma (right). The samples are smoothed by the Ar plasma to $R_{RMS} < 4\,\text{nm}$, as listed in Tab. 5.1.

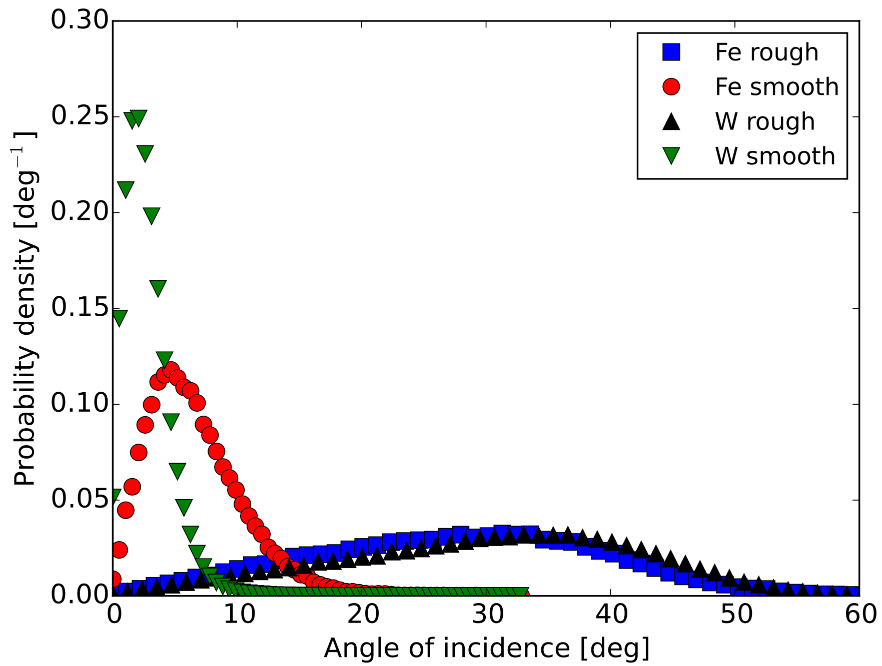

Figure 5.2: Typical distributions of local slopes of rough and smooth Fe and W thin films deposited on Si by magnetron sputtering. The local slope corresponding to the 95th percentile is listed in Tab. 5.1.

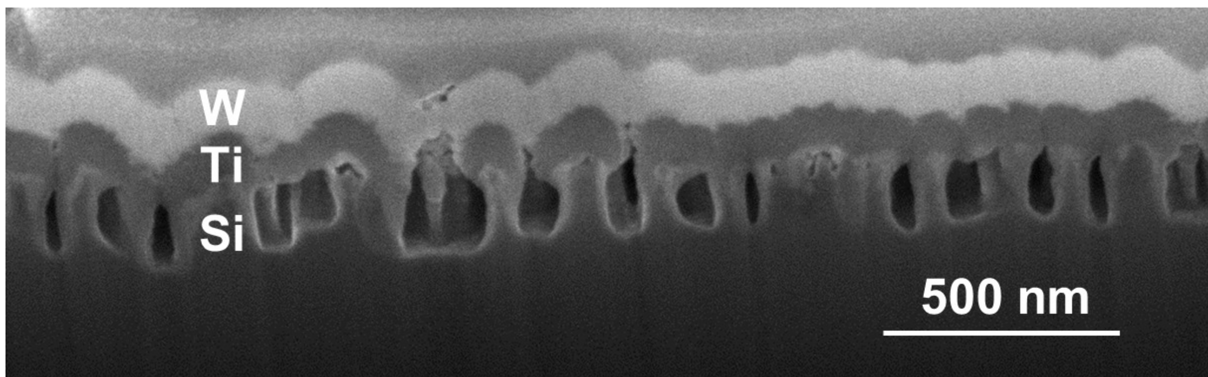

Figure 5.3: Scanning electron microscopy cross-section of a rough W sample, produced by focused ion beam cut. The W and Ti thin films and roughened Si substrate have been labeled in white.

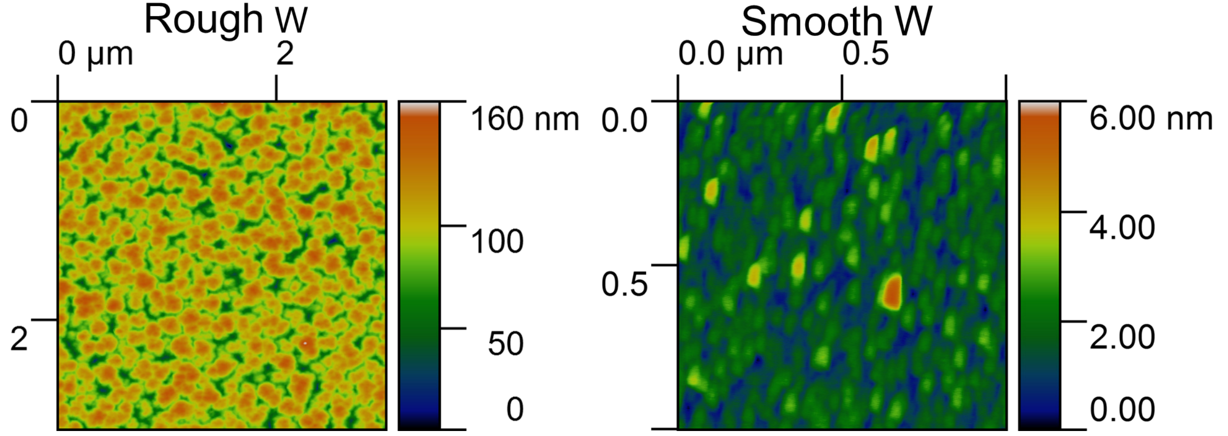

Figure 5.4: AFM images of rough (left, 3×3 µm^2) and smooth (right, 1×1 µm^2) W samples. The height scale of the smooth W image has been reduced to improve the visibility of the surface roughness. The R_{RMS} values of the samples are listed in Tab. 5.1.

The samples were exposed under incident angles of 0° (normal incidence), 45°, 60° and 75° to a 6 keV D_3^+ beam (2 keV/D) at SIESTA [24]. The surface area of the beam footprint at the target was measured in all cases by eroding 70 nm-thick amorphous hydrogenated carbon layers (a-C:H) on a Si substrate under identical exposure conditions as for the metal thin films. The measured surface area was used to estimate the ion fluence to the targets. The samples were eroded to fluences in the range of 10^{22} D/m^2, equating to an erosion of $\sim$ 10 nm. Before and after erosion, the samples were analyzed by RBS at the Tandem accelerator at IPP, using 2 MeV He ions and a scattering angle of 165°. Figure 5.5 shows typical spectra from a rough W sample analyzed before and after erosion at SIESTA. The integral of the W signal is proportional to the areal density of the W surface layer. The layer thickness can be deduced from the measured areal density by dividing by the atomic density of the W layer, which as a first approximation can be assumed to be the atomic density of bulk W.

From the data, the sputter yield for each angle of incidence was calculated by applying the equation:

$$Sputter\,Yield = \frac{N_{eroded}\,[\mathrm{at/cm^2}]\times S\,[\mathrm{cm^2}]}{N_{impinging}\,[\mathrm{at}]}, \tag{5.1}$$

where N_{eroded} denotes the thickness of the eroded layer in atoms per unit surface, S is the surface area of the beam-spot at the target and $N_{impinging} = 3\times Q/e$ is the total amount of impinging deuterons. Q is the collected charge at the target and e is the elementary charge. These results were compared with literature data and with the sputter yields calculated with SDTrimSP (explained in Sec. 3.6) for the given experimental conditions. Said simulations were performed with the standard parameters (Gauss-Mehler quadrature integration method with 8 pivots and ipot set to 1) [42]. For the static simulations of erosion of the rough W samples with SDTrimSP-3D [60], the surface geometry was directly extracted from the AFM scans of the samples (Fig. 5.4), consisting of a simulated surface of 440.25×440.25 nm^2. This is considered a

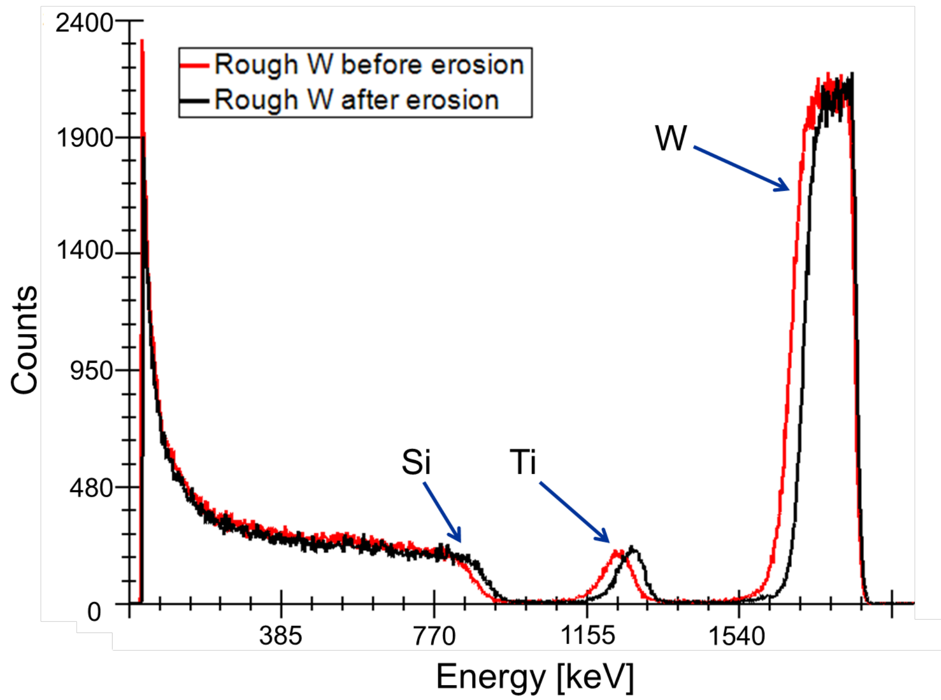

Figure 5.5: RBS spectra of a rough W sample before (red) and after exposure at SIESTA (black) under 0° incidence. The integral of the W peak is proportional to the thickness of the W layer. The width of the W peak after exposure has diminished due to erosion. The peak labeled “Ti” corresponds to the Ti interlayer, while the “Si” shoulder denotes the silicon substrate.

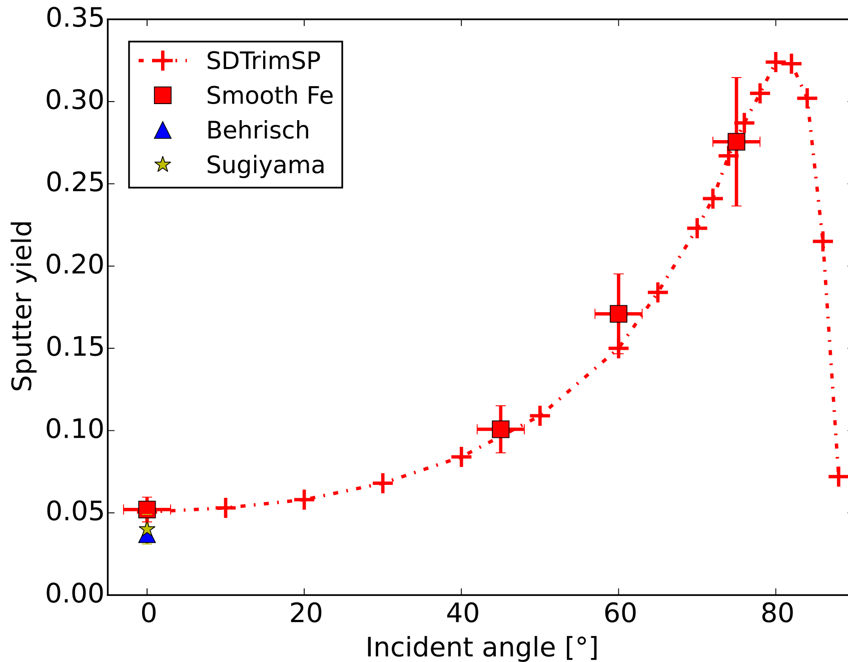

Figure 5.6: Sputter yields of a 6 keV D_3^+ beam (2 keV/D) on smooth Fe thin films under incident angles of 0° (normal to surface), 45°, 60° and 75°, determined by RBS. SDTrimSP simulations and literature values from Behrisch and Eckstein [61] and Sugiyama [79] are included for comparison.

representative area of the overall surface morphology. The cell resolution for the 3D simulation was $5.87 \times 5.87\,\mathrm{nm}^2$.

The experimental uncertainties of the measured sputter yields were calculated. The measurement uncertainty depends on the variance of N_{eroded} (number of counts of the integral of the RBS spectrum), S (beam footprint at the target) and Q (accumulated charge). In practice, the uncertainty due to N_{eroded} is negligible due to sufficient statistics in the RBS spectra. The uncertainty in S is in the range of $\pm 0.05\,\mathrm{cm}^2$ (approx. 7 % of surface area) at low angles of incidence (impinging ion beam footprint is well defined and homogeneous), but it is significant at high angles of incidence, up to $\pm 0.3\,\mathrm{cm}^2$, corresponding to 30 % of surface area, for samples eroded under 75° incidence. The uncertainty in Q is linked to the relative uncertainty of the ion current measurement, which was estimated to be 14 % in the previous chapter [24].

5.1.2 Comparison of simulations with the experimental data and discussion

The experimental and simulated results for the smooth Fe thin films are shown in Fig. 5.6. The experimental results agree fully with the simulated values within the experimental uncertainty. The sputter yield increases with the angle of incidence. In the simulation, the SY reaches a maximum for an angle of about 80° and then sharply decreases due to increased reflection. The experimentally determined sputter yield under normal incidence agrees within the experimental uncertainty with the value given in [79], and is approximately 20 % larger than the value given

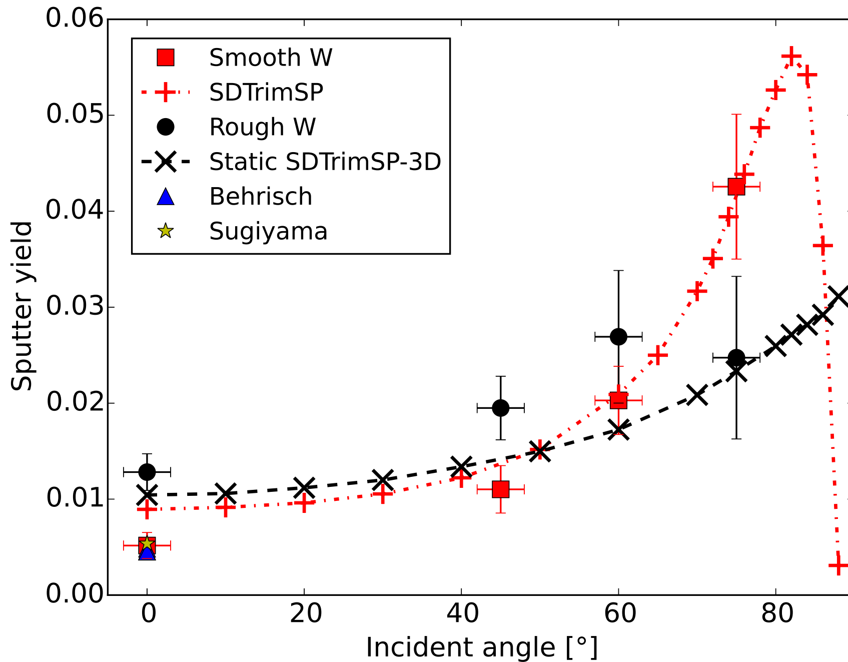

Figure 5.7: Sputter yields of a 6 keV D_3^+ beam (2 keV/D) on smooth (red squares) and rough (black circles) W thin films under incident angles of 0° (normal to surface), 45°, 60° and 75°. The smooth W data can be directly compared to 1D SDTrimSP simulations (red curve with + signs), while the rough W data may be compared with static SDTrimSP-3D simulations (black curve with × signs). Literature values from Behrisch and Eckstein [61] and Sugiyama [79] are included for comparison.

in [61], where no estimation of uncertainty is given.

The results from the smooth and rough W thin films are shown in Fig. 5.7. The experimentally determined sputter yield of the smooth W sample under 0° incidence displays a discrepancy of a factor of 2 with SDTrimSP. However, there is good agreement with the literature data for smooth W at normal incidence from [61, 79], indicating that this discrepancy may be an issue with SDTrimSP and not with the experiment. All other data points of the smooth W sputter yields are in agreement with the SDTrimSP calculations. Both experimental and simulated curves show a similar trend to what is observed with smooth Fe.

Contrary to the sputtering behaviour of the synthetic surfaces shown in [60], the static SDTrimSP-3D calculations of the rough W surface indicate an increase in the SY at normal (i.e., 0°) incidence. The reason for this different behaviour is likely the very different slope distributions of the rough W samples and the synthetic surface, when the latter is evaluated at roughness values comparable to those measured on the rough W samples. The simulations agree qualitatively with the sputter yields of the rough W thin films. As was the case with the smooth samples, the sputter yield of the rough samples increases as a function of the nominal incident angle within the measured range of 0° to 75°, though this increase is less pronounced than for the smooth samples and no sputter yield maximum is observed. SDTrimSP-3D correctly predicts

increased sputtering of the rough surfaces at low angles of incidence ($< 50°$) and decreased sputtering at high angles of incidence ($> 60°$) as compared to the smooth surfaces. However, SDTrimSP-3D deviates significantly from the measurements at 45° and 60° incidence, which could be in part a consequence of the limited resolution of the AFM scans when imaging sharp changes in the slope of the surface, as the scan is “smoothed” over the scanning tip radius of 10 nm.

Overall, the results for the smooth and rough W thin films present a similar trend to those observed by Küstner et al. in [41] and [76], where, respectively, the sputter yields of 2 keV D^+ on pyrolytic and isotropic graphite, and of 3 keV Be^+ on polished, roughened and unpolished Be were measured as a function of the angle of incidence and compared to SDTrimSP.

The mismatch of a factor of 2 between SDTrimSP and the smooth W sample at 0° incidence is not observed between SDTrimSP-3D and the rough W sample. A static SDTrimSP-3D simulation was performed with the surface morphology of the smooth W samples. The resulting sputter yields correctly reproduced the SDTrimSP results, presenting the same mismatch at 0° incidence. In order to assess whether this discrepancy is related to the chosen projectile or target, the sputter yields of 6 keV D_3^+ (2 keV/D) on Au and 6 keV He^+ on W were measured under normal incidence and compared to data from SDTrimSP simulations and literature [61, 74]. The measurements on Au have been previously described in section 4.3 and in [24]. All data are listed in Tab. 5.2.

As was the case with Fe, the experimental sputter yield of D on Au agrees reasonably well with SDTrimSP (experimental sputter yield is 14 % larger), and is slightly higher than other values from literature. The experimental sputter yield of He on W shows very good agreement with the data from literature, but is approximately 35 % smaller than the value given by SDTrimSP. While this mismatch is significant, it is substantially smaller than the factor of 2 discrepancy between experiments and simulation for D on smooth W. Similar discrepancies between sputter yields determined experimentally and calculated with SDTrimSP were also observed in literature data for W and other brittle materials (e.g., Mo, B, Be), both in magnitude and direction ($SY_{simulated} > SY_{experimental}$), regardless of impinging ion species, while the agreement is better for more ductile materials (Cu, Ni, Au) [61].

It is possible that the binary collision approximation, on which SDTrimSP is based, is less applicable for brittle materials than for ductile ones. However, this conjecture alone would fail to explain why said discrepancy is not observed in the case of rough W at normal incidence or smooth W at larger angles. One explanation for this lack of discrepancy could be that W exhibits grain-orientation-dependent sputtering and the predominant grain orientation, i.e., the texture of the two sets of samples, may be different. Recent experiments with W have indicated a strong (factor of 10) dependence of the sputter yield on the W grain orientation [80], and since the surface morphologies of the substrates on which the smooth and rough W thin films were deposited were different, it is conceivable that the two sets of samples exhibited preferential layer growth in different crystallographic orientations. Such effects require further investigation in the future.

Sputter yields	2 keV/D on Fe	2 keV/D on W	2 keV/D on Au	6 keV He on W
Experimental	0.0459 ± 0.0075	0.0052 ± 0.0014	0.0419 ± 0.002	0.0474 ± 0.0099
SDTrimSP	0.051	0.0128	0.037	0.063
Behrisch [61]	0.040	0.0048	0.031	0.045
Sugiyama [79]	0.040 ± 0.009	0.0054 ± 0.001		
Bay [74]			0.038	

Table 5.2: Sputter yields under normal incidence of 6 keV D_3^+ (2 keV/D) on smooth Fe and on smooth W and Au, and of 6 keV He^+ on W, determined experimentally (with uncertainty), via SDTrimSP simulations, or from literature (with uncertainty where available). The experimental data for D on Au was determined by mass-loss measurements and was previously presented in [24].

5.1.3 Summary

A series of smooth Fe and W and rough W thin films were eroded by ion bombardment with a 6 keV D_3^+ (2 keV/D) ion beam under well-defined laboratory conditions at SIESTA. The sputter yield under these conditions was measured as a function of the angle of incidence by determining the eroded layer thickness with 2 MeV He^+ RBS measurements performed before and after erosion. The surface morphology of the thin films was characterized with AFM before erosion. The ensuing sputter yield values are compared with SDTrimSP simulations, literature data at 0° incidence and, in the case of the rough thin films, static SDTrimSP-3D simulations based on the sample surface morphology from the AFM scans. This constitutes the first experimental benchmark of SDTrimSP-3D.

The sputter yield data from the smooth Fe thin films showed quantitative agreement with the SDTrimSP simulations in all cases. The sputter yields from the smooth W thin films agreed quantitatively with the SDTrimSP simulations in all cases except under normal incidence, where a discrepancy of a factor of two was observed. Since the experimentally-determined sputter yield under normal incidence agrees with the data from literature, it was concluded that this mismatch was due to an issue with SDTrimSP and not with the experiment. Reasons for this mismatch were proposed, consisting of a systematic error by SDTrimSP when calculating the sputter yield of brittle targets, as indicated by a review of the existing literature [61]. Another factor could be the effect of the grain orientation of the W films on the measured sputter yields, as recent investigations have shown that W may exhibit grain-orientation-dependent sputtering under certain exposure conditions [80]. This last point is currently the focus of ongoing investigations.

There is qualitative agreement between the sputter yields of the rough W thin films and the SDTrimSP-3D calculations. In this experimental benchmark, the code correctly predicted an increase of the sputter yield with the angle of incidence, increased sputtering of the rough surface relative to the smooth case at small angles of incidence and decreased sputtering compared with the smooth case at large angles of incidence. The aforementioned discrepancy in the sputter yield at normal incidence was not observed when comparing the rough samples with SDTrimSP-3D simulations.

The sputter yield trends observed in the experiments and simulations can be explained

qualitatively. If the local incident angle of the projectile on the surface is large, a large fraction of the projectile energy is deposited closer to the surface. This increases the probability for a surface atom to receive enough energy to be sputtered. However, at very large angles (close to grazing incidence), decreased sputtering is observed. In the case of rough surfaces, when the angle of incidence is close to the surface normal, the local incident angles (slopes) are steeper than the nominal angle of incidence, contributing to an increase in the local sputter yield. When the angle of incidence is large, there are contributions from both sides of the sputtering maximum: parts of the surface may exhibit increased sputtering due to steep local slopes, while others may exhibit decreased sputtering due to flat local slopes or grazing incidence. Additionally, in the case of rough samples there is a probability of re-deposition of a sputtered atom, contributing to lower net sputtering. However, in the case of the morphology of the rough W samples examined in this work, the effect of re-deposition seems to be less important than the effect of the angles of incidence.

5.2 Experimental validation of SDTrimSP-3D

As mentioned in section 3.6, the functionality of SDTrimSP was expanded to accommodate fully 3-dimensional targets [60]. Section 5.1 detailed a first benchmark of the code, which was performed employing a static target, i.e., the modelled target morphology and composition were not altered during the simulation. Based on the promising results from this first benchmark, an experiment using SIESTA was devised to validate SDTrimSP-3D when simulating fully dynamic 3-D targets. The approach used here was similar to the work of Bizyukov et al. on the validation of the 2-D version of the code, SDTrimSP-2D [59, 58]. In this case, samples with a pre-defined surface morphology were repeatedly exposed to an ion beam at SIESTA under well-defined exposure conditions in successive fluence steps. Between each exposure, the sample morphology was characterized and was compared to that of SDTrimSP-3D simulations of the samples bombarded under the same exposure conditions. As previously explained in 3.6, all simulations with SDTrimSP-3D shown in this work were not performed personally by the author, but were the result of collaborations with others.

The choice of sample morphology and the experimental procedure are explained in detail in section 5.2.1. The results of the comparison with SDTrimSP-3D are presented in sec. 5.2.2. Section 5.2.3 constitutes a summary of these results.

5.2.1 Characterization of morphology and sputtering of samples

For this experiment, textured samples with custom-tailored 3-D periodic pillars were employed, as this kind of sample provided numerous advantages. Chiefly, when exposed under the same conditions, the evolution of the sample morphology of the pillars is identical, allowing for several pillars to be characterized at each fluence step for improved statistics. Furthermore, destructive analysis methods (e.g., focused ion beam milling) can be used on the individual pillars at each fluence step. As previously mentioned in section 3.6, the size of the simulated volume plays

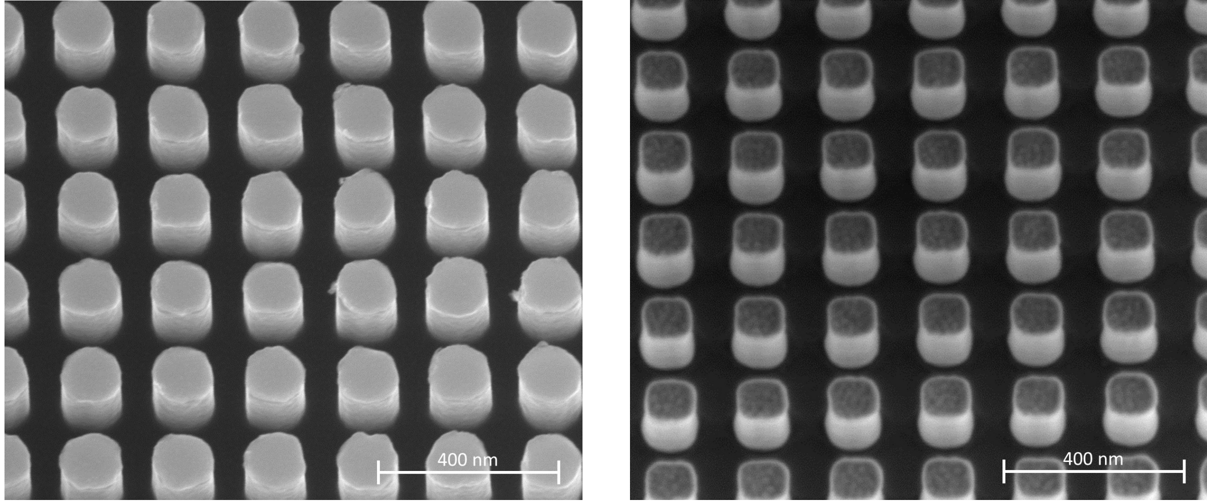

Figure 5.8: SEM images of Si (left) and Ta (right) columnar structures. The columns are roughly 100 nm in diameter, 200 nm in height and spaced 200 nm apart.

a major role in the computation time of SDTrimSP-3D. Therefore, surface morphologies with features in the range of tens or hundreds of nm are preferred to features in the μm range. The minimum size of the features is limited by the resolution of the imaging method. Based on this, it was decided to characterize the samples via SEM imaging with the use of focused-ion-beam cross-sections, as this method allows accurate imaging of the structure morphology with a lateral and height resolution of nanometers.

The samples consist of a $10 \times 10\,\mathrm{mm}^2$ square array of columns with an approximate diameter of 100 nm and a height of 200 nm, spaced in 200 nm intervals. Two kinds of samples were procured: four samples with Si columns on a Si substrate, produced by NILT[2], to benchmark SDTrimSP-3D with previous versions, and one sample with Ta columns on a Si substrate, produced by MaTecK[3], with Ta serving as a surrogate for W. The Si samples consisted of cylindrical columns. The columns of the Ta sample were slightly rounded square pillars. SEM images of Si and Ta columns are shown in Fig. 5.8.

5 keV Ar^+ was chosen as the impinging ion species and energy in SIESTA, as this would lead to a high sputter yield (for instance, SY of 5 keV D on Si is 0.012, while SY of 5 keV Ar on Si is 1.02 [61]). High sputter yields are preferred, since small total fluences to the target would be required to produce a high level or erosion, therefore reducing computation time. Three exposure scenarios were devised: ion bombardment under normal incidence, bombardment under 45° incidence with the columnar structures parallel to the projection of the ion beam on the target surface, and bombardment under 45° incidence with the columnar structures rotated 15° relative to the projection of the ion beam on the target surface. These three cases are respectively referred to as (0°,0°), (45°,0°) and (45°,15°), and are displayed schematically in Fig. 5.9. The (0°,0°) scenario is the most simple case, since cylindrically symmetric erosion of the columns is expected. In the (45°,0°) scenario asymmetric erosion is expected, since one side of the columns

[2]Trademark of NIL Technology ApS
[3]Trademark of MaTecK Material-Technologie & Kristalle GmbH

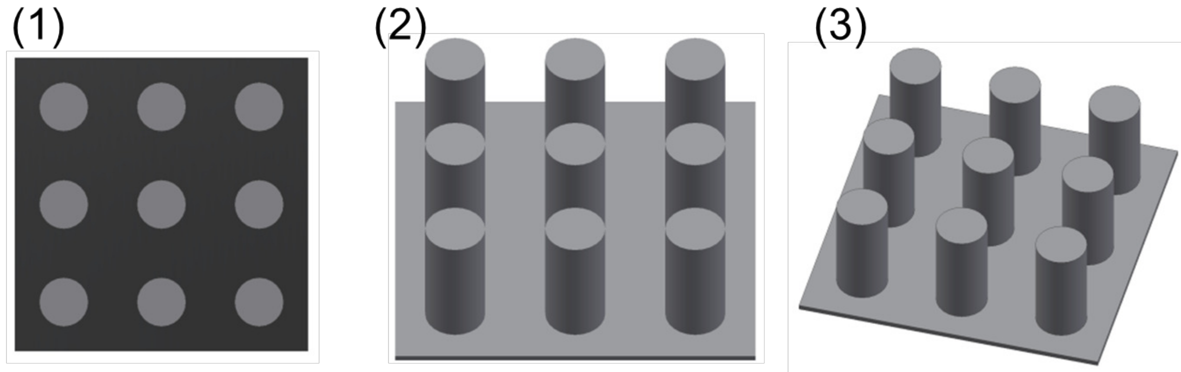

Figure 5.9: Schematic representation of the 3 exposure scenarios for the Si and Ta columnar structures. 1: (0°,0°), 2: (45°,0°) and 3: (45°,15°). The view of the structures in these images is along the impinging beam axis.

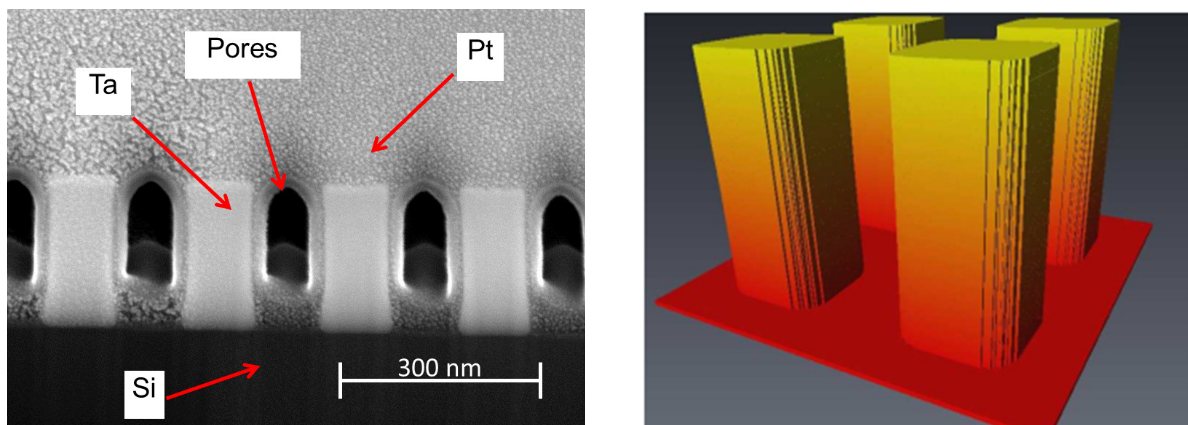

Figure 5.10: SEM image of Ta column cross-section (left) and 3-D model of several columns (right). In the left image, the Ta columns, Si substrate, pores and protective Pt cover layer are labeled.

will be screened from the ion beam by the preceding column. In this case, erosion along the midplane of the columns should be 2-dimensional. The (45°,15°) scenario is the most complex. As in the (45°,0°) case, each column partially screens the column downstream from it, but the screening is in this case localized to one edge of the sample, so the erosion behaviour is fully 3-dimensional. All three scenarios were investigated with the Si samples. The Ta sample was exposed exclusively under scenario (45°,15°).

The samples were characterized prior to exposure at SIESTA via SEM imaging with FIB cross-section milling. Measurements were taken of the sample geometry in these images and were employed to build 3-D models of the Si and Ta sample morphologies, which were used for the SDTrimSP-3D simulations in this work. No parameters were fitted in the simulations. Fig. 5.10 shows an SEM cross-section image of the Ta columns prior to exposure and a 3-D view of the model geometry. As explained in chapter 3, a protective cover layer is applied before FIB milling. In some instances, the cover layer did not correctly fill the space between columns, leaving pores. Such pores are visible in the SEM image of the Ta columns in Fig. 5.10.

The samples were exposed at SIESTA to a maximum final fluence of $2.3 \times 10^{21}\,\mathrm{Ar\,m^{-2}}$, as the SDTrimSP-3D simulations performed prior to exposure indicated a height reduction of the columnar structures of at least 50 % when bombarded to said fluence. Based on this, it was decided to perform the first fluence step to a fluence of approximately $7 \times 10^{20}\,\mathrm{Ar\,m^{-2}}$.

It was determined that, despite beam sweeping (described in section 4.2.3), the 5 keV Ar^+ beam footprint at the target was not homogeneous, due to strong focusing of the beam with the quadrupole doublet lens that was required to achieve sufficiently high flux densities. Consequently, different fluences were achieved at different positions on the target. The local ion flux density at each lateral position of the exposed samples was determined by exposing Au thin films of 50 nm thickness on a Si substrate to the Ar^+ beam under the same exposure conditions directly before exposing the Si and Ta samples. The lateral variation of the layer thickness of the Au thin films was measured by RBS before and after exposure. The local ion flux density was deduced from the eroded layer thickness at each position and the nominal fluence.

Each sample was exposed twice. After each exposure, the sample morphology was characterized at two lateral positions, corresponding to different accumulated fluences. Therefore, each sample was imaged at four fluences, ranging approximately from $3 \times 10^{20}\,\mathrm{Ar\,m^{-2}}$ to $2.3 \times 10^{21}\,\mathrm{Ar\,m^{-2}}$. In all cases, cross-sections were performed along the grid directions of the columns. For the samples exposed under the (45°,15°) scenario, additional cross-sections were performed in directions parallel and normal to the ion beam projection. These directions are illustrated in an image of the Ta sample in figure 5.11.

5.2.2 Experimental results and comparison to SDTrimSP-3D

In this section, for brevity, results of two samples are shown: the Si sample exposed under the (0°,0°) scenario and the Ta sample exposed under the (45°,15°) scenario. The results of the other two samples - the Si samples exposed under (45°,0°) and (45°,15°) - are not displayed here but show good agreement with the SDTrimSP-3D model.

Figure 5.12 shows the simulated 3-D sample morphology of the Ta columns after several fluence steps, exposed under the (45°,15°) scenario. In the 3-D model, the ion beam impinges from the top right. It can be seen in the images how one column is partly screened by the column preceding it. On the images on the right, re-deposition can be observed at the sides of the column and at its base, where the composition of the sample is a mixture of Ta and Si (color scale represents Si concentration).

Tilted SEM images and cross-sections of the Si (0°,0°) sample are shown in Figs. 5.13 and 5.14 at various fluence steps, showing the progressive erosion of the Si columns. In Fig. 5.14, the imaged cross-sections are compared to the simulated target structure at the same fluence steps (solid red line), indicating a very good agreement between experiment and simulation, thereby proving the validity of SDTrimSP-3D in this scenario.

In figure 5.15, a birds-eye SEM image of the Ta sample eroded to a fluence of $7 \times 10^{20}\,\mathrm{Ar\,m^{-2}}$ is shown. The column morphology modelled with SDTrimSP-3D for the same fluence has been overlaid, showing very good agreement with the experimental data. The modelled geometry is

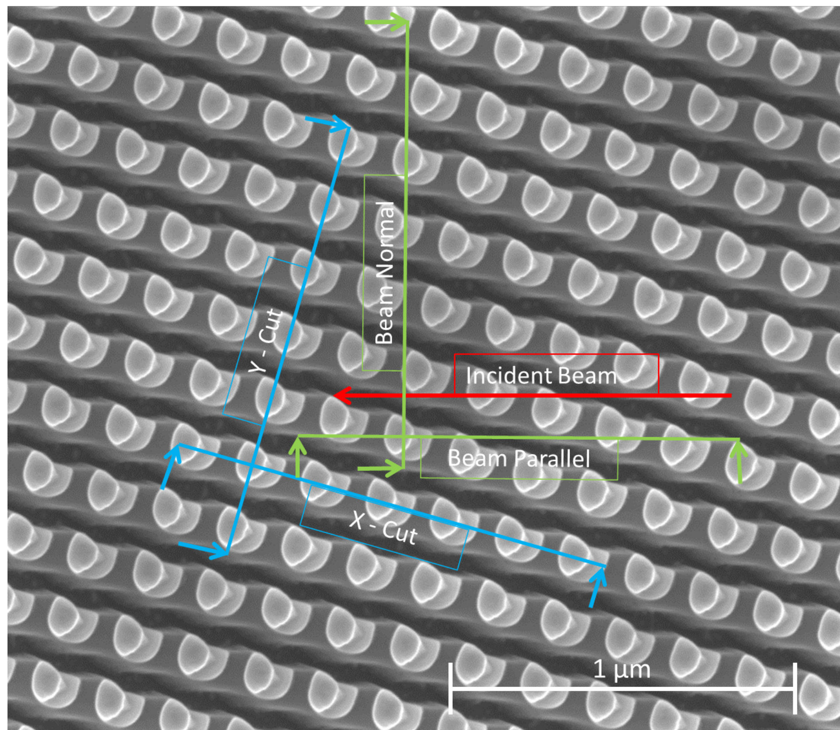

Figure 5.11: FIB cut directions in samples eroded under the (45°,15°) scenario. The blue arrows (X-cut and Y-cut) indicate the directions of the grid of columns. The green arrows indicate the directions parallel and normal to the ion beam. The red arrow indicates the projected direction of the incident ion beam.

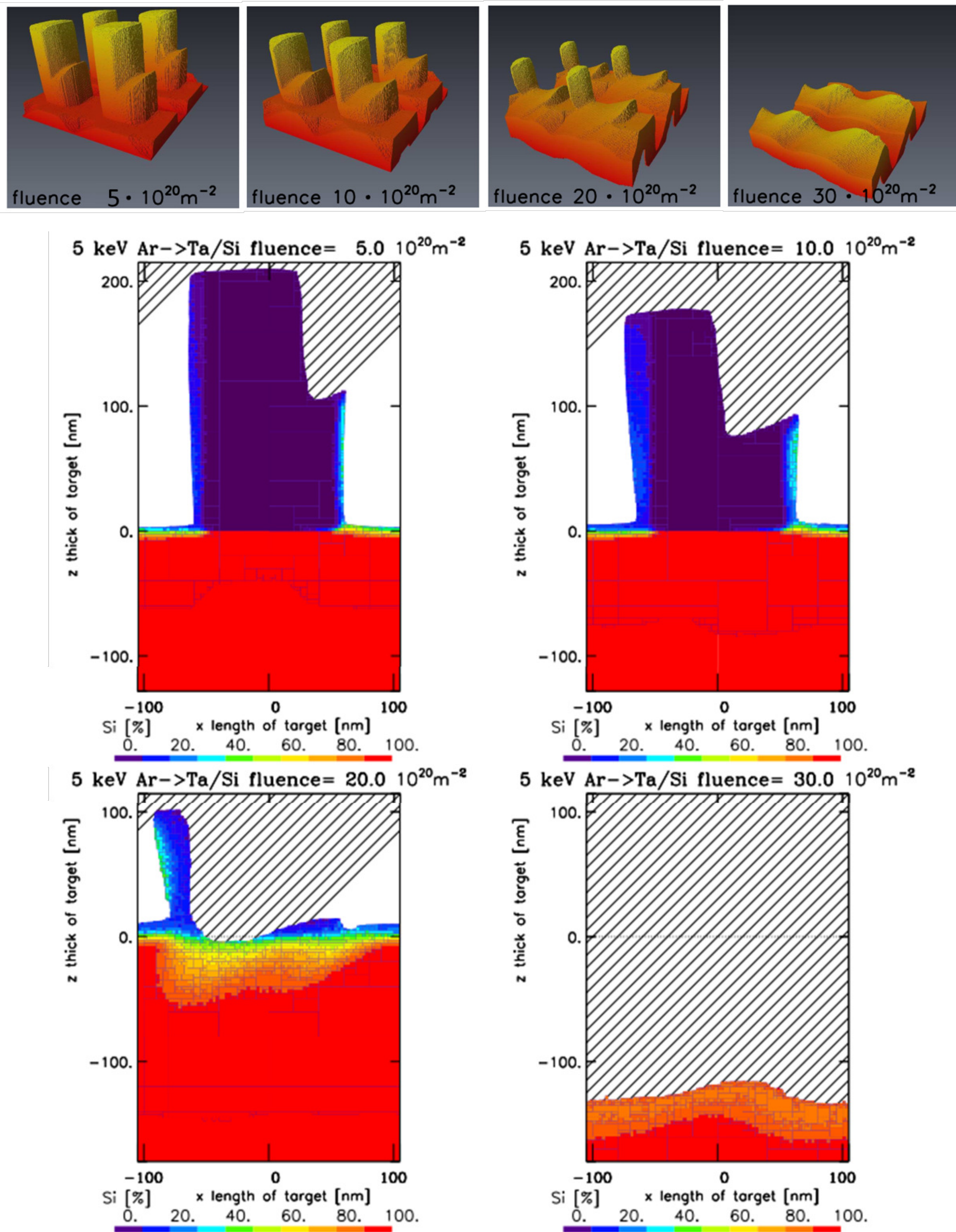

Figure 5.12: 3-D model and cross-sections of Ta columns after several fluence steps, simulated with SDTrimSP-3D. The color scale of the top images is arbitrary. In the lower images, it indicates Si concentration. Initially, part of the column is screened from the ion beam by the preceding column. With increasing fluence, the top and the front (i.e., right side in the cross-section) of the column is eroded, with part of the eroded Ta re-depositing on top of the Si substrate. Si from the substrate is also eroded and partly re-deposited, and is responsible for the structure growth observed on the left (i.e., back) part of the column.

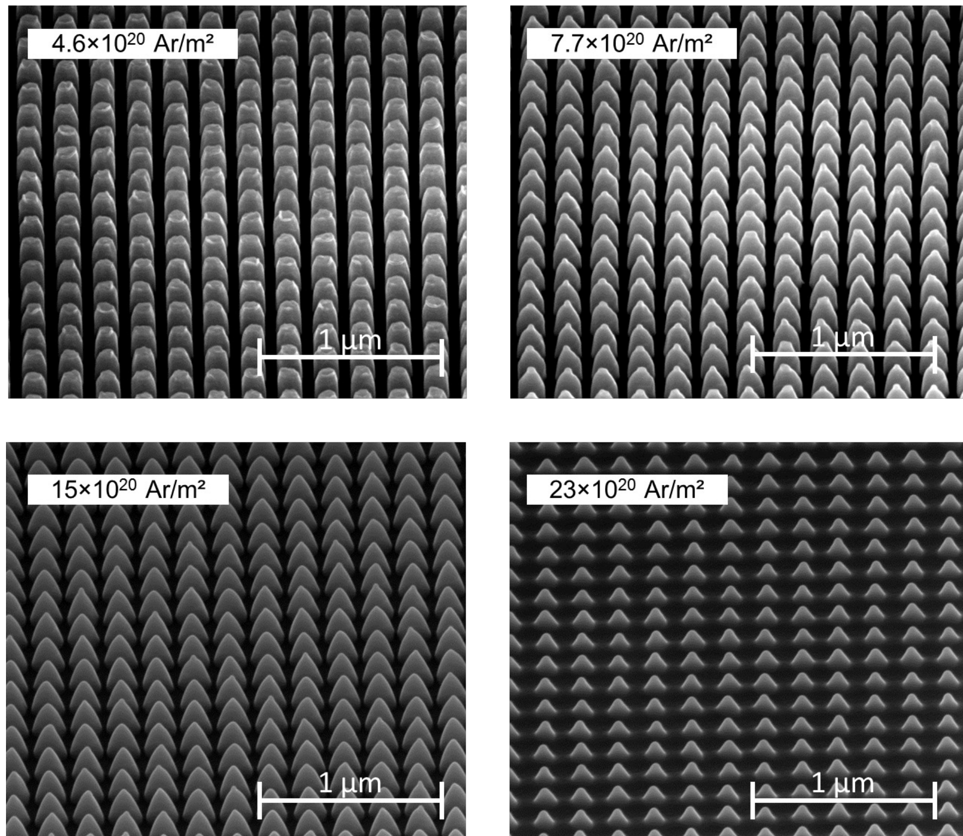

Figure 5.13: Tilted SEM images of the Si sample exposed under the (0°,0°) scenario, imaged a various fluence steps. The progressive erosion of the columns is clearly visible. At the largest fluence, the columns have been almost completely eroded.

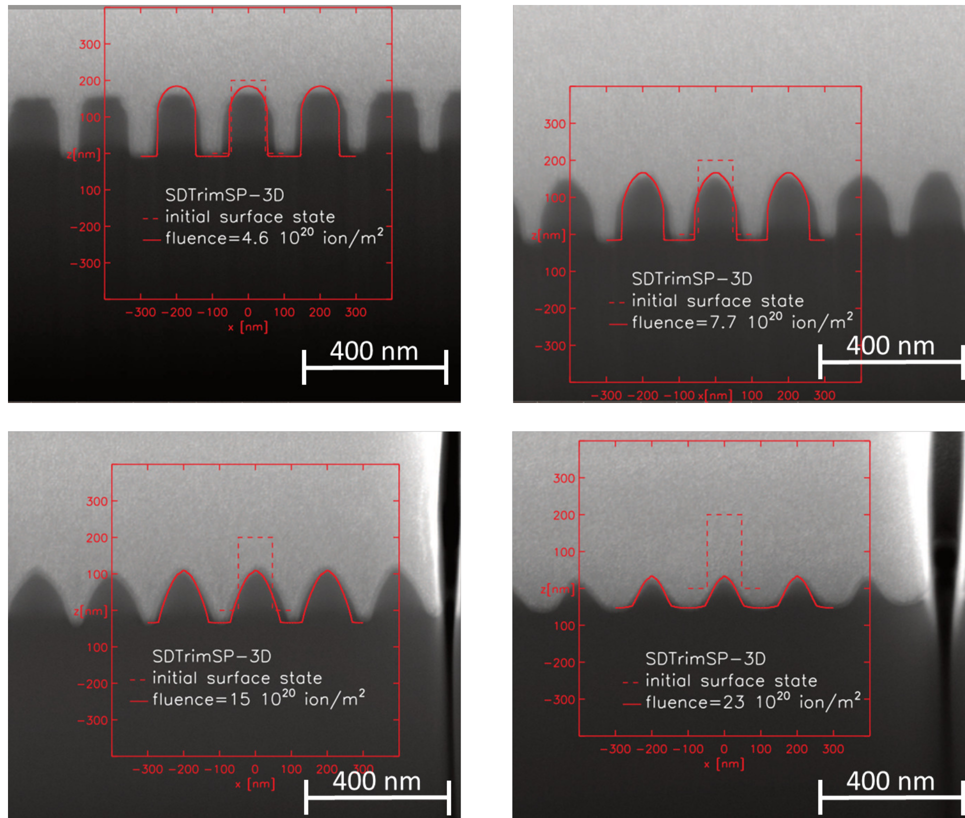

Figure 5.14: FIB-enabled cross-sections of the Si sample exposed under the (0°,0°) scenario, imaged a various fluence steps. The solid red line denotes the cross-section of the target morphology generated by SDTrimSP-3D at the same fluence steps. The dashed red line indicates the cross-section of the initial target model used in the simulation.

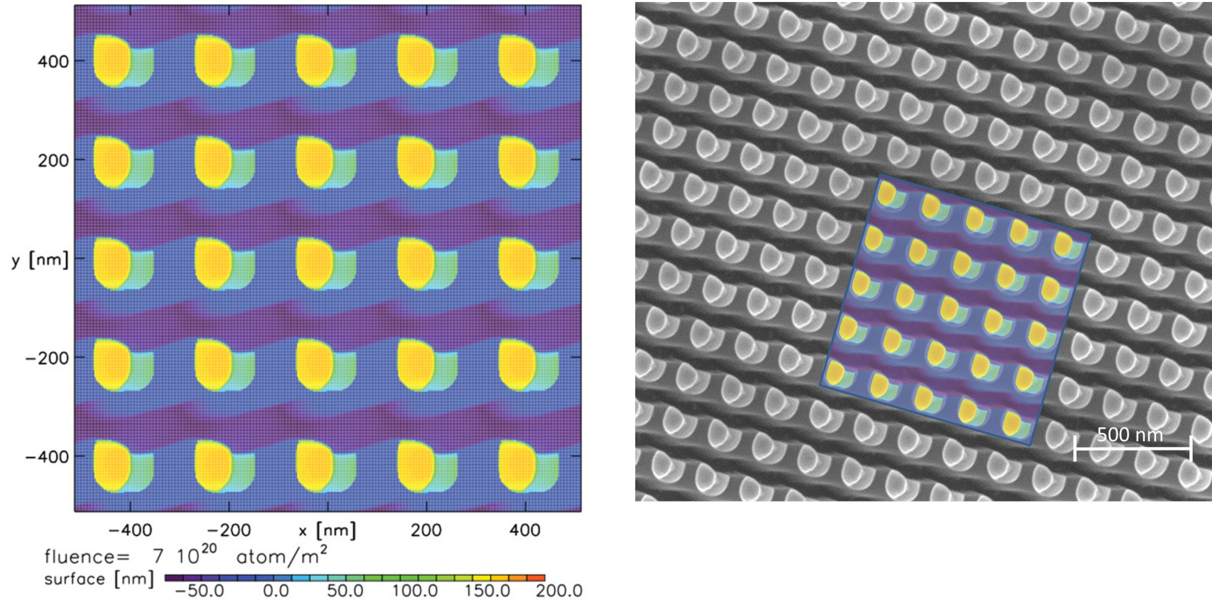

Figure 5.15: Left: SDTrimSP-3D model of Ta sample exposed to a fluence of $7 \times 10^{20}\,\mathrm{Ar\,m^{-2}}$. Right: Birds-eye view of Ta sample exposed to the same fluence, on which the modelled geometry has been overlaid, showing good agreement with the experimental data.

also displayed separately with its corresponding height gradient.

Similarly to Fig. 5.13, figure 5.16 displays tilted SEM images of the Ta sample after exposure to various fluence steps under the (45°,15°) scenario, showing progressive erosion of the columns. Similarly to Fig. 5.14, in Figs. 5.17 and 5.18, FIB-enabled cross-sections of the Ta columns are shown, imaged at various fluence steps in the orientations explained in Fig. 5.11. The target outline from SDTrimSP-3D has been overlaid. In some parts of the images (for example in the "Beam Parallel" and "Beam Normal" images), some of the Si or Ta pillars appear hazy. This is typically an artefact of the SEM imaging technique: the image is formed by secondary electrons emitted at a depth of up to a few nanometers from the imaged surface. Consequently, the SEM image of the cross-section includes features that may appear blurry, but which are in fact situated at some depth inside the material. These structures do not appear in the representation of the SDTrimSP-3D model, since only the structure at the cross-section is outlined. There is generally very good agreement at each fluence step between the experimental data and the simulation. SDTrimSP-3D correctly predicts the morphology of both the Ta columns and the Si substrate for all fluence steps.

5.2.3 Summary of the SDTrimSP-3D validation experiments

The goal of this experiment was to provide an accurate validation of SDTrimSP-3D, an expansion of the pre-existing SDTrimSP code which accommodates fully 3-D target geometries and is capable of dynamically altering the target's geometry and composition [60]. To this end, samples with a periodic 3-D texture were acquired, consisting of a $10 \times 10\,\mathrm{mm^2}$ area with columnar structures of either Si or Ta with an approximate height of 200 nm, diameter of 100 nm and

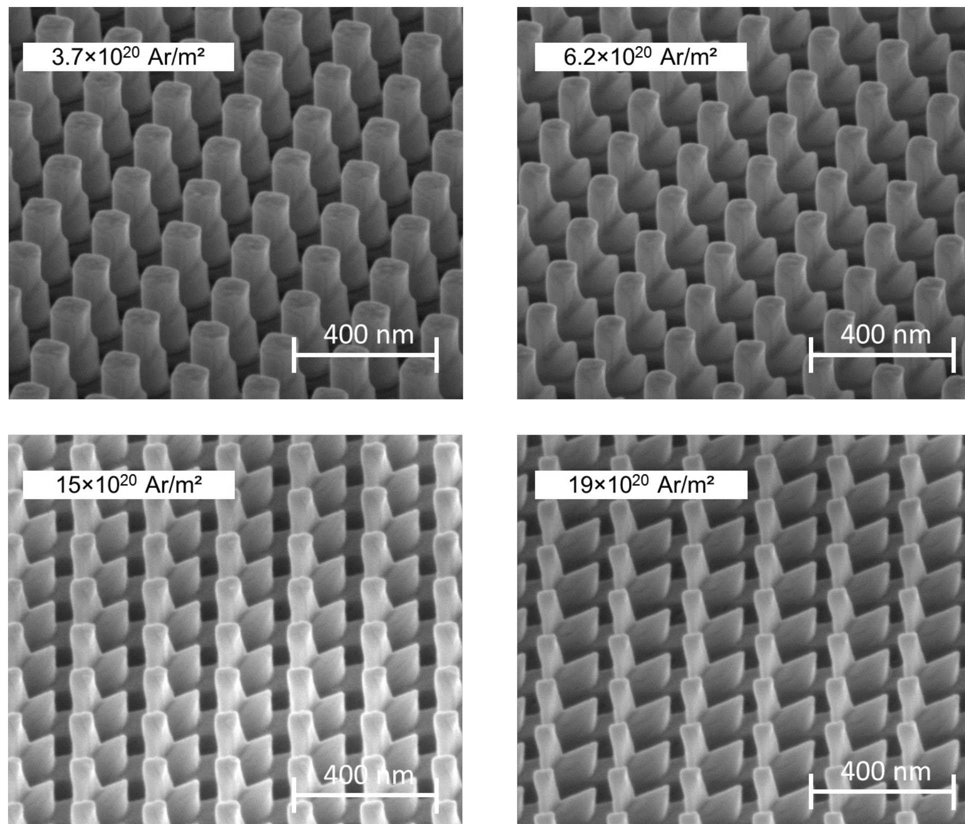

Figure 5.16: Tilted SEM images of the Ta sample exposed under the (45°,15°) scenario, imaged a various fluence steps. As shown in Fig. 5.13 for a Si sample, the progressive erosion of the columns can be clearly observed.

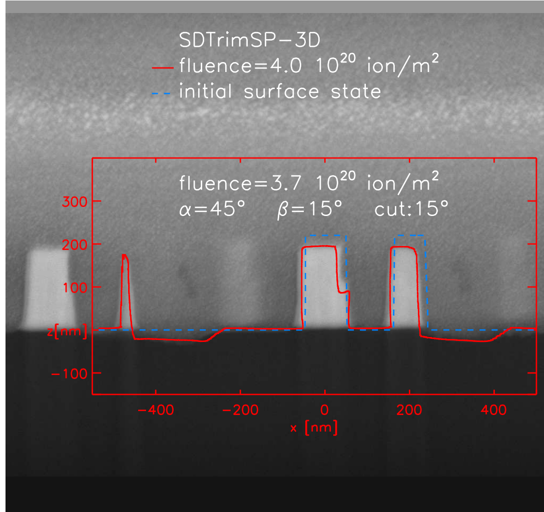

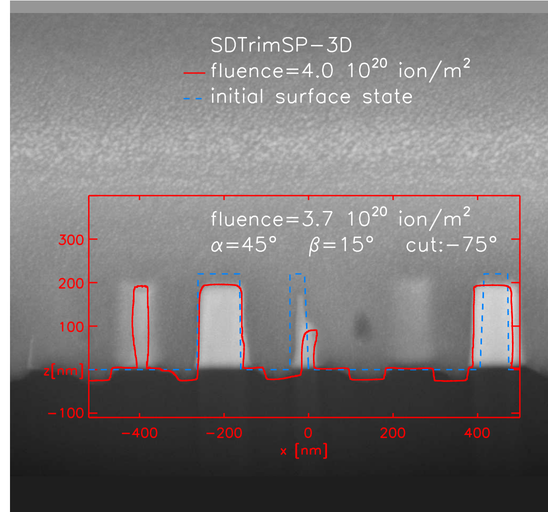

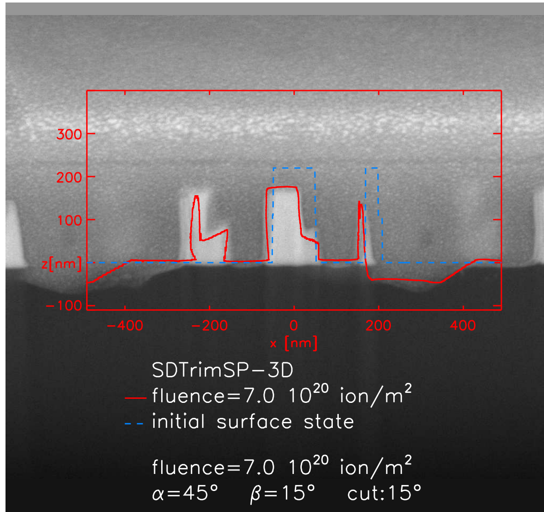

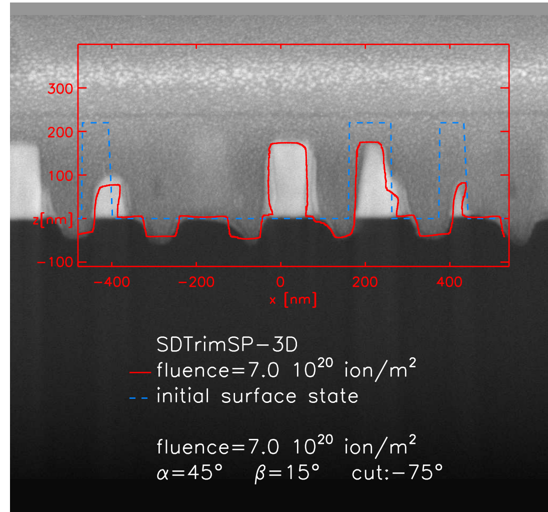

Figure 5.17: FIB-enabled cross-sections of the Ta sample exposed under the (45°,15°) scenario, imaged at fluences of $3.7 \times 10^{20}\,\mathrm{Ar\,m^{-2}}$ and $7 \times 10^{20}\,\mathrm{Ar\,m^{-2}}$. The solid red line denotes the cross-section of the target morphology generated by SDTrimSP-3D at the same fluence steps, rounded to the nearest $1 \times 10^{20}\,\mathrm{Ar\,m^{-2}}$ (i.e., $4 \times 10^{20}\,\mathrm{Ar\,m^{-2}}$ instead of $3.7 \times 10^{20}\,\mathrm{Ar\,m^{-2}}$). "Cut: 15°" denotes a cross-section parallel to the beam. "Cut: -75°" denotes a cross-section normal to the beam. The dashed blue line indicates the cross-section of the initial target model used in the simulation.

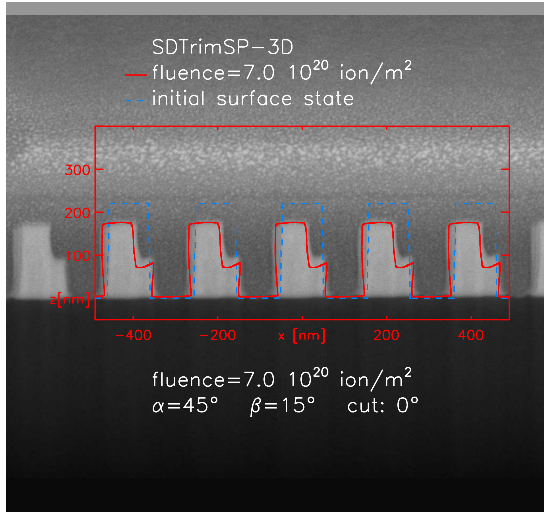

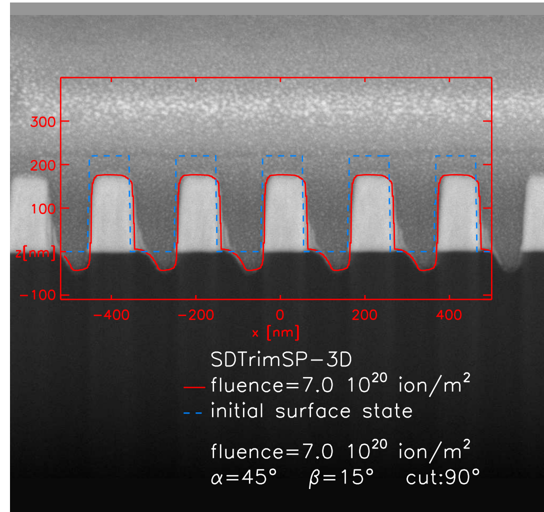

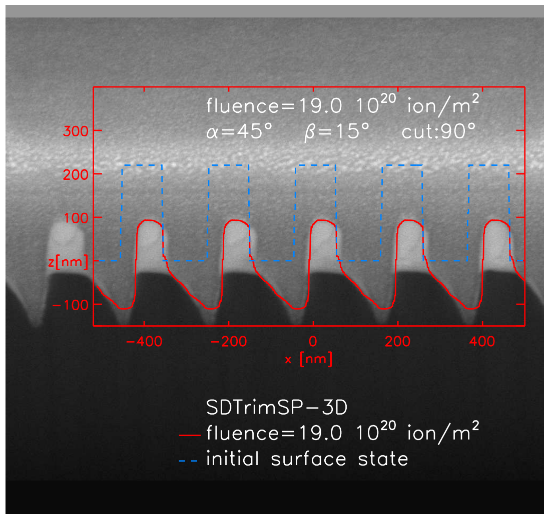

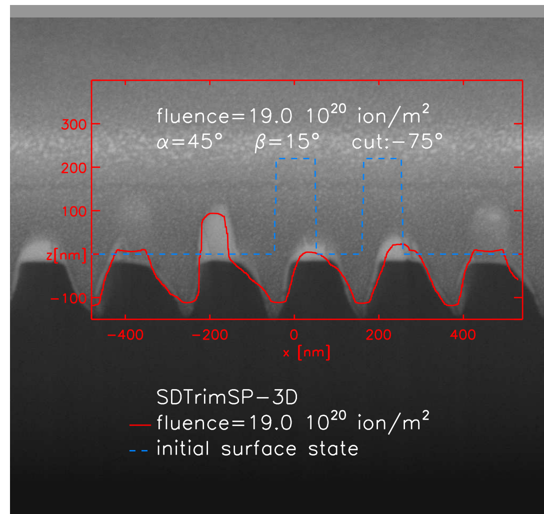

Figure 5.18: FIB-enabled cross-sections of the Ta sample exposed under the (45°,15°) scenario, imaged at fluences of $7 \times 10^{20}\,\mathrm{Ar\,m^{-2}}$ and $19 \times 10^{20}\,\mathrm{Ar\,m^{-2}}$. The solid red line denotes the cross-section of the target morphology generated by SDTrimSP-3D at the same fluence steps. “Cut: 0°” and “90°” are cross-sections along and across the rows of columns, respectively. “Cut: -75°” denotes a cross-section normal to the ion beam. The dashed blue line indicates the cross-section of the initial target model used in the simulation.

spacing of 200 nm, set out in a square array. The samples were characterized via SEM imaging on FIB-enabled cross-sections and the sample geometry was used as a basis for simulations with SDTrimSP-3D. The samples were exposed to a 5 keV Ar^+ beam at SIESTA to various fluence steps and the sample morphology was subsequently characterized at various positions after each fluence step. Several exposure geometries were investigated. Four sets of images corresponding each to a different impinging ion fluence were acquired for each sample. Cross-section images of the samples from each set were compared to the sample morphology modelled with SDTrimSP-3D. In this work, comparisons between SDTrimSP-3D and experimental data were shown for Si columns on a Si substrate exposed under normal incidence - the (0°,0°) scenario - and Ta columns on a Si substrate exposed under 45° incidence and 15° rotation - the (45°,15°) scenario.

In all cases the modelled target morphologies agree very well with the experimental data at all fluence steps. In the case of the Ta sample, SDTrimSP-3D is able to correctly model the geometry of both the Ta columns and the Si substrate, thereby validating its use for fully 3-D targets of variable composition exposed under geometrically complex scenarios. The code is ready for use to tackle other unresolved questions where dynamically-evolving, complex target geometries may play a role. An example of such a case is the erosion of EUROFER and other RAFM steels under deuterium bombardment, where the sputtering behaviour of the material is simultaneously affected by W-surface enrichment as well as the formation of a characteristic surface morphology in the nm-range. This case will be the focus of the following section.

5.3 Sputtering behaviour of EUROFER97 under deuterium bombardment

EUROFER is a Reduced Activation Ferritic Martensitic (RAFM) steel developed by the European Union fusion materials community as structural material for use in fusion applications. It is optimized for low neutron activation and good mechanical properties. Additionally EUROFER displays low H solubility, ease of manufacturing and low cost (compared to W). Similarly to other RAFM steels (e.g., RUSFER [81]), EUROFER is composed of Fe, Cr ($\sim$ 9 at.% for EUROFER), C ($\sim$ 0.45 at.%), Mn ($\sim$ 0.4 at.%), W ($\sim$ 0.33 at.%), V ($\sim$ 0.2 at.%), Ta ($\sim$ 0.04 at.%) and small amounts of other alloying elements [82]. EUROFER or other RAFM steels are foreseen as structural material in DEMO. Their use is also planned for the breeding-blanket (i.e., first wall elements) [82], where they would be clad with W to prevent erosion. W cladding is technologically challenging and could prove expensive. Therefore, it would be technically and economically advantageous to forego the W cladding in areas where the erosion of pure EUROFER would be sufficiently low. Such areas could be parts of the first wall which have no direct plasma contact and are exposed to a flux of neutral particles with a typical impinging energy in the range of several hundred eV, though a small fraction of the impinging particles may have keV energy [22, 82]. Consequently, erosion of EUROFER and other RAFM steels due to sputtering must be investigated. The following work focuses exclusively on EUROFER under one specific exposure scenario.

If EUROFER is bombarded with D, it exhibits W (and, more modestly, Ta) surface enrichment which can be attributed to preferential sputtering (explained in chapter 3) [83, 84, 85]. Additionally, during bombardment EUROFER develops a distinct, heterogeneous surface morphology. The morphology of the surface is dependent on the sample temperature during exposure, the incident particle energy and the accumulated fluence [83, 84, 86]. A progressive reduction in the sputter yield has been confirmed experimentally, which would be consistent with the progressive formation of a surface layer rich in W due to preferential sputtering [83]. It is worth noting that the impact of the surface morphology of EUROFER on the sputter yield has not yet been investigated.

While simulations with SDTrimSP do predict W (and Ta) surface enrichment, when simulating the exposure, the evolution of the sputter yield of EUROFER does not agree quantitatively with the experimental data [83]. The evolution of the enriched surface layer stretches the limit of the physics model of the code, predicting, for example, the formation of a 90 at.% W layer of a thickness below 0.05 nm, i.e., $1/5^{th}$ of an atomic monolayer of W, when exposing EUROFER to 200 eV D to a fluence of $5 \times 10^{23}\,\mathrm{D\,m^{-2}}$ (shown in Fig. 2.9) [83]. Furthermore, presently, due to the complex structure and composition of the material, the validity of dynamic SDTrimSP calculations of the bombardment of D atoms on EUROFER is limited, as the target composition, both initially and during bombardment, is very different from a homogeneous mixture of its constituents.

In this work, it was attempted to disentangle the impact on the sputter yield of D on EUROFER of surface morphology and of W and Ta surface enrichment by studying each effect separately. The surface morphology of EUROFER extracted from SEM images was employed to provide a basis for SDTrimSP-3D simulations. These simulations were used to quantify the effect of the surface morphology on the sputter yield. The effect of the W and Ta surface enrichment on the sputter yield was quantified with 1-D SDTrimSP simulations with an enriched layer consistent with sputter-XPS measurements (explained in section 3.3). The corresponding reduction of the sputter yield due to these two effects is compared to experimental data determined in this work and to data from literature. Additionally, EBSD was performed in a first attempt to identify grain-dependent effects. This study constitutes a first of its kind, as it has hitherto not been attempted to investigate the impact of surface morphology on the sputtering behaviour of EUROFER. As such, it focuses on a single exposure scenario and offers limited statistics. Follow-up studies must be performed to further cement the findings shown here.

5.3.1 Experimental methodology and simulations

EUROFER samples were cut from a plate of EUROFER97 [82], each measuring $12 \times 15 \times 0.7\,\mathrm{mm^3}$. The samples were polished to a mirror finish and the surface morphology was characterized prior to exposure by SEM and AFM. A SEM image of EUROFER before exposure is shown in Fig. 5.19. The samples were determined to be sufficiently smooth, following the criteria discussed in section 5.1, with $R_{RMS} \simeq 2\,\mathrm{nm}$ and a distribution of local slopes lower than 15° at the 95th percentile. FIB markers were placed at several points on one sample to enable imaging

of the same location before and after exposure. Additionally, FIB coatings were placed at several locations. These localized coatings protected the underlying area from ion bombardment at SIESTA and allowed the identification of the position of the original surface after erosion. EBSD and EDX were also performed at pre-defined locations, thereby obtaining information on the grain orientation and initial distribution of W on the sample surface. It was suspected that degassing of the sample during exposure at SIESTA could lead to a change in the weight of the sample, thereby confounding the weight-loss measurements. To accurately measure the weight-loss due only to erosion, the sample was annealed in SIESTA at $\approx$ 600 K for 3 hours prior to exposure, thereby allowing it to degas. The sample was subsequently exposed to a 200 eV D beam (600 eV D_3^+) under normal incidence to a final fluence of $1.14 \times 10^{24}\,\mathrm{D\,m^{-2}}$ in three fluence steps. The temperature of the sample during exposure was $\approx$ 300 K. After the final erosion step, the sample was stored in a desiccator and the sample holder was stored in air. The sample with the sample holder was weighed in- and ex-situ before and after degassing and before and after each exposure, as detailed in the list below. Additionally, the sample with sample holder was again weighed in- and ex-situ 3 days after the final fluence step. The numbers 0-5 correspond to weight measurements. The letters D and E1-E3 respectively denote degassing and successive erosion steps.

0	In-situ weight measurement
0	Ex-situ weight measurement
D	Degassing (3 hours, 600 K)
1	In-situ weight measurement
1	Ex-situ weight measurement
1a	In-situ weight measurement
E1	Erosion step 1 to fluence of $0.48 \times 10^{24}\,\mathrm{D\,m^{-2}}$
2	In-situ weight measurement
2	Ex-situ weight measurement
E2	Erosion step 2 to accumulated fluence of $0.88 \times 10^{24}\,\mathrm{D\,m^{-2}}$
3	In-situ weight measurement
3	Ex-situ weight measurement
E3	Erosion step 3 to accumulated fluence of $1.14 \times 10^{24}\,\mathrm{D\,m^{-2}}$
4	In-situ weight measurement
4	Ex-situ weight measurement
4a	In-situ weight measurement
5	Ex-situ weight measurement
5	In-situ weight measurement

It is worth noting that between 1-1a and 4-4a, no sample modification occurred other than exposing the sample to air for the duration of the ex-situ measurement (approximately 1 hour). Between 4 and 5, the sample was demounted from the sample holder and stored in a desiccator for 3 days. The sample holder was exposed to air. The sample was remounted on the sample holder for the weight measurements labeled 5. By comparing these data points, the effect on the

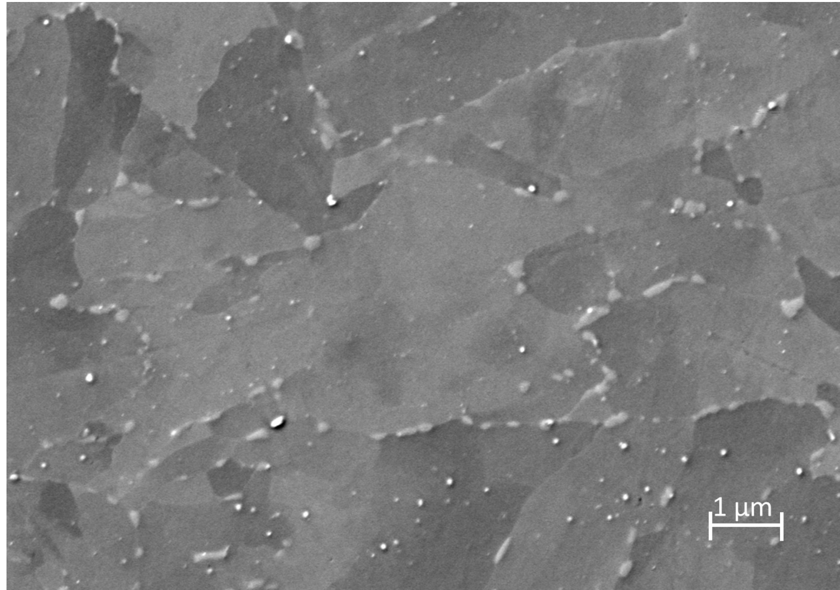

Figure 5.19: EUROFER sample imaged with SEM before exposure at SIESTA. EDX scans of the sample reveal that the small bright areas on the image correspond to segregations, predominantly carbides. In EUROFER, a significant fraction of the Cr, W and Ta is stored in segregations appearing preferentially near the grain-boundaries.

weight measurements of exposing the sample and sample holder to air could be quantified. The quasi-differential sputter yield was determined: the in- and ex-situ weight-loss measurements between 1-2, 2-3 and 3-4 were, respectively, divided by the additional fluence between 1-2, 2-3 and 3-4. Therefore, the calculated values correspond to the fluence-dependent sputter yields of EUROFER averaged over their respective fluence steps.

After the final exposure, the sample surface was again characterized with SEM, revealing two main types of morphologies: relatively flat, smooth areas much like the surface prior to exposure, and areas with spiked structures, both shown in Fig. 5.20 and Fig. 5.24. An SEM image of EUROFER before exposure is shown for comparison (Fig. 5.19). The spikes have a typical height, width and spacing of 25 nm, 17.5 nm and 24 nm, respectively, as measured on tilted SEM images (Fig. 5.20). AFM scans were attempted. However, the surface morphology of the spiked structures could not be correctly resolved. Due to the small size of the spikes relative to the scanning tip, the spikes were "smoothed" over the tip radius and the scanning tip could not probe the valleys between spikes. The absolute thickness of the eroded layer was calculated for the spiked morphology with the aid of FIB cross-sections of local FIB coatings deposited before the first erosion step (Fig. 5.23), and was determined to be approximately 120 nm. The eroded layer thickness was measured as the height difference between the section protected by the FIB coating (not eroded) and the neighboring eroded area, which featured the spiked surface morphology. Stereophotogrammetry was applied to SEM images taken normal to the surface and taken at an angle (Fig. 5.21) to determine the thickness of the eroded layer for the smooth morphology relative to the spiked morphology. It was determined that the smooth surface morphology was eroded approximately 90 nm less than the rough surface morphology.

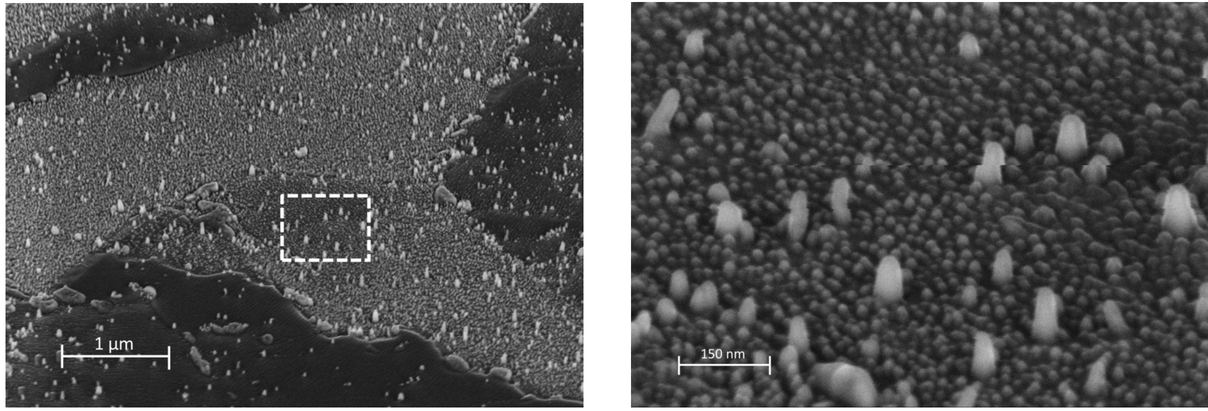

Figure 5.20: Left: Tilted SEM image of spiked and smooth surface morphologies of EUROFER exposed to a total D fluence of of $1.14 \times 10^{24}\,\mathrm{D\,m^{-2}}$ at 200 eV/D and 300 K. Right: Close-up of the area inside the dashed white square in the left image. The larger pillars are segregations, mainly carbides.

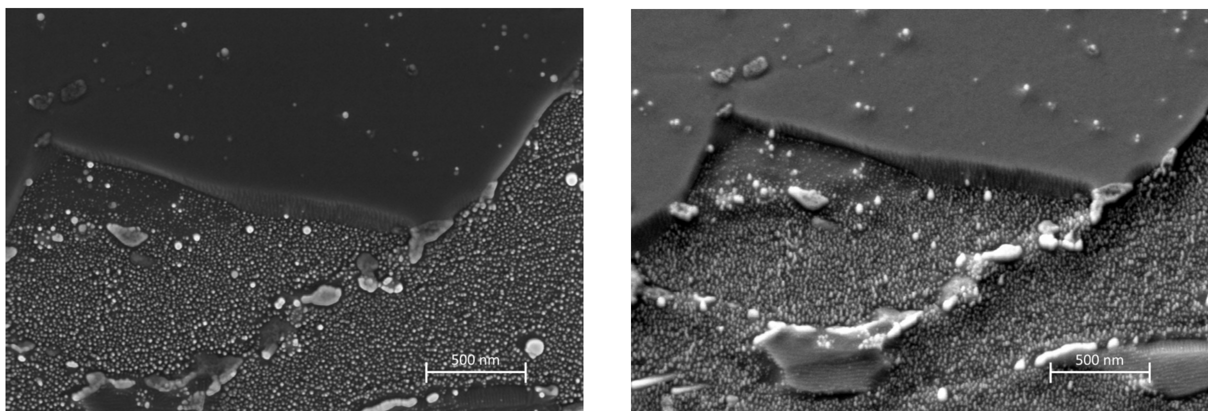

Figure 5.21: Left: SEM image of spiked and smooth surface morphologies of exposed EUROFER. Right: Tilted SEM image of the same area, indicating via stereophotogrammetry that the smooth surface was eroded 90 nm less than the spiked area. The bright particles correspond to segregations, chiefly in the form of carbides, as evidenced by EDX scans performed on similar structures.

The eroded layer thickness of the areas featuring a smooth morphology was used to quantify the sputter yield of these areas.

With the aid of the FIB markers, EDX was performed on the same locations as prior to exposure at SIESTA, thereby allowing a direct comparison of the W distribution near the surface. Sputter-XPS measurements of the sample were performed post-exposure to quantify the W, Ta and Cr concentration within the first 20 nm of depth.

Simulations to quantify the effect of the surface morphology on the sputter yield were performed by modelling the sputtering behaviour of the smooth surface with SDTrimSP (1-D) and that of the spiked surface with SDTrimSP-3D (shown in Fig. 5.22). In all simulations, a simplified, homogeneous EUROFER composition was used, consisting of 99.67 at.% Fe and 0.33 at.% W. The 9 at.% of Cr present in EUROFER were neglected (substituted by Fe) because

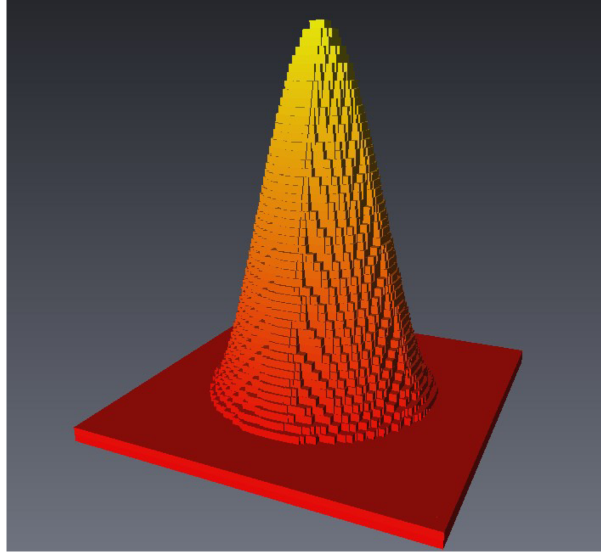

Figure 5.22: 3-D model of spike used in SDTrimSP-3D simulations of EUROFER, consisting of a truncated double cos^2 surface with a flat base and periodic boundary conditions on its sides.

the sputter yields of 200 eV D on Fe and on Cr are similar [79]. Therefore, their inclusion in this case would not alter the simulated sputtering behaviour. The rest of the alloying elements were also neglected: due to their small concentration and/or their comparable sputter yield, their substitution for Fe would not have an impact on the overall sputtering behaviour. The overall change in the sputter yield due to surface morphology was taken as a weighted arithmetic mean of the sputter yields of the flat and spiked surface morphologies observed in the SEM images. The weighting factor was the fraction of the surface area in which each kind of morphology was observed. The weighted mean was divided by the sputter yield from the 1-D simulation to calculate the degree of reduction of the SY due to surface morphology.

To calculate the effect of W and Ta surface enrichment on the sputter yield, sputter-XPS was performed with a PHI 5600 ESCA system equipped with an Al Kα X-ray source. W, Ta and Cr depth profiles were obtained by sputter-erosion using a beam of 10 keV Ar^+ ions at an incident angle of 20°, and periodically recording the photoelectron spectra between erosion steps (Fig. 5.25). Static SDTrimSP simulations were performed with the previously-mentioned bulk composition and with additional surface layers with a W and Ta concentration identical to the one measured by sputter-XPS. The sputter yields obtained from these simulations were divided by that of the previous SDTrimSP 1-D simulation (99.67 at.% Fe and 0.33 at.% W) to calculate the degree of reduction of the SY which could be attributed solely to W and Ta enrichment.

The overall reduction of the sputter yield due to the compounded effects of surface morphology and surface enrichment was calculated by multiplying the reduction factor calculated in each individual case. This merged value was compared to the reductions in the sputter yields calculated from the weight-loss measurements and from literature [83].

5.3.2 Effect of surface morphology and surface enrichment on the sputtering of EUROFER

The spiked morphology extracted from SEM images (Fig. 5.20) was modelled as a truncated cos^2 surface with a flat base in SDTrimSP-3D with periodic boundary conditions, shown in Fig. 5.22. Compared with a 1-D, static simulation with SDTrimSP, the sputter yield of the simulated surface is reduced by 24 % from 0.0364 to 0.0278, i.e.,

$$SY_{Rough} = (1 - 0.24) \times SY_{1D\,static} = 0.76 \times SY_{1D\,static}.$$

In all investigated SEM images, the areas with a smooth morphology have suffered less erosion than the areas featuring a spiked surface morphology. Figure 5.21 shows two SEM images of exposed EUROFER at the same position. One image is normal to the surface while the other is tilted at a 30° angle to the surface normal. Stereophotogrammetric analysis reveals that the smooth surface is elevated approximately 90 nm above the bottom of the spiked surface. Imaging of a FIB cross-section performed along an exposed area of the sample and an area protected by a FIB-coating indicates that the thickness of the eroded layer was of 120 nm for the spiked surface morphology, shown in Fig. 5.23. Therefore, the eroded layer thickness of the smooth surface shown in Fig. 5.21 is of 30 nm. However, the uncertainty of these measurements is significant. Within the experimental uncertainty, the eroded layer thickness of the smooth surface morphology is between 0 nm (no erosion) and 40 nm. If the sputter yield of EUROFER under the present experimental conditions were $SY_{1D\,static}$, the expected eroded layer thickness would be 135 nm. Therefore, the sputter yield of the areas with a smooth surface morphology is estimated to be between 0 (i.e., negligible erosion) and 30 % of the above-mentioned sputter yield calculated by SDTrimSP in a 1-D, static simulation, i.e.,

$$SY_{Smooth} = (0.15 \pm 0.15) \times SY_{1D\,static}.$$

Figure 5.24 shows a typical distribution of both kinds of surface morphologies on the exposed EUROFER sample. The fraction of surface area occupied by each kind of morphology was obtained by applying a contrast filter on SEM images of EUROFER after erosion, as it was noted that the secondary electron image was brighter for the spiked surface than for the smooth surface. Abundant segregations are visible in the SEM images in Figs. 5.21 and 5.24, corresponding to very light spikes or irregular structures. These are predominantly carbides. The majority of the exposed area (70 % ± 5 %) is covered by the spiked surface morphology, while the remaining area is mostly flat. Therefore, the sputter yield averaged over the two kinds of surface morphologies is:

$$SY_{Morphology} = S \times SY_{Rough} + (1 - S) \times SY_{Smooth}.$$

With $S = 0.70 \pm 0.05$, this value is:

$$SY_{Morphology} = (0.7 \times 0.76 + 0.15 \times 0.3 \pm 0.054) \times SY_{1D\,static} = (0.58 \pm 0.054) \times SY_{1D\,static},$$

i..e., a reduction of the sputter yield due to surface morphology of 42 % ± 5 %. The calculation of the uncertainty propagation is described in appendix B. It is still unclear why two distinct surface morphologies with different sputtering behaviours emerge in EUROFER bombarded under these conditions. Possible reasons are discussed in section 5.3.3.

Elemental depth profiles of the exposed EUROFER sample were performed by sputter-XPS. Between XPS measurements of the elemental composition, a 10 keV Ar^+ beam was used to progressively erode the sample to an accumulated fluence of $3.7 \times 10^{20}\,\mathrm{Ar\,m^{-2}}$. First, 22 measurements were taken in fluence steps of $5 \times 10^{18}\,\mathrm{Ar\,m^{-2}}$, followed by 5 measurements in fluence steps of $5 \times 10^{19}\,\mathrm{Ar\,m^{-2}}$ to obtain W, Cr and Ta concentrations deeper into the sample. Fig. 5.25 shows the sputter-XPS depth profiles of W, Cr and Ta. W and Ta surface enrichment was qualitatively confirmed, with measured concentrations peaking at the surface at 16 at.% for W and 4.5 at.% for Ta. Cr is depleted at the surface because of its high sputter yield (compared to that of W and Ta), thereby contributing to the W and Ta surface enrichment. Dashed lines indicating the W and Cr depth profiles of unexposed EUROFER are included for comparison [83]. In the unexposed EUROFER, Cr is enriched near the surface due to the formation of oxides when EUROFER is exposed to air. This enrichment is less pronounced in the EUROFER sample bombarded with D because the oxide layer was sputtered away and Cr was depleted near the surface. The top x-axis indicates the approximate depth at which the given W, Ta and Cr concentrations are found, and was calculated from the sputter yield of 10 keV Ar^+ on Fe from SDTrimSP simulations (= 3.73). It must be noted that the concentrations are averaged over the XPS information depth of approximately 4 nm. As the Ar beam sputters the surface of the sample, the sample composition is modified by preferential sputtering, thereby compromising the sputter-XPS measurement. However, the influence of preferential sputtering is in this case limited, since there is not such a large difference in the sputter yields of 10 keV Ar^+ on Fe (3.73) and on W (2.87), as obtained from SDTrimSP simulations; $\frac{SY_{Fe}}{SY_W} = 1.3$. For comparison, the sputter yield of 200 eV D^+ on Fe in EUROFER is, according to SDTrimSP, 4×10^{-2}, while on W it is 4×10^{-5} [43], i.e., $\frac{SY_{Fe}}{SY_W} = 10^3$. The uncertainty in the concentration of W and of Ta in the sputter-XPS measurements is estimated to be around 1.5 at.%. To assess the influence of the measured W and Ta enrichment on the experimental results for D sputtering, static SDTrimSP simulations were performed, including 27 surface layers of a total thickness of 16.3 nm, corresponding to the 27 XPS measurements. The W and Ta concentration in each layer was set to match the value determined by sputter-XPS. The sputter yield of these simulations was compared to that of simulations without the enriched W and Ta layers, i.e., with bulk concentrations. Simulations were performed with increased and decreased W concentrations to account for the uncertainty in the XPS measurement. The inclusion of the W- and Ta-enriched surface layers is responsible for a reduction of the sputter yield of 36 % ± 3 %, i.e.,

$$SY_{Enrichment} = (1 - 0.36 \pm 0.03) \times SY_{1D\,static} = (0.64 \pm 0.03) \times SY_{1D\,static}.$$

The approach taken in this work, namely, assessing the effects on the sputter yield of surface morphology and of surface enrichment independently, assumes that the two variables (morphol-

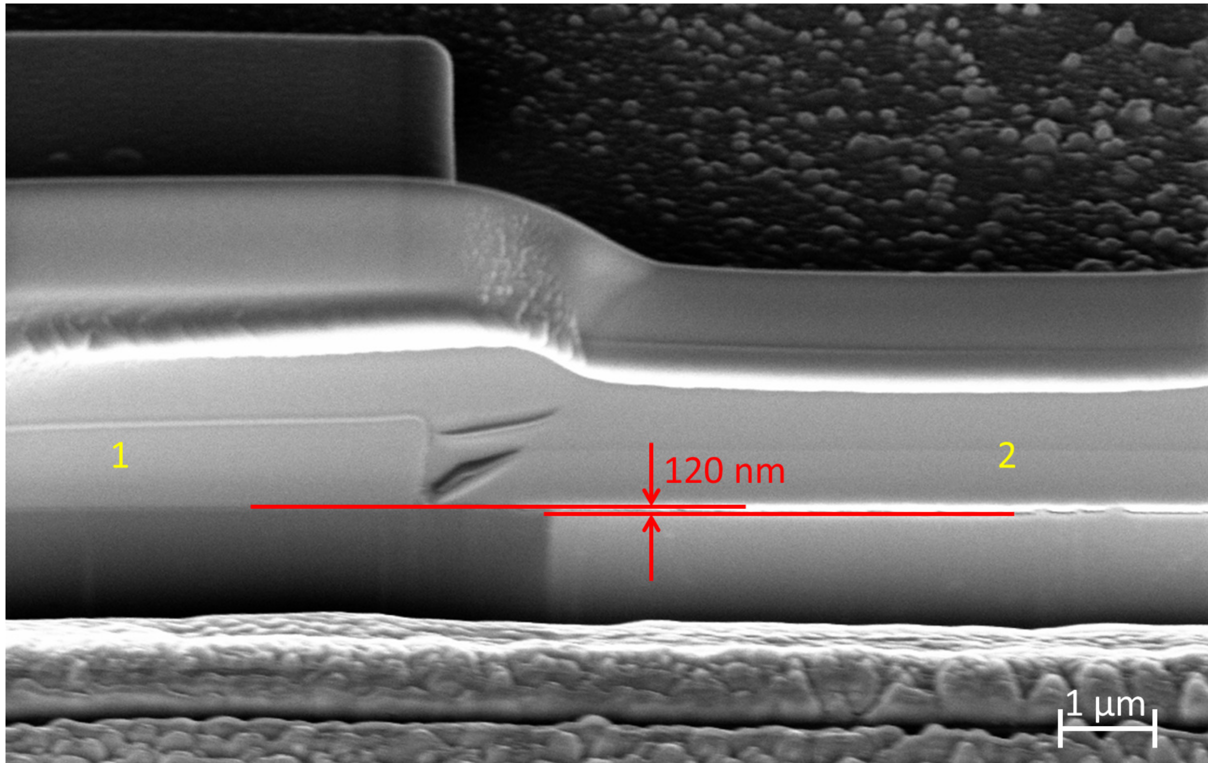

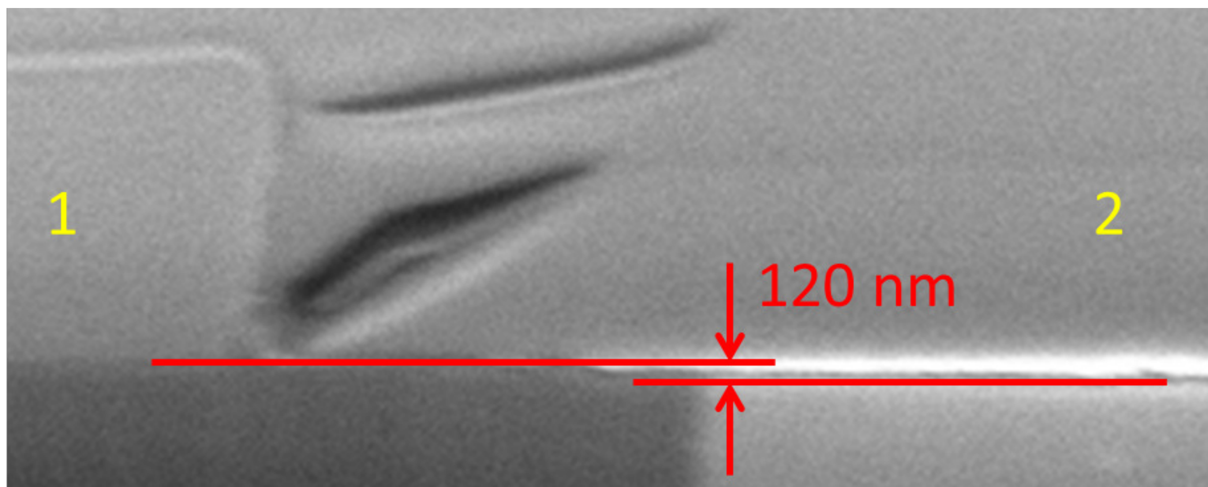

Figure 5.23: FIB cross-section of exposed EUROFER. The FIB cover layer labeled "1" was placed before bombardment of the sample at SIESTA, thereby protecting the underlying area from erosion. The cover layer labeled "2" was placed after exposure for the purpose of the FIB cut and overlaps layer "1". The thickness of the eroded layer is approximately 120 nm, and corresponds to the eroded layer thickness of the rough surface morphology, measured to the base of the spikes. The lower image is a close-up of the area where the eroded layer thickness was measured.

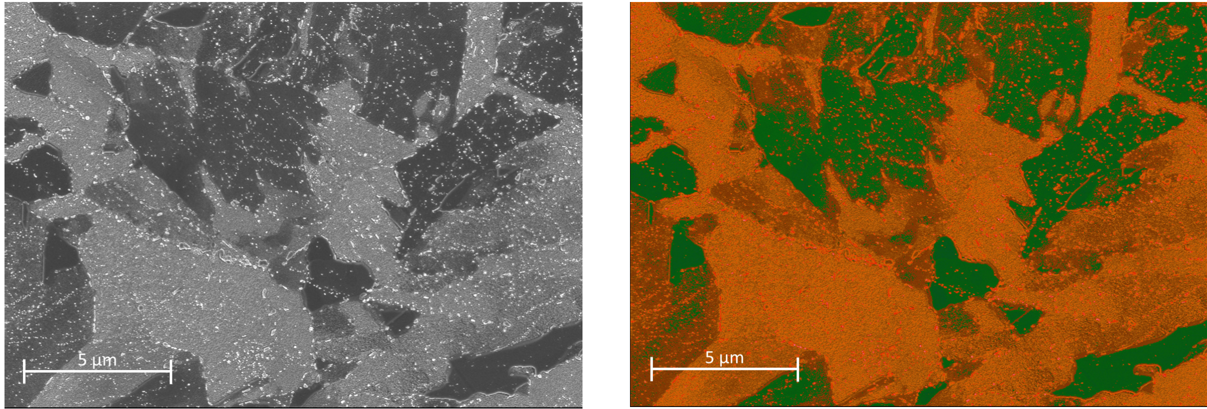

Figure 5.24: Left: SEM image of spiked (light) and smooth (dark) surface morphologies of exposed EUROFER. Right: A contrast filter was applied to the left image, marking the spiked areas in orange. 70 % of the exposed surface area displays the spiked surface morphology.

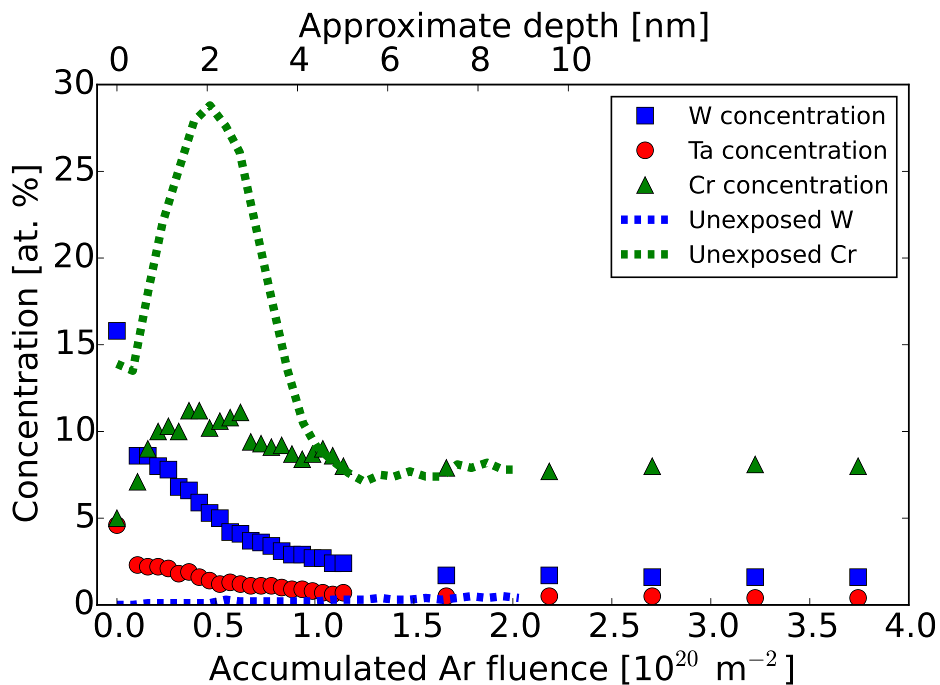

Figure 5.25: Elemental depth profile obtained by sputter-XPS of EUROFER bombarded with 200 eV D to a fluence of $1.14 \times 10^{24}\,\mathrm{D\,m^{-2}}$. Solid symbols: the elemental concentration of W, Ta and Cr are plotted as a function of the accumulated Ar^{+} fluence to which the surface was sputtered. The dotted lines indicate the concentrations of W and Cr in unexposed EUROFER [83]. For the calculation of the elemental concentration, oxygen and carbon were neglected. A second x-axis is included to illustrate the approximate depth.

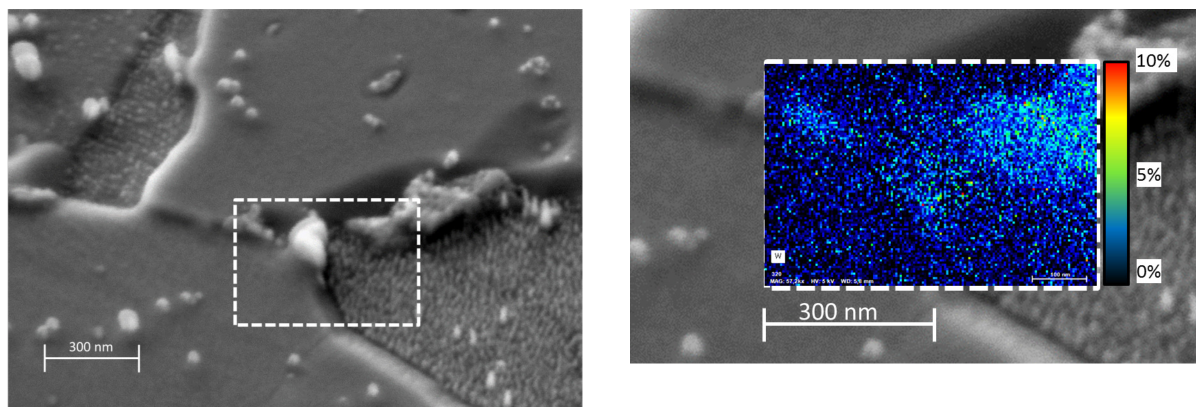

Figure 5.26: Left: Tilted SEM image of spiked and smooth surface morphologies of exposed EUROFER. Right: EDX map displaying the distribution of W within the white dashed rectangle in the left image, with a gradient indicating the approximate W concentration in at.%. The spiked and smooth surface morphologies appear to have roughly the same W content. The bright structures in the middle, top right and top left of the white dashed rectangle in the SEM image are carbides. These carbides have a higher W content than the areas exhibiting smooth or rough surface morphologies. A significant fraction of W in EUROFER is found in segregations such as carbides.

ogy and surface enrichment) are independent of one another, i.e., that the W concentration is similar in all areas of the sample. To check this, EDX scans were performed on areas featuring both kinds of surface morphologies, as shown in Figs. 5.26 and 5.27. No obvious variations in the W or Ta concentration for each kind of morphology are observed within the measurement uncertainty of EDX. Therefore, the proposed assumption is not invalidated by the EDX data. It is worth noting that, under these experimental conditions, the concentration of W quantified by EDX (given in Fig. 5.26 in at.%) corresponds to an interaction volume of up to 500 nm. Furthermore, quantification of EDX spectra may be compromised due to the presence of impurities such as C and Si. As mentioned at the beginning of this section, abundant segregations were observed in the SEM images (e.g., Fig. 5.24). These consist mainly of carbides with high concentrations (relative to bulk EUROFER composition) of Cr, W, Ta or other alloying elements, as evidenced in EDX spectra.

The EDX spectra performed on the same area before and after exposure of the sample, shown in Fig. 5.27, indicate a slight increase in the overall W near-surface content after exposure, qualitatively confirming the W enrichment measured by sputter-XPS. As was shown in Fig. 5.26, W concentration does not appear to strongly correlate with the type of surface morphology. In the EDX spectrum performed after erosion of the EUROFER sample, bright edges are visible. These do not correspond to areas of increased W concentration but are instead caused by Si contamination of the edge of the imaged region during EDX scanning. The EDX spectral lines for W measured in this scan are located close to the spectral lines for Si. Therefore, Si contamination at the edge of the scan region during EDX scanning was misinterpreted by the EDX analysis software as areas with high W concentration.

Figure 5.28 shows the data of the ex-situ and in-situ weight measurements that were listed at

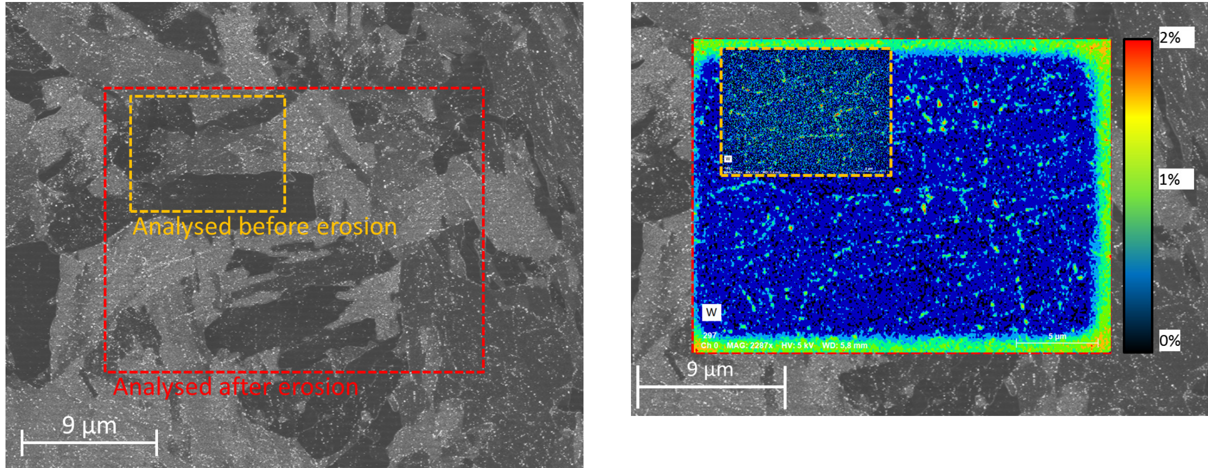

Figure 5.27: Left: SEM image of exposed EUROFER. Right: EDX maps displaying the distribution of W in at.% within the dashed rectangles in the left image. After exposure, the W surface concentration is larger than before exposure. The green edges in the EDX image after erosion are caused by deposition of impurities during the EDX scan and do not indicate areas of increased W concentration.

the beginning of section 5.3.1. The ex-situ and in-situ weight measurements of the sample with sample holder before degassing (labeled 0 in section 5.3.1) are plotted at the origin (0 g). All other ex-situ and in-situ weight measurements are plotted relative to the respective ex-situ and in-situ measurement before degassing. As shown in the figure, degassing leads to a significant mass loss (between steps 0 and 1) and the weight of the sample further decreases after each erosion step (1-2, 2-3 and 3-4). There is a recurring mismatch of approximately 80 μg between all the ex-situ and in-situ measurements performed after degassing. This is believed to be an artefact of the degassing process, as heating the sample and target chamber (with its ensuing degassing) may have altered the weight of other components of the in-situ microbalance (described in section 4.2.6). If the ex- and in-situ weight-loss measurements are plotted relative to the weight of the sample after degassing (i.e., weight-loss after degassing is set to 0 g), then the mismatch between ex-situ and in-situ measurements is reduced to 10 μg (Fig. 5.29). Furthermore, the comparison of measurements 1-1a and 4-4a, where the sample and sample holder are weighed in-situ, exposed to air and again weighed in-situ, indicates that this mismatch of 10 μg is likely a consequence of exposing the sample and sample holder to air for the ex-situ measurements. To test this, after step 4, the sample was demounted, stored in a desiccator, and the sample holder was exposed to air for a period of days, after which the sample was remounted on the sample holder and weighed (step 5). The ensuing ex-situ and in-situ weight measurements coincide (point 5 in Fig. 5.29), confirming that the 10 μg mismatch was most likely caused by exposure to air. The ex-situ and in-situ weight-loss measurements between each fluence step were used to calculate the sputter yield by applying Eq. 4.3. The resulting sputter yields are listed with their standard deviation in table 5.3. Sputter yields from [83] are included for comparison. Since the sputter yield is calculated from the difference of the weight measurements before and after each fluence step, the sputter yields listed here represent the average sputter yield at a fluence

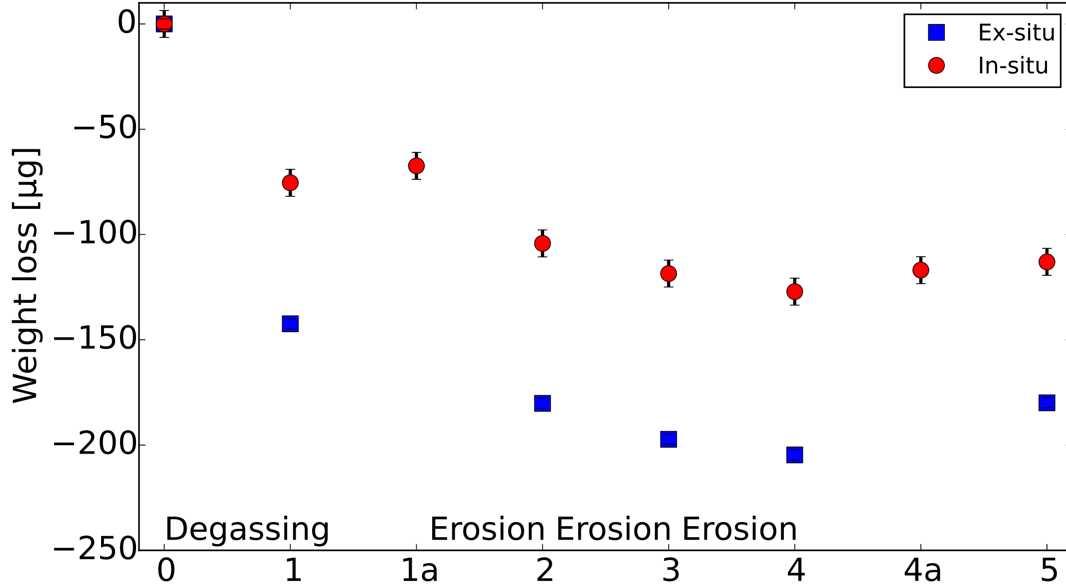

Figure 5.28: Ex- and in-situ weight-loss measurements of EUROFER. The weight-loss is plotted relative to the measured weight of the sample and sample holder prior to degassing, which is set to 0. The points on the x-axis correspond to successive weight measurements, as listed in 5.3.1.

between the initial and final fluence, labeled "Fluence mid-point" in Tab. 5.3. The sputter yields from literature and the experimentally-determined ex- and in-situ sputter yields agree in almost all cases within the given ranges of uncertainty.

The expected sputter yield due to the combination of surface morphology and W & Ta surface enrichment is:

$$SY_{Combined} = \frac{SY_{Morphology}}{SY_{1D\,static}} \times \frac{SY_{Enrichment}}{SY_{1D\,static}} \times SY_{1D\,static}.$$

This value is:

$$SY_{Combined} = (0.58 \pm 0.054 \times 0.64 \pm 0.03) \times SY_{1D\,static} = (0.37 \pm 0.046) \times SY_{1D\,static},$$

i.e., a reduction of the sputter yield of 63 % ± 5 %. The calculation of the uncertainty is described in appendix B. This value is compared to the reductions measured experimentally with ex-situ and in-situ weight-loss measurements and to values from literature, based on the empirical fit for the sputter yield of pristine EUROFER of 0.0237 given in [83]. In the case of the in-situ weight-loss measurements, for example, this constitutes a reduction in the sputter yield from 0.0237 to 0.0068 ± 0.0012 at an equivalent fluence of $10^{24}\,\mathrm{D\,m^{-2}}$, i.e., a reduction of 71% ± 5%. The calculation of the uncertainty of the sputter yield is described in appendix A, considering the uncertainty in the weight-loss measurements and the uncertainty in the current measurement at SIESTA. It must be noted that, while the data for the modelling of the surface morphology

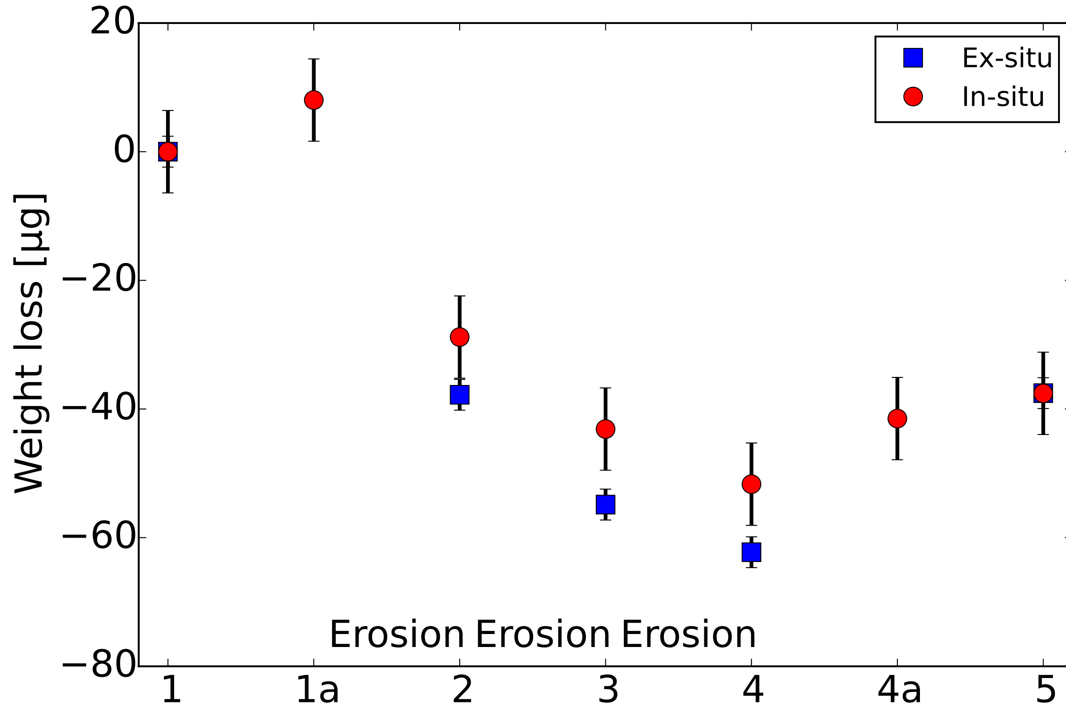

Figure 5.29: Ex- and in-situ weight-loss measurements of EUROFER. The weight-loss is plotted relative to the measured weight of the sample and sample holder after degassing, which is set to 0. The points on the x-axis correspond to successive weight measurements, as listed in 5.3.1.

	Ex-situ	In-situ	Literature [83]	Fluence [10^{24} D m^{-2}]	
Erosion step	Sputter yield	Sputter yield	Sputter yield	Mid-point	Final
1 to 2	0.0164 ± 0.0030	0.0160 ± 0.0039	0.012 ± 0.0009	0.24	0.48
2 to 3	0.0088 ± 0.0009	0.0074 ± 0.0017	0.0086 ± 0.0019	0.68	0.88
3 to 4	0.0059 ± 0.0005	0.0068 ± 0.0012	0.0074 ± 0.0009	1.01	1.14

Table 5.3: Sputter yield of EUROFER bombarded at 300 K by 200 eV D ions (600 eV/D D_3^+) to an accumulated fluence of 1.14×10^{24} D m^{-2}, determined via ex-situ and in-situ weight-loss measurements. Literature values from [83] are included for reference. Fluence mid-point indicates the intermediate fluence in that fluence step. The calculation of the uncertainty of the sputter yield is described in appendix A

(SEM imaging) and W & Ta surface enrichment (sputter-XPS depth profiling) correspond to EUROFER exposed to a fluence of $1.14 \times 10^{24}\,\mathrm{D\,m^{-2}}$, the weight-loss measurements are used to calculate a sputter yield averaged between a fluence of $0.88 \times 10^{24}\,\mathrm{D\,m^{-2}}$ and $1.14 \times 10^{24}\,\mathrm{D\,m^{-2}}$. The real sputter yield at a fluence of $1.14 \times 10^{24}\,\mathrm{D\,m^{-2}}$ may in fact be lower than the values listed in table 5.3, therefore leading to an even stronger reduction of the sputter yield. However, as shown in [83], the change in the sputter yield between accumulated fluences of $1 \times 10^{24}\,\mathrm{D\,m^{-2}}$ and $1.14 \times 10^{24}\,\mathrm{D\,m^{-2}}$ should be very small, and can be assumed to lie within the experimental uncertainty given in the weight-loss measurements. Table 5.4 lists the expected reduction in the sputter yield of EUROFER due to surface morphology and W & Ta surface enrichment at the final accumulated fluence, in comparison with the measured values.

It can be concluded that both surface morphology and surface enrichment play a role in the sputtering behaviour of EUROFER under under bombardment with 200 eV deuterium. Their combined effect can explain the reduction in the sputter yield observed experimentally and in the literature. The agreement between modelled and measured reduction in the sputter yield is not perfect (Tab. 5.4). However, it must be noted that no experimental data is available for the initial sputter yield of pristine EUROFER. The value used here to normalize the experimentally determined sputter yields is based on an empirical fit to experimental data from [83] obtained at higher fluences, and as such is subject to uncertainty. No quantification of this uncertainty is given in [83]. As previously mentioned at the beginning of this section, open questions still remain in the analysis of the surface morphologies present in exposed EUROFER. As is shown in this work, bombardment of mirror-polished EUROFER leads to the formation of two distinct morphologies for the here investigated exposure conditions (200 eV/D, about 300 K sample temperature), one smooth and one spiked, with the former proving much more resistant to sputtering than the latter. It is presently unknown why these two morphologies develop and why they exhibit such a strong difference in their sputtering behaviour. This effect cannot be due to the initial surface roughness as prior to sputtering AFM scans and SEM images revealed that all areas on the sample were smooth. Furthermore, as evidenced by the SDTrimSP-3D calculations, the spiked geometry that develops during exposure should lead to reduced sputtering compared with a smooth surface. Therefore, the cause for this difference in the sputtering behaviour must be some other factor, such as grain orientation or inhomogeneous material composition. The following section describes additional investigations performed on the EUROFER samples and possible avenues for further research.

5.3.3 Additional analyses of the surface morphology of EUROFER

As previously mentioned, EBSD was performed prior to exposure at pre-defined positions. One such position is shown after exposure in figure 5.30. An SEM image of exposed EUROFER is displayed alongside an EBSD image of the same area. In the SEM image, darker gray areas correspond to a rough surface morphology, while lighter gray areas feature a smooth surface morphology. The grains are clearly visible in the EBSD image and have been color coded according to the grain orientation given by their Miller indices. By comparing the two images it

		Fraction of $SY_{SDTrimSP}$	Reduction of
Modelled factors	Surface morphology	0.58 ± 0.054	42 % ± 5 %
	Surface enrichment	0.64 ± 0.03	36 % ± 3 %
	Total	0.37 ± 0.046	63 % ± 5 %
Weight-loss	Ex-situ	0.25 ± 0.02	75 % ± 2 %
	In-situ	0.29 ± 0.05	71 % ± 5 %
	Literature [83]	0.31 ± 0.04	69 % ± 4 %

Table 5.4: Reduction of the sputter yield of EUROFER bombarded with 200 eV deuterium to an equivalent fluence of $10^{24}\,\mathrm{D\,m^{-2}}$ due to surface morphology and surface enrichment of W and Ta, compared with the sputter yield reduction measured experimentally by weight-loss (ex-situ and in-situ) and from literature [83]. The calculation of the uncertainty is described in appendices A and B.

can be observed that boundaries between the two surface morphologies (visible as darker and lighter areas in the SEM image) coincide with grain boundaries. That is to say, within the same grain, only one type of surface morphology is present, either smooth or spiked. Therefore, it is assumed that the difference in sputtering behaviour between the two kinds of surface morphologies can be ascribed to differences between the grains themselves. A possible cause would be grain orientation. However, no obvious correlation between grain orientation and surface morphology was observed. This topic would warrant further study with quantifiable, computational image analysis techniques, e.g., systematic identification and binning of grains based on their surface morphology and grain orientation, as performed for W [80].

The different sputtering behaviour observed for the smooth and spiked surface morphologies could also be a consequence of differences in the composition of the grains. No measurable differences were observed in EDX spectra of the W or Ta surface concentrations (Figs. 5.26 and 5.27 for W), which could directly influence the sputter yield of the mixed material, though it should be noted that, given the interaction volume of EDX of approximately 500 nm, small differences in the concentrations of these elements within the top surface layers would be difficult to detect with EDX. Differences in the concentration of C, Fe and Cr were observed in EDX scans performed after exposure and were correlated with the type of surface morphology, as is shown in Fig. 5.31 for Cr. It is possible that different concentrations of these elements could provide alternative sputtering mechanisms or alter the physical and chemical potentials which play a role in sputtering, such as the surface binding energy. However, said differences in concentration were neither observed in the EDX spectra of the same areas prior to exposure (Fig. 5.31), nor in all the EDX spectra after exposure. The observed differences in the C, Cr and Fe concentration in some spectra could be an artefact caused by the inhomogeneous distribution of impurities such as C and O during the EDX scanning procedure. For instance, C contamination was observed in the spectra that showed differences in the C, Fe and Cr content, manifesting as areas of very high C concentration in the edges of the scanned region (akin to the W distribution in Fig. 5.27). In that same scan, areas with spiked surface morphology appeared to have a significantly increased C concentration (up to 60 %), while those with a smooth surface morphology appeared as having low C concentration. It is possible that high

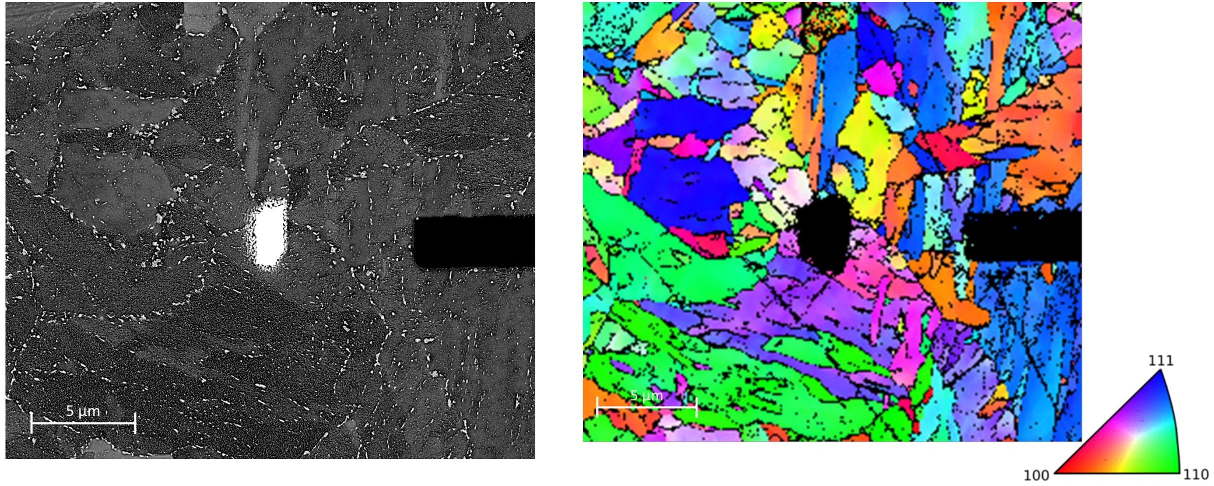

Figure 5.30: Left: SEM image of exposed EUROFER. The dark rectangle in the right edge corresponds to a FIB marker. The white area in the middle is a protective FIB coating applied prior to exposure at SIESTA. Areas with a rough surface morphology appear slightly darker in the SEM image. Right: EBSD image of the same area. The FIB marker and coating both appear as black areas. The grain orientations are color coded as indicated by the inverse pole figure in the lower right corner. No correlation between grain orientation and type of surface morphology (spiked or smooth) is immediately discernible.

concentrations of other elements such as Cr in Fig. 5.31 are caused by preferential deposition on the smooth regions of other impurities with similar EDX spectral lines, like O in the case of Cr. If the different sputtering behaviour of the smooth and rough surface morphologies is not a consequence of the grain orientation or of substantially different material composition, one hypothesis is that the different sputtering behaviours are a consequence of the multi-phase nature of EUROFER. The sputter yield calculated by SDTrimSP depends on material properties such as the mass and atomic density, surface binding energy, displacement energy, etc. As previously mentioned, EUROFER is a multi-phase ferritic-martensitic steel. It is possible that the ferritic and martensitic phases display a different sputtering behaviour, e.g., a different sputtering threshold, due to their differences in density, lattice constant, etc [87]; thereby leading to smooth (barely eroded) or spiked (significantly eroded) surface morphologies. This hypothesis shall also be the focus of future investigations.

5.3.4 Summary and discussion

In the experiments presented in this section, the surface morphology and composition of EUROFER were characterized before and after exposure to 200 eV D to a fluence of $1.14 \times 10^{24}\,\mathrm{D\,m^{-2}}$ at 300 K. The goal of these experiments was to assess the impact on the sputter yield of the surface morphology and of the W and Ta surface enrichment. The former was determined with the aid of SEM imaging and SDTrimSP-3D simulations. For the latter, sputter-XPS depth-profiling and static 1-D calculations with SDTrimSP were employed. The combined effect of these factors was compared with sputter yields determined experimentally via weight-loss measurements and with data from the literature.

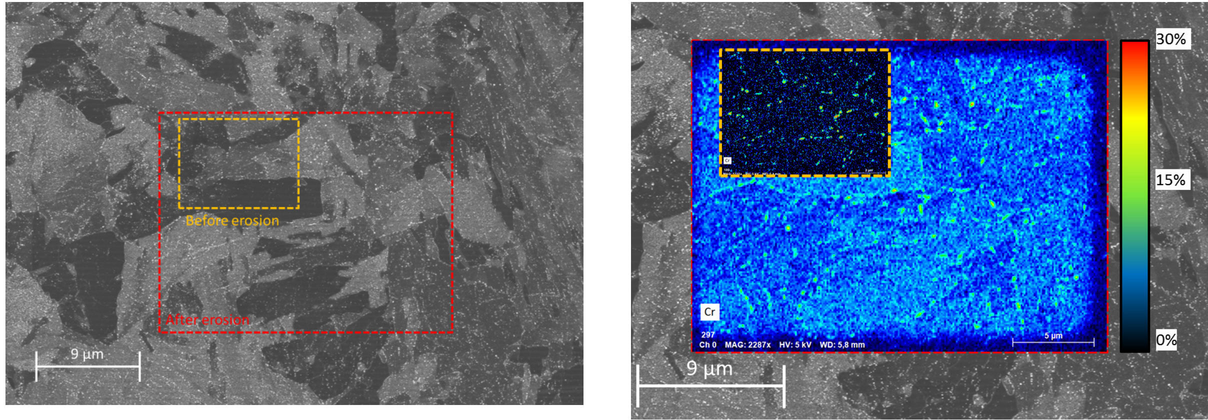

Figure 5.31: Left: SEM image of exposed EUROFER. Right: EDX maps displaying the distribution of Cr within the dashed rectangles in the left image. Before erosion, the Cr content appears to be uniformly distributed. After erosion, overall Cr concentration seems to have increased and areas with the smooth surface morphology appear to have a higher Cr content, than those with a rough surface morphology. However, this would contradict the measured XPS depth profiles (Fig. 5.25) and could be an artefact caused by an inhomogeneous distribution of C, O and Si impurities during EDX imaging. Cr is also concentrated in segregations along the grain boundaries.

SEM imaging after ion bombardment revealed two distinct surface morphologies, consisting of smooth areas and areas displaying a spiked morphology (shown in Fig. 5.20). EDX was employed to verify that the W content in the two surface morphologies is the same within the measurement uncertainty (Figs. 5.26 and 5.27). The size of these spikes was extracted from the SEM images and was used to construct a 3-D model of the surface for SDTrimSP-3D simulations (Fig. 5.22). According to these simulations, the spiked surface geometry is responsible for a 24 % decrease in the sputter yield compared with a perfectly smooth surface. It was observed that the smooth areas were eroded substantially less than the spiked areas (Fig. 5.21), corresponding to a sputter yield between 0 (no erosion) and 30 % of the value calculated with SDTrimSP. Approximately 70 % of the surface of the sample features the spiked morphology (Fig. 5.24), while the remaining 30 % is smooth. The overall effect of surface morphology on the sputtering of EUROFER under these conditions is a reduction in the sputter yield of 42 % ± 5 %.

Depth profiles performed by sputter-XPS confirmed surface enrichment of W and of Ta, with measured concentrations of W at the surface of 16 at.% averaged over the information depth of approximately 4 nm, as shown in Fig. 5.25, i.e., enriched by almost a factor of 50. For comparison, if the W concentration obtained from dynamic SDTrimSP calculations like the ones performed in [83] were integrated over the XPS information depth, the resulting W content would be approximately a factor of 10 lower than the W concentration measured by XPS. Static SDTrimSP simulations employing the experimentally-obtained W and Ta depth profiles revealed a reduction of the sputter yield of 36 % ± 3 % when compared with simulations with a homogeneous W and Ta distribution corresponding to bulk EUROFER. The combined effects of surface morphology and W & Ta enrichment on the sputter behaviour of EUROFER under these conditions are therefore estimated to be responsible for a reduction in the sputter

yield of 63 % ± 5 %. This value is compared with a measured reduction in the sputter yield from 0.0237 (initial value based on empirical fit from [83]) to 0.0068 ± 0.0012 (determined by in-situ weight-loss at an equivalent fluence of $1 \times 10^{24}\,\mathrm{D\,m^{-2}}$), i.e., a reduction of 71 % ± 5 %. Both surface morphology and surface enrichment contribute significantly to the reduction of the sputter yield of EUROFER under the given experimental conditions, and only their combined effect is sufficient to explain the reduction in the sputter yield observed in weight-loss experiments and in the literature (Tab. 5.4).

Open questions remain regarding the sputtering behaviour of EUROFER under deuterium bombardment. It is unclear why two distinct surface morphologies form for the here investigated exposure conditions and why they exhibit such disparate sputtering behaviours. EBSD measurements confirmed that the separation between each kind of morphology corresponded in all cases to grain boundaries, i.e., each grain displayed only one kind of surface morphology (Fig. 5.30). It is concluded that differences between grains are responsible for the observed differences in the sputtering behaviour. No obvious dependence of the sputtering behaviour on the grain orientation was identified, though this question warrants further study with dedicated analysis tools. Differences in the elemental composition of the grains were investigated with EDX, but no differences could be conclusively proven beyond the experimental uncertainty. It is, however, possible that the W concentration at the near-surface (first 5 nm) is laterally inhomogeneous. For instance, if W were to accumulate on the smooth surface morphology and on the tips of the spikes in the rough surface morphology, it is conceivable that similar EDX spectra would be obtained, as changes of W concentration at these depth scales would be hard to resolve. This hypothetical scenario would potentially provide an explanation for the reduced erosion of the smooth surface morphology, namely, increased W content in the near-surface layer. Finally, another possibility is that the evolution of one surface morphology over the other is determined by the metallurgic phase or structure of the grain. Since EUROFER is a ferritic-martensitic steel, both kinds of phases are present in the material. It is conceivable that the two phases display different sputtering behaviours, e.g., different binding energies, as material parameters such as lattice constant or density are known to be different among different phases of steel [87].

The existence of a heterogeneous surface morphology with different sputtering behaviour within EUROFER has hitherto not been taken into account in simulations with tools such as SDTrimSP. The methodology shown here constitutes the first approach to consider the effect of surface morphology on the sputter yield of EUROFER and provides a better quantitative agreement with the experimental data than other works from literature that only considered W surface enrichment [83]. However, it should be noted that this experiment comprises only one exposure scenario and hinges on several assumptions that could not be proved or disproved, such as the lateral homogeneity of the W concentration. It can be anticipated that further research on the differences in the sputtering behaviour of the observed surface morphologies may allow for better understanding of the sputtering evolution of EUROFER. This would further enable better predictions of the sputter yield of EUROFER under reactor-relevant exposure conditions.

Chapter 6

Summary

The inner walls of current and future magnetic fusion devices will be required to withstand significant heat loads and particle impacts during their lifetime. Erosion of plasma-facing materials, tritium retention and dust formation are identified as significant challenges for the lifetime and operation of future devices, and are highly dependent on the choice of wall material. There is, therefore, a strong interest in developing and testing materials suitable for use in a nuclear fusion reactor. Such materials include tungsten to withstand the high heat loads and particle fluxes of the divertor and EUROFER and other advanced multi-phase steels at the first wall. Dedicated experimental setups to test the behaviour of these materials under energetic particle bombardment play an essential role in the characterization of candidate materials. Of these devices, ion sources allow for greater control over the experimental conditions, as they can be designed to produce monoenergetic single-species ion beams to achieve well-defined, tailored exposure conditions. However, the ion fluxes to the target are typically significantly smaller than those found in plasma devices, thereby requiring substantially longer exposure times to reach the desired particle fluence.

Within the scope of this work, SIESTA (Second Ion Experiment for Sputtering and TDS Analysis) was designed, put into operation and extensively characterized as an experimental setup equipped with a custom-made high-current ion source and specifically suited for well-defined ion-induced erosion and retention studies. With the inclusion of a quadrupole doublet lens, it is capable of supplying mass-filtered ion fluxes in the range of 10^{19} ions $m^{-2}s^{-1}$ with impinging particle energies between 200 eV and 10 keV and has been successfully tested and characterized with H, D, He and Ar ions. The position-resolved proportion of neutral particles impinging on the target was measured by eroding a 50-nm-thick Au film on a Si substrate and measuring the change of the layer thickness by Rutherford Backscattering Spectrometry (RBS). The low fluxes of neutral particles enable the use of SIESTA for sputtering experiments near the threshold energy for all relevant materials (e.g., 200 eV D on W). With the use of adjustable beam-defining apertures, beam sweeping and asymmetric beam focusing, an almost homogeneous beam footprint of adjustable size can be achieved a the target. Samples to be exposed can be quickly inserted into the target chamber via a lateral load-lock and can be rotated for sputtering at oblique angles of incidence and heated up to 1300 K for high-temperature exposure. The

sample can be electrically biased and weighed in-situ with a magnetic suspension balance for weight-loss measurements. Thermal desorption spectrometry is available in a dedicated vacuum chamber located below the load-lock for in-vacuo retention studies. The sputter yield of pure Au exposed to a 6 keV D_3^+ beam (2 keV/D) was determined from ex-situ and in-situ weight-loss measurements, agreeing within experimental scatter with values from literature and agreeing within 15 % with the sputter yield calculated by the Monte Carlo code SDTrimSP.

During the course of this work, SIESTA was used to study the angle-dependent sputtering behaviour of smooth Fe and W and rough W thin films exposed to a 6 keV D_3^+ ion beam. The samples were produced by magnetron sputter-deposition of the desired elements on Si substrates and the morphology was characterized with Atomic Force Microscopy (AFM). The sputter yield was determined as a function of the angle of incidence by measuring the eroded layer thickness by means of Rutherford Backscattering Spectrometry (RBS) before and after erosion and was compared with SDTrimSP simulations. Agreement with SDTrimSP was excellent for the smooth Fe and W thin films, though a mismatch was observed at normal incidence for the smooth W thin films. It is believed that the binary collision approximation (BCA), on which SDTrimSP is based, may be the cause of this discrepancy between simulation and experiment, as the BCA may not be fully applicable to W under the simulated conditions. This is the subject of ongoing investigations. The surface morphology of the rough W thin films was used as a basis for static simulations with the recently-developed code SDTrimSP-3D, a new version of SDTrimSP capable of simulating dynamic bombardment of fully 3-dimensional targets. This experiment constitutes the first experimental benchmark of SDTrimSP-3D, which correctly predicted the dependence of the sputter yield on the angle of incidence for rough W as compared with smooth W. The variation of the sputter yield with the angle of incidence could be explained qualitatively for both the smooth and rough samples.

Based on these results, dedicated experiments were performed to fully validate SDTrimSP-3D with well-defined, 3-D targets whose surface morphology and composition changed during ion bombardment. These targets consisted of Si and Ta columnar structures of approximately 200 nm in height, 100 nm in diameter and spaced 200 nm, distributed in an orthogonal formation on a mirror-polished Si substrate. Scanning Electron Microscopy (SEM) imaging prior to exposure was employed to construct a 3-D model of the target morphology for the corresponding SDTrimSP-3D simulations. The samples were exposed to a 5 keV Ar^+ beam at SIESTA to various fluence steps and the sample morphology was characterized at various positions before and after each fluence step via SEM imaging of Focused Ion Beam (FIB) cross sections. Several exposure geometries were investigated. Cross-section images of the samples were compared with the sample morphology modelled by SDTrimSP-3D, providing excellent agreement with the experimental data at all fluence steps. In the case of the Ta sample, SDTrimSP-3D was able to correctly model the geometry of both the Ta columns and the Si substrate, thereby validating its use for fully 3-D targets of variable composition exposed under geometrically complex scenarios.

The last series of experiments performed in this work related to studying the evolution of the sputter yield of EUROFER bombarded with D as a function of its surface morphology and its W and Ta surface enrichment. To this end, EUROFER samples were mirror-polished and

characterized with various SEM techniques prior to exposure at SIESTA to 200 eV D ions to an accumulated fluence of $1.14 \times 10^{24}\,\mathrm{D\,m^{-2}}$. Ex-situ and in-situ weight-loss measurements were performed periodically to calculate the sputter yield as a function of the accumulated fluence. SEM imaging after exposure revealed a heterogeneous surface morphology consisting of smooth and spiked surfaces. The combined effect of these surface morphologies on the sputter yield was calculated with the help of SDTrimSP-3D simulations, FIB cross-sections and stereogrammetry of SEM images. Sputter-X-ray Photoelectron Spectroscopy (XPS) was performed to obtain depth profiles of the W and Ta concentrations within the first several nanometers, which were employed in SDTrimSP simulations to calculate the degree of reduction in the sputter yield of EUROFER attributable to W and Ta surface enrichment. Combined, surface morphology and surface enrichment are responsible for a reduction of 63 % ± 5 % of the original sputter yield. This value is compared with data determined experimentally and from literature. In this work, in-situ weight-loss measurements show a decrease in the sputter yield of 71 % ± 5 % from its pristine state to the above-mentioned accumulated fluence. Surface morphology and surface enrichment are both responsible for a significant reduction in the sputter yield under the specified exposure conditions, and combined are capable of explaining the reduction in the sputter yield of EUROFER observed experimentally. This experiment constitutes the first of its kind to consider the effect of the observed surface morphology (in addition to W enrichment) on the sputtering behaviour of EUROFER, and achieves better agreement between modelling and experimental results than previous studies that neglected the influence of surface morphology.

It is still unclear why, for the here investigated exposure conditions, two distinct surface morphologies form and why they exhibit such disparate sputtering behaviours. It is concluded that differences between grains are responsible for the observed differences in the sputtering behaviour. However, no conclusive dependence of the sputtering behaviour on the grain orientation or elemental composition was identified. Another possibility is that the ferritic and martensitic phases of EUROFER exhibit different sputtering behaviours due to differences in their material properties. These questions warrant further study with dedicated analysis tools and will be the focus of future investigations.

Chapter 7

Conclusions

As evidenced in this work, SIESTA has been developed into an experimental setup well suited for investigation of complex issues related to the impact of hydrogen irradiation on wall materials for use in nuclear fusion reactors. SIESTA is now sufficiently matured to enable other researchers to perform their own experiments in the fields of ion-induced erosion and retention.

The operational reliability and the accuracy of the measurements is sufficient to identify limitations of SDTrimSP and to successfully benchmark and validate the recently-developed dynamic, 3D version of the code, SDTrimSP-3D. With the aid of this new simulation tool, the evolution of the surface morphology and its impact on the sputter yield in physical sputtering processes can now be calculated as a function of the impinging particle fluence with unprecedented accuracy.

As a singular case study employing these techniques, the influence of surface morphology on the erosion behaviour of EUROFER under D bombardment was assessed for the first time. This work also constitutes the first estimation of the combined impact of surface morphology and W surface enrichment on the sputter yield of EUROFER bombarded with D. It can now be concluded that, at least for the here investigated experimental conditions, both surface morphology and W surface enrichment play an important role in the sputtering behaviour of EUROFER, and therefore neither should be ignored in similar investigations in the future.

Overall, this work has furthered our understanding of the interplay between sputtering and surface morphology and has helped to elucidate the mechanisms for progressive sputter yield reduction in EUROFER, which remains a promising wall-material candidate for recessed areas in DEMO.

Bibliography

[1] International Energy Agency, *World Energy Outlook 2017.* OECD Publishing, Paris, nov 2017.

[2] U. N. F. C. on Climate Change, "Adoption of the paris agreement," 2015.

[3] International Energy Agency, "Key world energy statistics," 2017.

[4] N. E. Agency and I. A. E. Agency, *Uranium 2014: Resources, Production and Demand.* OECD Publishing, sep 2014.

[5] D. Bodansky, "Reprocessing spent nuclear fuel," *Phys. Today*, vol. 59, pp. 80–81, December 2006.

[6] IPP, "Does fusion involve radioactive waste?." https://www.ipp.mpg.de/2769068/faq9, October 2018.

[7] IPP, "Kernfusion - berichte aus der forschung (folge 2)." http://www.ipp.mpg.de/46732/3_berichte, October 2016.

[8] A. Glaser and R. Goldston, "Proliferation risks of magneetic fusion energy: Clandestine production, covert production and breakout," tech. rep., Princeton Plasma Physics Laboratory, mar 2012.

[9] G. McCracken and P. Stott, *Fusion: The Energy of the Universe.* 2 ed., June 2012.

[10] I. R. E. Agency, "From baseload to peak: renewables provide a reliable solution," *IEA Information Paper*, p. 5, 2015.

[11] A. Bradshaw, T. Hamacher, and U. Fischer, "Is nuclear fusion a sustainable energy form?," *Fusion Engineering and Design*, vol. 86, pp. 2770–2773, October 2011.

[12] S. Shafiee and E. Topal, "When will fossil fuel reserves be diminished?," *Energy Policy*, vol. 37, pp. 181–189, January 2009.

[13] G. P. Thomson and M. Blackman, "Improvements in or relating to gas discharge apparatus for producing thermonuclear reactions," 1946.

[14] S. Pfalzner, *An Introduction to Inertial Confinement Fusion.* Taylor & Francis, March 2006.

[15] L. L. N. Laboratory, "About NIF & photon science." https://lasers.llnl.gov/about/, June 2016.

[16] ITER, "Facts and figures." http://www.iter.org/factsfigures, December 2016.

[17] ITER, "ITER and beyond." http://www.iter.org/proj/iterandbeyond, December 2016.

[18] ITER, "The ITER tokamak." https://www.iter.org/doc/all/content/com/gallery/Media/7%20-%20Technical/2009_04_29%20MACHINE.jpg, December 2016.

[19] ITER, "How Fritz Wagner "discovered" the H-Mode." http://www.iter.org/newsline/86/659, December 2019.

[20] ITER, "KSTAR announces successful ELM suppression." http://www.iter.org/newsline/198/950, December 2011.

[21] H. Zohm, "Edge localized modes (ELMs)," *Plasma Physics and Controlled Fusion*, vol. 38, pp. 105–128, February 1996.

[22] G. Federici *et al.*, "Assessment of erosion and tritium codeposition in ITER-FEAT," *J. Nucl. Mater.*, vol. 290-293, pp. 260 – 265, 2001.

[23] J. Roth *et al.*, "Recent analysis of key plasma wall interactions issues for ITER," *J. Nucl. Mater.*, vol. 390-391, pp. 1–9, 2009.

[24] R. Arredondo, M. Oberkofler, K. Schmid, T. Schwarz-Selinger, W. Jacob, and R. Neu, "SIESTA: a high current ion source for erosion and retention studies," *Rev. Sci. Instrum.*, vol. 89, 2018.

[25] P. A. Sturrock, *Plasma Physics: An Introduction to the Theory of Astrophysical, Geophysical & Laboratory Plasmas.* No. ISBN 978-0-521-44810-9, Cambridge University Press (CUP), 1994.

[26] B. Chapman and J. L. Vossen, "Glow discharge processes: Sputtering and plasma etching," *Phys. Today*, vol. 34, no. 7, p. 62, 1981.

[27] MIT OpenCourseWare, "Overview of the physics in the plasma sheath." https://ocw.mit.edu/courses/aeronautics-and-astronautics/16-522-space-propulsion-spring-2015/lecture-notes/MIT16_522S15_Lecture9.pdf, November 2018.

[28] T. Kalvas, *Development and use of computational tools for modelling negative hydrogen ion source extraction systems.* PhD thesis, University of Jyväskylä, 2013.

[29] M. B. Shah, D. S. Elliott, and H. B. Gilbody, "Pulsed crossed-beam study of ionisation of atomic hydrogen by electron impact," *Journal of Physics B: Atomic and Molecular Physics*, vol. 20, pp. 3501–3514, July 1987.

[30] E. Krishnakumar and S. Srivastava, "Electron correlation effects in the dissociative ionization of H2," *J. Phys. B: At. Mol. Opt. Phys.*, vol. 27, pp. L251–L258, June 1994.

[31] M. B. Shah, D. S. Elliott, P. McCallion, and H. B. Gilbody, "Single and double ionisation of helium by electron impact," *J. Phys. B: At. Mol. Opt. Phys.*, vol. 21, pp. 2751–2761, August 1988.

[32] W. R. Thompson, M. B. Shah, and H. B. Gilbody, "Single and double ionization of atomic oxygen by electron impact," *J. Phys. B: At. Mol. Opt. Phys.*, vol. 28, pp. 1321–1330, April 1995.

[33] C. D. Child, "Discharge from hot CaO," *Physical Review (Series I)*, vol. 32, no. 5, pp. 492–511, 1911.

[34] E. Speth, "Neutral beam heating of fusion plasmas," *Reports on Progress in Physics*, vol. 52, no. 1, p. 57, 1989.

[35] M. Minty and F. Zimmermann, *Measurement and Control of Charged Particle Beams.* Springer Berlin Heidelberg, 2003.

[36] J. Grösser, *Einführung in die Teilchenoptik.* B. G. Teubner Stuttgart, 1983.

[37] H. Liebl, *Applied Charged Particle Optics.* Springer-Verlag Berlin Heidelberg, 1 ed., 2008.

[38] N. Chauvin, O. Delferriere, R. Duperrier, R. Gobin, P. A. P. Nghiem, and D. Uriot, "Transport of intense ion beams and space charge compensation issues in low energy beam lines (invited)," *Rev. Sci. Instrum.*, vol. 83, no. 2, p. 02B320, 2012.

[39] T. Kalvas, "IBSIMU Ion Beam Simulator," 2014.

[40] R. Behrisch and W. Eckstein, *Sputtering by Particle Bombardment IV*, vol. 110 of *Topics in Applied Physics.* Berlin: Springer Berlin Heidelberg, 2007.

[41] M. Küstner, W. Eckstein, V. Dose, and J. Roth, "The influence of surface roughness on the angular dependence of the sputter yield," *Nucl. Instrum. Methods Phys. Res., Sect. B*, vol. 145, pp. 320–331, November 1998.

[42] A. Mutzke, R. Schneider, W. Eckstein, and R. Dohmen, *SDTrimSP Version 5.00.* IPP Report 12/08, Max-Planck-Institut für Plasmaphysik (Ed.) http://hdl.handle.net/11858/00-001M-0000-0026-EAF9-A, 2011.

[43] M. Oberkofler, "Private communication." 2018.

[44] G. Binnig, C. F. Quate, and C. Gerber, "Atomic force microscope," *Phys. Rev. Lett.*, vol. 56, pp. 930–933, March 1986.

[45] M. von Ardenne, *Elektronen-Übermikroskopie.* Springer Berlin Heidelberg, 1940.

[46] P. Podsiadlo and G. Stachowiak, "Characterization of surface topography of wear particles by SEM stereoscopy," *Wear*, vol. 206, no. 1, pp. 39 – 52, 1997.

[47] W. H. Bragg and W. L. Bragg, "The reflection of x-rays by crystals," *Proceedings of the Royal Society of London A: Mathematical, Physical and Engineering Sciences*, vol. 88, no. 605, pp. 428–438, 1913.

[48] S. Nishikawa and S. Kikuchi, "Diffraction of cathode rays by mica," *Nature*, pp. 1019–1020, 1928.

[49] K. Siegbahn and K. Edvarson, "β-ray spectroscopy in the precision range of $1 : 10^5$," *Nuclear Physics*, vol. 1, no. 8, pp. 137 – 159, 1956.

[50] D. Briggs. and M. Seah, *Practical Surface Analysis, Auger and X-ray Photoelectron Spectroscopy*, vol. 1 of *Practical Surface Analysis*. Wiley, 1990.

[51] I. A. E. A. Nuclear Data Section, "Ion beam analysis nuclear data library IBANDL." `http://www-nds.iaea.org/ibandl/`, October 2018.

[52] J. R. Tesmer and M. A. Nastasi, eds., *Handbook of Modern Ion Beam Materials Analysis*. Materials Research Society, 1995.

[53] L. C. Feldman and J. W. Mayer, *Fundamentals of surface and thin film analysis*. North-Holland, 1986.

[54] H. Tompkins and E. A. Irene, *Handbook of Ellipsometry*. William Andrew, 2005.

[55] A. Rothen, "The ellipsometer, an apparatus to measure thicknesses of thin surface films," *Review of Scientific Instruments*, vol. 16, no. 2, pp. 26–30, 1945.

[56] T. Schwarz-Selinger, A. von Keudell, and W. Jacob, "Novel method for absolute quantification of the flux and angular distribution of a radical source for atomic hydrogen," *Journal of Vacuum Science & Technology A: Vacuum, Surfaces, and Films*, vol. 18, no. 3, pp. 995–1001, 2000.

[57] W. Eckstein, *Computer Simulation of Ion-Solid Interactions*. Springer Berlin Heidelberg, 1991.

[58] A. Mutzke, R. Schneider, and G. Bandelow, *SDTrimSP-2D: Simulation of Particles Bombarding on a Two Dimensional Target*. IPP Report 12/11, Max-Planck-Institut für Plasmaphysik (Ed.) http://hdl.handle.net/11858/00-001M-0000-0026-E06F-E, 2013.

[59] I. Bizyukov, A. Mutzke, R. Schneider, and J. Davis, "Evolution of the 2D surface structure of a silicon pitch grating under argon ion bombardment: Experiment and modeling," *Nucl. Instrum. Methods Phys. Res., Sect. B*, vol. 268, no. 17, pp. 2631 – 2638, 2010.

[60] U. von Toussaint, A. Mutzke, and A. Manhard, "Sputtering of rough surfaces: a 3D simulation study," *Phys. Scr.*, vol. 2017, no. T170, p. 014056, 2017.

[61] W. Eckstein, "Sputtering yields," in *Sputtering by Particle Bombardment IV* (R. Behrisch and W. Eckstein, eds.), vol. 110 of *Topics in Applied Physics*, ch. Sputtering Yields, pp. 33–187, Berlin: Springer Berlin Heidelberg, 2007.

[62] W. Eckstein, C. Garcia-Rosales, J. Roth, and W. Ottenberger, *Sputtering data.* IPP Report 9/82, Max-Planck-Institut für Plasmaphysik (Ed.) http: //hdl.handle.net/11858/00-001M-0000-0027-6324-6, 1993.

[63] A. V. Golubeva, M. Mayer, Y. M. Gasparyan, J. Roth, and V. A. Kurnaev, "The ion-driven permeation experiment PERMEX," *Review of Scientific Instruments*, vol. 80, no. 7, p. 073501, 2009.

[64] R. C. Davis, O. B. Morgan, L. D. Stewart, and W. L. Stirling, "A multiampere DuoPIGatron ion source," *Review of Scientific Instruments*, vol. 43, no. 2, pp. 278–283, 1972.

[65] G. Schilling, "High power neutral particle beams for fusion research," vol. 5, pp. 309–313, 1974.

[66] R. Smallwood, *ASTM special technical publication 849: Refractory metals and their industrial applications: a symposium.* ASTM International, 1984.

[67] F. Paschen, "Über die zum Funkenübergang in Luft, Wasserstoff und Kohlensäure bei verschiedenen Drucken erforderliche Potentialdifferenz," *Ann. Phys.*, vol. 273, no. 5, pp. 69–96, 1889.

[68] H. von Koch and L. Friedman, "Hydrogen-helium ion-molecule reactions," *The Journal of Chemical Physics*, vol. 38, no. 5, pp. 1115–1122, 1963.

[69] M. Sode, *Quantitative Beschreibung von Wasserstoff-Stickstoff-Argon-Mischplasmen.* PhD thesis, Christian-Albrechts-Universität Kiel, Kiel, 2014.

[70] L. Seidl, *Optimierung des Ionentransports an der Hochstrom-Ionenquelle HSQ-II.* Bachelor Thesis, Technische Universität München, 2016.

[71] J. Wang, E. Boggasch, P. Haldemann, D. Kehne, M. Reiser, T. Shea, and D. Wang, "Performance characteristics of a variable-perveance gridded electron gun," in *IEEE Transaction on Electron Devices*, vol. 37, pp. 2622–2628, IEEE, 1990.

[72] J. Wang, D. Wang, and M. Reiser, "Beam emittance measurement by pepper-pot method," *Nucl. Instrum. Methods Phys. Res., Sect. A*, vol. 307, pp. 190–194, 1991.

[73] R. Janev, W. Langer, K. Evans, and D. Post, *Elementary Processes in Hydrogen-Helium Plasmas*, vol. 4. Springer-Verlag Berlin Heidelberg, 1 ed., 1987.

[74] H. L. Bay, J. Roth, and J. Bohdansky, "Light-ion sputtering yields for molybdenum and gold at low energies," *J. Appl. Phys.*, vol. 48, no. 11, pp. 4722–4728, 1977.

[75] R. Arredondo *et al.*, "Angle-dependent sputter yield measurements of kev D ions on W and Fe and comparison with SDTrimSP and SDTrimSP-3D," *Nuclear Materials and Energy*, vol. 18, pp. 72–76, 2018.

[76] M. Küstner, W. Eckstein, E. Hechtl, and J. Roth, "Angular dependence of the sputtering yield of rough beryllium surfaces," *J. Nucl. Mater.*, vol. 265, no. 1, pp. 22 – 27, 1999.

[77] R. Behrisch and W. Eckstein, "Introduction and overview," in *Sputtering by Particle Bombardment*, ch. 1, Springer Berlin Heidelberg, 2007.

[78] E. Vassallo *et al.*, "Black-silicon production process by CF4/H2 plasma," *Thin Solid Films*, vol. 603, pp. 173 – 179, 2016.

[79] K. Sugiyama, K. Schmid, and W. Jacob, "Sputtering of iron, chromium and tungsten by energetic deuterium ion bombardment," *Nucl. Mater. Energy*, vol. 8, pp. 1–7, 2016.

[80] K. Schlüter, "Private communication." 2018.

[81] V. Chernov *et al.*, "Structural materials for fusion power reactors - the RF R&D activities," *Nuclear Fusion*, vol. 47, no. 8, p. 839, 2007.

[82] R. Lindau *et al.*, "Present development status of EUROFER and ODS-EUROFER for application in blanket concepts," *Fusion Eng. Des.*, vol. 75-79, pp. 989–996, 2005.

[83] K. Sugiyama, M. Balden, S. Elgeti, T. Höschen, M. Oberkofler, J. Roth, and W. Jacob, "Erosion of EUROFER steel by mass-selected deuterium ion bombardment," *Nuclear Materials and Energy*, vol. 16, pp. 114 – 122, 2018.

[84] P. Ström, D. Primetzhofer, T. Schwarz-Selinger, and K. Sugiyama, "Compositional and morphological analysis of FeW films modified by sputtering and heating," *Nuclear Materials and Energy*, vol. 12, pp. 472 – 477, 2017.

[85] P. Ström *et al.*, "Sputtering of polished EUROFER97 steel: Surface structure modification and enrichment with tungsten and tantalum," *Journal of Nuclear Materials*, vol. 508, pp. 139 – 146, 2018.

[86] M. Balden, S. Elgeti, M. Zibrov, K. Bystrov, and T. Morgan, "Effect of the surface temperature on surface morphology, deuterium retention and erosion of EUROFER steel exposed to low-energy, high-flux deuterium plasma," *Nuclear Materials and Energy*, vol. 12, pp. 289 – 296, 2017.

[87] M. F. Ashby and D. R. H. Jones, *Engineering Materials 2.* Pergamon Press, Oxford, 1992.

[88] S. L. Meyer, *Data Analysis for Scientists and Engineers.* Wiley, 1975.

[89] R. Arredondo *et al.*, *SIESTA: a High Current Ion Source for Erosion and Retention Studies.* IPP Report 2018-21, Max-Planck-Institut für Plasmaphysik (Ed.) http://hdl.handle.net/21.11116/0000-0002-53CD-A, 2018.

Appendix A

Calculation of uncertainty in the sputter yield

In this work, the standard error of the sputter yield is calculated by applying the chain rule to equations 4.3 and 5.1. In the case of the sputter yield determined from weight-loss measurements, it can be written as:

$$SY = \frac{\triangle mass\ [\mathrm{g}] \times N_A\ [\mathrm{atoms/mol}]}{N_{ions} \times M\ [\mathrm{g/mol}]} = \frac{\triangle mass\ [\mathrm{g}] \times N_A\ [\mathrm{atoms/mol}] \times e\ [\mathrm{C}]}{3 \times Q\ [\mathrm{C}] \times M\ [\mathrm{g/mol}]},$$

where $\triangle mass$ represents the weight-loss, N_A is Avogadro's number, M is the molar mass of the sample and $N_{ions} = 3 \times Q\ [\mathrm{C}]/e\ [\mathrm{C}]$ is the number of impinging particles when using D_3^+ ions. Q is the accumulated charge and e is the elementary charge. By applying the chain rule [88]:

$$\sigma_{SY} = \sqrt{\left(\frac{dSY}{d\triangle mass}\right)^2 \sigma^2_{\triangle mass} + \left(\frac{dSY}{dQ}\right)^2 \sigma^2_Q}$$

$$\frac{dSY}{d\triangle mass} = \frac{N_A \times e}{3 \times Q \times M}$$

$$\frac{dSY}{dQ} = -\frac{N_A \times e \times \triangle mass}{3 \times Q^2 \times M}.$$

$\sigma^2_{\triangle mass}$ is calculated as the sum of the variances of the weight-loss measurements. σ^2_Q is calculated by applying the relative error of 14% in the current measurement to the accumulated charge. The uncertainty of N_A, e and M is neglected.

When calculating the sputter yield from the thickness of the eroded layer, measured by RBS:

$$SY = \frac{N_{eroded}\ [\mathrm{at/cm^2}] \times S\ [\mathrm{cm^2}]}{N_{ions}\ [\mathrm{at}]} = \frac{N_{eroded}\ [\mathrm{at/cm^2}] \times S\ [\mathrm{cm^2}] \times e\ [\mathrm{C}]}{3 \times Q\ [\mathrm{C}]}.$$

Here N_{eroded} denotes the thickness of the eroded layer in atoms per unit surface and S is the

surface area of the beam-spot at the target. Neglecting the uncertainty of e:

$$\sigma_{SY} = \sqrt{\left(\frac{dSY}{dN_{eroded}}\right)^2 \sigma^2_{N_{eroded}} + \left(\frac{dSY}{dQ}\right)^2 \sigma^2_Q + \left(\frac{dSY}{dS}\right)^2 \sigma^2_S}$$

$$\frac{dSY}{dN_{eroded}} = \frac{S\times e}{3\times Q}$$

$$\frac{dSY}{dQ} = -\frac{N_{eroded}\times S\times e}{3\times Q^2}$$

$$\frac{dSY}{dS} = \frac{N_{eroded}\times e}{3\times Q}.$$

$\sigma^2_{N_{eroded}}$ is the sum of the variances of the RBS measurements of the layer thickness before and after sputtering. σ^2_Q is calculated by applying the relative error of 14 % in the current measurement to the accumulated charge and σ^2_S is the variance in the measurement of the beam footprint, obtained by measuring the beam footprint several times for each sputter yield measurement.

Appendix B

Calculation of uncertainty in the EUROFER experiments

In section 5.3, the reduction of the sputter yield of EUROFER bombarded with 200 eV D to a fluence of $1.14 \times 10^{24}\,\mathrm{D\,m^{-2}}$ at 300 K was assessed as a function of the surface morphology and the W surface enrichment. The equations listed there can be stated as:

$$F = \frac{SY_{Morphology}}{SY_{1D\,static}} = S \times M_R + (1 - S) \times M_S$$

$$E = \frac{SY_{Enrichment}}{SY_{1D\,static}}$$

$$G = \frac{SY_{Combined}}{SY_{1D\,static}} = \frac{SY_{Morphology}}{SY_{1D\,static}} \times \frac{SY_{Enrichment}}{SY_{1D\,static}} = F \times E.$$

Here, F is the overall sputter yield reduction factor attributable to surface morphology. $SY_{1D\,static}$ denotes the sputter yield of EUROFER under the experimental conditions as calculated with SDTrimSP without the influence of surface morphology or surface enrichment. $SY_{Morphology}$ is the combined sputter yield due to smooth and rough surface morphologies, weighted by the relative area occupied by each kind of surface morphology $S = 0.70 \pm 0.05$. $M_R = 0.76$ is the reduction factor found in the rough surface morphology and $M_S = 0.15 \pm 0.15$ denotes the corresponding reduction factor in the smooth surface morphology. $SY_{Enrichment}$ is the sputter yield of enriched EUROFER, with E being the reduction factor due to W and Ta surface enrichment ($E = 0.64 \pm 0.03$). $SY_{Combined}$ denotes the combined sputter yield due to surface morphology and surface enrichment, and $G = F \times E$ is the corresponding reduction factor. By applying the chain rule, assuming $\sigma_{M_R} = 0$:

$$\sigma_F = \sqrt{\left(\frac{dF}{dS}\right)^2 \sigma_S^2 + \left(\frac{dF}{dM_S}\right)^2 \sigma_{M_S}^2}$$

$$\frac{dF}{dS} = M_R - M_s$$

$$\frac{dF}{dM_S} = 1 - S\,.$$

Finally, σ_G can be estimated by applying [88]:

$$\sigma_G \approx G \times \sqrt{\left(\frac{\sigma_F}{F}\right)^2 + \left(\frac{\sigma_E}{E}\right)^2}\,.$$

Appendix C

Sputter yields simulated with SDTrimSP

All simulations were performed with the following parameters:

idrel = 1 (full static calculation)

iintegral = 2 (Gauss-Legendre quadrature)

ipivot = 8 (8 integration pivots)

ipot = 1 (KrC interaction potential)

isbv = 3 (determines the composition dependent surface binding energy)

The sputter yields calculated in this work are listed in the following table.

Projectile	Energy [eV]	Target	Angle of incidence	Sputter yield
D	2000	Fe	0°	0.051
D	2000	Fe	45°	0.094
D	2000	Fe	60°	0.15
D	2000	Fe	75°	0.28
D	2000	W	0°	0.013
D	2000	W	45°	0.018
D	2000	W	60°	0.028
D	2000	W	75°	0.051
D	2000	Au	0°	0.037
D	200	Fe	0°	0.040
D	200	Bulk EUROFER	0°	0.040
D	200	Enriched EUROFER	0°	0.026
Ar	10000	Fe	0°	3.73
Ar	10000	W	0°	2.87

Table C.1: Sputter yields calculated with SDTrimSP used in this work.

Appendix D

SIESTA technical documentation

Technical documentation for SIESTA (operating instructions, safety documentation and vacuum pump specifications) is available in the SIESTA IPP report [89].